Fakultät Maschinenbau
fortschritt studieren

RUHR UNIVERSITÄT BOCHUM **RU**B

Fundamental investigation of the atomic structures of [111] tilt grain boundaries, their defects and segregation behaviour in pure and alloyed Al

Dissertation

zur

Erlangung des Grades

Doktor-Ingenieur

der

Fakultät für Maschinenbau

der Ruhr-Universität Bochum

von

Saba

aus

Nagina, Indien

Bochum 2022

When one door closes, another opens; but we often look so long and so regretfully upon the closed door that we do not see the one, which has opened for us.

-By Alexander Graham Bell

-Dedicated to my lovely family

Acknowledgements

Abstract

Aluminum (Al) and its alloys are in great demand and are vital to various industries such as aerospace, construction, transportation and packaging industries, etc. From an engineering perspective, a lot of research has been carried out with the aim to gain a comprehensive understanding of their behavior and performance, which paved the way to design Al alloys with enhanced properties. One of the most influential factors, which strongly affects the behavior and properties of the materials, is the lattice defects. This includes grain boundaries (GBs), dislocations and disconnections, etc. Furthermore, in the last few decades, special attention is being paid to unearth the impact of the GB's atomic structures and chemistry on the GB properties, since bulk properties can be impacted by the GB properties. Improvements in transmission electron microscopy (TEM) and atomistic simulations have made this possible. However, yet, the experimental observation of the local atomic structure and chemistry introduces extremely challenging experimental conditions and restricts this field today. The PhD thesis focuses on the in-detailed investigation of the atomic structures of [111] tilt grain boundaries in pure Al and its alloys by atomic resolution scanning TEM (STEM) in combination with atomistic simulations. The main aim of the thesis is to discover the atomic structures of pure Al GBs as a function of different macroscopic and microscopic GB parameters and then to understand how the structure is influencing the local excess properties of the GBs. Furthermore, how the solute elements are interacting with the pure [111] tilt boundaries is investigated in detail and its implications have been discussed.

In the first part of the thesis, in order to fabricate [111] tilt GBs (to investigate the atomic structures), pure Al thin films are grown on (0001) sapphire (α-A_2O_3) substrate with the temperature range between room temperature and 300°C via e-beam evaporation. A template of processing parameters are developed for depositing the films with the desired characteristics such as smooth and dense surface, large grain size and a wide distribution of [111] tilt columnar GBs. Due to the strong [111] texture of the Al films, we have now two adjacent [111] oriented grains allowing to resolve the GBs motifs on atomic scale. The electron back scattered diffraction investigations revealed that the Al film mainly consists of a high fraction of low angle tilt GBs followed by a low fraction of high angle special tilt GBs such as $\Sigma3$, $\Sigma13b$, $\Sigma7$, $\Sigma19b$, $\Sigma21a$, $\Sigma37c$ and other higher Σ coincidence site lattice (CSL) boundaries. Furthermore, high angle annular dark

field investigation of the atomic structure of a low angle GBs (LAGBs), discloses the dissociation of perfect dislocations into partial dislocations at the GBs (in a direction normal to the GB), despite having a high stacking fault energy (SFE) of Al. Moreover, how the configurations of partial dislocations vary with increase in the misorientation angle is explored and its association with the GB energy is further discussed.

Besides the low angle GBs, it is known from the literature that high angle GBs' (HAGB) properties and behavior are very different to LAGBs. Hence, in order to understand the global behavior of a polycrystalline material, the atomic structures of HAGBs need to be examined. Hence, in the next part, the effect of microscopic translations of the atoms at the GBs with fixed macroscopic parameters are investigated. Two different microstates of incoherent $\Sigma3$ [111] $(11\overline{2})$ GBs from two different orientation relationships (ORs), comprised of slightly different structural units, are identified. The structural units in ORII ($\{111\} \pm <0\overline{1}1>$ Al $||$ (0001) $<2\overline{1}\overline{1}0>$ α-Al$_2$O$_3$) exhibit hexagonal units while in ORI ($\{111\} \pm <0\overline{1}1>$ Al $||$ (0001) $<10\overline{1}0>$ α-Al$_2$O$_3$), the hexagonal units are slightly distorted. Molecular statics simulations, employed to understand the difference in excess properties of both states revealed that strain could potentially contribute to the stability of the ORII GB microstate over the ORI microstate. In addition, the atomic structure of the two ORs along the <110> zone axis shows the rigid body microscopic translations of different magnitude of $\{111\}$ planes across the GB experimentally. Furthermore, in the case of asymmetric variants of the same GBs, different types of $\Sigma3$ [111] disconnections with Burgers vectors ($\mathbf{b}_1 = 1/6[\overline{11}2]$), ($\mathbf{b}_2 = 1/2[\overline{1}01]$) and varying step heights ($h = 2a_{\mathrm{dsc}}$, $5a_{\mathrm{dsc}}$) are investigated and their implications on the GB behaviour are discussed.

Thereafter, the relationship between the structures of various GBs throughout a misorientation (θ) range for a particular tilt axis i.e. [111] and inclination of the boundary plane is explored. The atomic structures of high angle symmetric tilt GBs such as $\Sigma21a$, $\Sigma13b$, $\Sigma7$, $\Sigma19b$, $\Sigma37c$ and $\Sigma3$ are investigated. One of the major findings is that two different misorientation groups (Group 1 and 2) consisting of two distinct type of structural units (SUs), are found. The $\Sigma21a$, $\Sigma13b$ and $\Sigma7$ CSL GBs belong to group 1 with a misorientation range of $21° < \theta < 34°$. Here, the atomic structures of the GBs consist of "bow and arrow" shaped units (B/B') or a combination of B/B' and A units, also termed "bow and arrow" type structure. While $\Sigma19b$, $\Sigma37c$ and $\Sigma3$ GBs are associated to group 2 with a misorientation range of $46° < \theta < 60°$. They have either square shaped units (E, E' and

E'') or a combination of square units and trapezoidal shape F units. The atomic structure of the GBs in group 2 is referred to "zipper" type structure. It is observed that as the misorientation increases from Σ21a to Σ7 GB, A units are disappearing from the GBs and diminishes completely at 38°. With the corresponding atomistic simulations, the influence of the atomic structure on the interfacial excess properties of the GBs like different excess volumes and stresses are evaluated. Interestingly, we found our simulated structures matches quite closely with the experimental ones and possess different excess properties. However, no trend in excess properties is found with increasing misorientation unlike in the experimental observation i.e. reduction of A type units. In addition, different atomic structures of the GBs are found on investigating the symmetric variants (GB plane inclination changes by 30°) of the GBs in group 1. Apart from a very different atomic arrangement for the two symmetric variants of a GB with fixed misorientation, also their excess properties are found to be very different to each other.

In the final part of the thesis, conventional TEM and aberration-corrected STEM coupled with energy dispersive X-ray spectroscopy are used to explore the interaction of the solute elements like Cu and Zr with the [111] tilt GBs in pure Al, in terms of how a solute atom is segregating to the GB and affecting its atomic structure. For that, the surface of the pre examined Al film is first cleaned with Ar-sputtering to remove the strong native Al_2O_3 oxide (which always prevails on Al surface and acts as a barrier to diffusion). Thereafter, the Al-(Zr/Cu) films are annealed in two steps. This is done to have the sufficient amount of diffusion of the solute elements from the top layer towards the GBs. The results obtained after the first annealing of Al films (with Zr-Cu reservoir on top) to 450°C for 6 hrs showed that the GBs are highly inclined in comparison to the pure Al films (with native oxide). Due to an abrupt change in the inclination of the GB plane, a higher number of facets/steps are introduced at the GBs. Furthermore, Cu is identified as the only primary alloying element that is segregated at the Al GBs and leads to the occurrence of two different segregation patterns at the GBs i.e. monolayer (from low angle up to misorientation of 26°) and bilayer segregation (with a misorientation of 31°). No Zr is found at all after first annealing, neither at the GB nor in the bulk. The absence of Zr segregation after 450°C annealing indicates that Cu (present in the reservoir at the top of the Al) is diffusing very fast to the GBs as well as in the bulk, while Zr has very low diffusion rate at 450°C. The solubility of Cu in Al is high at elevated temperatures in contrast to Zr. However, upon cooling, the Cu solubility is decreasing with lower temperature and Cu is found to be segregating to the GBs.

Hence, to enhance the diffusivity of Zr, the film is further annealed in a second thermal treatment at 520°C for 32 hrs. Interestingly, despite being exposed to such high temperature, no Zr segregation was found at any of the GBs, be it low angle GBs or high angle Σ21a GBs. Rather, it is found that needle shaped precipitates are formed at high angle Σ21a GB that correspond to the L1$_2$ Al$_3$(Cu$_x$Zr$_{1-x}$) cubic (metastable) phase with some amount of Cu in it. This suggested that the pre-segregated Cu at the GB reduces the nucleation barrier for the formation of Al$_3$(Cu$_x$Zr$_{1-x}$) precipitates. Furthermore, there is a clear indication that the presence of Cu limits the Zr segregation into the GBs.

Preface

Manuscript I

Influence of substrate temperature on the distribution of edge-on [111] tilt grain boundaries (GBs) in Al thin films deposited via e-beam evaporation

Saba Ahmad, Hanna Bishara, Christian H. Liebscher and Gerhard Dehm

Manuscript ready for submission

Manuscript II

Microstates and defects of incoherent Σ3 [111] twin boundaries in aluminum

Saba Ahmad, Tobias Brink, Christian H. Liebscher and Gerhard Dehm

Acta Materialia, **p.118499** (November 2022)

Manuscript III

Deciphering the atomic structures of [111] tilt GBs as a function of 5 macroscopic parameters in Al by correlating STEM with atomistic simulations

Saba Ahmad, Tobias Brink, Christian H. Liebscher and Gerhard Dehm

Manuscript ready for submission

Manuscript IV

Interaction of Cu and Zr with the atomic structures of pure [111] tilt boundaries in Aluminum

Saba Ahmad, Simon Evertz, Jochen Schneider, Christian H. Liebscher and Gerhard Dehm

Manuscript in preparation

Paper I: Hanna Bishara grew all the Al thin films used in this paper at the Max-Planck-Institut für Eisenforschung GmbH in Düsseldorf. The scanning electron microscopy (SEM) and electron back scattered diffraction (EBSD) characterization of the Al films were performed by Saba. She also prepared all the electron transparent specimens by plasma focused ion beam and carried out all the scanning/transmission electron microscopy (S/TEM) measurements including all the analyses. The manuscript was written by Saba. All authors have contributed to the interpretation and discussion of the results and revised the manuscript.

Paper II: The Al thin film employed in this paper was grown and annealed by Gerhard Dehm and Gunther Richter at the Max-Planck-Institut für Metallforschung (now MPI for Intelligent Systems) in Stuttgart. Saba did all the experimental work that includes SEM, EBSD and S/TEM measurements and the corresponding analysis. She also conducted the image simulations using the ab-TEM code. Tobias Brink performed all the molecular static simulation and DFT calculations. The manuscript was written by Saba with the contribution from Tobias Brink about the simulation techniques and their results. All authors have discussed the results, interpreted the data and revised the manuscript.

Paper III: For this work, the same Al film grown and annealed by Gerhard Dehm and Gunther Richter as in Paper II was employed. The SEM, EBSD and the S/TEM measurements on the Al film and the GBs were performed by Saba. She conducted all the analyses associated with the experimental data. Tobias Brink performed the GB structure prediction and evaluation of their excess properties by using atomistic simulations. Saba wrote the manuscript with the contribution from Tobias Brink. All authors have discussed the results and revised the manuscript.

Paper IV: Simon Evertz performed the cleaning of the native oxide from the surface of the Al film with Ar and performed the sputtering of Cu and Zr on the top of the pure Al films. Saba has conducted the annealing experiments and the characterization of the alloyed Al films and the GBs with the help of SEM, EBSD and S/TEM measurements. All the corresponding analysis were done by Saba. In addition, she is writing the final manuscript. The discussion and analysis of the findings have been aided by contributions from all authors.

Table of contents

Abbreviation

AC	Alternating current
Al	Aluminium
ABF	Annular bright field
Ar	Argon
Z	Atomic number
BFP	Back-focal plane
BSE	Backscattered electrons
BF	Bright field
CCD	Charge coupled device
CSL	Coincidence-site lattice
CMOS	Complementary metal oxide semiconductor
CTF	Contrast transfer function
CTEM	Conventional transmission electron microscopy
CBED	Convergent beam electron diffraction
DF	Dark field
DOF	Degrees of freedom
DP	Diffraction pattern
DC	Direct current
DSC	Displacement shift complete
EBSD	Electron Backscatter Diffraction
e-beam	Electron beam
EM	Electron microscopy
EBSP	Electron-backscattered pattern
EAM	Embedded atom model
EDX	Energy Dispersive X-ray Analysis
ET	Everhart-Thornley
FIB	Focused ion beam
GIS	Gas injection system
GPA	Geometric phase analysis
GB	Grain boundaries

HAADF	High angle annular dark field
HIPIMS	High power impulse magnetron sputtering
HRTEM	High-resolution transmission electron microscopy
ICP	Inductively coupled plasma
IC	Integrated circuits
LME	Liquid metal embrittlement
LMIS	Liquid metal ion source
LAADF	Low angle annular dark field
LAGBs	Low angle grain boundaries
MS	Molecular static
OIM	Orientation Imaging Microscopy
PVD	Physical Vapor Deposition
PFIB	Plasma focused ion beam
Pt	Platinum
RF	Radio-frequency
SEM	Scanning Electron Microscope
STEM	Scanning transmission electron microscopy
SE	Secondary electrons
SAD	Selected area diffraction
SFE	Stacking fault energy
SCC	Stress corrosion cracking
SUM	Structural unit model
SZM	Structure zone model
3D	Three – dimensional
TEM	Transmission electron microscopes
2D	Two – dimensional

Chapter 1 Introduction

1.1 Aim and outline of the thesis

Aluminium (Al) and its alloys are one of the most commercially used engineering metallic materials, opening up new paths into the modern world. Al alloys are availed for widespread industrial application to make a wide range of products such as marine parts, automotive parts, structural parts and components of smart phones, etc. [1–4]. Al alloys are in great demand due to their superior properties that includes lightweight together with very high strength, excellent thermal and electrical conductivity, outstanding machinability, etc. [5–7]. Furthermore, Al alloys recyclability and their high resistance to oxidation and corrosion make them unique and special in terms of their versatility and environmental amiability [8–10]. However, several technically important alloys such as 2XXX, 6XXX and 7XXX series alloys, which are used in structural applications, are highly susceptible to intergranular corrosion and stress corrosion cracking (SCC). In both cases, the materials fail along the grain boundaries (GBs), on exposure to stresses and/or certain environment (solutions/ liquids/ air/ water vapour etc.) [11,12]. This has led to the failure of the structural components in aircrafts as reported in the literature [13]. Similarly, several heat treatable Al alloys are also highly prone to abnormal grain growth, which substantially deteriorates their strength such as during friction stir welding while joining components of these alloys [14–16]. Given that the majority of engineering alloys are polycrystalline and made up of a 3D network of GBs (regions of atomic mismatch between the two differently oriented grains) distributed throughout the material, their bulk behavior are significantly influenced by the properties of these internal interfaces (GBs) [17,18]. These GB properties are mainly translated by the local atomic structure and chemistry of a GB. This means that the type of a GB, segregated impurity on a GB and presence of different defects at it play an important role in driving all the aforementioned GB related phenomena in materials [19–21]. Therefore, in order to comprehend the atomistic mechanism of these phenomena fundamentally, it is of utmost importance to understand the underlying atomic structure and chemistry of a GB. This facilitates us to answer the many unresolved scientific questions related to GBs such as whether a specific segregating element,

causing an abrupt change in GB properties is detrimental or beneficial to a GB. The knowledge about these fundamental attributes of the GBs paved for advanced new alloys to be designed via GB engineering.

Geometrically, eight degrees of freedom (DOF), including five macroscopic and three microscopic DOFs, are used to fully define GBs. Out of the 5 macroscopic DOFs, three of the them specify mutual misorientation of the two adjoining grains and two of them represent the orientation of the GB plane between the two crystals [22]. However, these five parameters do not adequately describe the atomic structure of a GB. Numerous studies disclose the existence of multiple stable and metastable states for a GB with fixed macroscopic parameters, that are distinguished by distinct thermodynamic excess properties [23–27]. This is due to the possible rigid body microscopic translations in the GB plane that lead to the emergence of different states (atomic structures) of the GBs [28–31]. These states have also been called GB phases [32] or complexions [33–35]. In the last few decades, many efforts have been made in order to unravel the atomic structure of these states or phases, but the majority of them are limited to simulations [36–38]. However, in many cases, real experimental structures of the GBs look very different compared to the predicted ones obtained by the simulation methods [25,36,39]. Recent advancements in aberration-corrected transmission electron microscopes (TEM) have made it possible to see the actual atomic structures and chemistry of the GBs. However, yet, very few experimental studies in combination with simulations correlating the atomic structures of GBs and their properties are reported in the literature [25,40–44]. Furthermore, there is still a lack of a detailed understanding of the atomic structures, segregation, defects, and phase transformations of a GB and how they influence the GB properties, which is the motivation behind all the current work in the following thesis.

The main aim of the work described in the thesis is to investigate the atomic structure of the [111] low angle tilt GBs and special high angle GBs in order to establish a link between the structures and the GB properties. Furthermore, another objective of the work is to study the implications of solute segregation on the atomic structures of the pre-examined pure Al GBs. Pure Al has been chosen as a model system in this study. The reason for that is although a lot has been investigated about the properties and the macroscopic behaviour of Al GBs, however very little is known about the local atomic scale configurations of the GBs, which plays a vital role in several GB related

phenomena such as GB cohesion, stress corrosion cracking at the GB, abnormal grain growth, etc. Understanding the pure and segregated atomic structures of the GBs and their effect on the GB properties lay the foundations for controlling such GB related phenomena. In order to accomplish the aim, Al thin films having pure [111] tilt GBs are grown via physical vaporization techniques. The combination of electron backscatter diffraction (EBSD) and plasma focused ion beam (PFIB) make the recurrent extraction of specific pre-examined GBs possible, in order to compare the pure, annealed and alloyed GB. Methods such as thin film depositions, scanning electron microscopy (SEM), and aberration-corrected TEM techniques together with energy-dispersive X-ray spectroscopy (EDS), are coupled with atomistic simulations in this study with the aim to observe the GB structures and the local chemistry. The current outline of the work consists of following main investigations:

After the introduction, **Chapter 2** describes the background details and the literature study related to the GBs in general, their atomic structures, chemistry, defects and transitions. This chapter also consists of the background description and studies on Al and its alloys. **Chapter 3** provides a brief introduction to all the experimental techniques employed in this work. The comprehensive characterizations carried out on the Al thin films and Al GBs are explained in detail in **Chapter 4**. This chapter focuses on the experimental details of the Al thin film growth, annealing treatments, sample preparation and the characterization techniques involved.

Chapter 5 reports the results obtained in this thesis on the synthesis of tilt GBs in Al thin films, GB atomic structures and segregation in the following 4 sub-chapters. A detailed study on the synthesis of defined epitaxial thin films in order to design a template of the processing parameters is reported in **Chapter 5.1**. The influence of the substrate on the microstructural evolution of the Al film has been studied in this chapter. In addition, the configuration of fcc dislocations at the low angle GBs in Al has been examined and the effect of the misorientation on the dislocation configuration has been explored.

Chapter 5.2 focuses on the findings of the microscopic investigation of the atomic structures of several high angles GBs (with different misorientation). Furthermore, the influence of different GB habit planes of a CSL GB on their atomic structures and the interfacial excess properties is explored and discussed in detail. **Chapter 5.3** discusses the influence of microscopic translations on the atomic structure of an incoherent twin GBs in both the ORs in the Al film, despite having

similar macroscopic degrees of freedom. This chapter reports the detailed analysis of the experimental structure by STEM in combination with atomistic simulation and DFT calculations, which together explains the emergence of two different structural motifs and further evaluate the excess properties of both the structures. Furthermore, the defects present in both the ORs, investigated by STEM are also reported and their implications on the GB behaviour is discussed.

In the final part, the interaction of segregating elements like Cu and Zr with the atomic structure of Σ21a and Σ13b GBs has been systematically studied and reported in **Chapter 5.4**.

Chapter 6 summarizes the outcomes of the study. The results obtained in the study are combined to give an overview of the atomic structures of the [111] tilt GBs in pure and alloyed Al. The detailed microstructural characterization via electron microscopy techniques and simulation results are coupled to explain the atomic structure and properties of the GB. The investigations carried out help in comprehending the correlation between the structure and properties of the GBs in general.

Chapter 2 Background and Literature

2.1 Introduction to grain boundaries

Grain boundaries are the internal interfaces between two differently oriented crystals inside the polycrystalline materials. GBs are the two – dimensional (2D) defects that are paradoxical in nature. On the one hand, GBs acts as an obstacle to dislocation glide, thereby providing resistance to deformation in the material [45]. While on the other hand, due to their high energy, they are the preferential sites for many degradation processes such as crack formation [46,47], reduced strength due to enrichment of impurity atoms causing GB decohesion [48,49], abnormal grain growth [50] and GB corrosion [51], etc. Since the GBs spread throughout the polycrystalline materials in the form of a three – dimensional (3D) net, undoubtedly, they substantially affect the global properties and behaviour of the materials. This is because the bulk behaviour of the material is highly controlled by the GB properties such as GB interfacial energy, GB cohesive strength, and GB sliding, etc. More or less, all of these GB properties are highly influenced by the complex atomic structure and chemical state of a GB that often possesses a different atomic arrangement than the two adjoining crystals. In the past decades, many efforts have been made in order to understand the atomic structure of the GBs and their properties, but are mainly limited to simulation. This is due to the experimental constraints associated with it, mainly, the unavailability of advanced STEM techniques during former times (with better atomic resolution) and the stringent edge-on conditions of the GBs to study the structures. There is still a lack of understanding of several aspects related to the GBs such as how the local atomic structure is changing as a function of misorientation angle or GB plane, interfacial defects, various impurity elements in reality and how these structures are associated to GB properties.

2.2 Grain boundaries geometrical description

Geometrically, GBs are described by a total of eight parameters [52] that include five macroscopic degrees of freedom (DOFs) and three microscopic DOFs, schematics of which are illustrated in **Figure 2-1**. Out of the five independent macroscopic parameters, three of them illustrate the misorientation between the two adjacent crystals described by a rotation axis $\vec{r} = [h_0 k_0 l_0]$ and a

misorientation angle θ. While two of them specify the orientation of the GB plane w.r.t the two adjacent crystals, defined by a normal vector to the GB plane i.e. $\vec{n} = [h_g k_g l_g]$. By utilizing these five parameters, GBs are formally expressed as follows:

$$\theta \, [h_0 k_0 l_0] \, , (h_{g1} k_{g1} l_{g1}) \, / \, (h_{g2} k_{g2} l_{g2}) \qquad\qquad 2.1$$

(a)

(b)
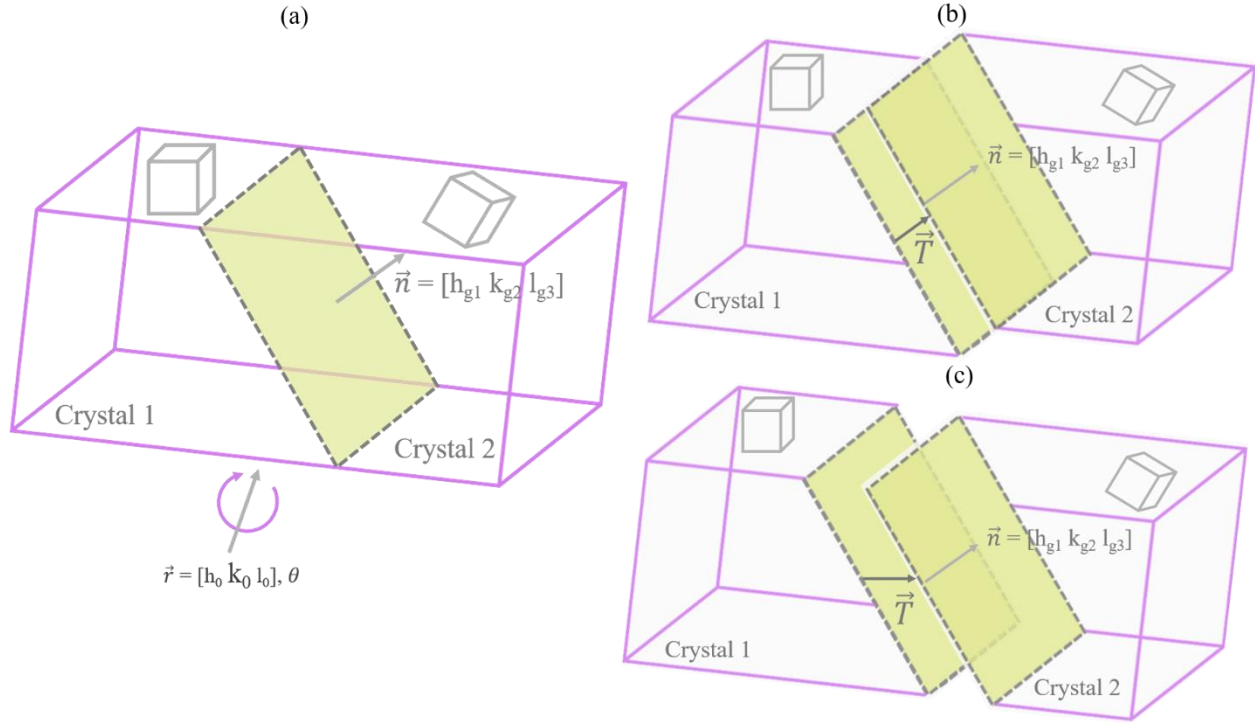
Figure 2-1: Schematic illustration of eight degrees of freedom to define a GB. **a)** represents five macroscopic degrees of freedom described by $\vec{r}$, θ, and $\vec{n}$. **b)** and **c)** depict two different modes of rigid body translation i.e. sliding and volume expansion of the GB, described by a translation vector $\vec{T}$.

Apart from this, three parameters are required to describe the microscopic degrees of freedom that specify the rigid body translation of both the grains, characterized by a translation vector $\vec{T} = [t_1 t_2 t_3]$ [52]. These translations can occur in both the directions: the parallel and/or the perpendicular to the GB plane $\vec{n}$ leading to volume expansion and shear between the two adjacent crystals, respectively [53]. These rigid body translations are thought to occur from relaxation events in order to reduce the energy of the boundary, corresponding to the equilibrium structure of a GB [22,52]. The atomic structure of a GB is highly sensitive to all the aforementioned parameters and therefore variation in any of the GB parameters influences the atomic arrangement of the GB and eventually affect the GB properties. Hence, in general, GBs are categorized into various sub groups depending on the correlation between the discrete geometric parameters [22]. This signifies

the infinite number of possible GBs theoretically, however in reality only few GB inclinations are possible due to energetic reasons. For example: on observing a GB at low magnification (in SEM), a curved boundary may indicate that many different GB plane inclinations coexist. However, on the atomic scale (in S/TEM), the boundary could consist of only specific symmetric and asymmetric inclinations associated with lower energy.

Based on the relationship between rotation axis $\vec{r}$ and the GB plane $\vec{n}$, GBs are described as a tilt ($\vec{r} \perp \vec{n}$) or a twist ($\vec{r} \parallel \vec{n}$) GB. Similarly, tilt GBs are further characterized into symmetric and non-symmetric GBs depending on the type of GB plane. The boundary is referred to as symmetric, if the GB plane lies exactly on the mirror symmetric plane between the two adjoining crystals such that $(h_{g1}k_{g1}l_{g1}) = (h_{g2}k_{g2}l_{g2})$. Other GBs, which do not satisfy the above criteria, are called asymmetrical. Moreover, GBs can also be classified as low angle ($\theta < 15°$) and high angle GBs ($\theta > 15°$), depending on the magnitude of the misorientation angle θ. Currently, it is unquestionably an established fact that in general most of the GBs in metals and alloys are crystalline in nature [22,52]. From the definition of a GB as mentioned above, it is evident that the positions of the atoms are usually displaced in the mismatched region relative to the interior of the crystal. Taking into account the crystalline nature of a GB, there are several models developed to describe the atomic structure of a GB. Starting from the very first Read and Shockley dislocation model [54], which describes that the structure of GBs having a low misorientation angle are accommodated by an array of dislocations (edge dislocations forms tilt GBs, while screw dislocations forms twist GBs), also shown in **Figure 2-2 a)** [55]. This model provides an expression that relates the misorientation angle θ to the dislocation spacing D and the magnitude of the Burgers vector $|\vec{b}|$, described as follows:

$$2 \sin\frac{\theta}{2} \approx \theta = \frac{|\vec{b}|}{D} \qquad\qquad 2.2$$

Based on the theory of elastic continuum, the energy of a low angle tilt GB (γ_{GB}) as a function of misorientation angle (For Al, please see **Figure 2-2 b)**) is expressed as:

$$\gamma_{GB} = \frac{\mu b}{4\pi(1-\nu)}\left(\frac{b}{2\pi r_0} - \ln\theta\right)\theta \qquad\qquad 2.3$$

Here, r_0, μ and ν are the dislocation core radius, the shear modulus and the Poisson's ratio, respectively. However, the model only holds well for the GBs with misorientation angle of $\theta <$ 15°. For higher misorientation angle, D decreases and the dislocation gets so close that the dislocation cores start to overlap each other, thereby reaching the limit of this model. Furthermore, the energy of a GB becomes independent of the misorientation angle for higher angles [56]. Moreover, this dislocation model does not take into account the interaction of the GBs with the nearby defects or vacancies and the influence of microscopic translations etc. on the atomic structure. **Figure 2-2 b)** is adapted from the ref. [57,58]
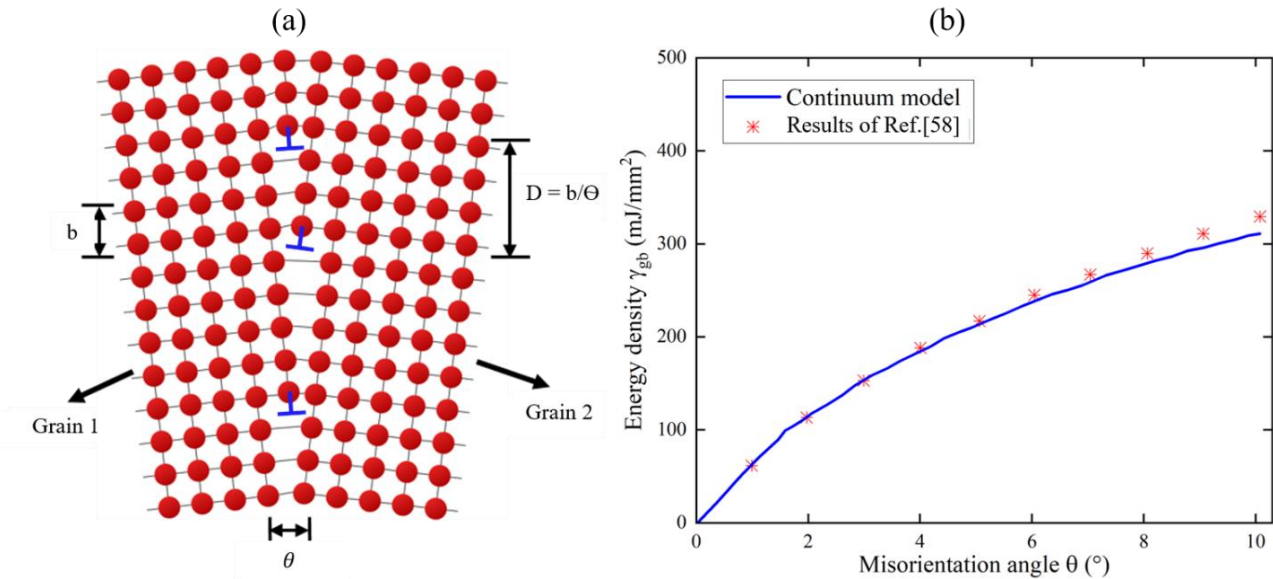
Figure 2-2: Illustration of a low-angle GB. a) represents the structure of a low-angle GB consisting of an array of edge dislocations at the GB. **b)** shows the plot of the energy of a low angle tilt GB as a function of the misorientation angle. The plot clearly indicates that the energy of a LAGB increases as the misorientation angle increases, following the Read-Shockley model. Both the figures **a)** and **b)** are adapted with permission from the Refs [57,58], respectively.

It is found that there is the potential that a complex dissociated dislocation configuration may emerge at these low angle grain boundaries (LAGBs) in order to further reduce the energy of the GBs such as dissociation of a full dislocation into a periodic array of two partials dislocations [59,60]. The presence of different configurations is highly dependent on the stacking fault energy (SFE) of the material, which means these different configurations are possible only at the GBs in low SFE material. However, so far such configurations have not been examined for high SFE materials like Al experimentally by any atomic scale observations. Since LAGBs are present in significant amount in polycrystalline Al, investigating the different possible configurations at LAGBs may advance our understanding on the plastic deformation of Al.

8

Moving forward to the high angle GBs, there exists a special class of GBs called coincidence-site lattice (CSL) boundaries. Around 60 years ago, Kronberg and Wilson [61] developed this CSL model to describe these special GBs. It was postulated on the basis that the special GBs have less number of broken bonds, hence possess a lower GB energy than the random high angle GBs [22]. This model proposed that the overlay of the two lattices oriented along a specific direction having a certain misorientation between them leads to the emergence of a dichromatic pattern, which has a coincidence/overlap of some of the lattice points, called coincidence sites. The superlattice consisting of all these coincided lattice points is called the coincidence-site lattice (CSL). Σ defines the ratio of the CSL lattice points to the total number of lattice points that signifies the degree of matching between the two grains. A particular example of Σ5 in a cubic crystal is illustrated in **Figure 2-3**.
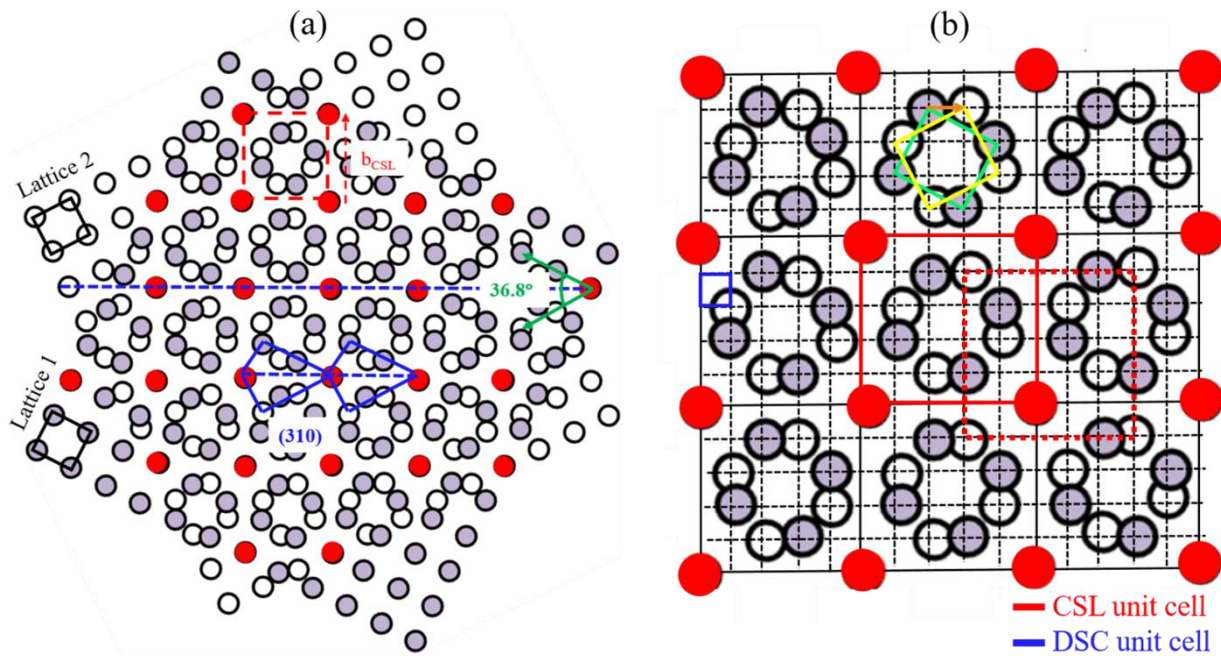
Figure 2-3: Generation of a coincidence-site lattice for a Σ5 GB with a misorientation angle of 36.87°. a) Two identical [001] lattices 1 and 2 are rotated by a specific misorientation angle corresponding to Σ5, resulting in a dichromatic pattern with some coincidence lattice points (indicated by red colour circle) called CSL points/sites. Blue dashed horizontal line indicates the trace of the GB plane. **b)** shows CSL and displacement shift complete (DSC) unit cell, indicated by red and blue squares respectively. Translation of lattice 1 w.r.t lattice 2 (from green to final yellow square) shifts the origin of the CSL lattice without changing the CSL pattern, corresponding to a DSC lattice vector (indicated by an orange arrow). A newly placed CSL unit cell is shown as a dashed red square.

It is evident from the figure that every fifth atom is coinciding in the dichromatic pattern. In many studies [62–65], special behaviour of some of the GBs was found, where there is a high density of

atomic fit at the GB (means low mismatch), especially associated with the low value of Σ, also shown in **Figure 2-3 a**).

Apart from being very successful and popular, the CSL model is very simple and purely geometrical model that does not take into account the impact of the GB plane [25] and microscopic translations into the structure of a GB [36]. Furthermore, GBs in reality may also consist of defects at the GB such as dislocations, steps or disconnections. Therefore, in order to describe such defects at the GB, the "displacement shift complete" (DSC) lattice is established. These defects at the GB should be associated to the Burgers vector that preserve the CSL relationship. The DSC lattice is a sub-lattice of CSL that consists of all such minimum displacement vectors (as highlighted by black dashed line in **Figure 2-3 b**)), which conserve the CSL relationship. This means on translating lattice 1 w.r.t lattice 2 along the displacement vectors, the CSL pattern remains the same, however its origin is shifted. DSC lattice vectors describes the possible Burgers vector of a disconnection and/or height of a step, which are often present at the GB structure. A detailed description of the DSC lattice is provided in the Ref [66].
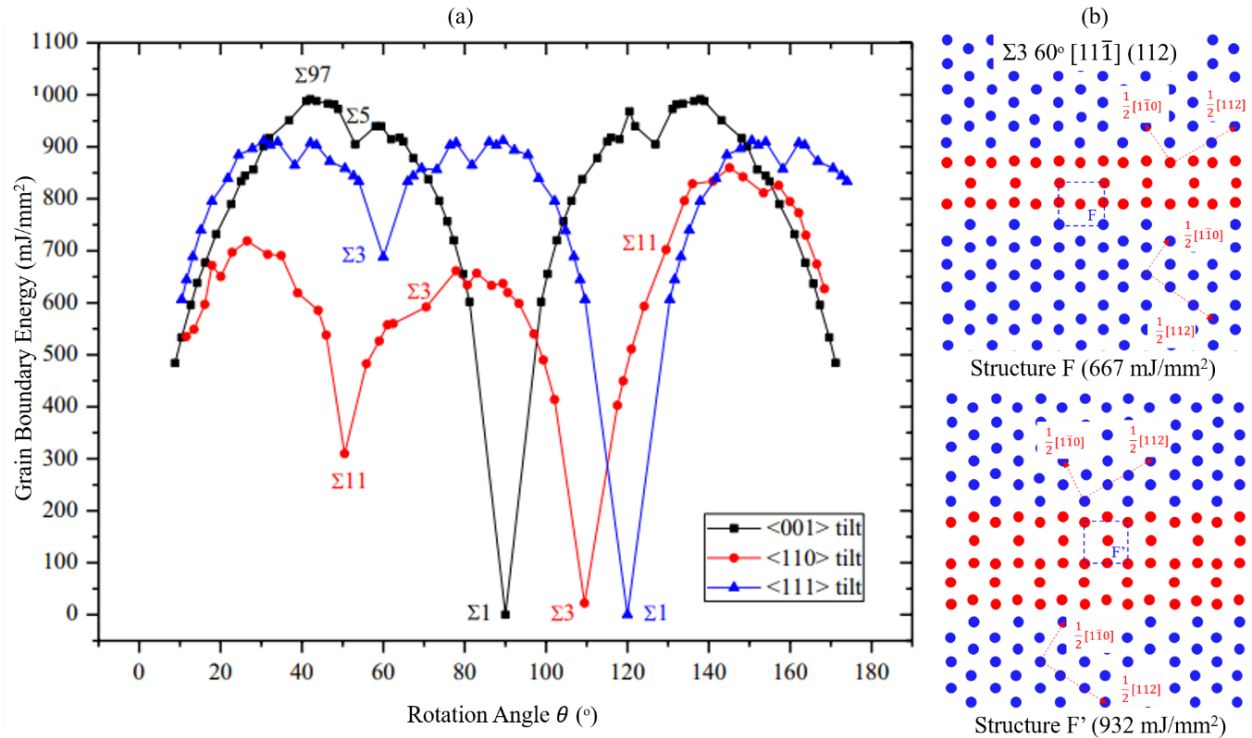
Figure 2-4: High-angle GBs a) Grain boundary energy as a function of misorientation angle θ for symmetric Al tilt grain boundaries. This plot indicates that the GB energy does not increase consistently with the misorientation angle. The simulated graph is taken with permission from the Ref. [71]. **b)** Two different atomic structure for Σ3 [11$\bar{1}$] (112) GB having quite significantly different interfacial energies in Cu [36].

10

Furthermore, considering the energy of the HAGBs, Balluffi [67] found in 1987 that the correlation between the energy and the geometry of the GBs is much more complex than the computed or experimentally measured energies by Hasson [68]. Simultaneously, it is also evident from the more recent simulation studies [38,69–71] performed in order to compute the energies of HAGBs in the fcc material (shown in **Figure 2-4 a)**) that only the misorientation angle or GB plane alone is not sufficient to evaluate GB energies. For example: Σ3 {111} and Σ3 {112} having a misorientation of 60° will have different energy corresponding to their different habit planes. In addition, it is not always necessarily true that low value of Σ represents low energy. Furthermore, GBs with the same Σ value, having the same tilt axis and the identical GB habit plane may have distinct atomic structures with substantially different energies. This is also illustrated in **Figure 2-4 b)** for Σ3 <111> {112} GB in Cu. This means the Σ value has very little association with GB energy. Nowadays, it is well-accepted that other than the geometry of a GB, its energy is highly dependent on the atomic structure, presence of interfacial defects, and the nature of bonding at the GB.

Recently, great advancements in the field of electron microscopy techniques such as aberration-corrected STEM and atomistic simulations with more accurate embedded atom model (EAM) potentials have substantially advanced the topic. The atomic structure of the HAGBs are highly influenced by the microscopic relaxations at the GB, which is dictated by the bonding nature and forces between the atoms. There have been several systematic simulation studies [19,21,28,36,37] done in order to understand the structures of GBs, which have led to the evolution of the structural unit model (SUM). In accordance with the SUM, the atomic structure of a high angle GB can be described by a single/combination of repeating 2D structural units (a specific arrangement of a certain quantity of atoms) [72]. The GBs having a single structural unit are referred to as delimiting GBs and are considered as a reference structure for other GBs. The combination of SUs from the respective delimiting GBs can be used to explain the structure of any GB that has a misorientation between the two delimiting GBs. Although the SUM has been highly effective over the past few decades, particularly in the area of modeling, differences between the simulated and the experimental structure of a GB have frequently been found. [73,74]. One reason for such a discrepancy could arise from the simulation method itself, which is used to predict the atomic structures of the GBs. Another major reason for such contradiction is the non-unique atomic structure of a GB with fixed macroscopic DOFs [36,53,72,75]. Several studies reveal the existence of multiple stable and metastable states for a GB with fixed macroscopic DOFs, characterized by

distinct thermodynamic excess properties [23–27]. Due to energetic reasons, a large number of possible rigid body microscopic translations in the GB plane give rise to the different atomic structures of a GB [28–31]. Apart from that, it is often found that various interfacial defects at the GB like full dislocation, step and/or disconnections, etc. also dictate the GB behavior.

It is well known that the creation and dynamics of disconnections play a vital role in various GB kinetics such as the existence of disconnections along thermally equilibrated GBs [76], disconnection movement during GB sliding [77] and deformation coupled GB motion [78]. GB disconnections are line-defects exhibiting both dislocation and step character in grain boundaries or phase interfaces and are characterized by a Burgers vector **b** and step height *h*. In addition, both **b** and *h* must be a translation vector of the DSC lattice. Bollman first advanced and expanded the idea of disconnections in 1970 [66,79–81]. In their analysis of the atomistic migration mechanism of the Σ11(113) coherent GB, Zhu et al. [82] found that the regular coalescence and dissociation of two disconnections with the height of either one or two atomic layers has an impact on the GB migration. Other than the boundary structure, the type and density of the disconnections have a significant impact on the GB's properties as well as their macroscopic behavior. Thus, there is a need for direct experimental evidence of the local atomic structures of defects present at the GBs in order to discern their impact on the interfacial properties.

2.3 Grain boundary thermodynamics and phase transitions

Grain boundaries are one of the interfacial defects represented by the presence of broken atomic bonds. Hence, their thermodynamic treatment should be in accordance with the general well-developed thermodynamic description of other interfaces such as free surfaces [19]. Gibbs [83] has provided the very first thermodynamic description for the dividing interfaces. Later, Cahn [84] adapted Gibb's description and redeveloped a more convenient thermodynamical model for the grain boundaries. Considering a system having a bi-crystal with two differently oriented crystals, separated by a grain boundary interface. According to Gibbs, the internal energy of a system increases as the bi-crystal grows and can be expressed by the following equation [83]:

$$dU = TdS - PdV + \sum_{i=1}^{N} \mu_i dN_i + \gamma dA \qquad 2.4$$

Here, T, S, P, V indicate the thermodynamic state variables i.e. the temperature, the entropy, the pressure and the volume of the system; while N is the number of constituents with their chemical potential μ_i. Furthermore, A and γ represent the grain boundary area and the free energy of the boundary per unit area, which is defined by Cahn [84] at constant V and N_i, as follows.

$$\gamma = \left(\frac{\partial U}{\partial A}\right)_{S,V,N_i} = \left(\frac{\partial G}{\partial A}\right)_{T,P,N_i} \qquad 2.5$$

The grain boundary energy can additionally be expressed in terms of other thermodynamic state variables such as Gibb's energy (G) as in equation 2.5. This equation indicates that the existence of interfaces increases Gibb's energy of the whole system, which depends on the thermodynamic state variables (pressure, temperature and composition) as described above and also on the GB geometry and the atomic structure [22,52].

Furthermore, more recently, Frolov et al. [85,86] have developed the thermodynamic description for planar coherent interfaces under non-hydrostatic elastic stresses and also introduced several other interface excess quantities that may affect the GB properties. According to Frolov and co-workers, the GB free energy is defined as the reversible work of the formation of an interface from a single crystal under stress and the total interfacial energy (γA) is given by the following expression:

$$\gamma A = \Delta U - T\Delta S - M_{21}\Delta N_2 - A \sum_{i=1,2,3} B_i\, \sigma_{3i} \qquad 2.6$$

Here, ΔS, M_{21}, ΔN_2, B_i, and A is the entropy change of the region, the diffusion potential of component 2 relative to 1, the change in the number of atoms 2, the displacement vector and the GB area. In this thermodynamic approach, instead of chemical potentials, diffusion potentials are considered. In addition, the terms ΔU, $T\Delta S$, $M_{21}\Delta N_2$ and $A\sum_{i=1,2,3} B_i\, \sigma_{3i}$ describes the energy change, the total sum of the heat, the chemical work and the mechanical work done by stress, respectively, during GB formation. Any extensive property such as ΔN_2 can also be described in terms of excess quantity notation i.e. $[N_2]_N$, where $[N_2]_N$ indicates the segregation of component 2 at the GB. The GB excess of a property is defined relative to a homogeneous region from the grain having the same amount of atoms as in the GB. Hence, the above equation can also be expressed in terms of excess quantities as follows:

$$\gamma A = [U]_N - T[S]_N - M_{21}[N_2]_N - \sigma_{33}[V]_N - A \sum_{i=1,2} B_i\,\sigma_{3i} \qquad 2.7$$

Furthermore, a generalized fundamental adsorption equation for an interface is derived (see equation 2.8), whose differential coefficients give several GB excess properties such as GB stress tensor, GB segregation, GB excess shear and GB excess volume.

$$d\,(\gamma A) = -[S]_N dT - [N_2]_N dM_{21} - [V]_N d\sigma_{33} - A \sum_{i=1,2} B_i\,\sigma_{3i} - A \sum_{i,j=1,2} \tau_{ij}\,de_{ji} \quad 2.8$$

In the right-side terms in equation 2.11, $[V]_N$ is the GB excess volume, the coefficients AB_1 and AB_2 represent the excess shears of a GB. The coefficients of de_{ji} define how lateral strains at the GB influences the total GB free energy. τ_{ij} is a stress tensor and an excess quantity that describes the stress state of the core of a GB (whether it is compressive or tensile).

In the last few decades, it has been recognized that GBs can also be considered as 2-D phases analogous to bulk phases and hence can undergo phase transformations (structural and chemical change) as a function of thermodynamic state variables [27,34,87]. These transitions can be described using the GB excess free energy, which is a function of thermodynamic excess properties as described above equation 2.8 [85,86]. These grain boundary phases are also termed "complexions" [33–35,40], however in this thesis term 'phase' is utilized. Gibbs [88] was the first one who theoretically identified these transitions at the interfaces and formulated their stability and equilibrium criterion. Hart [26], later introduced the possibility of such transitions at the planar GBs and suggested that the GB properties such as GB migration, cohesion, GB sliding resistance and diffusivity, among others, will also alter on transition. This suggested that if a substantial fraction of GBs in a material undergoes such transitions, this will lead to a dramatic and abrupt influence on the GB properties and eventually will have implications on the bulk behaviour of a material.

Several indirect measurements (both experimental and/or simulation) have provided insights into the understanding of the atomic structure and phase behaviour of the GBs, revealing the presence of such transitions in several materials system [23,29,36,37]. In addition to that, in some studies, researchers have also tried to correlate the change in properties of the GBs with these GB phase transitions [30,89–92]. Divinski [93] studied the relationship between Ag diffusivity and

temperature in Cu Σ5 (310) GB and discovered a sharp change in diffusivity at a particular temperature value. He proposed that the abrupt shift in the diffusion value points to a change in the atomic structure of the grain boundary, which was later confirmed by Tim Frolov [89] using atomistic simulation.
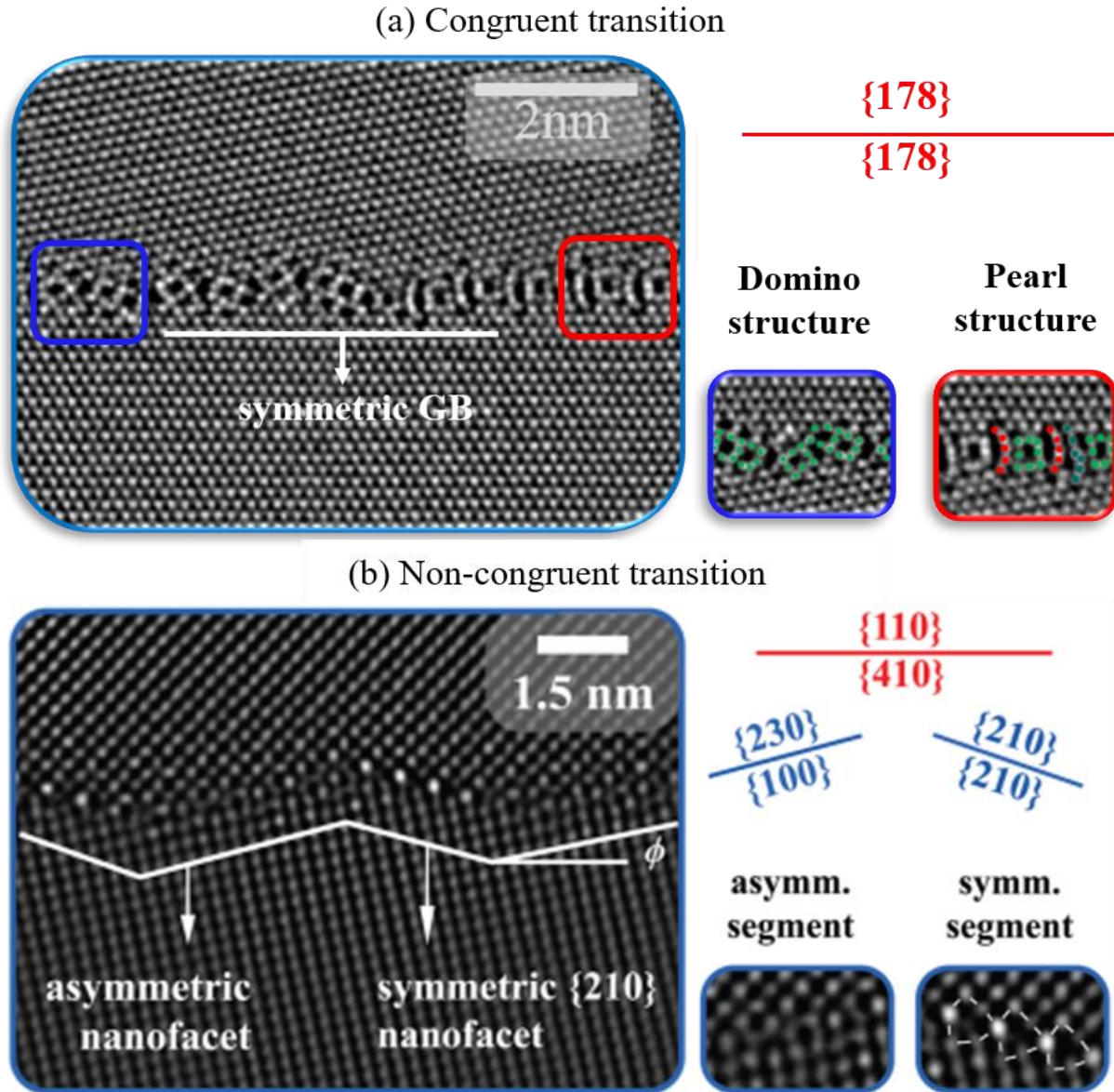
Figure 2-5: Experimental observation revealing phase transitions. a) congruent transition observed in Σ19 GB and b) non-congruent transition in Σ5 GB by STEM-HAADF in Cu [40,41].

Similarly, Bojaski and co-workers [94] have tried to correlate the abnormal grain growth phenomena found in yttria-doped Alumina with GB phase transformations. According to their argument, higher energy GBs are more likely to go through transitions to a new phase with high

mobility than lower energy GBs. Furthermore, changes in the mechanical properties may also indirectly reveal such transitions such as the occurrence of liquid metal embrittlement in $\Sigma 11(110)[311]$ Al GB due to the segregation of Ga into the GBs [95]. Depending on the macroscopic degrees of freedom, the phase transitions can be classified into congruent and non-congruent transitions [34]. In addition to the change in the atomic structure, the latter is accompanied also by a change in geometrical DOF and chemistry while the former has fixed DOF [27,34]. Despite the fact that Cahn's [27] initial theory claimed that congruent transitions in pure component systems are extremely uncommon. It is now well recognized via direct experimental observations and/or simulations [23,40,42] that both kinds of transitions can occur for pure as well as for multicomponent system as shown in **Figure 2-5**.
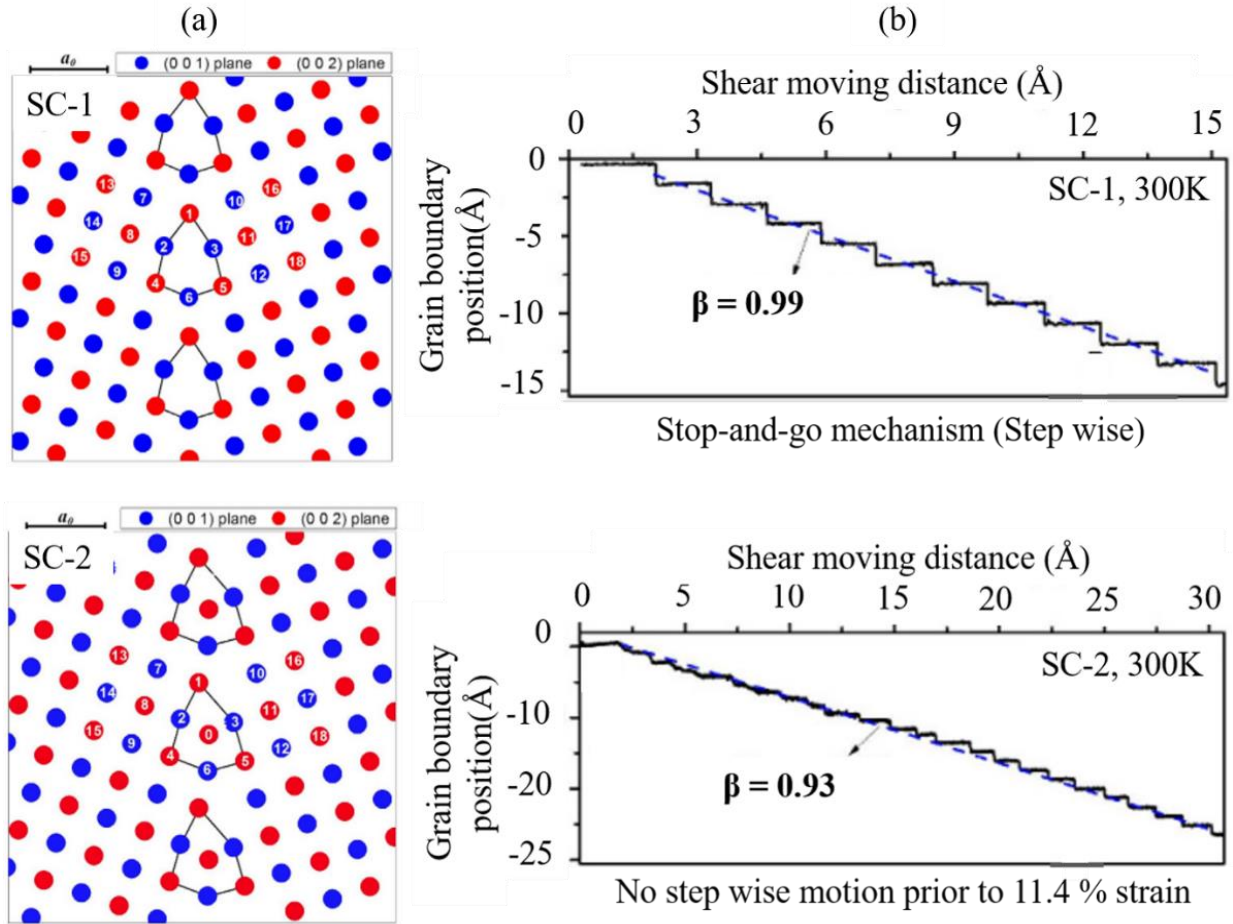
Figure 2-6: Depiction of stress induced GB migration in $\Sigma 5$ (310) GB in Aluminum at 300 K. a) Two different GB structures SC-1 and SC-2 were found for $\Sigma 5$ GB. **b)** Calculated GB position as a function of shear moving distance. It clearly shows different shear-coupling factor (β) for both the structures, and thus differences in GB behavior. SC-1 exhibits a stepwise motion of the GB while SC-2 does not exhibit sharp stepwise motion until 11.4 % strain. The images are taken with permission from Ref. [20].

Furthermore, it is important to take into account that in a pure component system, the presence of two different atomic states (called microstates) at a GB with fixed macroscopic DOFs does not necessarily corresponds to a phase transition. This is because sometimes these two different microstates may not coexist at the same GB and may not transform into each other. Hence, in order to confirm whether two microstates can be transformed into each other or not, in-situ transmission electron microscopy experiments or molecular dynamics simulations need to be performed. Numerous atomistic computer simulation studies [36–38] have been carried out to investigate the structure, possible transitions and energy of various tilt GBs in pure component systems, but mainly for the [001] or [011] tilt axes. For example: Cheng et al. [20] and co-workers investigated the influence of different microstates on the shear coupling motion of Σ5 (310) GB in Al via molecular dynamics (MD) simulations. They predicted three different atomic structures for Σ5 GB, two of which SC-1 and SC-2 at 300 K are depicted **Figure 2-6 a**). Each GB structure exhibits a distinct GB migration pattern behaviour when shear strain is applied, as shown in **Figure 2-6 b**). However, GB structures and properties evaluated via simulation highly depend on the accuracy of the interatomic potential. It is of utmost importance to verify whether the simulated structures resemble the real experimental one or not. Hence, new advances have been made by combining the results of the calculated boundary structures with relevant experimental atomic scale observation [24,96–98]. Recently, Meiners et al. also observed the coexistence of two distinct GB phases (pearl and domino structure) at Σ19b [111] GB in elemental copper by atomic-resolution STEM imaging and further explored the coexistence and transformation kinetics of these GB phases by MD simulation [40]. However, there is a scarcity of such combined studies on atomic level, especially for [111] tilt GBs in metals [36,37,99]. Therefore, in order to establish the structure-property correlation, we need to understand the atomic-scale GB structures as a function of misorientation angle and the GB plane (i.e. change from one symmetric variant to another symmetric one or from a symmetric to an asymmetric one).

2.4 Grain boundary segregation

GB segregation defines the increase in the concentration of solute atoms at a GB [100]. Generally, the solubility of the solute atom at the GBs is different than in the bulk [101]. There are primarily two types of segregation called equilibrium and non-equilibrium GB segregation. Equilibrium segregation is the thermodynamically-driven distribution of the solute atoms at the GB with the

goal of lowering the system's overall Gibb's energy. The system's thermodynamical characteristics exclusively determine the extent of the chemical enrichment at a GB at equilibrium, and this determination is straightforward reproducible. While non-equilibrium segregation occurs because of the concentration gradient due to the interaction of the solute atoms with the vacancies. It is highly sensitive to the rate of cooling from an elevated temperature and is more prevalent in certain processes such as quenching and irradiation [102].

In the thesis, more or less all of the annealed specimens have been cooled slowly in the furnace, thus equilibrium segregation has a great significance here. Wynblatt and Chatain [103] very thoroughly explore a variety of various approaches that might be used to describe interfacial segregation. In general, there are two most common approaches to describe GB segregation thermodynamically: the Gibbs adsorption isotherm [104] and the Langmuir–McLean types of segregation isotherm [105]. The fundamental Gibbs adsorption theorem can be used to illustrate how the GB energy changes in relation to the bulk solute concentration and is derived from the equation 2.4 as follows:

$$\Gamma^{GB} = -\frac{1}{RT}\left(\frac{\partial\gamma}{\partial\ln(X_i)}\right)_{P,T} \qquad 2.9$$

Here, Γ^{GB} is the adsorption of solutes i at the GB, $\partial\gamma$ is the change in GB energy upon segregation at constant temperature T and pressure P and X_i is the molar fraction of the solute in bulk. Equation 2.9 correlates the change in the GB energy due to a change in solute concentration of the bulk to the amount of solute being adsorbed at the GB. This way one can determine the solute excess by plotting the interface energy vs solue concentration of the bulk. This model is successfully applied for the first experiments on GB segregation such as to quantify the solute excess in the segregation of phosphorus, tin and sulphur in iron [106,107]. Despite its success, this approach is not as fruitful as it is experimentally challenging to measure the GB energy and the accurate bulk concentration at different temperatures.

Hence, these shortcomings led to the development of more complementary analytical models such as the McLean model, which explicitly dealt with the GBs. McLean model defines the segregation equilibrium based on the aspect of the Gibbs energy minimization coupled with the statistical mechanics approach [108]. In this model, he put forward that there are fixed number of atomic sites at the GB and the solute atoms are distributed among these sites, corresponding to

a minimization of the free energy. The classical Langmuir-McLean isotherm is described as follows:

$$\frac{X_i^{GB}}{X_i^{GB,sat} - X_i^{GB}} = \frac{X_i}{1 - X_i} \, exp\left(\frac{-\Delta G_i^{GB}}{RT}\right) \qquad 2.10$$

Here, $X_i^{GB,sat}$ is the saturation concentration of solute i at the GB, X_i^{GB} is the measured solute concentration at the GB, X_i is the solute concentration in the bulk and ΔG_i^{GB} represents the change in Gibbs free energy due to the GB segregation. According to equation 2.7, it is evident that the segregation increases as the solute content increases and the temperature drops. Furthermore, the segregation reaches towards a saturation value $X_i^{GB,sat}$, when all the adsorption sites at the GBs are filled with solutes and correspond to one monoatomic layer at the GB [108]. If that happens, $X_i^{GB,sat}$ becomes equal to one and equation 2.10 can be rewritten as:

$$\beta = \frac{X_i^{GB}}{X_i} = \, exp\left(\frac{-\Delta G_i^{GB}}{RT}\right) \qquad 2.11$$

Here, β is referred to as the enrichment factor. Since the Langmuir-McLean model does not require comprehensive information about the variation in the GB energy with the temperature, it becomes widely useful and popular to quantify GB segregation [109].

2.5 Al and Al-(Cu/Zr) systems

Al is the most abundant element on the earth's crust, found as bauxite ore and the third most significant material, commercially used worldwide. However, pure Al is very soft with low flow stress; therefore, certain alloying elements are added to improve its properties, followed by specific heat treatments like annealing, strain hardening and precipitation hardening. Al alloys with Cu, Mg, Si, and Mn have a very good strength and are greatly used for the manufacturing of a huge variety of products like structural components, utensils, automobile parts, doorframes, roofs, windows, foils, wiring in microchips, coatings, etc. [3,10,110]. This is owing to their excellent properties such as resistance to corrosion and oxidation, good electrical conductivity, environmental friendly (recyclable), high thermal conductivity, easily castable and machined. Globally, the transportation industry accounts for the major use of Al alloys. Al consumption is increasing currently and will continue to increase in the future. According to the fortune business

insights' report, it is estimated that the global Al market share is going to expand approximately by 48%, from 2019 to 2027 [111]. There are various key factors responsible for driving such growth of Al that include the continuous expanding automotive industry, adaptation of Al products in robotics technology, increasing popularity of recycled products, strict government policies and regulations to produce vehicles with improved carbon footprint [112].
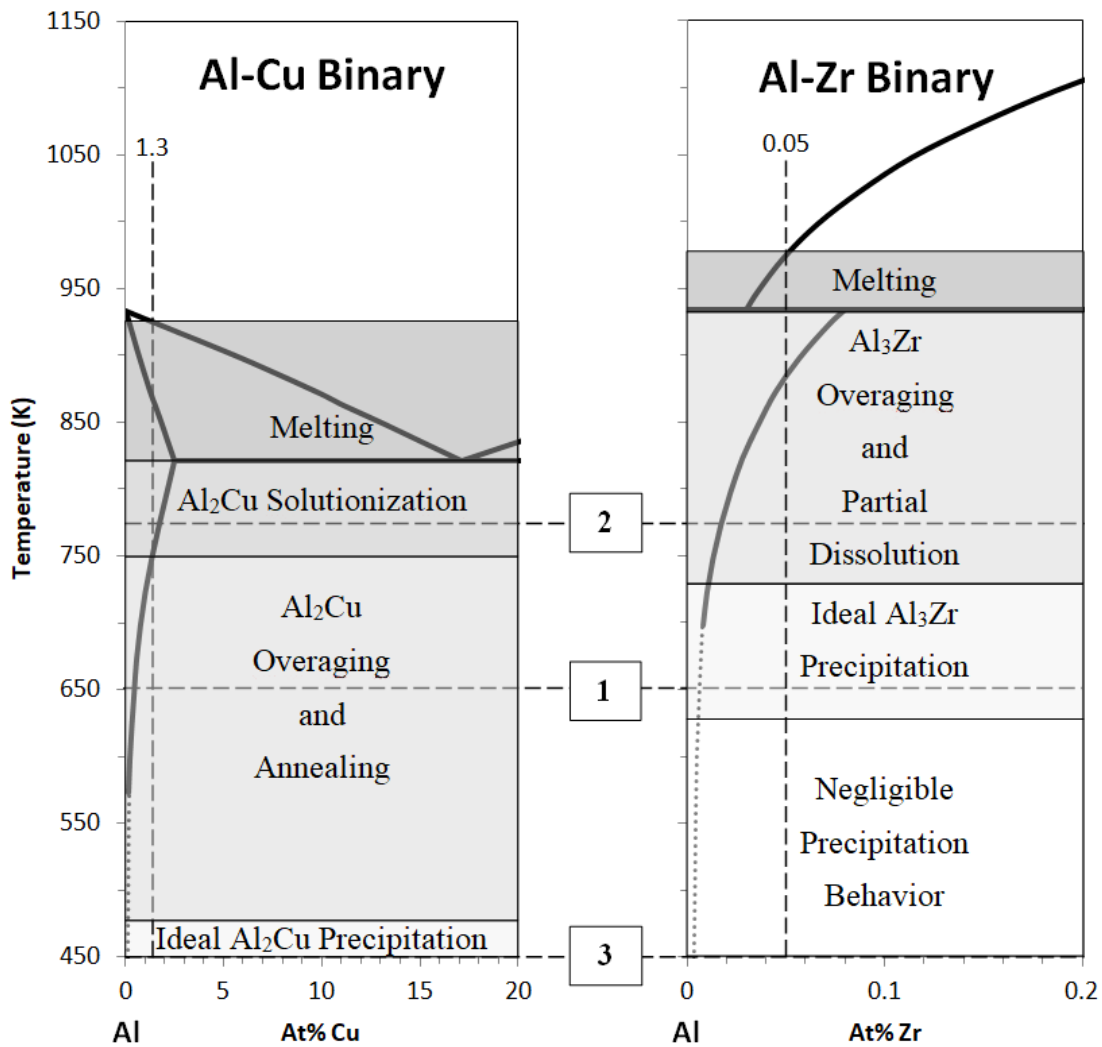
Figure 2-7: Al-Cu system: A typical binary phase diagram for Al-Cu and Al-Zr system. This figure is taken from Ref [126].

Besides the high demand and popularity, it has been realized that many Al based engineering components are also prone to metallurgical failures. There are several causes, which contribute to the failure of these alloys that include porosity, corrosion, crack formation and fatigue (the most common one). Numerous studies [113–115] have reported that fatigue damage to aircraft under the atmospheric environments such as rain, water, fog and humid air may often result in the failure

20

of the aircraft and endanger its security. More specifically, it is well known for 2XXX (Al-Cu) and 7XXX (Al-Zn) series Al alloys, which are widely used for making commercial products for structural applications. However, in general, the most prevalent problem with these alloys is that they do not have very good stress corrosion cracking resistance compared to other Al alloys [13,116], which accounts for 90% of the service failures. Similarly, another big problem with Al-Cu alloys is the electro-migration failure [117] of interconnects in integrated circuits (IC), which leads to open circuit failures and pose a big reliability threat in the fields of microelectronics. All these failures are dependent on several factors such as alloying element, heat treatment, microstructural characteristics, mainly by grain boundaries distribution, character and their behaviour [118]. Therefore, it is of great interest to understand the GBs structure and the impact of impurities on the structures fundamentally, on the atomic level in order to improve the properties of these alloys from engineering aspect so that such failures can be avoided in future.

Since Al-Cu alloy (2XXX series) are technically very important and one of the most widely used alloys, hence we have chosen the Al-Cu system in this study. These alloys have been studied extensively to understand the impact of the alloying elements to enhance their mechanical properties. Several studies [119–121] found that Cu has a strong segregation tendency towards Al GBs and can stabilize the ultra-fine grained size in Al alloys. Additionally, it is well-known that Cu can strengthen Al alloys via precipitation hardening [122]. However, it is yet unclear how the Cu solute influences the local atomic structure and the properties of Al GBs. Zhao et al. [123] systematically simulated the impact of Cu solute on the strength of $\Sigma5$ (210)[001] GB in Al. Zhao and co-workers found that the preferred interstitial segregation of Cu on Al GBs is enhancing the cohesive strength of the Al GBs, which also increases the resistance to inter-granular fracture at Al GBs. Campbell [124] also found that the preferred interstitial segregation of Cu is also causing a change in the atomic structure of a $\Sigma5$ Al GB (210)[001]. The modified structure of Al also altered the mass transport behaviour, which will eventually have a considerable impact on the understanding of the electro-migration process. However, there is a scarcity of such atomic level studies on pure and alloyed Al system, especially for [111] tilt GBs. More recently, Prakash [125] has reported the atomic scale Cu segregation on [111] tilt GBs as a function of misorientation angle between the two neighbouring grains. He found two types of segregation behaviour i.e. point (for < 28°) and parallel segregation (for > 28°) and concluded that the GBs with high misorientation angle are more segregated than the lower angle ones. However, this study was performed on 7075

21

Al alloy with the following composition (based on EDS from a substantial sample area) : Al 96.77%, Zn 0.15%, Mg 1.47%, Cu 1.13%, Si 0.5%. It is important to take into account that this system has Mg, which also has a very high segregation tendency in Al and is available even in higher percentage than the Cu. However, no Mg segregation was observed. Hence, it is difficult to rule out the influence of Mg and Zn on the two discrete types of segregation. Therefore, it is of great interest to study the independent effect of Cu on pure Al GB structures in order to understand the segregation.
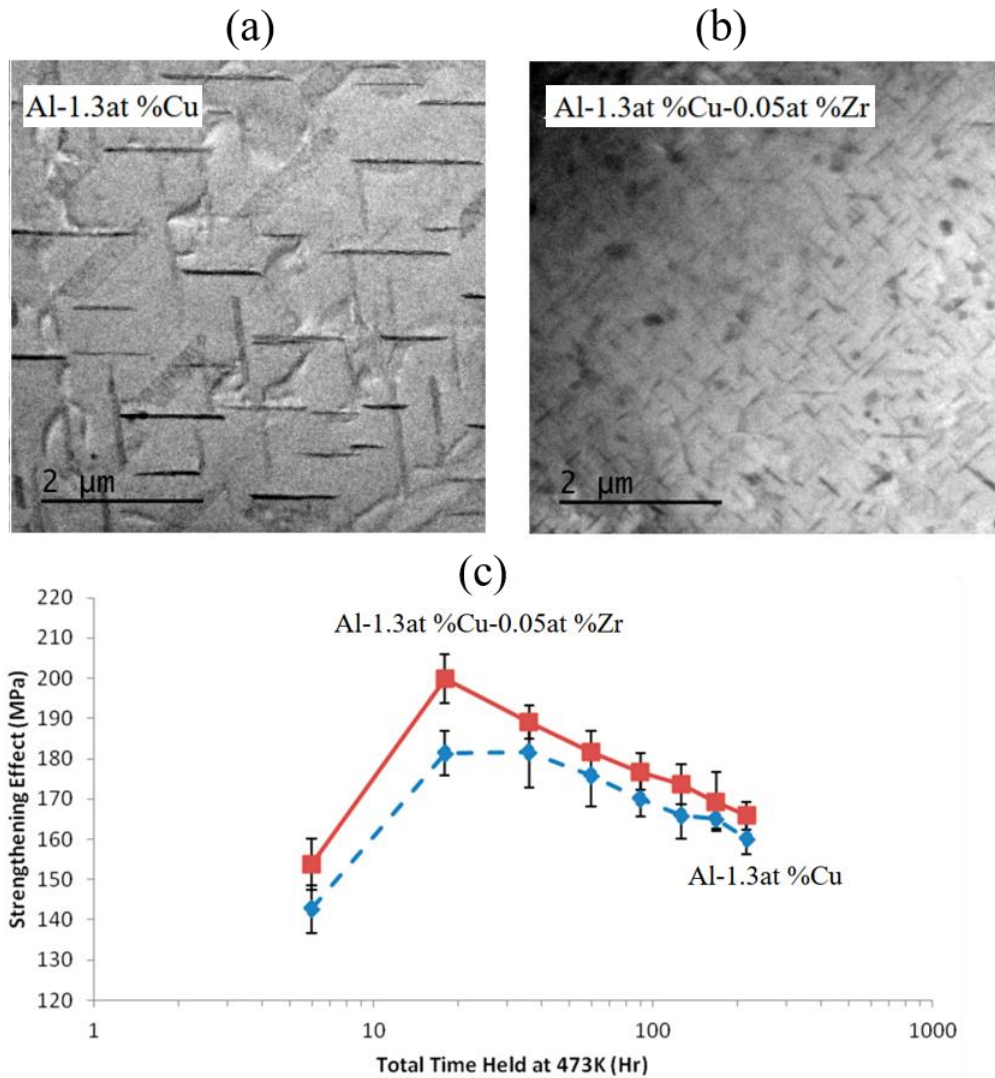
Figure 2-8: Different precipitation behavior for a) Al-Cu and b) Al-Cu-Zr alloys, as revealed by TEM studies following the heat treatment at 643 K (370 ◦C) as described in the ref [126]. It is shown that the lengths of the Al-precipitates in **b)** is 3 times higher than **a)** and possesses fine microstructure. **c)** The plot reports the overaging of two Al-Cu alloys with and without Zr addition at 473 K. It is found that Zr-containing alloys persistently had a higher strength than the one without Zr addition [126].

Furthermore, Zr is also an important alloying element, which is routinely added to control grain size via formation of large precipitates of Al_3Zr, which further strengthen the Al-Cu alloys [126–128]. For example, Dean and his coworkers found the Al-Cu alloys containing Zr had a different precipitation behavior of Al-Cu precipitates (Al_2Cu) in the system, along with the formation of Al_3Zr precipitates [126]. A typical phase diagram for Al-Cu and Al-Zr systems are shown in **Figure 2-7** [126]. The size of the Al-Cu precipitates in Al-Cu-Zr alloys becomes fine as compared to the Al-Cu alloys (without Zr), as reflected in **Figure 2-8 a)** and **Figure 2-8 b).** Furthermore, the Al-Cu-Zr alloy possessed slightly higher strength than the Al-Cu alloys without Zr as depicted in **Figure 2-8 c)**. However, prior to precipitation, the Cu and Zr interaction at the GBs locally on an atomic scale is not understood. Thus, a systematic and comprehensive investigation of Cu and Zr segregation on pure Al GBs needs to be done. This will provide further insights into compositional control of solute in the material system and their implications on various GB related mechanisms such as crack formation, de-cohesion and strengthening via solute precipitation.

Chapter 3 Methods

3.1 Thin film deposition by physical vapour deposition techniques

A thin film deposition technique known as Physical Vapor Deposition (PVD) involves vaporizing the material to be deposited from a solid material, conventionally called target. The deposited material first transforms into a vapor phase and then develops atom-by-atom in the form of a condensed phase onto the substrate. PVD deposited thin films may have layers with thicknesses as thin as few atomic layers up to several microns [129]. The atomic deposition process can possibly be done in a variety of distinct environments such as gaseous, vacuum, plasma, or any electrolytic environment. Several deposition parameters like the type of the substrate, the thickness of the film, the deposition rate, the temperature of the substrate, the annealing conditions and the surface properties of the substrate dictate the microstructural features and properties of the thin films deposited [130]. Typical deposition rates in PVD generally vary between 1-100 Å/s [131]. The most widely used and popular surface coating methods in the PVD process are sputtering and evaporation. Schematics of those are shown in **Figure 3-1** (based on the Refs [132,133]).
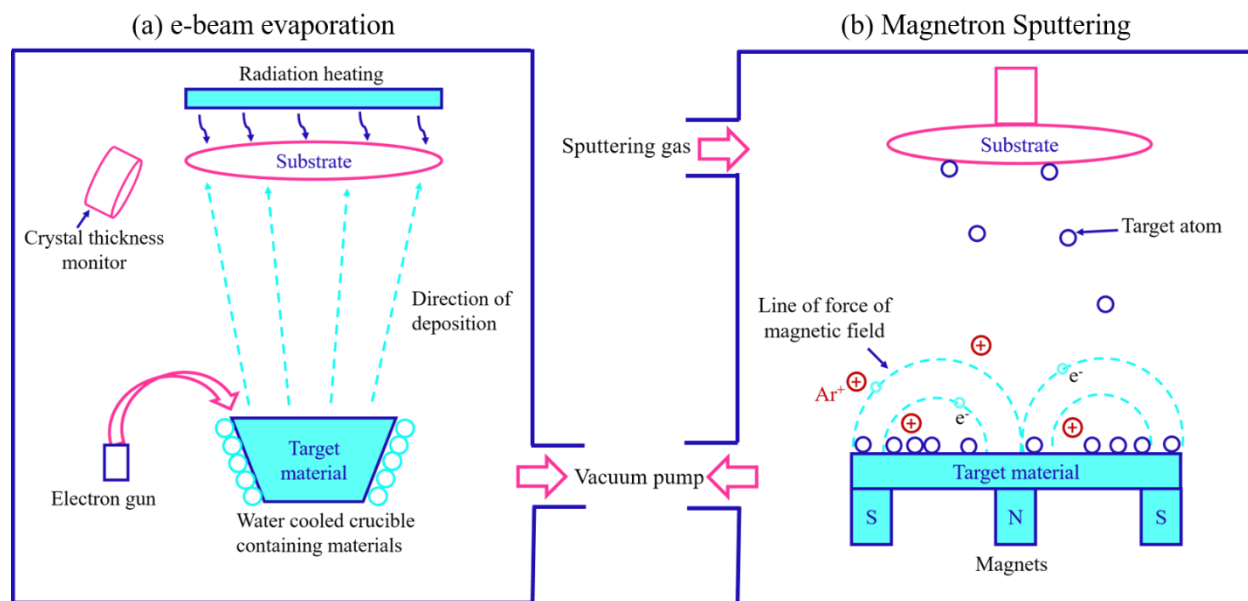

Figure 3-1: Schematic of the working principle of the PVD techniques a) e-beam evaporation and **b)** magnetic sputtering. The images are taken from the Refs [132,133].

Both of these techniques enable the ejection of the atoms from the target material at a very low pressure, which facilitates the deposition of these particles onto the substrate. Furthermore, the

presence of vacuum in the deposition chamber during deposition significantly lowers the contamination [134]. In the current thesis, all of the Al thin film growth was carried out using either electron (e)-beam evaporation or sputtering techniques.

3.1.1 Electron-beam evaporation

In the electron (e)-beam evaporation method, a high-energy electron beam is created from an electron source, which is further escalated to a high kinetic energy. The beam is then steered with the help of electric and magnetic fields towards the target material placed in the crucible. As the electrons irradiate the source material, heat produced during interactions increases the temperature of the target material. Once the surface atoms have sufficient energy, they transform into gaseous state and start evaporating from the melt or solid. These atoms then transmit through the vacuum, get deposited onto the substrate, and coat the surface as shown in **Figure 3-1 a**). In order to assure the uniform deposition of the film, the substrate holder on which the substrate is fastened, rotates at a distinct speed. For high temperature depositions, infrared heater lamps are utilized to preheat the substrate. The main advantage of this technique is the low deposition rates achievable as low as 0.16 Å/s and a great structural and morphological control of the thin films [135].

3.1.2 Magnetron sputtering

In Magnetron sputtering, the substrate is placed in a high vacuum chamber containing a sputtering gas, usually Argon (Ar), which reduces the partial pressures of all the potential gases and impurities inside the chamber. A magnetically confined plasma is generated near the surface of the target material to be deposited onto the substrate. Negative charge is applied to the target material that onsets the acceleration of electrons present in the Ar gas atoms. Accelerated electrons collide with the nearby Ar gas atoms causing an electrostatic repulsion, leading to the knocking off electrons from the Ar atom thereby causing the ionization of the gas. When they reach the negatively charged target (in our case, Al), these positively charged Ar ions in the plasma are accelerated and sputter off the atoms from its surface. As they go through the vacuum chamber, these sputtered particles deposit a thin film on the substrate's surface (which needs to be coated). Several types of power sources are available for sputtering, which includes direct current (DC), radio-frequency (RF), pulsed DC, alternating current (AC) and the newly evolving high power

impulse magnetron sputtering (HPIMS) techniques [136,137]. Typically, DC power source is used for magnetron sputtering of target materials that are conductive in nature such as metals. This technique offers many advantages over other PVD techniques as it does not need melting or evaporation of the source material. Thus, even materials with a high melting point can be sputter-deposited with excellent adhesion and high density [137].

3.2 Electron microscopy techniques

Electron microscopy (EM) is a multifaceted tool with a range of techniques used for material characterization at different length scales by using electrons as a source of illumination. Scanning electron microscopes (SEM) and transmission electron microscopes (TEM) are the two main types of electron microscopes.
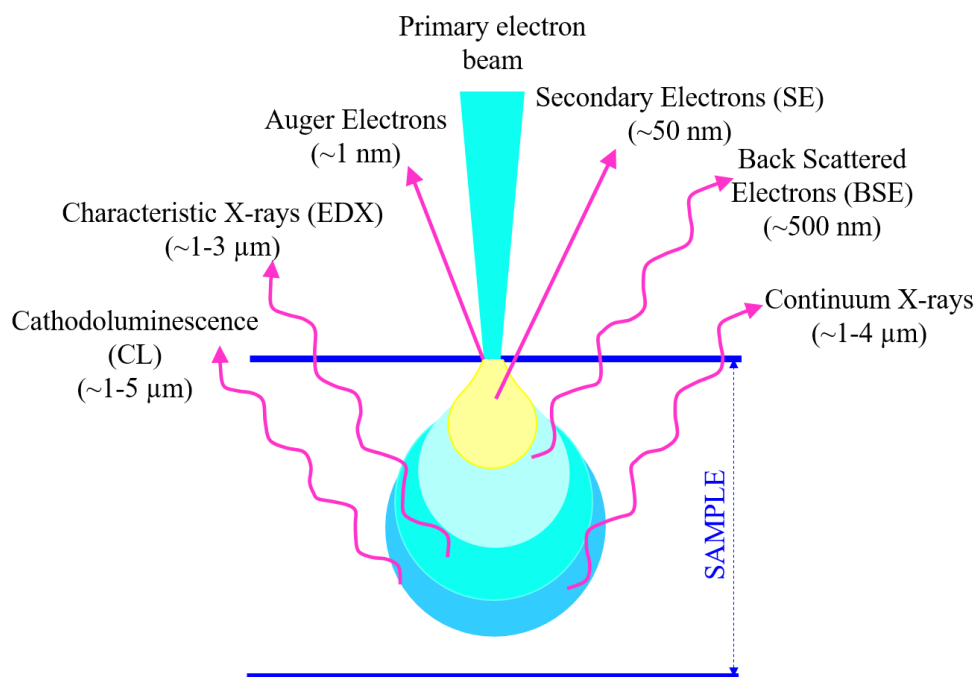
Figure 3-2*: **Electron – specimen interactions:** This figure depicts several types of signals generated from different parts of the electron-specimen interaction volume. The length scale gives approximated interaction volumes. The image is redrawn after [138].

During the interaction between the primary incoming electrons and the atoms in the sample in SEM, different types of elastic and inelastic scattering processes occur which lead to the generation of various types of signals [138] as shown in **Figure 3-2**. The specimen generates secondary and backscattered electrons, which the SEM detects [139]. The TEM method, however, is dependent

26

on the detection of transmitted electrons that are travelling through the specimen [140]. SEMs usually use acceleration voltages up to 30 kV, whereby TEMs can be operated in the voltage range of typically 60–300 kV. SEM allows characterization of the microstructural features at the macro, micro and nanoscales, i.e., from several micrometers down to few nanometers while transmission electron microscopy (TEM) provides information of even smaller features with fine details down to atomic resolution.

3.2.1 Scanning electron microscopy

A high-energy focused beam of electrons is used for imaging in SEM in a similar way as light microscope uses visible light. Electrons are emitted via thermionic or field emission phenomena by the electron gun placed at the top part of the column. The path of electrons inside the microscope column can be controlled using electromagnetic lenses. Specific set of coils are used to raster the electron beam over the sample surface that generates variety of signals during electron sample interaction (see **Figure 3-2**). The two primary signal types employed in SEM imaging are secondary electrons (SE) generated by inelastic interaction from the sample's near-surface regions and backscattered electrons (BSE) produced by elastic interaction from the sample's deeper sections. SE provide detailed information about the surface topography while BSE provide information on crystallography and composition in the specimen. Different types of detectors detect both SE and BSE. For the detection of BSE, solid state detectors are used that is placed concentrically to the electron beam just above the sample while for the SE, mainly Everhart-Thornley (ET) detectors and in-lens detector are used. The scintillator for the ET detector is housed in a Faraday cage that is tilted and fastened to the side of the microscope chamber. A small positive voltage is applied to the Faraday cage to attract the relatively low-energy (<50 eV) secondary electrons [141]. Applying a strong positive voltage to the scintillator, where the impinging electrons are converted into light, accelerates them even further. These photons then travel along the light guide to a photomultiplier tube, where they are amplified. However, some BSE may also reach the ET detector in addition to SE. Consequently, under these situations, the resultant image is not a pure SE image. In addition, modern SEM instruments use in-lens detector, which is positioned above the objective lens inside the microscope column. In order to increase the spatial resolution and collection efficiency of SEs, in-lens detector is equipped rotationally symmetric around the optical axis of the microscope [142]. A comprehensive overviews of SEM techniques can be found in the literature [139,143].

3.2.2 Electron backscatter diffraction

For the literature of this section, please refer to the Ref. [144,145]. Electron backscatter diffraction (EBSD) is a microscopy technique that provides rich crystallographic information about the microstructure of a crystalline specimen that includes determination of the crystal structure of phases, grain orientation, texture and local strain.

In this technique, an electron beam interacts with a fine polished crystalline specimen tilted at 70° and undergoes both elastic and inelastic scattering. As the elastically scattered BSEs came out of the specimen, coherent Bragg scattering by the atoms in the crystal lattice further diffracts them. As long as the diffraction conditions are satisfied, electrons are diffracted from the individual grains in all directions in the form of a diffraction cone, called Kossel cones.

On intersecting with the phosphor screen, these Kossel cones form Kikuchi lines/bands in a projection that corresponds to the diffracting lattice planes present in the crystal. The Kikuchi pattern generated from each grain is also referred to as electron-backscattered pattern (EBSP). These patterns are detected by a special detector equipped with a phosphor screen and a charge coupled device (CCD) camera that record the diffraction pattern for each pixel over which the beam is raftered across the specimen.

Hence, this results in a full EBSD map. Once the Kikuchi patterns are collected for each pixel, a mathematical Hough transformation is used that converts straight line in the image space (x, y) into a single point. The Kikuchi bands appear as peaks in Hough space that are easily detected and used to determine the original band positions. From that identified position, the angle between the detected bands is calculated. On comparing it with the database available in the TSL-Orientation Imaging Microscopy (OIM) EBSD software, crystal orientation of the specimen is determined.

3.2.3 Plasma focused ion beam microscopy

The literature for this section is based on Refs. [146–148]. A focused ion beam (FIB) instrument is almost equivalent in principle to an SEM, besides it uses a beam of ions alternative to electrons. The plasma focused ion beam (PFIB) dual beam system utilized here uses a Xenon ion beam and an electron beam. Both intersect at an angle of 52° at a coincident point (also called eucentric point/height) near the sample surface for milling of micro/nanometer size sample and subsequent

imaging of the FIB milled surface. The system has a five-axis piezo-driven motorized sample stage for precise control of the sample position. In contrast to Ga-FIB, which utilizes liquid metal ion source (LMIS), PFIB employs an inductively coupled plasma (ICP) source. Both type of sources are schematically illustrated in **Figure 3-3** [149]. Xenon (Xe) ions are generated from Xenon gas, using a mini RF-generator that inductively heats the gas with the help of an electromagnetic induction coil and ionizes it.
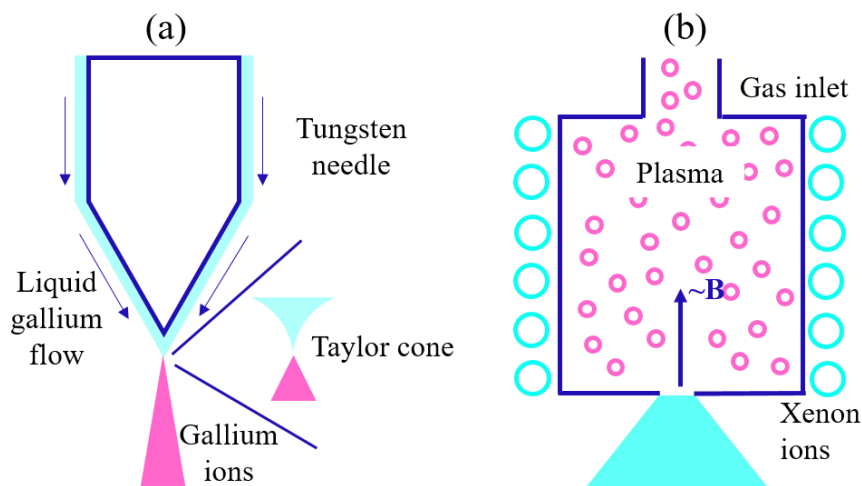

Figure 3-3: Schematic illustration of FIB sources a) Liquid metal ion source (LMIS) in Ga-FIB. **b)** Inductively coupled plasma (ICP) source in Xe-PFIB. Images are redrawn after Ref [149].

A combination of electrostatic and electromagnetic lenses is used for focusing the ion beam onto the specimen surface and the beam is rastered across defined patterns with the help of scanning coils. As the impinging ions interact with the sample surface, secondary electrons are generated and the high mass and kinetic energy of the ions leads to removal of the material by the sputtering process. Furthermore, the heavy incoming ions also induce damage to the region of interest in the form of point defects such as vacancies and interstitials. Therefore, modern FIB systems also possess a gas injection system (GIS) to deposit protective layers (commonly Pt, W or C) by beam induced precursor gas decomposition.

The main advantage of using a Xe+ Plasma FIB over a conventional Ga FIB is that it offers much higher currents up to tens of nA (up to 60nA) compared to a Ga FIB. This allows high milling rates for large volume sections, which are impossible to achieve with a Ga FIB in a reasonable time. In addition, it also eliminates Xe enrichments and contamination at the interfaces in contrast to Ga

enrichments with conventional FIB, especially for Al and its alloys. On performing EDS on the GBs, no trace of Xe is found in the Al specimen prepared by PFIB in contrast to Ga FIB.

3.2.4. Transmission electron microscopy

For the literature of this section, please refer to ref. [140,150–153]. Transmission electron microscopy (TEM) uses a high-energy electron beam having very small wavelength (as small as 2.24 pm at 300keV). These electrons are generated from an electron source by either thermionic emission (LaB6 crystal/tungsten filament) or field ion emission (FEG). These electrons are then accelerated to a high voltage of typically 60-300kV in a high vacuum. The condenser lens system focuses the electron beam on to the specimen in parallel beam illumination (conventional TEM) or convergent beam mode (scanning transmission electron microscopy (STEM)). While convergent beam mode is largely utilized for STEM imaging, convergent beam electron diffraction (CBED), and chemical analysis using electrons and X-ray spectrometry, parallel beam mode is primarily used for TEM imaging and selected-area diffraction (SAD).

The incoming electrons transmit through a very thin specimen of below 100 nm thickness where all the beam-specimen interactions take place. In a broader sense, this results in two type of electrons: unscattered electrons (corresponds to central spot in diffraction pattern (DP)) and scattered electrons (produced by different elastic and inelastic scattering processes). There is no energy loss during elastic scattering, which happens when the primary electron beam is scattered to merely a few degrees (100 mrad $\approx$ 5°) when interacting with the electrons in the outer shell or to a significant angle while experiencing Coulombic interaction with the positive nucleus. While inelastic scattering results from loss of energy from the primary beam to the specimen and produces several useful signals that provides information about the chemistry and electronic structure of the specimen. In TEM, electrons are transmitted through a thin specimen (<100 nm) and are elastically scattered to form either a DP in the back-focal plane (BFP) or an image in the image plane. This is done by varying the strength of the electro-magnetic field of an intermediate lens. In STEM, a convergent beam is focused onto the sample and rastered pixel by pixel across the whole sample. High angle annular dark field (HAADF) images, created by incoherent elastically scattered electrons that have scattered to high angles, are the most well-known and often used images in STEM. The objective lens, the intermediate lenses and the final lens, which serve

as the projector lens, make up the imaging system in TEM. The DP or an image is magnified and further projected onto the phosphorus screen using the projector lenses. A detector such as a charge coupled device (CCD) or complementary metal oxide semiconductor (CMOS) records an image or a DP. While in STEM, annular detectors are used to collect the transmitted electrons as a function of the location of the beam. Depending upon the range of scattering angles recorded, STEM can be used in various different modes such as bright field, dark field and HAADF. A detailed account of STEM methods and modes used in this thesis is discussed below in the upcoming sections.

3.2.4.1 Conventional transmission electron microscopy technique

In conventional transmission electron microscopy (CTEM), primarily two kinds of interactions take place between the incident beam and the atoms within the specimen: elastic and inelastic scattering. Elastic scattering occurs when the incident primary electrons interact with the screened Coulomb potential of a nucleus in the specimen such that the energy and momentum of the interacting electrons remains unchanged after the interaction. The unscattered electrons form the direct beam in the diffraction pattern (DP) (indicated by a yellow line in **Figure 3-4** [154]). In addition, the diffracted beams arise from elastically scattered electrons fulfilling the Bragg's law:

$$2d_{(hkl)} \sin \theta_{(B)} = n.\lambda_{(electrons)} \qquad 3.1$$

Here, $d_{(hkl)}$ is the lattice spacing between the *hkl* planes, $\theta_{(B)}$ is the Bragg angle and $\lambda_{(electrons)}$ is the wavelength of the primary electrons. On the other hand, inelastic scattering occurs when the primary incoming electrons interact with the shell electrons and/or the nucleus of an atom via Coulombic interaction and results in a loss of energy. Due to that, the energy and the momentum of the primary electrons are not conserved after the inelastic interaction. The back focal plane, where the diffraction pattern appears, is the position where the objective aperture is located. This aperture is used in two distinct imaging modes, known as bright field (BF) mode and dark field (DF) mode, to produce images with enhanced contrast. When an objective aperture is placed positioned around the direct beam, only non-scattered electrons contribute to image formation, thereby excluding the scattered ones, also referred to as bright field image as shown in **Figure 3-4 a)**. However, it is important to take into account that the diffracted beams due to the interference also modulate the intensity of the unscattered electron beam. In the BF imaging mode, the objective

aperture obstruct the diffracted electrons, thereby collecting only the unscattered electrons. Hence, the strongly scattered regions emerge dark in an image. This strong scattering takes place due to thick or high Z regions via Rutherford/incoherent scattering and for crystalline samples mainly via coherent elastic scattering.
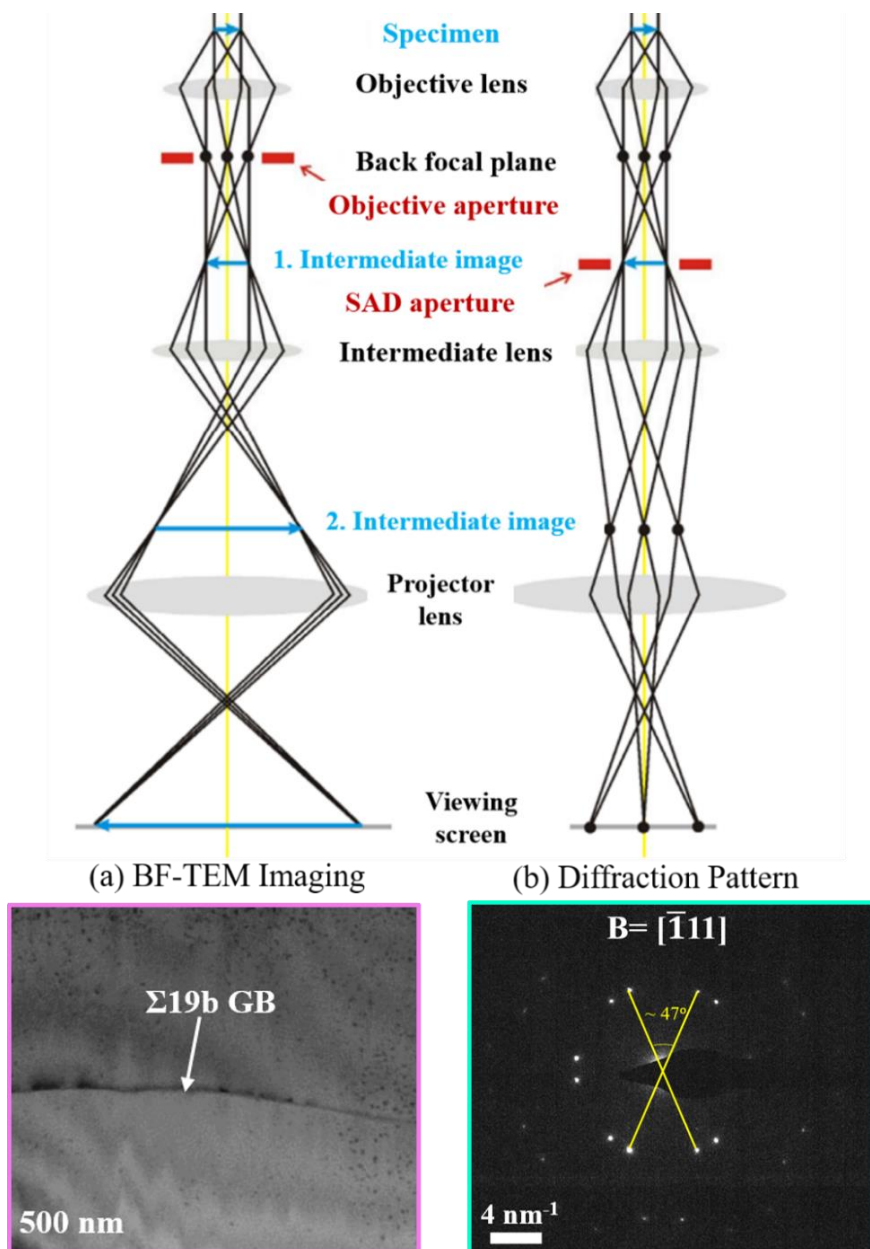

Figure 3-4: Ray diagrams for a TEM in a) the bright-field mode and **b)** selected-area diffraction (SAD) mode**.** The BF-TEM image in the left comprises a long segment of a curved Σ19b type grain boundary. The right image shows the diffraction pattern of the same Σ19b GB, giving information about GB crystallography such as tilt axis, misorientation and GB plane. The ray diagram is redrawn from [154].

An incident beam is tilted in the DF imaging mode so that one of the diffracted beams comes onto the optical axis of the microscope. The objective aperture is placed around that specific reflection and the regions scattering in that specific direction appear bright in the DF image. Selected area diffraction (SAD) aperture, situated in the image plane, is used to select an area of interest to obtain the SAD pattern (SADP) as shown in **Figure 3-4 b**). A sample's crystal structure that satisfies the diffraction requirement is related to the information offered by each spot in SADP, which includes information on phase identification, orientation relationship and crystal defects in materials, etc. The intermediate lens allows to switch between diffraction and imaging in a way that it selects either the BFP or the image plane of the objective lens as its object. In the following thesis, DP and BF images (that gives GB plane trace) are used to examine the GB type and orientation of the grain, and subsequently determining grain boundary plane. In addition, systematic investigation on the growth of Al films and orientation relationship between the Al film and the substrate is done by using CTEM.

3.2.4.2 High-resolution transmission electron microscopy

This section is based on the following Refs [140,150,152]. While conventional microscopy uses the amplitude and thus the intensity of the diffracted waves to form an image, high-resolution transmission electron microscopy (HRTEM) employs the phase of the diffracted electron wave that interferes constructively or destructively with the phase of the transmitted wave to create an image. The most obvious difference between HRTEM and conventional TEM imaging is the large number of diffracted beams collected with no or a large objective aperture in HRTEM. The plane electron wave incident on the surface of the TEM specimen, propagates through the crystal and interacts with the atomic potentials of the atoms. During interaction between the plane wave and the periodically ordered atoms, there is an emission of secondary wavelets from atoms (following Huygens-Fresnel' principle). Since the secondary wavelets originate from the interaction with the atoms, they are shifted in phase. Consequently, another phase shift is introduced when they interfere with the incident plane wave. Due to the occurrence of phase shifts, the electron wave's phase changes as it passes through the specimen, also known as the "exit wave". The superposition of the modulated waves at the image plane results in interference effects and causes phase contrast that primarily depends on defocus and spherical aberration and the particular illumination conditions. The phase modulation contains the information of the crystalline structure of the

specimen, however cannot be interpreted straightaway. The phase modulation is translated into real space in the form of an image, by tuning the amount of defocus that depends on the spherical aberrations of the objective lens. Hence, the amount of information translated to the real image is influenced and determined by the contrast transfer function (CTF), which is exemplary depicted in **Figure 3-5**. The CTF can be described as follows:

$$CTF(\vec{u}) = A(\vec{u})B(\vec{u})E(\vec{u})$$ 3.2

Here, $\vec{u}$, $A(\vec{u})$, $E(\vec{u})$ and $B(\vec{u})$ represents the spatial frequency, the aperture function, the envelope function and the aberration function. $A(\vec{u})$ describes the spatial frequencies cut off associated with the defined size of the aperture. The aberration function describes an oscillation of the contrast transfer as a function of the spatial frequencies and can be approximated to $2 \sin \chi(\vec{u})$ for weak phase objects (very thin specimen thicknesses).

$\chi(\vec{u})$ is mainly a function of the spherical aberration coefficient C_s of the microscope and the defocus Δf of the objective lens and is described by:

$$\chi(\vec{u}) = \frac{2\pi}{\lambda}\left(\frac{1}{4}C_s\lambda^4 u^4 - \frac{1}{2}\Delta f\lambda^2 u^2\right)$$ 3.3

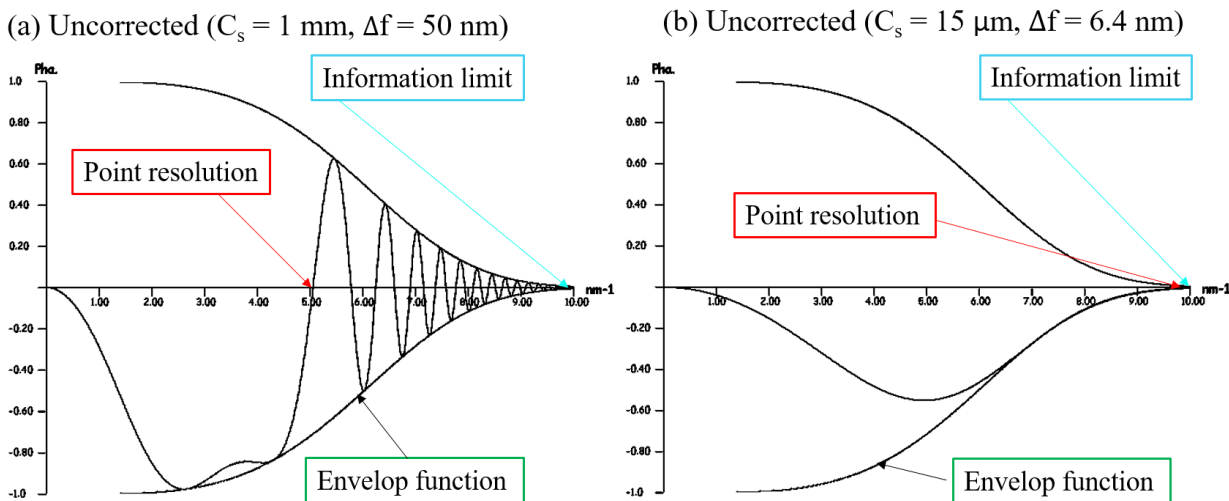Here, λ is the electrons' wavelength, which is controlled by the accelerating voltage.

Figure 3-5: Plot of the Contrast Transfer Functions (CTF) as a function of spatial frequency u (nm⁻¹) a) CTF corresponding to an uncorrected TEM having a spherical aberration coefficient of Cs = 1mm under Scherzer defocus Δf = 50 nm conditions. **b)** shows the CTF for a corrected TEM with Cs = 15 μm and Δf = 6.4 including the envelope function. These images are simulated using JEMS software.

At high spatial frequencies, the contrast transfer oscillates and a contrast inversion occurs at the first zero crossing of the CTF. The resolution limit of the instrument, often known as the point resolution, is defined as this crossing point. **Figure 3-5 b)** illustrates how the influence of spherical aberration C_s can be countered using a discrete negative value of Δf_{sch}, known as Scherzer defocus, to achieve the best CTF. The Scherzer defocus can be stated as follows:

$$\Delta f_{sch} = -1.2\sqrt{C_s \lambda} \hspace{4cm} 3.4$$

Up to the point resolution, the contrast in the image is directly decipherable (all the atoms look dark on a bright background). $E(\vec{u})$ describes the effect of the chromatic aberration and the spatial coherence of the electron source that limits the resolution because of the damping of higher spatial frequencies. The envelope functions in the BFP of the objective lens produce a virtual aperture that suppresses higher-order spatial frequencies. This cut-off has resulted in a new resolution limit for the microscope known as the "information limit".

In an uncorrected microscope, correlative image simulations are required for a detailed interpretation of HRTEM micrographs in order to prevent fallacy due to the inversions in the contrast. However, in a corrected microscope, there are no oscillations in contrast until the information limit in the CTF. In this case, the information limit and the point resolution are nearly equal. Therefore, optimization of the microscope aberrations cautiously with an aberration corrector makes the interpretation of HRTEM images uncomplicated and direct.

3.2.4.3 Scanning transmission electron microscopy

The basics of both SEM and TEM techniques are combined in STEM, which can be implemented nowadays on each kind of instrument. The most predominant advantage of STEM over TEM is to avail the other supplemental signals that cannot be spatially correlated in TEM that includes characteristic X-rays, electron energy loss and secondary electrons [155].

While the specimen is exposed to a parallel beam in the TEM, a fine focused converged beam is employed in the STEM to raster scan the sample at each pixel. Elastic and inelastic scattering events are the consequences of the electron beam's interaction with the sample. Plotting the particular scattered electrons as a function of probe position eventually yields a magnified image. The STEM imaging optics (before the sample) are identical to the imaging optics (after the sample)

in the CTEM because of the reciprocity theorem of scattering theory [156]. As a result, the illumination configuration in CTEM and the detector plane in STEM have identical functions.
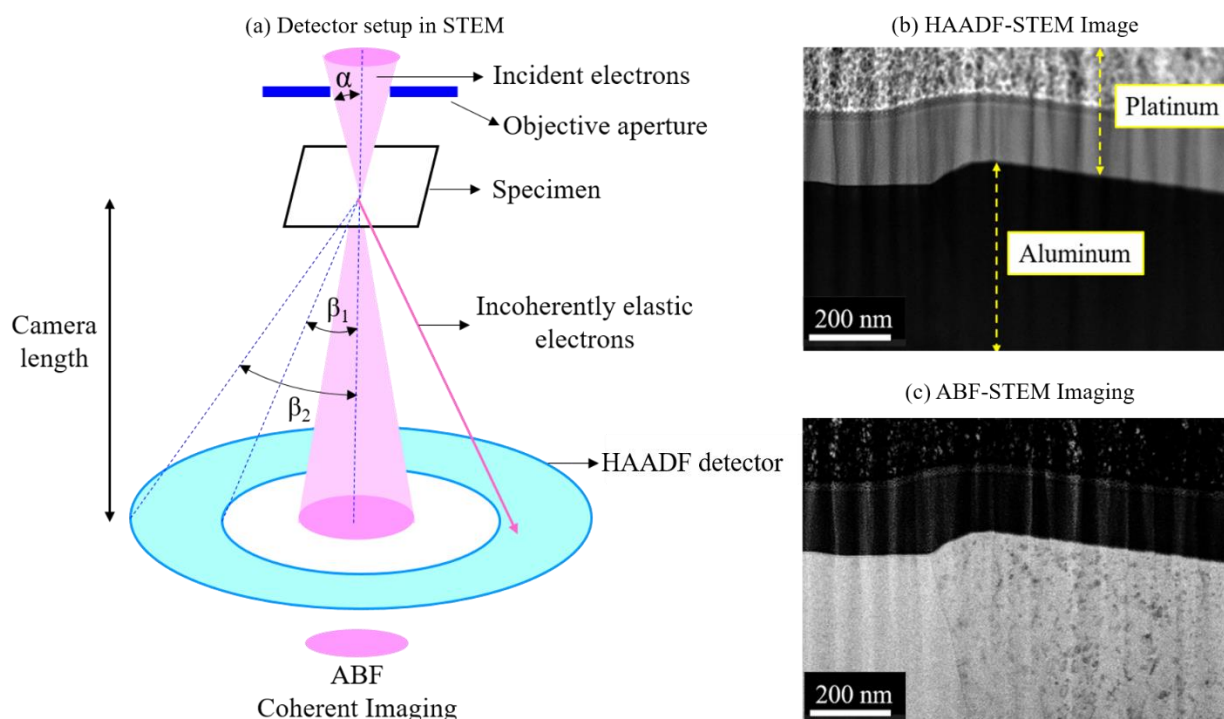

Figure 3-6: A schematic of the HAADF detector setup in a STEM. The β_1 = 78 mrad and β_2 = 200 mrad indicate the inner and outer semi-angles of the HAADF detector, detecting incoherent elastically scattered electrons at high angles. Image is redrawn from [157]. For a 300 kV Cs-corrected STEM, the convergence semi-angle's usual values fall between 15 and 30 mrad. Here, a convergence angle of 23.8 mrad is used. HAADF (figure **b)**) and ABF STEM (figure **c)**) of an Al thin film with a Pt protection layer from the identical sample position.

Concentric annular detectors with different diameters were recommended by Crew (1975) for STEM in order to detect electrons scattered over a wide angular range. A specific annular region can be selected for collecting the electrons scattered up to the specific angles by controlling the semi- collection angle (β) and the semi convergence angle (α). The focus of the electron beam is described by the semi-convergence angle α of the probe, which is directly proportional to the size of the condenser aperture (in this case, the C2 aperture). While the semi collection angle β is adjusted by changing the microscope's camera length (L) as shown in **Figure 3-6 a)**. For each different imaging condition, an angular range having an inner (β1) and an outer angle (β2) represents the semi-collection angles [157]. For example: for a fixed camera length of 100 mm and a semi-convergence angle α of about 17 mrad, different imaging conditions are attributed such as below 16 mrad annular bright field (ABF) imaging, 17 - 78 mrad low angle annular dark field

(LAADF) imaging and above 78 - 200 mrad HAADF imaging, respectively. These angular ranges are also similar in other microscopes; however, they are still quite specific to our in-house instruments at MPIE (Titan Themis, 60-300 keV). Each detector collects the electrons only in a specific angular range. One such example is depicted in **Figure 3-6 b)** and **c)**, where an identical region from the cross-sectional sample of an Al thin film with a Pt protection layer is shown in both annular bright filed (ABF) and HAADF STEM images to compare the contrast. The dislocations in ABF clearly shows the presence of diffraction contrast due to the low collection angle in contrast to the absence of such contrast observed in HAADF. The higher atomic number (Z) element Platinum (Pt) in the HAADF image appears brighter due to more high angle scattering than in the low Z element Al. The two different Pt layers at the top of the Al correspond to the electron and ion-assisted Pt deposition by GIS in the PFIB.

Incoherent (elastic) scattering is the foremost mechanism for image formation in HAADF imaging, which is also known as Z-contrast imaging. It is important to use the optimum large collection angles for the detector in order to enhance the Z-contrast and suppress the effects of diffraction contrast [158]. This is because both the presence of high diffraction contrast at small scattering angles and the emergence of diffused signals at very high scattering angles will lead to the degradation of Z contrast in the images [159].

As the beam is rastered across the specimen, every atom behaves as an independent scattering center. Therefore, there is no phase relation between the incoming electron wave and the scattered wave, thereby making this imaging mode incoherent. In a mathematical sense, this is described by the fundamental equation of image intensity from incoherent imaging [160]:

$$I\,(\vec{r}) = O\,(\vec{r}) \otimes |(P(\vec{r})|^2 \qquad\qquad 3.5$$

Here, the object function ($O\,(\vec{r})$) is defined by the scattering cross section. The above equation depicts that the image intensity emerges from a convolution of the object function ($O\,(\vec{r})$) with the intensity of the electron probe i.e. squared point spread function ($P\,(\vec{r})$) as shown in **Figure 3-7**. Incoherent imaging leads to easily interpretable data with no contrast reversals or delocalization, as well as the point resolution is almost equal to the information limit. However, this is true only for an aberration corrected instrument, since lens aberration, diffraction etc. lead to blurring of the beam.

To a first approximation, the intensity in HAADF micrographs can be described by the screened, relativistic, differential Rutherford cross-section by the equation [160]:

$$\frac{d\sigma}{d\Omega} = \frac{\lambda^4 \times Z^2}{64\ \pi^4\ a_0^2 E_0 \left(\sin^2\left(\frac{\theta}{2}\right) + \left(\frac{\theta_0}{2}\right)^2\right)^2}$$

3.6

Here, Z is the atomic number, a_0 is the Bohr radius, E_0 is the probe's energy, θ is the scattering angle, θ_0 is the characteristic screening angle, and λ is the mean free path for elastic scattering.
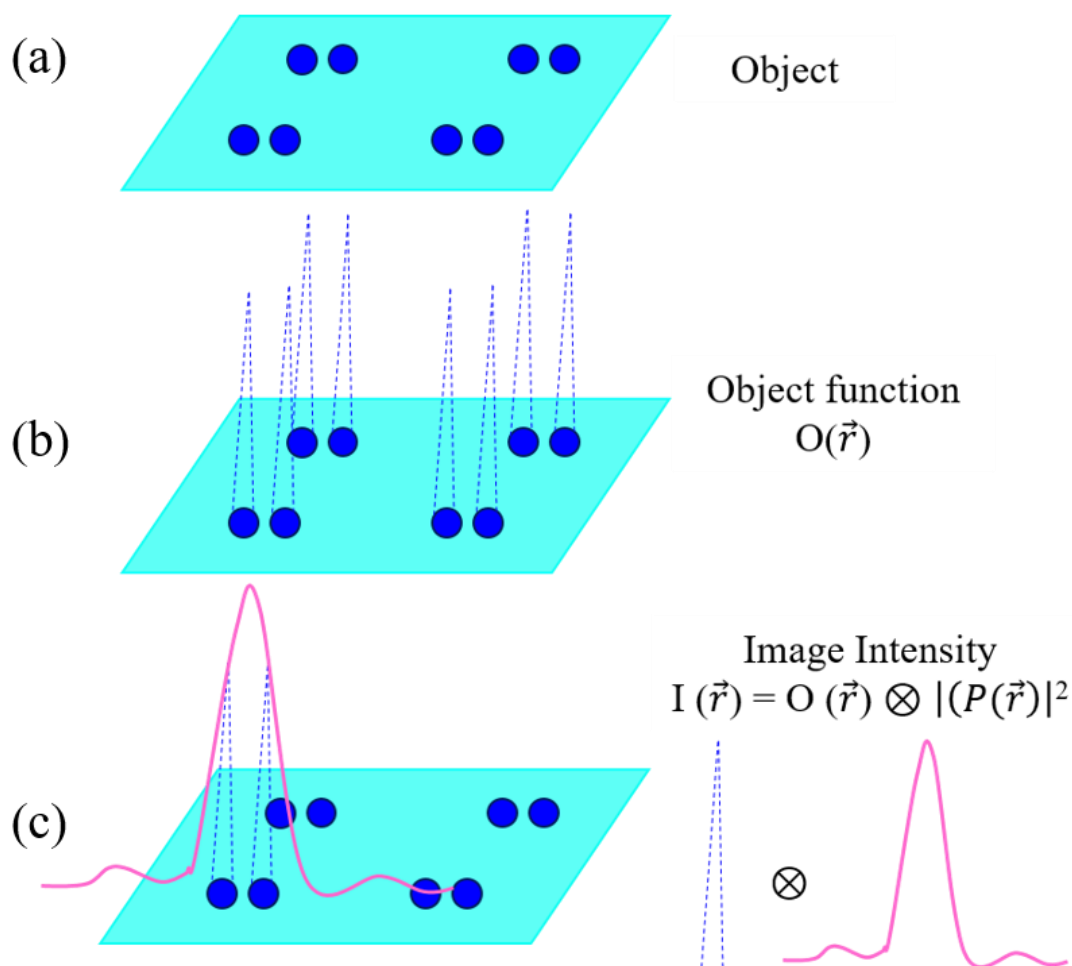
Figure 3-7: A schematic illustration of the formation of an incoherent Z-contrast image in STEM. a) A crystalline monolayer of atoms. **b)** The object function of the sample constitutes the scattering cross sections for each atom, which are roughly proportional to Z^2. **c)** Interaction of a pair of atoms with a Gaussian shaped probe. Rastering of the probe across the specimen maps the objective function, resulting in a direct incoherent image manifesting the position of the atoms. The image gives a depiction of the object, which is blurred by the size of the probe. Hence, its intensity is a convolution of the object function with the intensity of the electron probe i.e. the point spread function. The image is adapted with permission from Ref. [160].

The angular distribution of the scattered electrons is directly proportional to the square of the atomic number Z of the elements in a specimen. HAADF STEM imaging is quintessential for analyzing GB structures and segregation events down to the atomic level because of the strong Z contrast that results from the high-angle scattering. This results in a high-contrast, chemically sensitive imaging mode. The shape and size of the electron probe are the major factors that decide the resolution in STEM, which is eventually governed by the objective aperture and its aberrations. In order to attain the atomic resolution in STEM, the probe size should be smaller than the atomic distances in the specimen. Therefore, minimizing aberrations and creating the smallest, most intense probe with a Gaussian intensity shape are the ideal conditions for incoherent imaging in STEM. The strength of the condenser lens can be increased to provide higher source demagnification. However, doing so results in a lower beam current. Therefore, higher brightness is necessary to provide a reasonable current and it is for this reason that the modern STEM instruments are equipped with high-brightness gun in order to have enough current left after demagnification to detect larger signals. On the other hand, the probe size is also limited by the aberrations in the objective lens, which are defined as the deviation in path length between the ideal spherical wave and the actual wave front emerging from the lens in the microscope [152,160]. There exists a myriad of aberrations in addition to the more typical ones like first-order astigmatism and coma. The scattering angle θ power series that represents the aberration coefficients is described as follows:

$$\chi(\theta) = \frac{2\pi}{\lambda}\left[\frac{1}{2}\Delta f\theta^2 + \frac{1}{4}C_s\theta^4 + \frac{1}{6}C_5\theta^6 + \frac{1}{8}C_7\theta^8 + \cdots\right] \qquad 3.7$$

Here, C_s, C_5 and C_7 stands for the coefficients of third, fifth, and seventh order spherical aberration, respectively and Δf is defocus. Furthermore, STEM's resolution is also highly controlled by the diffraction limit from the probe-forming aperture. The bigger the aperture, the higher the resolution, however with the incorporation of the stronger aberrations of the lenses, namely astigmatism, coma and spherical aberration such as chromatic aberrations, thereby effecting the beam shape and size. Therefore, a balance between diffraction limit and aberration is required in order to achieve the best STEM resolution. Correction of these resolution-limiting factors is not trivial and can be well compensated by the aberration correctors. Such aberration-correctors require very complex assemblies of electromagnetic lenses (such as quadrupole, hexapole and octopole lenses) in order to compensate for the aberrations and allow an increase in the semi-

convergence angles to 23.8 mrad or even larger (in comparison to ~10 mrad in uncorrected STEM instruments). This paved the way to form probes with a diameter of several hundred pico-meters, well below the distances between the neighboring atomic columns for most of the materials and hence remarkably improved the resolution of STEMs.

3.3 Energy dispersive X-ray spectroscopy

For the literature of this section, please refer to refs. [160–162]. Energy dispersive X-ray analysis (EDX), also referred to as EDS or EDX, is an X-ray method that provides access to various compositional details at the atomic level.
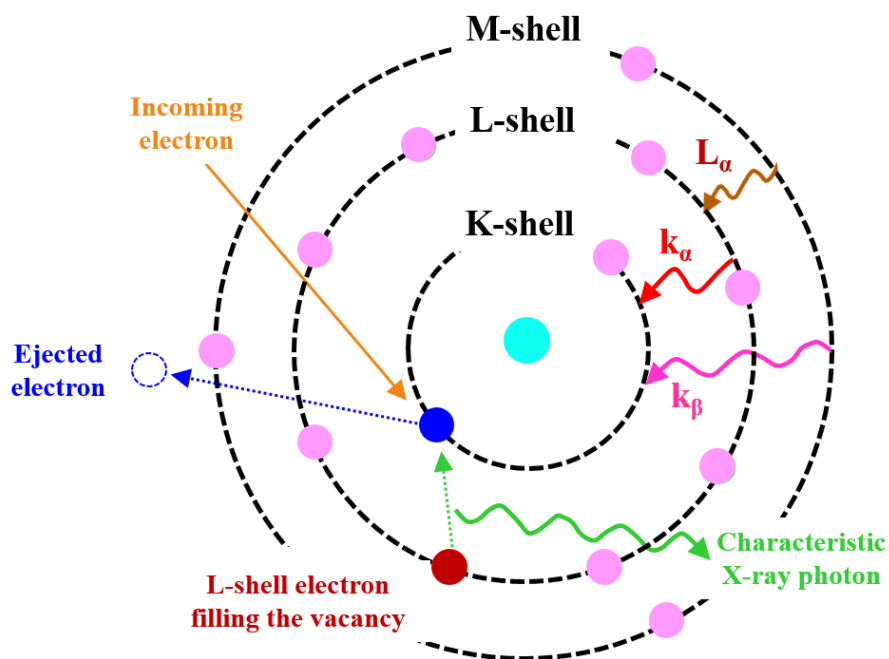
Figure 3-8: Energy dispersive X-ray spectroscopy (EDS) principle: A schematic of the incident beam electrons interaction with the electrons and the nucleus of an Al atom. The impinging electron transfers energy and ejects a core shell electron, which leaves an atom in excited/ionized state. A higher shell electron (in this case from the L shell) filled the created empty state. This transition is followed by an emission of an X-Ray photon that is element specific.

EDS relies on X-ray radiation originating from inelastic scattering events between impinging electrons and electrons belonging to the specimen. The incident electron transfers energy to an inner shell electron of an atom and that electron is excited into an unoccupied state above the Fermi level. The ionized atom returns to a low energy state by filling in the hole with an outer shell electron. This transition can be accompanied by the emission of an X-ray photon carrying the exact

40

energy equivalent to the energy difference between the two energy levels and this energy difference is unique to each element. According to Moseley's Law, there is a direct correlation between the energy emit by the outer shell electron and the atomic number (Z) of the atom. Therefore, these generated X-rays are used to identify what elements are present, as well as in what proportion they are present in the TEM specimen. If an electron from the K shell is ejected and then filled by an electron from the L or the M shell as illustrated in **Figure 3-8**, a K_α or K_β type X-ray photon is generated, respectively. The number of electrons present in an atom of that specific element determines the number and type of transitions that can occur. In order to obtain a good signal to noise ratio and efficiency, large detector areas are required to capture a lot of X-rays. Due to geometrical limitations, such as a lack of space to accommodate a much larger area detector and the sample's location between the two pole components of the objective lens, it is not possible for the detector to detect all of them. Nevertheless, the usage of multiple small detectors may enhance the collection efficiency, which increase the total solid angle and ultimately the X-ray counts. The aberration corrected modern microscopes allow improved detector arrangements with large detector areas. Yet, the efficiency of EDS system is still low, because many X-rays do not reach the detector due to shielding by the specimen holder. However, this has been robustly developed lately.

Nowadays, the most common X-ray detector used to detect the generated X-rays is silicon drift detector. The incoming X-rays transfer energy into a semiconductor thereby creating electron-hole pairs due to the ionization process. The energy of the entering X-ray photon directly correlates to the quantity of electrons or holes produced in the detector. Applying a reverse bias separates the electrons and holes, and a pulse of electrons can be detected at the rear interface. Once each X-ray has been counted, a pulse charge is produced in proportion to the energy of the X-ray. This pulse, produced by an X-ray of particular energy, is first transformed to a voltage, pre-amplified using a field-effect transistor, and then electrically recognized. An energy-specific channel in the computer display is designated to store a digitized signal. The quantity of X-ray counts (Intensity) is finally plotted against the X-ray energy to create a characteristic spectrum. An example of an EDS spectrum of an Al alloy 7075 thin film and its quantification results (inset) is shown in **Figure 3-9**, which reveals the percentage of different elements present in the specimen [125]. It is important to note that some additional smaller X-ray peaks might arise in the spectrum, which may not be from the specimen. They might come from either the pole piece or the specimen holder or the other

parts of the microscope and have to be taken into account for accurate quantification. For more details, please refer to [150,153]. EDS can be done in both TEM (parallel beam) and STEM (convergent beam) mode. However, STEM-EDS is more advantageous because a spectrum is collected at each pixel of the STEM image in contrast to parallel illumination in TEM, where only one spectrum is acquired representing that entire illuminated area. Interestingly, EDS can be used for qualitative and quantitative investigation, such as identifying the types of elements present and the proportion of each element's concentration. (in the form of maps or line profiles) within the specimen. Castaing Raimond [163] in 1951 showed that the relative intensity of an X-ray line is approximately proportional to the mass concentration of the element concerned. The ratio of the samples measured intensity I_A of element A to the measured intensity of element A in a well characterized standard reference sample $I_{(Standard)}$ can be related to the concentration ratio of the element present in weight percentage according to the following relationship:

$$\frac{C_A}{C_{(Standard)}} = K \frac{I_A}{I_{(Standard)}} \qquad 3.8$$

Here K is a sensitivity factor that takes into account the difference between the generated and measured X-ray intensities for both the standard and the unknown specimen. The three factors that contribute the most to K are: (i) the atomic number (Z) effect, which is connected to the ionization cross section of each element, (ii) X-ray absorption (A), and (iii) the fluorescence yield (F) of X-rays within the specimen. The correction procedure in bulk analysis in the SEM is usually referred to as the ZAF correction. It was shortly realized that the A and F factors could be ignored in TEM, but only the Z correction would be necessary for a thin electron-transparent specimen. Later in 1975, Cliff and Lorimer [164] proposed a simpler quantification without incorporating intensity from standard specimen but simply the ratio of the intensities gathered from two elements acquired simultaneously in the EDS. According to Cliff and Lorimer equation, the weight percent of each element C_A and C_B can be related to I_A and I_B as:

$$\frac{C_A}{C_B} = K_{AB} \frac{I_A}{I_B} \qquad 3.9$$

The term, K_{AB} is often termed the Cliff-Lorimer factor and depend on the EDS system and the operating voltage of the TEM. It is simple to modify equation 3.9 to take into consideration alloys having more than two components. Ignoring the effects of absorption and fluorescence, K_{AB} is related only to the atomic-number correction factor (Z) in Castaing's original ratio equation. Once

enough counts are accumulated in the characteristic peaks, I_A, I_B, etc., the peak intensities are determined after removing the background counts from the spectrum and then integrating the peak counts. After that, the value for the K_{AB} factor is evaluated.
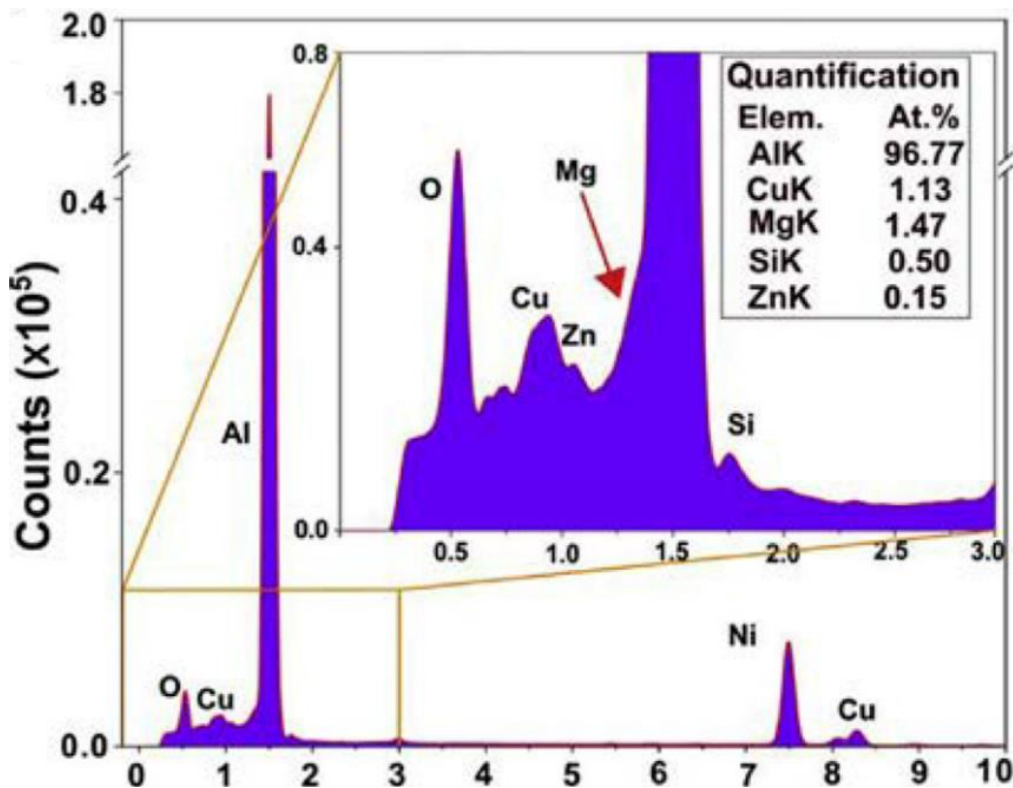

Figure 3-9: An EDS spectra and quantification results (inset) from a larger area of an Al alloy 7075 thin film specimen [125]. The plot here shows the number of elements and their amount present in the specimen.

An unfortunate feature of the simple Cliff-Lorimer ratio equation is relatively large errors associated with it. The very nature of the thin specimen minimizes the problems of absorption and fluorescence, but also generates relatively less X-ray photons, compared with bulk specimens. This can be overcome by using higher-brightness FEG sources, C_s correction, large electron probes, and thicker specimens, which is consistent with maintaining the desired spatial resolution and current into the sample. With these latest advancements, it is now possible to perform quantitative X-ray mapping with a spatial resolution of a less than a nanometer and detection limits of a few atoms.

3.4 Simulation techniques

3.4.1 STEM image simulation: The multi-slice simulation

High-resolution S/TEM is a powerful tool used to avail information about crystal structures and lattice imperfections such as point defects, and dislocations, etc. in advanced materials on an atomic scale. However, a number of parameters, including sample thickness, exact beam alignment with respect to the specimen and the optical axis, defocus, and lens imperfections, have a significant impact on the contrast of these high-resolution micrographs. Due to the aforementioned factors, there is a loss of phase information of the wave function in an experimental intensity map acquired, which makes the image quantification and interpretation difficult. Therefore, in the pursuit of quantification of image intensity of atomic columns in an atomically resolved S/TEM image, image simulations are used. There are two different methods for performing the atomic resolution simulation i.e. multi-slice and Bloch waves techniques. In this work, the multi slice approach was employed, as it is fast and more efficient for large electron scattering simulation. A more detailed description can be found in [165–167].

In the multi slice method, the specimen is divided into thin 2-D slices along the optical axis, which are described by an electrostatic potential V(r). A convergent probe is initiated and transmitted through a potential slice. The amplitude and phase of the electron wave function are modulated by the interaction with the potential of the atoms in the slices. The transmitted wave function is explicitly propagated from one layer to the next by convolution with the propagator function until it has passed through all the slices, across the entire crystalline TEM sample. The resulting exit wave function (Ψ_{exit} $(\vec{r})$) is described by the following equation:

$$\Psi_{exit} (\vec{r}) = p (\vec{r}) \otimes t (\vec{r}) . \Psi (\vec{r}) \qquad\qquad 3.10$$

Here $\Psi (\vec{r})$, $t (\vec{r})$, and $p (\vec{r})$ are called wave function, transmission function and propagation function, respectively. The vibration of the atoms from its equilibrium position in a material at room temperature results in a thermal diffuse scattering background in the experimental images. The frozen phonon approximation approach is utilized to numerically simulate the influence of thermal vibrations in the sample. In this approach, the intensity of the simulated image is the intensity averaged over various distinct layouts of atoms, with different random offsets from their ideal positions in each slice.

STEM image simulation can be computationally very expensive and much more time consuming compared with conventional TEM image simulation, as the simulation has to be performed at each probe position. In the current thesis, simulations were carried out using the multi-slice algorithm

44

within abTEM (a Python API) that provides straightforward and intuitive user interface. For a detailed description of how the simulation codes actually works, please refer to abTEM documentation [168,169].

3.4.2 Molecular static simulation

This section is based on the ref. [22,170,171]. In order to establish a structure-property correlation, it is essential to determine the excess properties of the GB structures, which are not easily accessible. Therefore, in order to establish a structure-property correlation, a computational technique such as molecular static is utilized in the thesis to complement the experimentally obtained GB structures. Molecular static (MS) simulations are employed to simulate the atomic structure of the interfaces for the given boundary conditions at 0 K by minimizing the system's potential energy. Let us consider a simulation cell containing N interacting atoms and V_n be the total potential energy of interaction between the nth atom and the rest of the system. The total potential energy of the system V_t is expressed as:

$$V_t = \sum_N V_n \qquad\qquad 3.11$$

This method is based on the determination of a static atomic configuration in the system, that minimizes the V_t. The total force applied by the rest of the system on the nth atom is given by:

$$\overrightarrow{F_n} = -\nabla_n V_t \qquad\qquad 3.12$$

Here, ∇_n indicates the gradient w.r.t the position of the nth atom in the 3-D space. The forces among the particles are evaluated and then the atoms are artificially displaced in the direction of the $\overrightarrow{F_n}$ vectors. An equilibrium stable configuration is reached when the net force in the system is zero i.e. all the forces are absent and energy minimization takes place i.e. V_t is minimized. Since the presence of minima is sensitive to the initial starting geometry of the system, the minimization usually depicts only local energy minima but not the global minimum. Regardless, it is a very fast computational technique and is comprehensively applied in atomistic simulations of GB structure. The MS simulation provides information on the interfacial excess properties, such as grain boundary energy, the GB stress tensor (τ_{ij}) and the excess volume [86]. The calculated GB structures can then be compared to the experimentally observed STEM images in order to correlate the GB structure with the GB properties.

Chapter 4 Materials and experimental details

4.1 Deposition and alloying of Al thin films on (0001) α-Al₂O₃ samples

Firstly, pure Al (99.995%) thin film depositions investigated in the **Chapter 5.1** (Paper I) were carried out using electron beam (e-beam) evaporation at the BesTec PVD cluster located at the Max-Planck-Institut für Eisenforschung GmbH in Düsseldorf[*]. The films were deposited on two inch (0001) oriented α-Al₂O₃ (sapphire) wafers (miscut of <0.25°, one side polished, CrysTec Kristalltechnologie, Berlin, Germany). The deposition conditions are described in **Table 1**. These substrates weren't given any additional surface treatments; they were used just in as arrived state. The base pressure of the deposition chamber was $\sim 5 \times 10^{-8}$ mbar for all the depositions.

Table 1: List of Al films that were deposited using e-beam deposition, along with the deposition parameters for each film

Thin film Nr.	Deposition temperature (∘C)	Deposition rate (Å/s)	Post annealing of the Al film		Thickness (nm)
			Temperature(T)	Time (t)	
S1	35	0.5	-	-	145
S2	200	3	-	-	400-465
S3	300	3	-	-	408
S4	300	3	300∘C	3hrs	665

The distance between the substrate and the target was ∼250 mm. The thicknesses of the Al films were measured using a quartz microbalance, and constantly monitored during deposition. For all high temperature depositions, the samples were slowly cooled down to room temperature in the vacuum subsequently after the deposition.

Furthermore, pure Al thin film, used in the **Chapter 5.2** and **Chapter 5.3** was grown by magnetron sputtering technique on a 2 inch (0001) oriented sapphire wafer as described above. The deposition

---

[*] Dr. Hanna Bishara is gratefully acknowledged for the deposition of the Al films at MPIE

was carried out at the Central Scientific Facility for Materials of the Max Planck Institute for Intelligent Systems (formerly known as MPI für Metallforschung) in Stuttgart under ultra-high vacuum conditions, followed by a post deposition annealing for several cycles at 400°C at the rate of 6 K/hr in Argon atmosphere[†]. Firstly, the sapphire substrate was Ar-sputter cleaned at 200eV to remove the surface contaminants in the UHV system and then annealed at 800°C for 2 hr to further remove structural defects. Subsequently, the substrate was cooled down to 100°C and the Al films were sputtered with a deposition rate of 0.11 nm/s. Finally, the sample was slowly cooled down to room temperature in vacuum. The nominal film thickness was chosen to be 800 nm. The film was subsequently annealed in three cycles at 400°C in an inert Ar atmosphere.

For studying segregation effects of Cu and Zr on Al GBs in **Chapter 5.4**, the same Al films (used for **Chapter 5.2** and **Chapter 5.3**) were Ar-sputter cleaned from the top surface to remove the strong native oxide layer. After the removal of the native oxide, a very thin (approximately 180 nm) layer of Zr was deposited separately on the top surface of the two pure Al film parts, at room temperature[‡]. Deposition of Zr was done without taking out the sample from the chamber after Ar-cleaning. SEM-EDS analysis revealed that Cu is also present with Zr on the top of the Al film, due to cross-contamination from the deposition chamber. Therefore, now we have a Zr-Cu reservoir on the surface of the Al film. The Al film with the Zr-Cu top layer was first annealed in the vacuum furnace at 450°C for 6 hrs and slowly cooled down to room temperature inside the furnace. Since no Zr segregation was observed after the first annealing, a second annealing to 520°C for 32 hrs was carried out in order to enhance the diffusion kinetics of Zr.

4.2 Sample preparation

SEM samples used in the **Chapter 5** were prepared by cutting out the small rectangular pieces from the film, with the help of a diamond pen. All the plan view and cross sectional view site-specific TEM specimens from the thin film (pre-analyzed by EBSD) were lifted out in a dual-beam SEM/focused ion beam instrument (Helios Nanolab G3 CX Dual Beam FIB, Thermo Fisher Scientific) having Xe as an ion source. Using Xe-FIB instead of conventional Ga-FIB avoids the problem of implanted Ga, which tends to segregate at the Al GBs and thus leads to very prompt,

---

[†] Sputter deposition and annealing was done by Dr. Gunther Richter and Dr. Gerhard Dehm
[‡] Dr.Simon Evertz is thanked for Ar-cleaning and subsequent Cu-Zr deposition.

substantial loss of Al ductility via liquid metal embrittlement (LME) [147]. An improvised wedge milling approach, described by Schaffer et. al [172] was adapted for the thinning of the lamella. Exact milling parameters depending on each sample are listed in **Table 2**, depicting a typical thinning procedure.

In principle, for coarse milling/ thinning the FIB was operated at 30 kV, for gentle thinning at 16 kV and 8kV from ~1000 nm down to ~200 nm thickness followed by final polishing at 2 kV, whereby the beam current was varied from high to low for each kV.

Table 2: Plasma (Xe) FIB operating parameters applied for the thinning of plan-view TEM lamella [§]

Lamella thickness	Ion accelerating voltages, relative tilt(°), ion beam current(s)
Coarse thinning (~ 1200nm)	30 kV, ± 0.5°, 0.10 nA
~ 1000 nm	16 kV, ± 1°, 0.30 nA - 0.10 nA
~ 800 nm	16 kV, ± 1.5°, 30 pA - 10pA
~ 200 nm	8 kV, ± 2°, 10 pA
Final polishing	2kV, ± 4°, 5pA - 4 pA

4.3 Characterization methods and parameters

The local surface morphology of the pure Al thin films deposited at different substrate temperatures and deposition rates were investigated by SEM with an acceleration voltage of 10 kV. The microstructural attributes (grain orientation, texture, grain size, CSL GB type and its distribution) of the thin film were characterized by using SEM-EBSD at 20 kV in a JEOL JSM-6490 SEM. EBSD data analyses were performed with the help of OIM 7.0 software. EBSD

[§] Refer to manuscript II by S. Ahmad (Acta Materialia, p.118499 (November 2022))

analysis was performed on the dataset to get rid of the noise by utilizing the following parameters: elimination of data points with a confidence index (CI) value below 0.1, grain tolerance angle of 5°, and neighbour CI cleanup was performed on data points with CIs below 0.3–0.4.

In the thesis, all conventional TEM characterization (BF, DF and SAD) was primarily carried out at the Thermo Fisher Scientific Titan Themis 80-300 X-FEG TEM. BF-TEM imaging was used to investigate the cross-sections of the Al thin films. The obtained TEM images were then analyzed in Image-J [173] in order to measure the microstructural features such as lateral grain size and thickness of the Al thin films. Selected area diffraction (SAD) and high-resolution transmission electron microscopy (HRTEM) were used to determine the orientation relationship (OR) between the Al grains and the sapphire substrate.

All images in HAADF-STEM were acquired using a C_s-probe corrected Titan Themis 60-300 (Thermo Fisher Scientific), equipped with a gun monochromator and operated at 300 kV and a probe current of about 70 to 90 pA. The semi-collection angles of the annular detector for HAADF imaging were set to 40 mrad/78 mrad – 200 mrad using a semi-convergence angle of 17 mrad. In order to reduce the effect of instrumental instabilities such as drift and noise in the images, image series comprising of 10–40 images with a dwell time of 2–20 μs were recorded and superimposed on each other. Furthermore, image processing was performed in the velox software, involving mainly radial wiener filtering. The misorientation angle of a GB is estimated from the atomically resolved HAADF image by drawing lines along the planes on both the adjoining grains forming the GB. Thereafter, the angles between the drawn lines are measured and averaged. The Strain++ software [174] was used to perform FFT analysis on the LAGBs (in **Chapter 5.1**), which uses geometric phase analysis (GPA) algorithm as described in the Ref [175].

4.4 Atomic-scale simulations

4.4.1 Multi-slice simulation

STEM image simulations were carried out using the multi-slice algorithm within abTEM [168,169] with simulation cells (at ε ≈ 0 % and ε ≈ 0.5%) from **Figure 5-15**. A 300 keV electron probe with a focal spread of 100 Å, a semi-angle of 17.8 mrad and defocus of 0 was generated in order to have the identical settings as utilized in the experiment. The step size used was 0.178 Å

and 0.008 Å, for the E and E' units respectively. The HAADF collection angles were set to 40.5 mrad/77.9 mrad – 200 mrad. A slice thickness of 2.5 Å was used as the atomic column separation along the z direction. The simulated cells used were of the different thickness (t) ranging from t = 14 nm to 56 nm to understand the influence of thickness on the projected atomic structure.

4.4.2 Molecular static simulation

In order to analyze the thermodynamic properties of the grain boundary structures in more detail, we also simulated them using an embedded atom method (EAM) potential for Al [176] using the LAMMPS software[**] [177]. We calculated the 0 K cohesive energy and lattice constant for the fcc structure. To prepare the GB structure search for Σ3 boundary, we constructed a bicrystal: with the following crystal directions along the Cartesian directions: $[111]$, $[1\bar{1}0]$, and $[11\bar{2}]$ for the first crystallite and $[111]$, $[0\bar{1}1]$, and $[2\bar{1}\bar{1}]$ for the second one. The tilt axis was therefore aligned in *x* direction and the GB normal in *z* direction. The crystallites were joined at their {112} surfaces and the system had periodic boundaries in *x* and *y* direction and open boundaries in *z*. The final boxes had a size of around 14×17×120 Å³ with 1440 atoms. Similarly, bicrystals for other Σ GBs are created. The 0 K structures were found by displacing one crystallite with regard to the other with constant simulation box size and optimizing the atomic positions with regard to the potential energy (γ-surface method). Thermodynamic excess properties were calculated as described in Refs. [85,86] and excess shears as described in Ref. [42].

[**] The MS simulations were performed by Dr. Tobias Brink.

Chapter 5 Results and discussion

5.1 Influence of substrate temperature on the distribution of edge-on [111] tilt grain boundaries (GBs) in Al thin films deposited via e-beam evaporation

In this chapter, an outline of deposition parameters is presented in order to fabricate the strongly [111] textured Al thin film with a wide distribution of [111] type columnar tilt GBs. In addition, the atomic structures of low-angle GBs are investigated and analysed. The work presented here is based on the unpublished manuscript I.[††]

5.1.1 Introduction

In the last few decades, pure aluminum (Al) films are in great industrial and scientific demand because of its numerous applications in the field of construction, optics, telecommunications and microelectronics, etc. [178–180]. They have outstanding coating properties such as low resistivity, high conductance, corrosion and oxidation resistant and good adhesion [181–183]. Al is known to be among the major materials in the microelectronics for the fabrication of interconnects [184,185]. A variety of Al thin films were successfully deposited using a wide range of substrates including glass, silicon (100), steels, NaCl, silver, polycarbonates, and sapphire etc. [186–189]. Nowadays, Al thin films are also utilized for experimental investigation of the atomic structures of tilt GBs in Al [125] to advance the fundamental understanding of GBs. The textured Al thin films having a flat, smooth surface and perfectly columnar GBs fulfill the strict requirements such as "edge on" GB and alignment of adjacent grains to a common low-index zone axis in order to investigate the GB structures on an atomic scale [34]. Furthermore, the ability to obtain a large distribution of different GB types in a thin film with the same tilt axis but varying GB plane and misorientation makes it one of the emerging methods for studying GBs.

It is well known that microstructural evolution and therefore the electrical and optical properties of metallic thin films are highly influenced by a variety of deposition parameters, such as the type of substrate, the thickness of the film, the deposition rate, the temperature of the substrate, the

---

[††] Based on manuscript I by S. Ahmad, H. Bishara, C. H. Liebscher, and G. Dehm

annealing conditions, and the background gas composition [130]. Among these parameters, the substrate temperature is extremely important for controlling the microstructure of the films as it directly influences the nucleation, coalescence, and film growth according to the structure zone models [130,190,191]. Several studies [192–197] have reported the influence of substrate temperature on the evolution of the microstructure and the physical properties of thin films of different materials such as Al, Ti, ZnO, CdS, and AlN, etc. However, the way that [111] tilt GB type and its fraction vary with substrate temperature has barely been reported [198,199]. Thus, it is of great interest to monitor the evolution of the GBs in the Al films deposited at different substrate temperature and investigate whether a template of processing parameters can be developed that will lead to the desired distribution of GBs, film morphology and thickness.

In this study, Al thin films were grown on (0001) sapphire substrate at the temperature range between room temperature and 300°C via e-beam evaporation technique In addition, SEM, EBSD, and S/TEM is used to study the microstructural characteristics of the deposited Al thin. The results acquired in this work provide insights of suitable deposition parameters to procure a variety of [111] tilt GBs (starting from low to high misorientation angle) in a textured Al thin film on sapphire substrate. Furthermore, the dislocation configurations at the [111] tilt low angle GBs in Al are examined by employing STEM-HAADF imaging.

5.1.2 Results

Surface topography/morphology of Al thin films

The morphology of the surface of the Al thin films deposited on sapphire substrates investigated by SEM are shown in **Figure 5-1**. The surface of the Al film deposited at room temperature (film S1) appears uneven, rough and porous with indifferentiable grains. Pores are present all over the surface of the film, where some large ones are indicated by the white squares in the **Figure 5-1 a)**. At 200°C deposition temperature (film S2), a non-homogeneous but denser surface is obtained, compared to the film S1.

Furthermore, the surface of the film is also irregular and rough as some of the grains are protruded (in a direction normal to the surface), which indicates the formation of hillocks [200,201], as indicated by white arrows in **Figure 5-1 b)**. However, the films deposited at 300°C (films S3 and S4), shown in **Figure 5-1 c)** and **d)** revealed that both films have a rather homogeneous, dense and

smooth surface in comparison to the films S1 and S2 deposited at lower temperatures. Note that the surface of the film S4, which has a thickness of 665 nm appears smoother than the film S3 with a thickness of 408 nm.
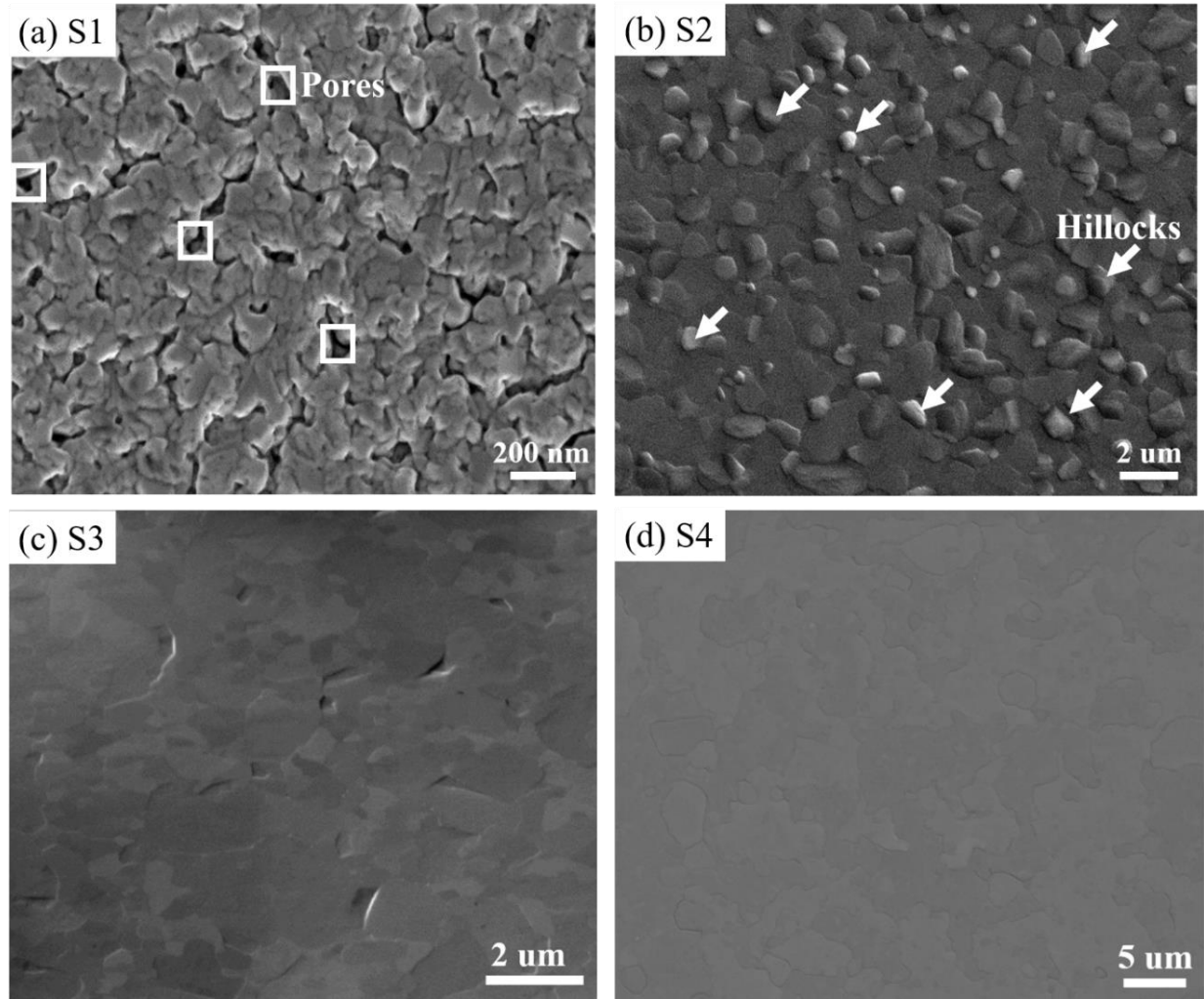
Figure 5-1: SEM Images showing the morphology of the Al thin film deposited at a) 35°C with thickness of 145 nm (film S1), **b)** 200°C with varying thickness from 400 up to 465 nm (film S2), **c)** 300°C with thickness of 408 nm (film S3), and **d)** 300°C with thickness of 665 nm (film S4).

Microstructural characterization of Al thin films deposited at 300°C

The surface roughness and porosity of the films S1 and S2 preclude further analysis of their grains and GBs by EBSD. Hence, we proceeded with the investigation of only S3 and S4 films by EBSD. **Figure 5-2**, **Figure 5-3** and **Figure 5-4** summarize the microstructural characterization of the Al thin

films deposited at 300°C focusing on texture, grain orientation, GB types and their distribution obtained by EBSD in the SEM.
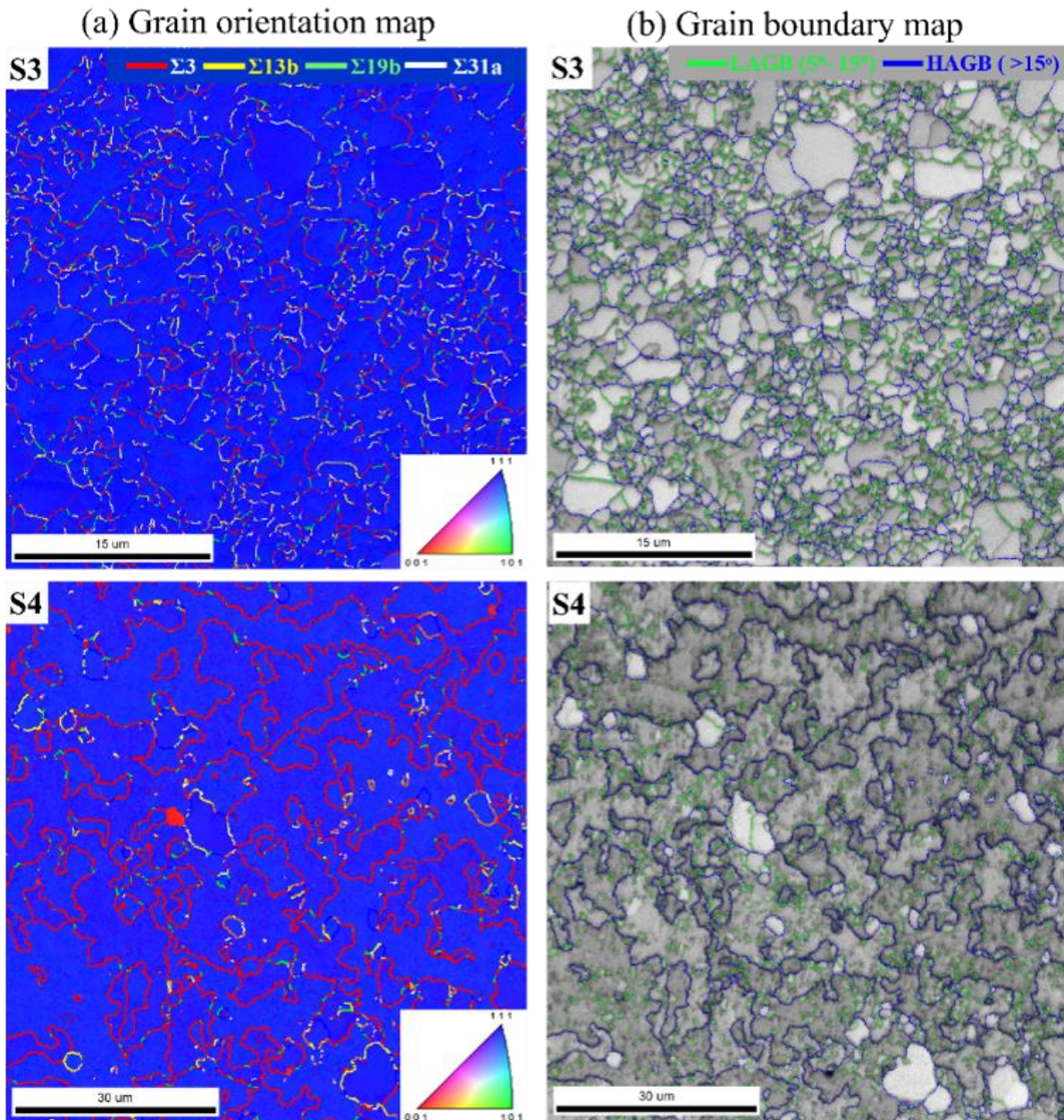
Figure 5-2: EBSD results for the S3 and S4 Al thin film. a) and **b)** represent the grain orientation map (in the film normal direction) and the grain boundary map, respectively. The grain orientation map is also called inverse pole figure (IPF) map, where blue color indicates {111} planes that are parallel to the surface of the film. The colored lines indicate different [111] tilt GB types in the film. $\Sigma3$ twin boundaries are illustrated in red, $\Sigma7$ GBs in blue, $\Sigma13b$ GBs in yellow and $\Sigma19b$ GBs in green. The green and blue color lines in the grain boundary map in **b)** indicate the LAGBs and HAGBs present in the films. A criterion of 15° was taken to discriminate between LAGB and HAGB.

54
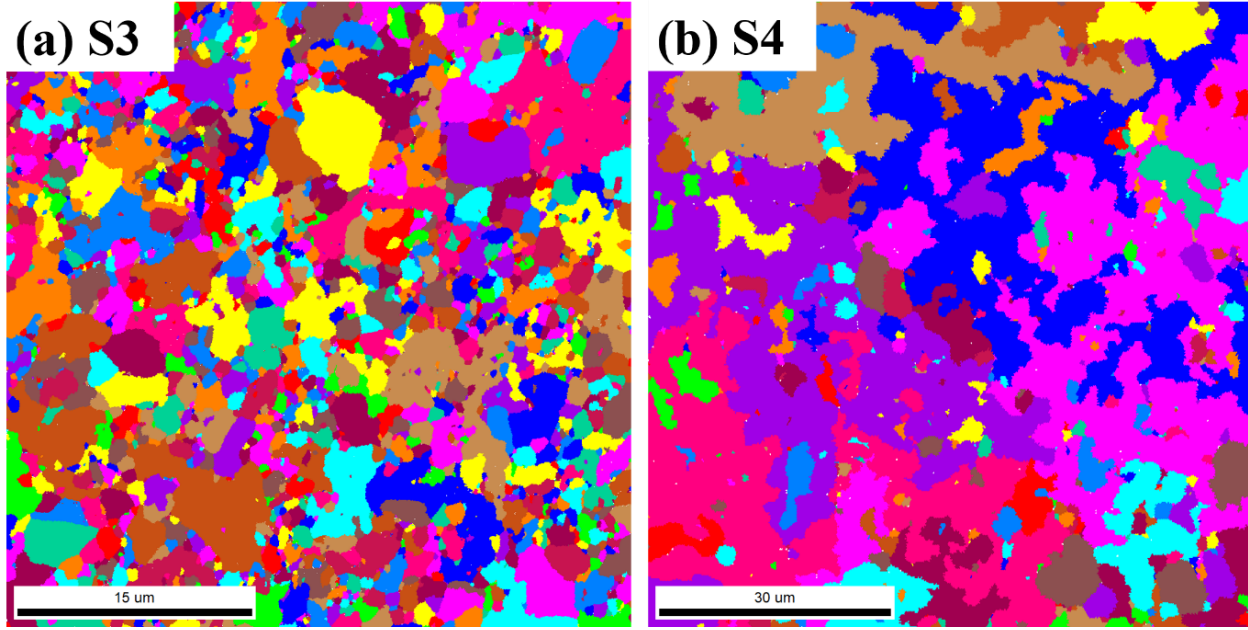
Figure 5-3: Unique grain color map showing the distribution of grains in the films S3 and S4. The different colors in the maps correspond to each unique grain for better visualization. Note that the different colors of the grain are not related to the orientation of the grains.

The EBSD IPF maps in **Figure 5-2 a)** ([111] direction) and the {111} Al pole figure in **Figure 5-4** clearly revealed a strong <111> fiber texture in the Al film. The central peak of the {111} Al EBSD pole figure refers to (111) Al planes that are parallel to the film surface. The presence of the strong {111} fiber texture is due to the favored orientation of the Al grains towards the lower surface energy planes in Al i.e. (111) planes [188,189,202]. Furthermore, the {111} fiber texture in both the films confirms the presence of both the ORs in the films, and are described as follows:

$$\text{ORI a/b } \{111\} \pm <0\bar{1}1> \text{Al} \,||\, (0001) <10\bar{1}0> \alpha\text{-Al}_2\text{O}_3 \qquad 5.1$$

$$\text{ORII a/b } \{111\} \pm <0\bar{1}1> \text{Al} \,||\, (0001) <2\bar{1}\bar{1}0> \alpha\text{-Al}_2\text{O}_3 \qquad 5.2$$

The corresponding GB characters and their distribution in S3 and S4 films are outlined in **Figure 5-4**. The microstructure of the S3 film is partially dominated by high angle boundaries such as Σ13b, Σ7, Σ19b, Σ21a, Σ31a and other higher Σ CSLs. Among the 44% of all the high-angle CSL boundaries, approximately 9% are Σ3 twin boundaries followed by 7% Σ13b, 7% Σ7, 4% Σ19b, 6% Σ21a, 5% Σ31a and a small percentage of other higher Σ CSLs. The remaining 56% percentage of the GBs in the film are the LAGBs, which are indicated by green colored lines in the grain

boundary map in **Figure 5-2 b)**. The grain size of the film S4 is much larger than the film S3. Furthermore, the fraction of the high angle CSL GBs reduces to 28%, with Σ3 twin boundaries making the largest fraction with ~20%, followed by a small fraction of other higher Σ CSLs. The amount of LAGBs in the S4 film is 72%, which is 1.3 times higher than in the film S3.
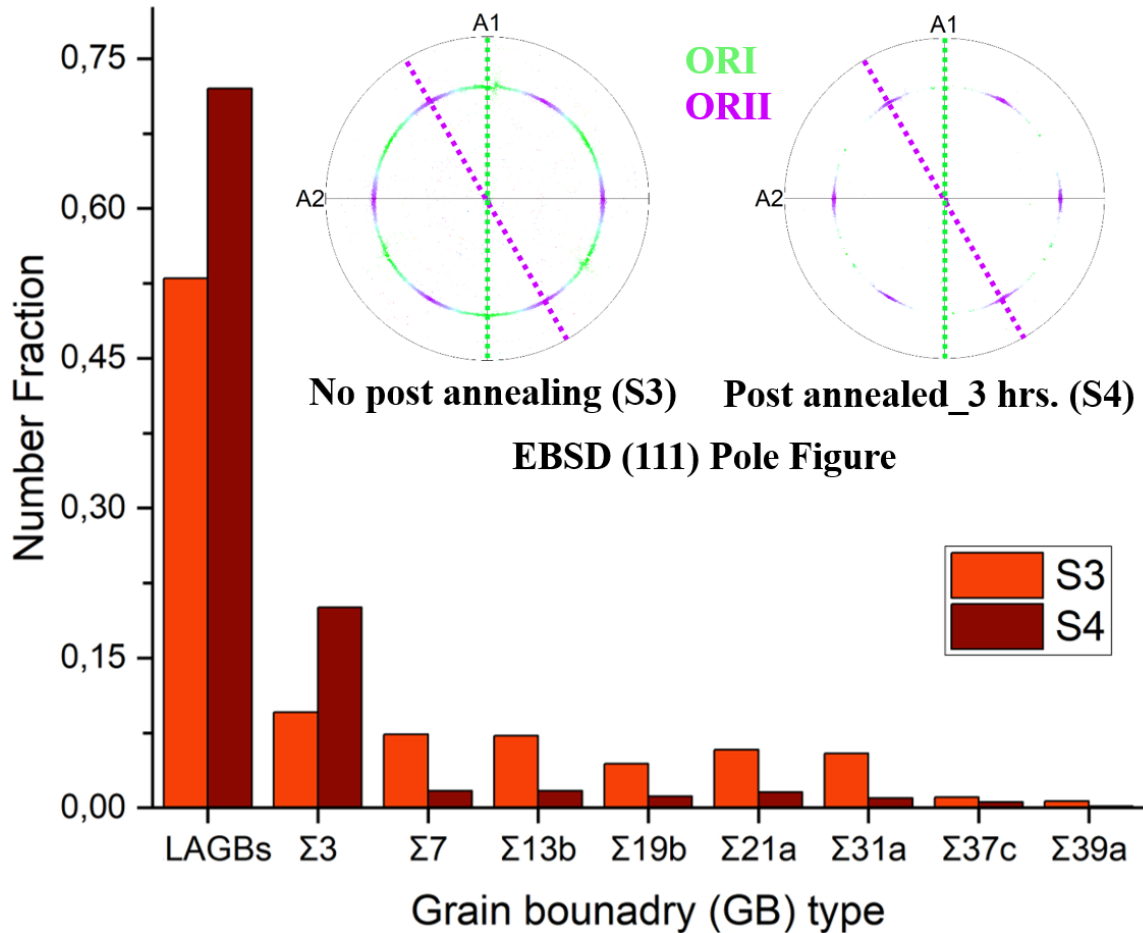
Figure 5-4: CSL distribution plot illustrating the fraction of each CSL boundaries present in the Al film. The {111} Al pole figure of the deposited film generated from EBSD data with OR I and OR II marked.

TEM investigation of Al thin film

Thin film growth and epitaxy

The cross-sectional bright-field (BF)-TEM images of the Al films deposited at high temperatures clearly reveal that the GBs are columnar, as shown in **Figure 5-5 a)** to **c)**. The thickness of the Al film S2 deposited at 200°C is non-uniform, ranging from 400-465 nm due to the protruding regions at the top surface. These protruding regions correspond to the hillocks, which are observed from the top surface of the film (see **Figure 5-1 b)**). In contrast, the thicknesses of the films S3 and S4

deposited at 300°C are uniform and 408 nm and 665 nm thick, respectively. The respective lateral grain size of S2, S3 and S4 films are <1 micron. This value is smaller than the grain size identified by EBSD (see **Figure 5-2**). This can be explained on one hand by the local measurement with poor statistics in cross-sectional TEM and on the other hand depends on the resolution limit and step size used in EBSD. For example: in the case of the S3 film, since the step size used in EBSD measurement is 600 nm, it is very likely that there are even sub-grain boundaries present within the grains (< 600 nm), which cannot be resolved with such a EBSD setting.
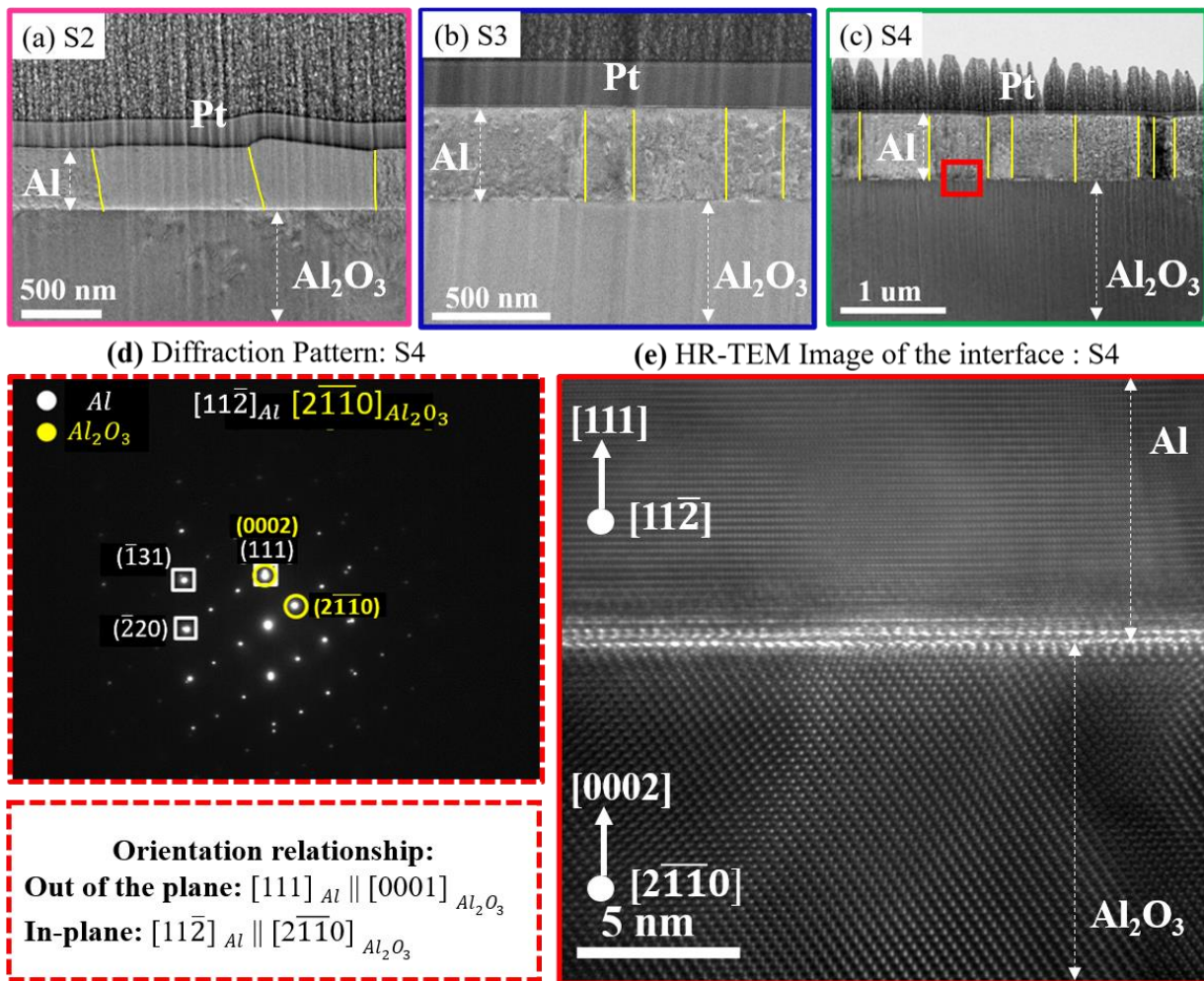
Figure 5-5: TEM investigation of the thin film growth and epitaxy. Cross-sectional view in **a), b),** and **c)** shows the thickness and film growth of the films S2, S3 and S4, respectively. The diffraction pattern and high-resolution image from the interface of the S4 film in **d)** and **e)** confirms the orientation relationship ORI between Al film and the sapphire substrate. The yellow color lines in all the Al film indicate the columnar grain boundaries, perpendicular to the sapphire substrate. The dark contrast region on the top of the Al film in **a), b)** and **c)** refers to the platinum deposition during sample preparation in FIB.

The corresponding selected area (electron) diffraction pattern (SADP) and high resolution-TEM of the interface between the Al film (S4) and the substrate is illustrated in **Figure 5-5 d)** and confirms the orientation relationship between the Al films and the sapphire obtained by EBSD pole figures. The film S4 is found to have an orientation relationship ORI i.e. $\{111\} \pm <11\bar{2}>$ Al ⎟⎟ (0001) $<2\bar{1}\bar{1}0>$ α-Al$_2$O$_3$ (0002), in agreement with the Ref [189,202]. However, it is worth noting that this is only a local analysis of ORI in the cross section lamella of the film S4. Whereas ORII must be present according to the EBSD-resolved pole figure in (Error! Reference source not found.). It is not captured in the TEM lamella. Energy-dispersive X-ray spectroscopy (EDS) performed in the STEM of the interface reveals that no reaction or segregation between the Al and the substrate occurred during deposition and subsequent annealing (not shown here).

Atomic structure of low angle GBs

So far, we have succeeded to obtain suitable Al thin films with various types of [111] tilt GBs, for studying their atomic structures. LAGBs in metals have been rarely observed experimentally at atomic resolution although they make up the largest fraction of the GBs in the Al thin film [125]. Hence, in order to understand the atomic structure of the [111] tilt LAGB for a high SFE material like Al, we investigated the atomic structure of three distinct LAGBs from the film S4 by HAADF-STEM. The GBs have a misorientation angle (θ) of nominally 13°, 10°, 6°, respectively, as illustrated in **Figure 5-6**. It is well known that a high density of edge dislocations along the LAGB is responsible for the accommodation of misorientation across the boundary. The relationship between the separation distance of a perfect dislocation D, the Burgers vector b, and the misorientation angle of a low-angle grain boundary θ is given by Frank's equation [19]:

$$D \cong \frac{|b|}{\theta}. \qquad\qquad 5.3$$

The orange Burgers circuit mapping in the STEM-HAADF images of the LAGBs (in **Figure 5-6 a)**, **c)** and **e)**) reveals that the edge dislocations along the GBs exhibit a Burgers vector of $1/2[\bar{1}01]$ and are aligned along the grain boundary with a dislocation spacing (D) of 1.3 ± 0.04 nm, 1.6 ± 0.04 nm and 2.8 ± 0.14 nm, respectively. We found that the dislocation spacing along the GBs decreases as expected with increasing misorientation angle. The measured D values match well with the theoretical values estimated following Frank's equation, as shown in the plot in **Figure 5-7**.
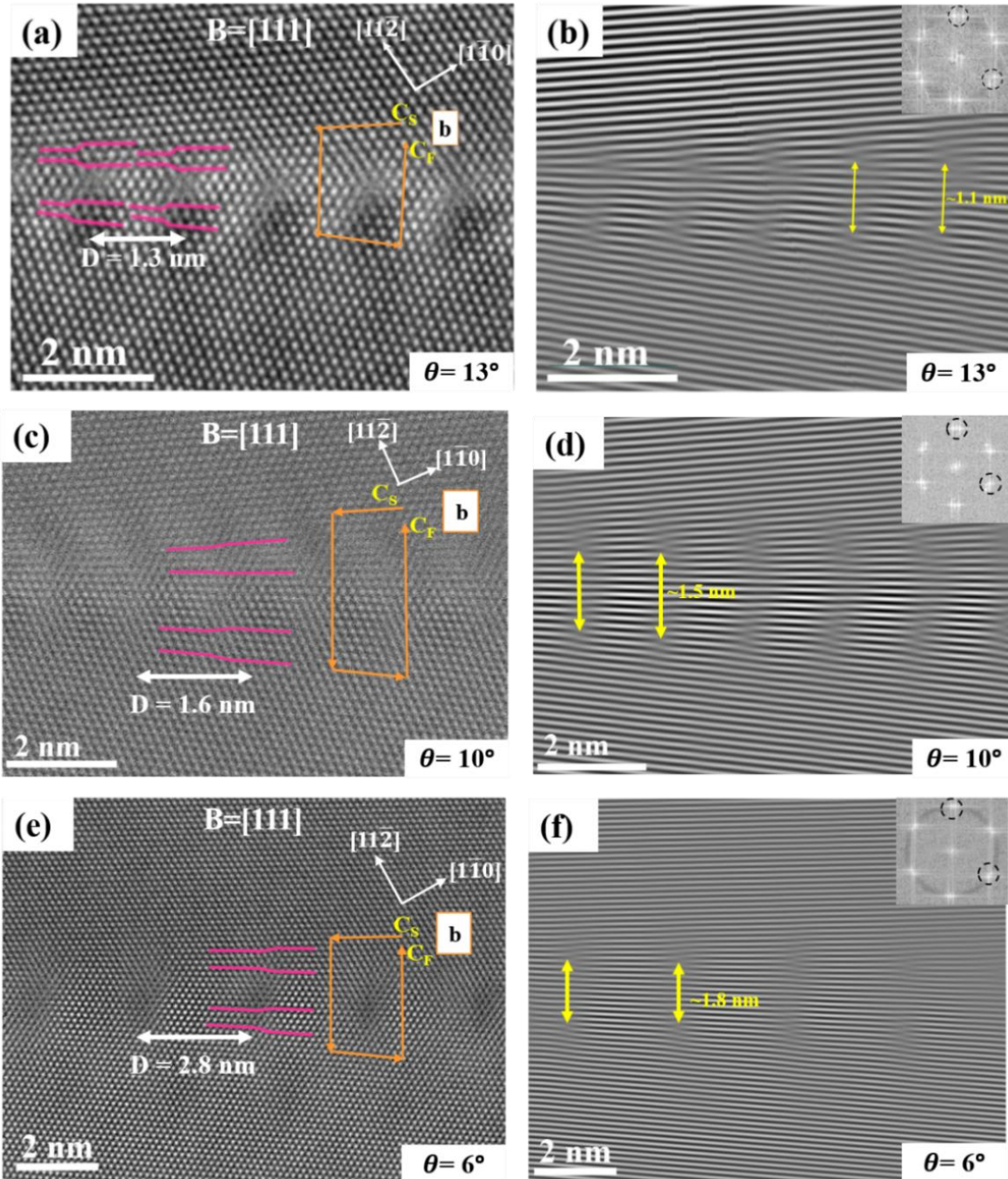
Figure 5-6: STEM investigation of three different LAGBs from S4 film. a), c) and **e)** show STEM-HAADF image of LAGBs with the misorientation angles (θ) of 13°, 10°and 6°, respectively. All the three LAGBs depict an array of dislocation at the GB with a total Burgers vector of $1/2[\bar{1}01]$, marked by orange colored Burger circuit map. Where, C_s and C_F represent the start and finish of the Burgers circuit mapping. **b), d) and f)** indicate Fourier-filtered image of **a), c)** and **e)** using the (200) lattice reflections of both grains, respectively as indicated by dashed black circles in the fast Fourier transform (FFT). The yellow colored arrows in **b), d)** and **f)** indicate the distances between the two partials. The pink lines in **a), c)** and **e)** represent two partials perpendicular to the GB plane.

We found that the dislocation spacing along the GBs decreases as expected with increasing misorientation angle. The measured D values match well with the theoretical values estimated following Frank's equation, as shown in the plot in **Figure 5-7**.
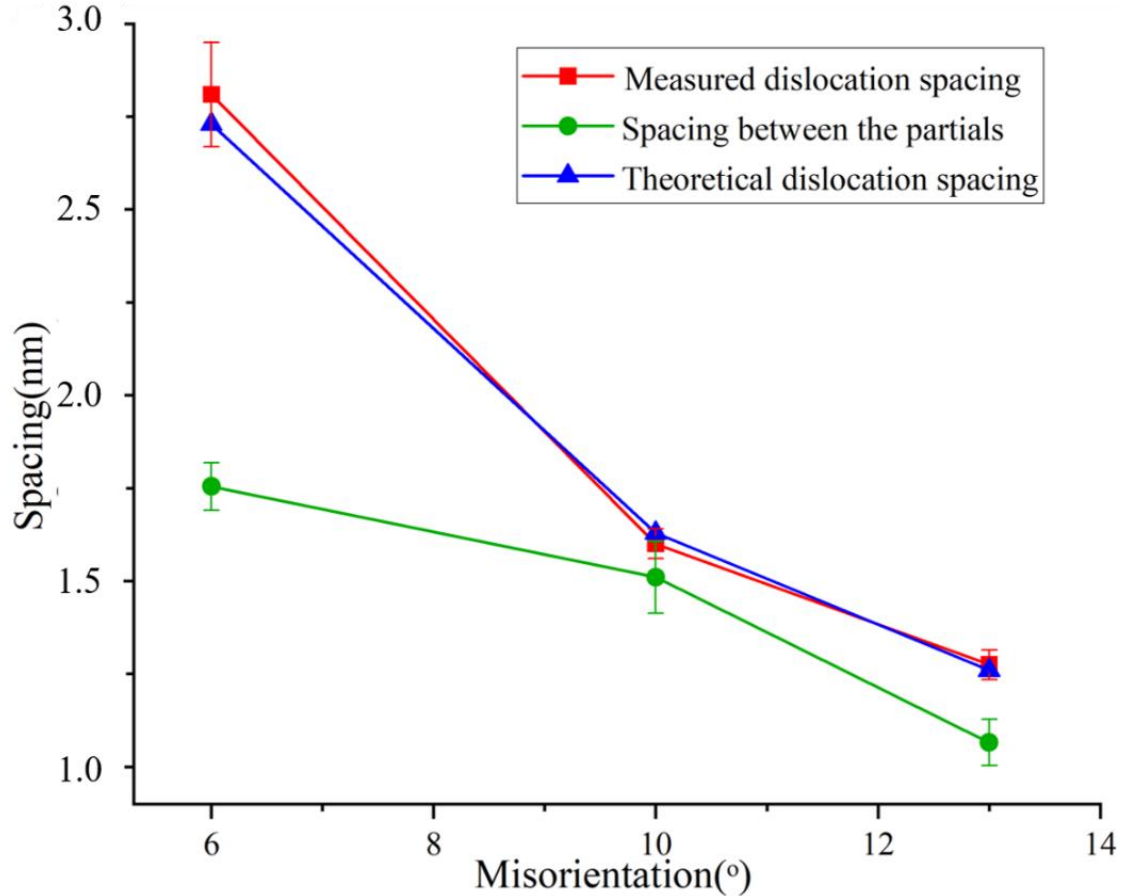
Figure 5-7: Dislocation spacing vs. misorientation angle plot for three different misorientation angle of 6°, 10°, and 13°. The measured spacing between the two partials along the GBs and perpendicular to the GBs decreases with the increase in the misorientation angle. The spacing between the partials along the GB matches well with the theoretical dislocation spacing following Frank's equation.

Already in the STEM images, it can be seen that the GB dislocations are dissociated. This becomes easily visible in the FFT constructed image visualizing the arrangement of the partial dislocations, as shown in **Figure 5-6 b)**. The (220) lattice reflections in the FFT are used to construct the IFFT image in **Figure 5-6 b)**, in order to quantify the dislocation dissociation spacing. A closer inspection reveals that each $1/2<\bar{1}01>$ dislocation is dissociated into two partials, described as follows:

$$\frac{1}{2}[\bar{1}01] = \frac{1}{6}[\bar{1}\bar{1}2] + \frac{1}{6}[\bar{2}11] \qquad\qquad 5.4$$

Note that 1/6<112> corresponds to the projected Burgers vector in the plane. The average measured distance between the two partials (perpendicular to the GB) is approximately 1.1 ± 0.06 nm, 1.5 ± 0.10 nm and 1.8 ± 0.06 nm, respectively. These spacing values follow a similar trend of decreasing with an increase in the misorientation angle (see **Figure 5-7**). A similar type of dislocation dissociation was also observed for a Cu GB, as reported in Ref [60,203]. This dissociation corresponds to the lower energy configuration at the GB in comparison to the full dislocation.

5.1.3 Discussion

The aim of the current study is to grow smooth and epitaxial Al films with an average grain size of > 10 µm, a wide distribution of [111] tilt GBs and columnar grains by varying the substrate temperature (T_s) during deposition. One of the crucial challenges in the growth of Al films with smooth dense surface, large grain size, optimum thickness and columnar GBs is controlling both the crystalline texture and surface structures of the material to be deposited. Such characteristics are highly influenced by the deposition temperature. High deposition temperatures govern 3D island growth and epitaxy of the film with respect to the substrate, while lower temperatures lead to roughness on the surface of the film and randomly oriented grains in the film [204]. We found that the growth behavior of Al thin films deposited at different temperatures here, can be categorized into different regimes, following the structure zone model (SZM) [190,205,206] as represented in **Figure 5-8**. The SZM provides a fundamental basis to interpret the microstructure evolution of metallic thin films as a function of deposition temperatures [205]. The presence of a high density of pores with indistinctive grains and non-columnar GBs in the Al film S1 occur as the deposition temperature lies in the very low temperature regime ($0 < T_s / T_m < 0.3$, up to 35℃), where adatom mobility is very low and surface diffusion is strongly constrained. However, at higher deposition temperatures ($0.3 < T_s / T_m < 0.5$, up to 200℃) i.e. for the film S2, the surface diffusion becomes substantial; however GB migration is quite constrained. As a result, the film S2 develops an inhomogeneous structure with V-shaped grains formed by the competitive growth [207,208] of nearby crystals with various orientations. On further increasing the deposition temperature to 300℃ (in the temperature interval $T_s / T_m > 0.6$) for the film S3 and S4, not only surface and GB diffusion, but also the bulk diffusion become active, which results in the lateral growth of the grains near the film-substrate interface. Furthermore, GB migration plays a vital role

in deciding the structure of the films, which is controlled by the minimization of the surface energy and the interfacial energy. This results in a homogeneous structure along the film thickness, consisting of columnar GBs from the substrate up to the surface of the Al film. The variation in grain size and the fraction of CSL GBs in S3 and S4 arises due to the post annealing of the S4 film that leads to higher grain growth in S4 and thus resulting in lower amount of CSL boundaries. Regardless, on closely inspecting the microstructure evolution, it is evident that growth of the Al thin films is following the structure zone model. Furthermore, we found that T_s / T_m for Al must be in the range of T_s / $T_m \approx 0.6$ (i.e. > 290°C) in order to get the film with flat smooth surface and a wide distribution of various [111] tilt columnar GBs.
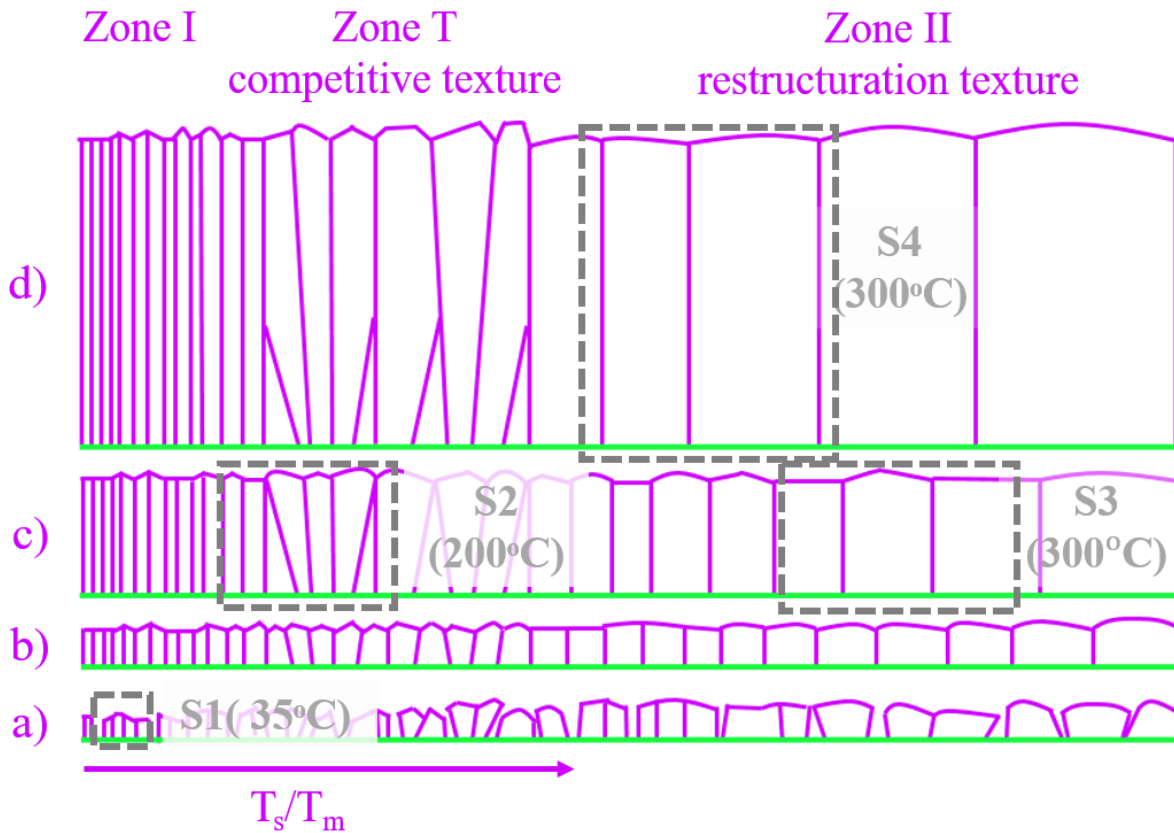
Figure 5-8: Experimentally observed structures of the deposited Al films superimposed on basic structure zone models at various film thicknesses redrawn in modified form from Ref [205]. **a)** to **d)** represent the increase in the thickness of the Al film. The thicknesses of the Al film S1, S2, S3 and S4 are 145 nm, from 400 up to 465 nm, 408 nm and 665 nm, respectively.

Furthermore, STEM-HAADF studies on the atomic structure of LAGBs (from S4 film) having a misorientation angle of typically 6°, 10° and 13°, respectively, demonstrate that the dislocations having a total Burgers vector of $1/2<\bar{1}01>$ are dissociated at the GB. Each full edge dislocation is

dissociated into periodic array of two partials dislocations with projected Burgers vectors i.e. 1/6 [$\bar{1}\bar{1}2$] and 1/6 [$\bar{2}11$]. Note that any Burgers vector component along the <111> beam direction remains unresolved. SFE plays a major role in determining whether emergent partials can exist as part of some GB structures or not. However, from the theoretical studies in the literature, it is found that there has been mixed reviews about the effect of SFE on the dissociation of the GB dislocation.

Rittner et al. [209] explored the structures of < 110 > tilt GBs by atomistic simulation for three metals (Au, Ni and Al) having different SFEs and reported such dissociation of GBs into stacking faults occurred only in Au and Ni but not in Al. This is due to the high SFE in Al that makes the dissociation of a full dislocation into two partials energetically unfavorable. Other studies also reported such dislocation dissociations at the GB is favorable only in low SFE materials like Cu, Au, etc. [74,210]. Recently, Zhang et al. [203] and Bishara et al. [60] also experimentally depicted [111] tilt GBs but in Cu with the help of high-resolution STEM studies and found dissociation of the LAGB dislocations into partials. Conversely, simulation studies [38,211–213] revealed that such GB dissociation is also possible in high SFE material like Al. Richard et al. [212] and Lu et al. [213] proposed that such dissociations in Al should also be possible, driven by vacancies in the vicinity of the dislocations and their corresponding energy.

Here, we found that the measured separation distances between the partials for 13°, 10° and 6° are typically 1.1 nm, 1.5 nm and 1.8 nm, a smaller distance than the equilibrium spacing between partials for Al, which typically amounts to 3-4 nm (inside the Al crystal) [214].

Furthermore, this distance decreases with in an increase in the misorientation angle in our observations. However, the observed partials' spacing cannot be compared to the classical SFE model [215] because of the following reasons: partials usually form in the grain interior and are separated by a stacking fault along a specific atomic plane (this is the origin of the correlation between SFE and partials). Nevertheless, in the case that we report here, partials are not separated by a well-defined atomic plane due to the presence of the GB and the crystal tilt. Therefore, the GB energy plays a vital role in setting the configuration of the partials along the boundary. This additional interfacial energy and possible GB stresses and strains couple with the partials' energy and make the classical approach to set the distance between partials with a SFE, incomplete. Nevertheless, the measured configuration with the two partials should have a minimum energy when accumulated at the GB.

5.1.4 Summary and Conclusion

In this study, the microstructural evolution and misorientation distribution of [111] tilt GBs in Al thin films was systematically analyzed by using electron microscopy techniques as a function of substrate temperature. The epitaxial Al thin films were grown by e-beam evaporation technique on (0001) α-Al$_2$O$_3$ substrates achieving a {111} texture with preferred in-plane orientation relationships to the substrate. The deposition at room temperature (35°C) revealed a highly porous film with not perfectly columnar GBs. It is found that on increasing the substrate temperature to 200°C, the film becomes dense. However, the 200°C film has often inclined GBs, revealing the columnar grains, which indicates that grain growth has not yet saturated. Therefore, it is imperative to further increase the deposition temperature to 300°C in order to obtain large grain size and perfectly columnar GBs, suitable for STEM analysis in <111> zone axis from plan-view samples. Furthermore, the grain boundary structure of different LAGBs revealed the dissociation of ½ <110> perfect edge dislocations into two partials at the GB, despite the high SFE of Al. The spacing of the dislocation in the LAGB follows Frank's rule. However, the spacing of the partials is much larger as expected for Al and seems to depend on the misorientation angle.

5.2 Microstates and defects of incoherent Σ3 [111] twin boundaries in aluminium

In this chapter, the atomic structures of Σ3 [111] GBs from two different ORs are investigated experimentally. In addition, their excess properties are presented, which explain the emergence of two different atomic structures in the two ORs.

Furthermore, the interfacial defects at Σ3 [111] are investigated in detail. The work presented here is based on the manuscript II, which is already published[‡‡].

5.2.1 Introduction

In the last few decades, it has been recognized that a single GB may exist in several different stable and metastable states, which differ in their atomic structure. However, experimental insights at the atomic structure level are rarely reported. In this study, efforts have been made to establish a direct correlation between the atomic structure of different structural states of Σ3 [111] tilt GBs and their effect on excess properties by using aberration corrected STEM techniques in combination with molecular statics and density functional theory simulations.

Two Σ3 [111] {112} GBs from two different ORs in an Al thin film grown on sapphire ((0001) oriented) were examined experimentally, and the differences in their structural motifs are discussed. Please note that the Al film that is employed to extract the Σ3 GBs (from PFIB) is different from the Al films in **Chapter 5.1**.

In addition, the atomic structure of the two ORs along the <110> zone axis are also investigated and compared. Furthermore, molecular statics simulations are utilised to investigate the different structural motifs that have emerged at the GB along the <111> and <110> directions as well as the variations in the excess properties of the Σ3 GBs.

Moreover, the asymmetric variants of the same GBs, as well as the type and number of interfacial defects (such as dislocations, steps or disconnections) present in them, are thoroughly investigated. Furthermore, their implications on GB mobility ares discussed.

[‡‡] Based on manuscript II by S. Ahmad, T. Brink, C.H. Liebscher and G. Dehm (Acta Materialia, p.118499 (November 2022))

5.2.2 Results

Microstructural characterization of thin films

Figure 5-9 shows a schematic of the geometry of the Al thin film on the sapphire substrate including the corresponding crystallographic directions. The microstructural attributes of the epitaxial Al thin film, especially texture, grain size, GB character and their distributions obtained by EBSD in the SEM are summarized in **Figure 5-10**. EBSD studies revealed a strong <111> texture in the Al film as shown by the {111} Al pole figure and IPF map (in the normal direction).
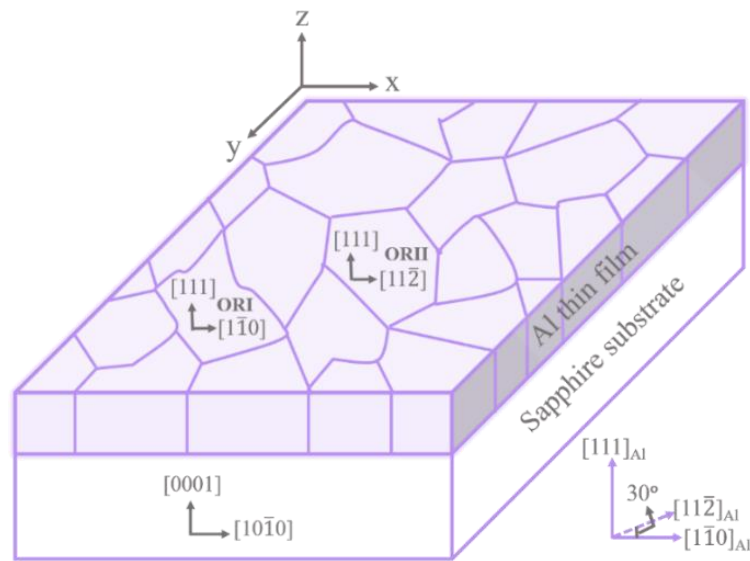
Figure 5-9: Schematic of the Al thin film grown on the sapphire substrate including corresponding crystallographic directions (for both ORI and ORII). The z-axis represents the out of the plane direction, i.e. [111], while *x*-axis and *y*-axis represent the in-plane directions. The in-plane directions for ORI and ORII are [1$\bar{1}$0] and [11$\bar{2}$], respectively, in the Al film.

The central peak of the {111} Al EBSD pole figure corresponds to (111) Al planes that are parallel to the film surface. In accordance with the literature [189,216] on vacuum deposited fcc metallic thin films, the {111} texture can be associated with the tendency towards minimum energy configuration, i.e. corresponding to the lower surface energy planes. The existence of two orientation relationships (OR I and OR II) between Al and Al_2O_3 – containing two twin-related growth variants rotated by 180° for each OR – is designated by the six other (111) peaks in pole figure. ORII corresponds to a 30° rotation of Al crystallite around the <111> direction with respect to the underlying (0001) oriented sapphire [188]. A 30° misorientation between OR I and OR II

grains is anticipated from the angle between $<10\bar{1}0>$ α-Al$_2$O$_3$ (ORI) and $<2\bar{1}\bar{1}0>$ α-Al$_2$O$_3$ (ORII). Both the ORs are described as follows:

$$\textbf{ORI a/b} \{111\} \pm <0\bar{1}1> \text{Al} \ | \ | \ (0001) <10\bar{1}0> \ \alpha\text{-Al}_2O_3 \qquad 5.5$$

$$\textbf{ORII a/b} \{111\} \pm <0\bar{1}1> \text{Al} \ | \ | \ (0001) <2\bar{1}\bar{1}0> \ \alpha\text{-Al}_2O_3 \qquad 5.6$$
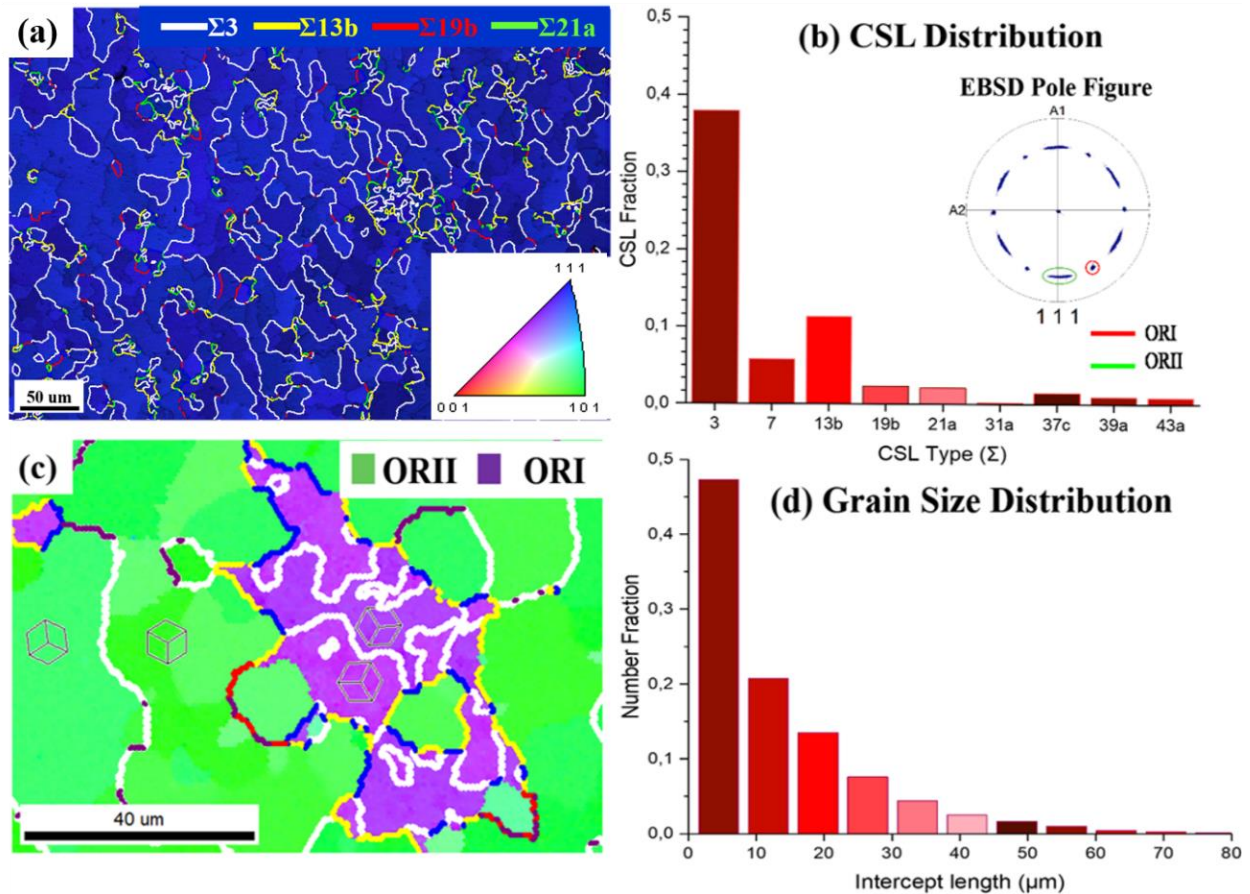
Figure 5-10: **EBSD results for the Al thin film on a sapphire substrate**. **a)** The inverse pole figure map in [111] direction. Blue color indicates {111} planes that are parallel to the surface. The colored lines indicate different [111] tilt GB types in the film. **b)** Relative occurrence of CSL boundaries. The inset shows a {111} Al pole figure of the deposited film generated from EBSD data with OR I a/b and OR II a/b marked. **c)** The inverse pole figure map in transverse direction represents the grain orientation, shown by superimposed cubes. The ORI and ORII are depicted in purple and green color, respectively. Σ3 twin boundaries are shown in white, Σ13b GBs in yellow, Σ 19b in red, Σ21a in green and further CSL boundaries of higher order in blue. **d)** Distribution of grain sizes in the film

It is important to note that in the (111) pole figure, sharp diffraction peaks are observed for both OR I twin variants. Conversely, less sharp peaks are observed for OR II with an angular deviation of ±8° (see the pole figure in **Figure 5-10 b)** and supplemental **Figure 5-26**). The corresponding CSL

boundaries and their distribution are shown in **Figure 5-10 b)**. The microstructure of the film is mainly dominated by high angle boundaries. Among 62% of all CSL boundaries, approximately 38% are $\Sigma 3$ twin boundaries followed by 11% $\Sigma 13b$, 6% $\Sigma 7$, 2% $\Sigma 19b$, 2% $\Sigma 21a$, 1.5% $\Sigma 37c$ and a very small percentage of other higher-order CSLs. The remaining percentage of the GBs in the film are low angle boundaries.

Atomic structure of $\Sigma 3$ grain boundaries with ORI and ORII

Representative atomic resolution images of symmetrical $\Sigma 3$ twin boundaries from the two different ORs are presented in **Figure 5-11**. The two adjacent grains are oriented along the [111] axis with a grain misorientation of 60° for ORI and 59° for ORII, with a GB habit plane of $(\bar{2}11)$. Due to the larger change in GB curvature locally in ORII, frequent changes in GB plane inclination lead to steps or facets in the GB. This is also demonstrated microscopically in **Figure 5-24** and **Figure 5-25** by using plane trace analysis in EBSD and in **Figure 5-16** (to be discussed in the upcoming section) by using BF-TEM imaging.
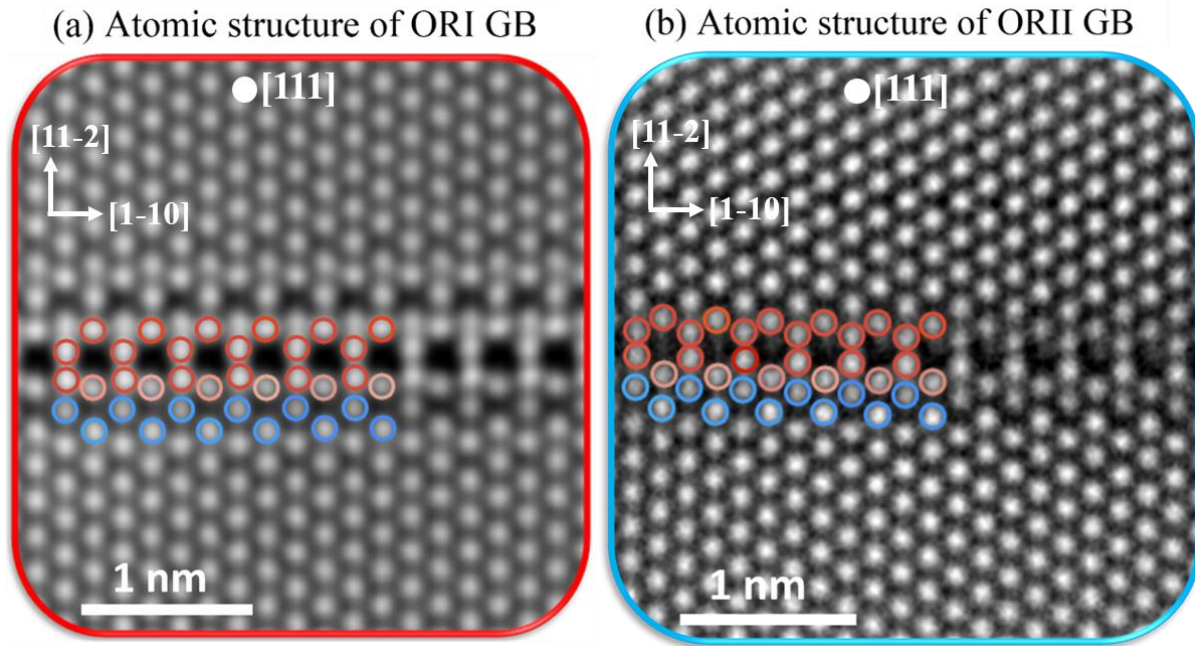
Figure 5-11: STEM-HAADF images showing the atomic-resolution details of incoherent symmetric $\Sigma 3$ grain boundaries viewed along the [111] zone axis. a) Atomic structure of symmetric $\Sigma 3$ $(\bar{2}11)$ from ORI. **b)** Atomic structure of symmetric $\Sigma 3$ $(\bar{2}11)$ from ORII. The red coloring of the atomic columns serves to highlight the structural units. The blue colored atoms highlight the motifs in the cross-sectional view of the GB (see **Figure 5-13** and **Figure 5-14**). Both the images were filtered using Wiener filter with the following parameters: Highest frequency = 80 and edge smoothing = 5%

Figure 5-11 shows straight, symmetric segments, which occur in between the steps. The structural unit (SU) model is utilized to describe the complete structure of Σ3 ($\overline{2}$11) GB. On closer inspection, it is found that despite having the similar macroscopic degrees of freedom, the characteristic structural units of Σ3 for both the ORs are slightly different from one another. The Σ3 ($\overline{2}$11) structure from ORI, is comprised of sub-units as highlighted by red circles in **Figure 5-11 a)**. In the projection, the red sub-unit possesses a distorted hexagon shape with no mirror symmetry across the GB. In accordance with the terminology of the SU model, the GB structure can be written as |E| for the Σ3 ($\overline{2}$11) from ORI, where E represents the distorted hexagon unit. The vertical lines | represent one GB period (unit cell at the GB) along the direction of the GB plane.
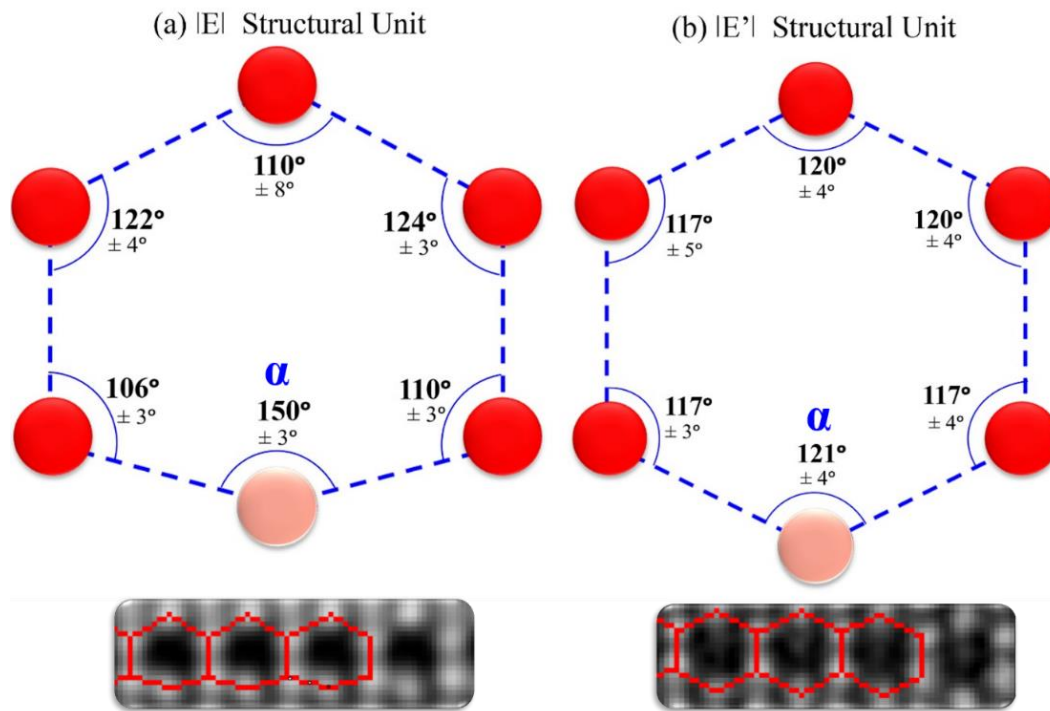
Figure 5-12: Schematic illustration of the projection of two different structural units of incoherent symmetric Σ3 grain boundaries from two ORs. a) Distorted hexagon units (|E| units) from ORI. **b)** Perfect hexagon units (|E'| units) from ORII. Images at the bottom show the experimental images of the structural units. The different values of angle α depicted in **c)** and **d)**, indicate a slight shift in the atomic position of the light red atomic column in the structural units.

In contrast, the Σ3 structure from ORII consists of red sub units that appear moderately different from the |E| units. It exhibits a perfectly hexagonal shape, which appears mirror symmetrical in the projection, and can be written as |E'|, where E' represents the perfect hexagon unit. The SUs from two different ORs are also compared quantitatively by measuring geometrical features

(atomic distances and angles subtended by the sides of the hexagon) of the units. The methodological error in measuring these angles and the atomic distances between the atoms is far smaller than the difference in the actual values from the two structures.

It is evident from the measurements that the angle *α* (as defined in **Figure 5-12**) in the distorted hexagon (|E| units) is around 29° larger than in the perfect hexagon (|E'| units). A large change in the *α* angle also results in slight shifts in the atomic positions of the surrounding atoms at the GB as can be seen in the supplemental *Figure 5-23*.

Cross-sectional view of the Σ3 GBs

A conventional BF-TEM image of the cross sectional view of the Σ3 GB from OR I in **Figure 5-13 a)** illustrates that the boundary is straight from the substrate to the surface of the film and does not contain any facets. The Al film thickness is determined to be 805 nm, approximately.
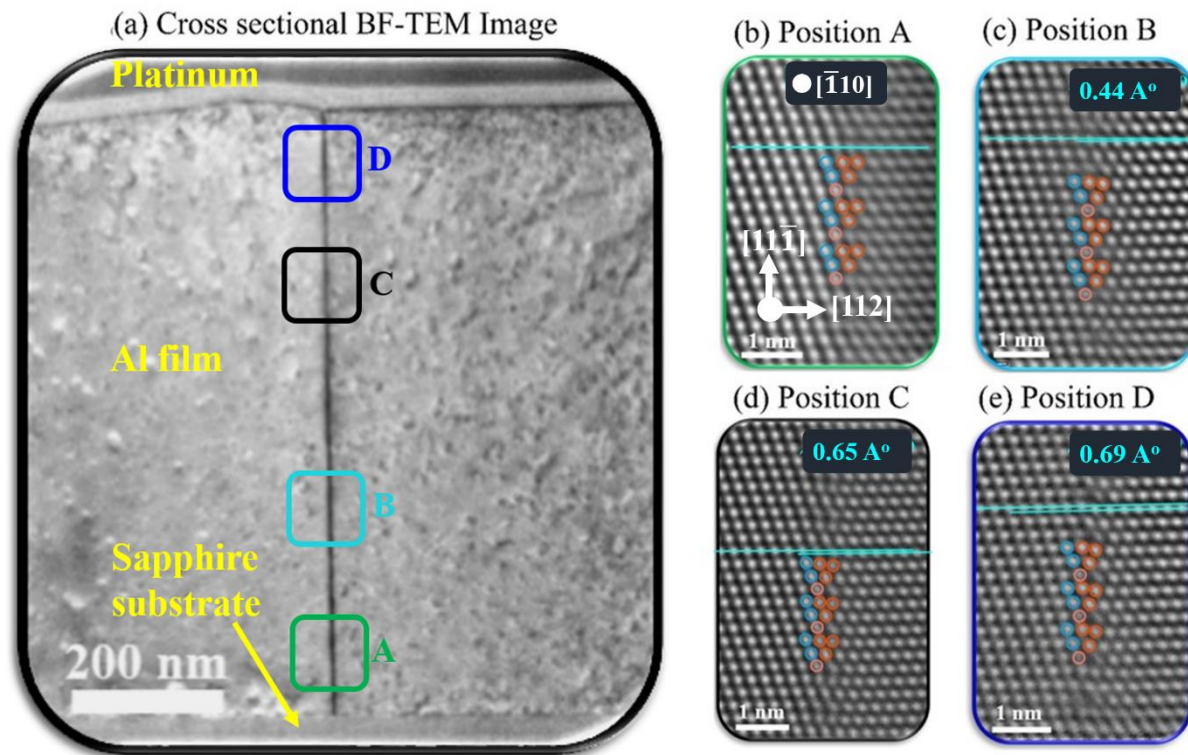
Figure 5-13: Cross-sectional view of the Σ3 ($\bar{2}$11) GB from ORI along <110> zone axis. a) Conventional BF-TEM image of the cross-section of Σ3 GB from ORI. STEM-HAADF images in **b)-e)** represent the atomic structure of the boundary marked by green, light blue, black and dark blue rectangles in **a)**. Translation of {111} planes across the GB is increasing gradually from the bottom near the substrate to the surface of the Al film

70

STEM-HAADF images in **Figure 5-13 b)-e)** represent the atomic structure of the boundary from the regions marked by the green, light blue, black and dark blue rectangles in **Figure 5-13 a)**. An interesting feature is the shift between the {111} planes at the GB: There is no such translation present at position A, which is very close to the sapphire substrate. As we move farther away from the substrate, it increases gradually up to approximately 0.69 Å near the surface of the Al film.
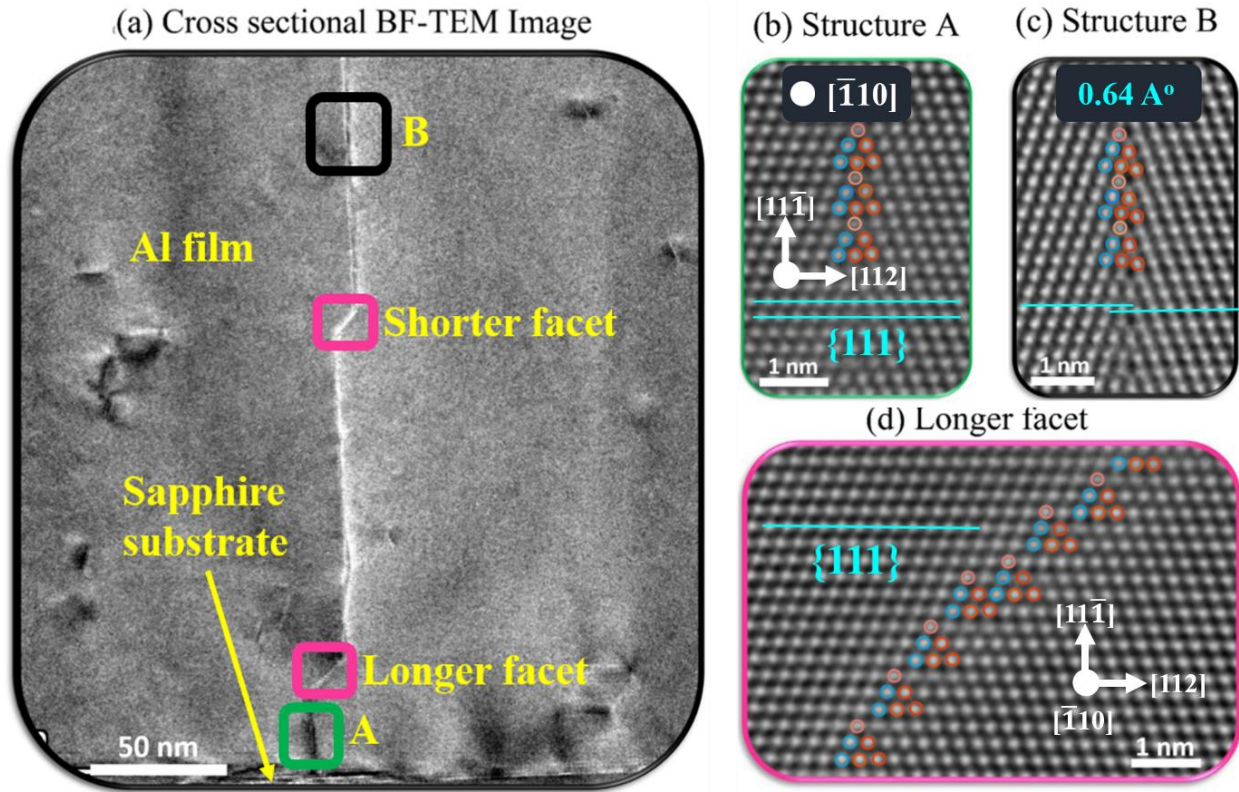
Figure 5-14: Cross-sectional view of the Σ3 ($\bar{2}$11) GB from ORII along <011> zone axis. a) Conventional BF-TEM Image of the cross-sectional of Σ3 GB from ORII. STEM-HAADF images in **b)** and **c)** represent the atomic structure of the boundary marked by the green and black rectangle in **a)**. **d)** Magnified view of the pink rectangle highlights the atomic structure of the asymmetric twin facet (122)/(100) with no rigid body translation of {111} planes but includes other structural units. For Σ3 ($\bar{2}$11), different microscopic rigid body translations are found along the boundary as shown in **b)** and **c)**.

A conventional BF-TEM image of the cross-section specimen of the Al film containing a Σ3 GB with ORII is shown in **Figure 5-14 a)**. The boundary appears to be mostly straight but with the incorporation of two asymmetric facets with GB plane {122} / {100} inclined towards the right grain, marked by a pink rectangle in the image. These facets are named asymmetric facet 1 and asymmetric facet 2. It seems that the boundary moves to the right during annealing at elevated

temperatures. The atomic structures at position A and B consist of the same triangular units along the GB as observed in ORI. Furthermore, the facets also consist of triangular units from the {211} symmetric twin with the incorporation of some additional units (**Figure 5-14 d)**), having either one or two atomic planes to accommodate the deviation in GB plane from the symmetric inclination.

Atomistic simulation

At this point, it is still unclear if the |E'| unit is simply an elastically distorted version of the |E| unit, or a more clearly delineated microstate. We could find the |E| motif at 0 K and without externally applied stress or strain using the γ-surface method as described in the section describing experimental details. The |E'| variant could not be found.
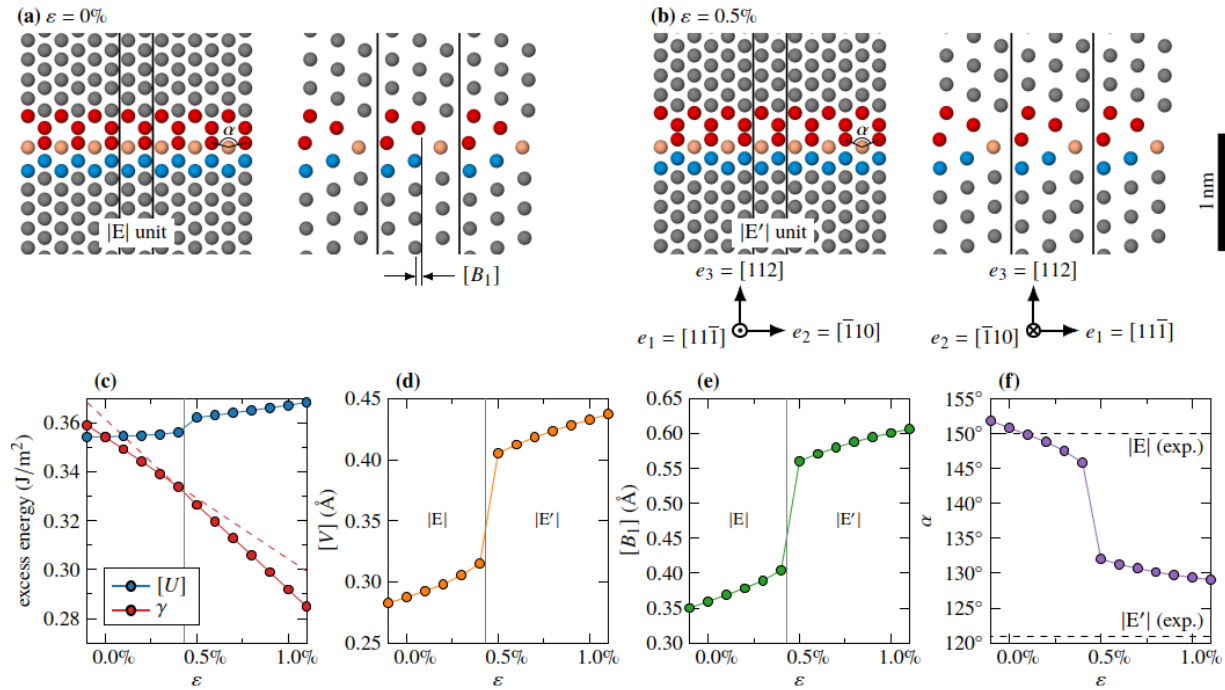
Figure 5-15: Simulation of the two different motifs |E| and |E'| observed in the experiment. **a)** In the stress and strain-free state, the |E| unit can be found. **b)** The |E'| unit appears when applying a strain of 0.5%. The coloring in the images highlights the structural units. The atom indicated in light red color shifts its position when transforming from |E| to |E'| units, leading to a change in the angle α when viewed in the projection from the $[11\bar{1}]$ direction. **c)–f)** The GB excess energy [U], excess free energy γ, excess volume [V], excess shear $[B_1]$ along the tilt axis are shown together with the angle α. A clear jump in these properties marks the transformation between the two motifs at ε ≈ 0.5%. In **c)**, the dashed lines are extrapolations of the excess free energy.

In the experiment, the film is grown on a sapphire substrate, which can lead to residual strains (the possible sources of these strains are discussed later). Here, we assume that this corresponds to an

isotropic strain in the *yz* plane ($\varepsilon = \varepsilon_{22} = \varepsilon_{33}$), i.e., the plane that is parallel to the substrate in the experiment, and open boundaries in the direction normal to the substrate (plane stress condition with $\sigma_{11} = 0$). Unfortunately, the plane stress condition leads to significant size effects, yielding different results for different ratios of GB volume vs. bulk volume [86].

We therefore utilized plane strain conditions ($\varepsilon_{11} = 0$) and verified that the results are unaffected by varying ε_{11} (Supplemental **Figure 5-27**). Due to the boundary conditions, we can furthermore only apply a stress normal to the GB (σ_{33}) and a strain (ε_{22}) in *y* direction without introducing size effects in a bicrystal setup [86]. In order to be able to apply a plane strain, we therefore computed the stress–strain relation of a similarly sized and oriented defect-free fcc slab and used this to estimate the stress needed to obtain a given ε_{33}. At a strain of around 0.5%, we observe a transition from the |E| to the |E'| structure (**Figure 5-15 b**)). Additionally, at each applied strain value, we could only observe one of these two structures, while the other one was always unstable and transformed immediately. That means that neither structure can exist in a metastable state.

To gain deeper insights, we also tracked several excess properties as a function of ε: The excess energy [*U*], the excess volume [*V*], and the excess shear [*B*$_1$]. At $\varepsilon = 0$, the latter corresponds to the shift between the {111} planes in tilt axis direction across the GB (as indicated in **Figure 5-15 a**)). Positive and negative values of [*B*$_1$] are equivalent in the case of Σ3 <111> {112} tilt GBs in fcc: These lead to equivalent, if differently oriented, GB structures due to the bicrystal symmetry. The values of [*B*$_1$] are of the same order of magnitude as in the experiment (**Figure 5-13** and **Figure 5-14**), but due to the small magnitude of the shift and the unknown stress state as well as measurement uncertainty in the experiment, a quantitative comparison is not possible.

We also calculated the GB free energy, which is $\gamma = [U] - \sigma_{33}[V]$ in this case [85,86], and the angle α as defined in **Figure 5-12**. All values are shown in **Figure 5-15 c)–f)**. We can see that there is a jump in the excess values and a discontinuity in the excess free energy at $\varepsilon \approx 0.5\%$. This indicates that |E| and |E'| are indeed distinct microstates. The reason for the transformation between the two states is that the atomic arrangement in |E'| leads to a larger excess volume, which becomes favorable under tension.

Asymmetric variants of Σ3 grain boundaries of ORI and ORII

The BF-TEM image in **Figure 5-16** shows the asymmetric variants of the Σ3 in two ORs. Both the

ORs incorporate facets regularly interrupted by steps with varying heights in order to accommodate the overall deviation in grain boundary plane deflection from the symmetric orientation. We found that the GB from ORII has a greater number of facets and steps in comparison to ORI, also demonstrated in **Figure 5-24** and **Figure 5-25**.
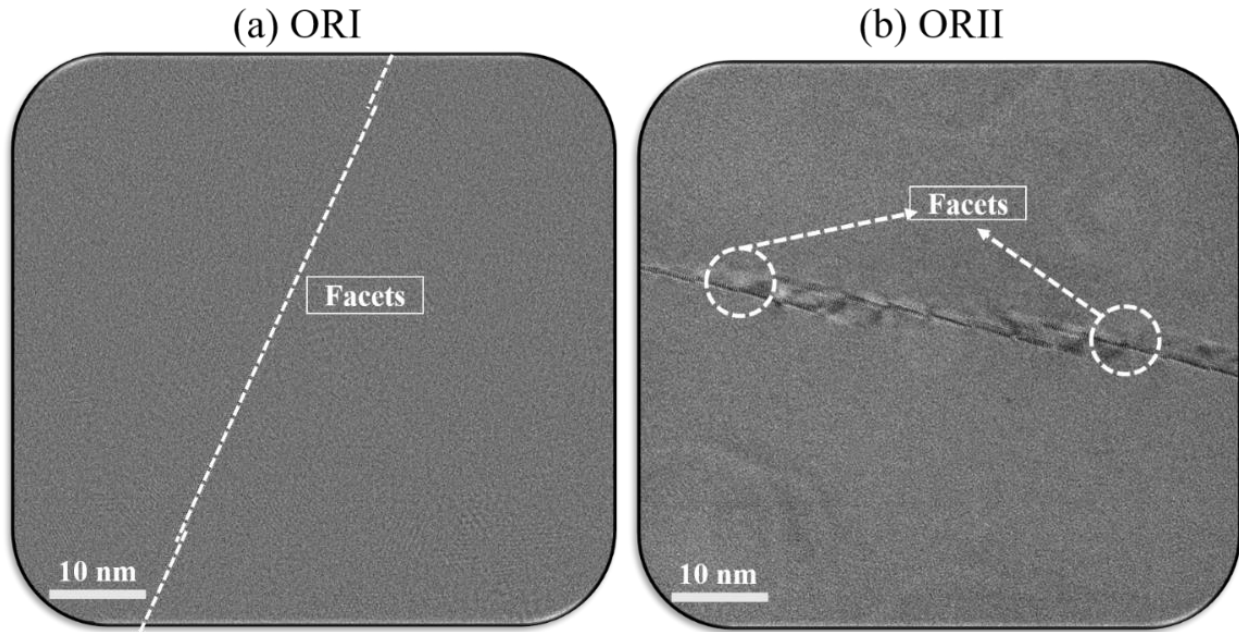
Figure 5-16: BF-TEM images of asymmetric variants of Σ3 ($\overline{2}$11) GB from a) ORI and **b)** ORII, showing facets of varying length separated by steps. Small circle marked in b) shows the smaller facets incorporated by small steps within longer facets.

The atomic structures of asymmetric variants of Σ3 are depicted in **Figure 5-17** and **Figure 5-18**. In the case of ORI, the GB consists of long facets of 40 nm up to 60 nm in length separated by small steps with a step height of 0.3 nm, but no facet with larger step heights are found. Unlike ORII, the absence of larger steps in ORI is due to a small deviation (because of the change in GB curvature locally) of approximately 1.2° in GB plane inclination from the exact habit plane in comparison to a large deviation of 5.5° deviation for ORII. We experimentally observed that the symmetric facets are disrupted by isolated defects in order to compensate for the deviation in GB inclination. Thus, it is unlikely that they are responsible for the differently reconstructed GB structural unit, especially considering that the deviation angles are quite small. In the case of Σ3 ($\overline{2}$11) GB from ORII, it consists of long facets of around 20 nm in length separated by steps with heights from 5 nm down to 1 nm. The longer facets are comprised of smaller facets of around 4 nm in length interrupted by steps with varying small step heights.

74

The magnified view in the light blue and blue boxes in **Figure 5-17 c)** and **d)** indicates a GB step and shows that the core structure of the step is quite ordered. Also, no incorporation of additional subunits has been observed in any of the cases.
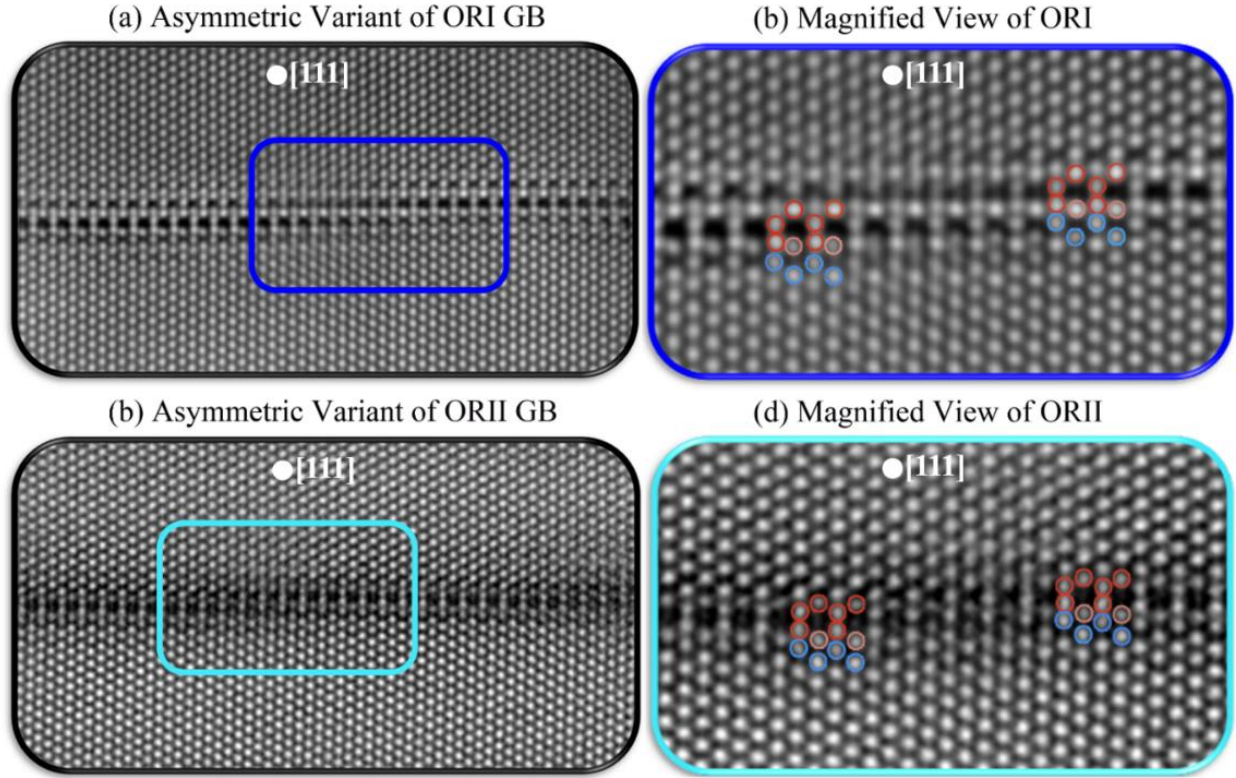
Figure 5-17: STEM-HAADF images showing asymmetric variants of the GBs in plan-view along [111] zone axis orientation. a) Atomic structure of asymmetric variant of Σ3 ($\overline{2}$11) from ORI. **b)** Atomic structure of asymmetric variant of Σ3 ($\overline{2}$11) from ORII. The images depicted in **c)** and **d)**, as marked by blue and light blue boxes, show a close-up view of the GB step highlighted in **a)** and **b).**

Dislocation characterization of GB steps

To analyze whether the steps present at the interface are associated with any secondary grain boundary dislocations or not, the Burgers circuit mapping method is adopted from Medlin et al. [217]. The Burgers vector **b**, of the interfacial steps can be determined as

$$\mathbf{b} = -(\mathbf{C}_\gamma + R\mathbf{C}_\beta). \qquad\qquad 5.7$$

Here, $\mathbf{C}_\gamma$ and $\mathbf{C}_\beta$ are the path of the Burgers circuit corresponding to the lattice translation vectors in the two grains (Grain γ and β) as shown in **Figure 5-18 a)** and **b)**. *R* is a rotation matrix that

converts a crystal reference system from grain γ to β, here representing a 60° rotation around the tilt axis:

$$R_{\Sigma 3} = \frac{1}{3} \begin{bmatrix} 2 & \bar{1} & 2 \\ 2 & 2 & \bar{1} \\ \bar{1} & 2 & 2 \end{bmatrix}$$

5.8

Circuit $\mathbf{C}_\gamma$ starts from A, follows B and ends at C while $\mathbf{C}_\beta$ path starts from D, follows E and ends at F in clockwise direction as shown in **Figure 5-18**. The circuits are constructed in such a way that they converge at crystallographically equivalent sites on both sides of the facet, so that $\overline{AF} = -\overline{CD}$, cancelling out the unknown parts of the Burgers circuit.
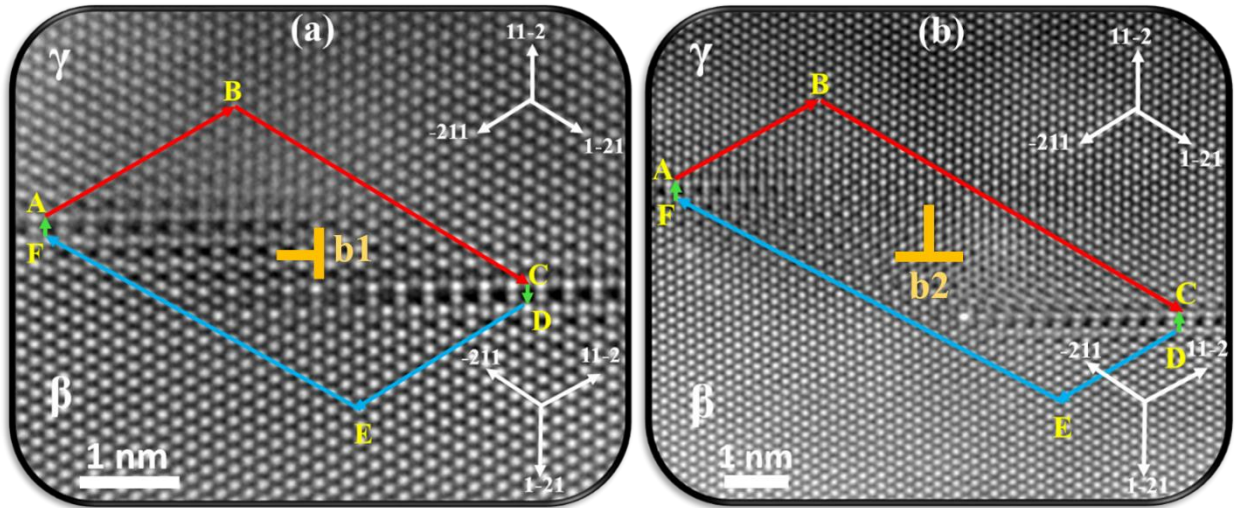
Figure 5-18: STEM-HAADF images showing two different types of steps along [111] zone axis at the Σ3 ($\bar{2}$11) GB from ORII. a) Atomic structure of GB step type A with 0.8 nm length. **b)** Atomic structure of GB step type B with 3 nm length. Burgers circuits depicted in **a)** & **b)** start from position A in a clockwise direction and end at position F. The red lines (ABC) in grain γ and blue lines (DEF) in grain β represent the upper and lower part of the Burgers circuit. As summarized in **Table 2**, the Burgers circuits in **a)** and **b)** give $\mathbf{b}_1 = 1/6[\bar{1}\bar{1}2]$ and $\mathbf{b}_2 = 1/2[\bar{1}01]$, respectively.

We found that the steps present in both the ORs are associated with Burgers vectors as listed in **Table 3** and the interfacial structure is identical on either side of the steps. Hence, it is clear that these steps shown in **Figure 5-17** and **Figure 5-18** are disconnections with varying heights (h), where both $\mathbf{b}$ and h are the translation vectors of the displacement shift complete (DSC) lattice. In the case of Σ3 from ORI, only one kind of disconnection with Burgers vector $\mathbf{b}_1 = 1/6[\bar{1}\bar{1}2]$ and a step height of $2a_{dsc}$ (0.3 nm) is observed, where a_{dsc} is the lattice parameter of the DSC lattice.

Table 3: Burgers vectors **b** determined using equation (1) for the circuit maps constructed around pairs of facet junctions in ORII as shown in Figure 10. The values of the two half-circuit C_γ and C_β are also provided, alongside the step height h.

Type of steps	C_γ:ABC (Grain γ)	C_β:DEF (Grain β)	b (Burgers vector)	h (Step height)
Type A	1/6 [46 $\overline{55}$ 8]	1/6 [$\overline{56}$ 10 46]	1/6 [$\overline{112}$]	0.8 nm
Type B	1/6 [69 $\overline{93}$ 24]	1/6 [$\overline{93}$ 27 66]	1/2 [$10\overline{1}$]	3.0 nm

In ORII, disconnections with the same Burger vector, i.e. $\mathbf{b}_1 = 1/6[\overline{112}]$, with different step heights of $2a_{dsc}$ (0.3 nm) and $5a_{dsc}$ (0.8 nm) are observed across the GB. The atomic structure of both types of disconnections look similar and quite ordered. We also found another type of disconnection with a different Burgers vector $\mathbf{b}_2 = 1/2[\overline{1}01]$ and a step height of approximately 3 nm as shown in **Figure 5-18 b)**.
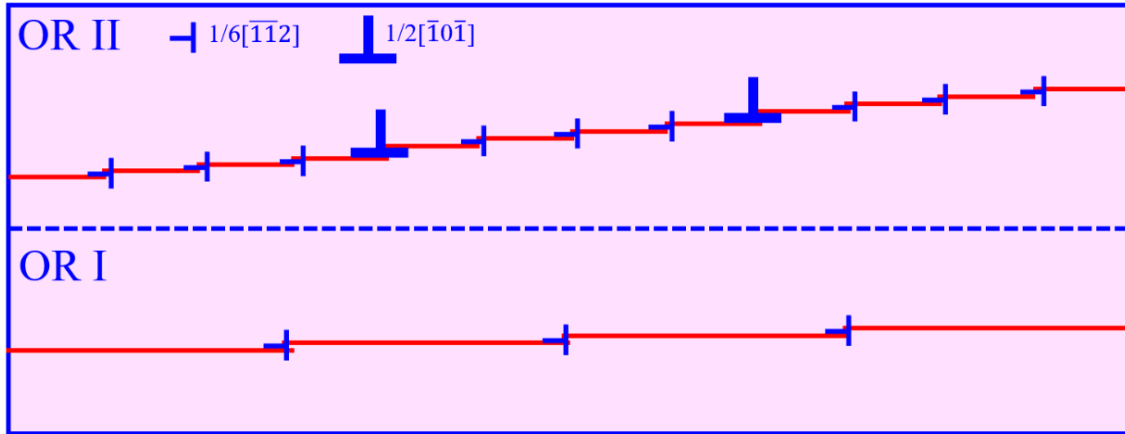
Figure 5-19: Schematic illustration of the distribution of two different types of grain boundary dislocations ($\mathbf{b}_1$ = 1/6[$\overline{112}$] and $\mathbf{b}_2$ = 1/2[$\overline{1}01$]) associated with different steps observed along the incoherent Σ3 ($\overline{2}11$) GBs from ORI and ORII.

The distribution of two distinct types of GB dislocations associated with different steps, recognized in the [111] Σ3 from both ORs is illustrated in **Figure 5-19**. It is important to take into account that in addition to the deviation in GB plane inclination, deviation in the misorientation is also

responsible for accommodating the disconnection kind of defects at the GB. In the case of ORI (for a longer segment including the disconnection with a Burgers vector $\mathbf{b}_1 = 1/6[\overline{11}2]$), we have approximately 1° of deviation from the ideal 60° misorientation. This average value of 1° deviation is estimated by using the lines along the planes on both the grains forming the GB and then measuring the angles between the drawn lines. However, when we zoom in locally, we have ideal 60° misorientation for the perfect Σ3 symmetric segment without any disconnection (see **Figure 5-11**). This clearly indicates that the deviation in the misorientation of the GB is compensated by the introduction of defects like disconnections. Likewise, in ORII (for a longer facets with disconnections corresponding to a Burgers vector of $\mathbf{b}_1 = 1/6[\overline{11}2]$), we have a deviation of ~2.3° in the misorientation for the longer facets, associated with an average spacing of 4.1 nm approximately. While locally, we have a deviation of 1° from the ideal misorientation for the perfect symmetric segment (see **Figure 5-11 b)**). Therefore, globally, both the deviation in GB misorientation and the GB plane inclination are responsible for incorporating the $\mathbf{b}_1 = 1/6[\overline{11}2]$) and/or $\mathbf{b}_2 = 1/2[\overline{1}01]$ disconnections at the GB. Moreover, it is very likely that the facets between the disconnections are the remainders of GB migration that occurred at high temperatures during the annealing of the film. Although, no pure steps (without any dislocation character) are found in the GBs examined, yet, there is also a possibility that pure steps may have been incorporated into the GBs instead of disconnections in order to compensate a deviation in GB plane inclination.

The aforementioned two different disconnections having the same Burgers vector $\mathbf{b}_1 = 1/6[\overline{11}2]$ and different heights can be explained with the help of a schematic illustration of disconnection formation in **Figure 5-20**. A dichromatic pattern is formed by overlaying the two [111] lattices A and B, which are rotated by 60° w.r.t to each other as demonstrated in **Figure 5-20 a)**. The pristine GB structure of Σ3 [111] (211) can be obtained by eliminating the lattice points from the respective lattices on each side of the GB plane (see **Figure 5-20 b)**). The CSL and DSC lattices emerging from the dichromatic pattern for the Σ3 [111] boundary are displayed in **Figure 5-20 c)**). Furthermore, translation of the lattice B relative to lattice A by a DSC vector relocates the CSL origin and the boundary plane to a new site (**Figure 5-20 d) –f)**). This results in the incorporation of a disconnection at the GB with a Burgers vector of $\mathbf{b} = 1/6[\overline{11}2]$ and a step height *h*. As equivalent locations of the GB plane in the shaded region exist, multiple disconnections with the same Burgers vector but different step height are possible, each with a different energy [66]. The two disconnections

observed experimentally are shown schematically in **Figure 5-20 e)-f))**. Both disconnections have the same Burgers vector but different step heights $2a_{dsc}$ and $5a_{dsc}$.

(a) Dichromatic Pattern

(b) Pristine GB

(c) CSL and DSC Lattice

(d) Shifting the lattice A by a DSC vector

(e) Disconnection Type A

(f) Disconnection Type B
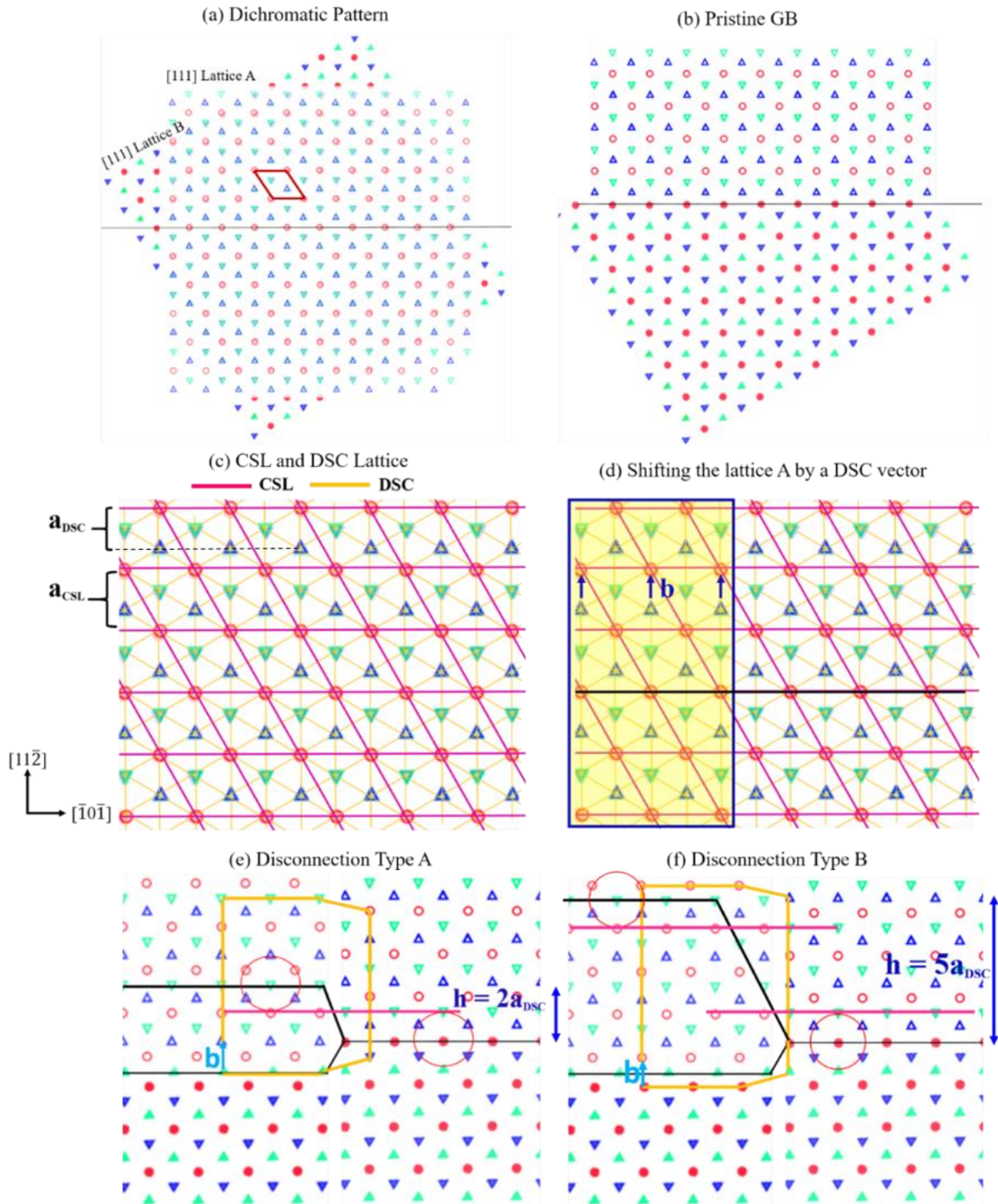
Figure 5-20: Schematic illustration of the disconnection defects in an incoherent Σ3 [111] symmetric tilt GB. a) Dichromatic pattern obtained by overlaying two lattices oriented along [111] direction: lattice A and lattice B (rotated by 60° relative to lattice A) containing filled and unfilled lattice points, respectively. The green, blue and red layers in both lattices indicate the typical (111) ABCABCABC… fcc stacking sequence. A new super lattice structure emerges due to concurrent lattice points (light red lattice points), called coincidence sites lattice (CSL). **b)** The pristine GB structure of Σ3 [111] with a GB plane of (211) is indicated by the black line. The pink and yellow lines in **c)** represent CSL and DSC lattice vectors, respectively. **d)** A shift of the lattice B relative to the lattice A by a DSC vector **b**= $1/6[\overline{11}2]$ indicated by blue arrows in the yellow region, relocates the origin of the CSL lattice and the boundary plane (black line). This leads to the formation of a disconnection with a Burgers vector **b** = $1/6[\overline{11}2]$ along the GB. **e)** and **f)** show the two kinds of disconnections associated with step heights h = $2a_{dsc}$ and h = $5a_{dsc}$ for the same Burgers vector **b**. Yellow lines depict the Burgers circuit around the disconnections. Pink circles in **e)** and **f)** represent structural units corresponding to the pristine GB structure.

5.2.3 Discussion

Atomic structure and excess properties

While the symmetric Σ3 [111] ($\overline{2}$11) GBs with OR I and OR II have the same macroscopic DOFs, the GBs exhibit two different microstates with subunits |E| (distorted hexagonal units) and |E'| (perfect hexagonal units). The |E'| structural unit was already predicted using atomistic simulations by Sutton et al. [37], however, that work does not contain the experimentally observed |E| motifs. In copper, Wang et al. [36] simulated two different structures with |F| (stable) and |F'| (metastable) units. The |F| motif bears some resemblance to the experimentally observed structure in Al, although the angles and interatomic distances do not match. It is important to note that these simulations used simple pair potentials, which are not capable of fully describing the physics of metals. Later, Hetherington et al. [99] combined both the atomistic simulation and the atomic resolution TEM to investigate the atomic structure of Σ3 [111] (211) facets of the incoherent twin GBs in gold (Au). It was identified that there was no one-to-one correlation between the simulated and the experimental images due to the lower resolution limit of the microscope. On closer comparison of the atomic structure of the GBs in Au with Al, we found that both the experimental and the simulated motifs in Au does not match with any of the motifs present in Al. We therefore investigated the structures with aberration corrected STEM and performed the simulations with a more realistic EAM potential in this work. Furthermore, we also verified the results using DFT simulations. We found that the |E| structure transforms into the |E'| structure when applying a stress

or strain in the plane parallel to the substrate. The reason for this is that the GB excess volume couples to stresses applied normal to the GB plane (σ_{33}), resulting in a GB free energy of $\gamma = [U] - \sigma_{33}[V]$. The |E'| motif has a higher excess volume and thus occurs under tension. Because neither variant is mechanically (meta-)stable concurrently with the other variant, both motifs can only be observed by applying stress or strain, which explains why these microstates were not found in earlier simulations.

High-resolution STEM imaging of the cross-sectional view along the <110> zone axis reveals that there is a slight shift of the {111} planes across the GBs in both ORs. The farther the boundary gets away from the substrate, the higher is the magnitude of the shifts between the {111} planes. These rigid body translations during grain boundary relaxation usually occur in order to reduce the grain boundary energy [53,189] and were also predicted by our simulations. No such shifts are observed for the segments close to the substrate for both ORs. Various studies reported that the magnitude of these translations at the GB is very sensitive to the surroundings of the boundary (such as presence of triple junction, phase interface or defects near the GB) [96,218]. The presence of sapphire near this segment of the symmetric twin imposes a rigid frame on the GB that prevents the occurrence of any rigid body translations of {111} planes near the substrate. In addition, asymmetric twin facets are present along the [110] zone axis in ORII as compared to the perfectly planar GB observed in ORI. It is important to note that there is no dislocation character associated with these steps, unlike the disconnections observed from the [111] zone axis direction. Nevertheless, these facets indicate that the boundary might have migrated from left to right at elevated temperature during the annealing treatment.

Regarding the transition from |E| to |E'| motifs, the simulations predict that a planar strain of at least 0.5% is required. One possible origin for such a strain could be the difference in the thermal expansion coefficients [219,220] between the substrate (8.18×10^{-6} K^{-1} in the basal plane) and the film (23.1×10^{-6} K^{-1}): $\varepsilon = \Delta\alpha \times 400$ K $= 0.6\%$. However, this does not explain the difference between the ORI and ORII motifs. Another possibility could be the different lattice mismatch between Al film and the sapphire substrate for ORI and ORII. Medlin et al. [216] considered the lattice parameter of sapphire for the lattice coincidence relationships analysis method [221] to calculate the lattice mismatch between Al and sapphire substrate in ORII and estimated it to be −4.3% for ORI and +0.4% for ORII. On the other hand, Hieke et al. [202] used

the lattice plane spacing values directly to calculate the lattice mismatch and found it to be −4.3% for ORI and −20 % for ORII. These results contradict with each other and only the approach by Medlin et al. fits qualitatively to the simulations, which predict |E| units occur under compression/slight tension and |E'| units under larger tension ($\varepsilon > 0.5\%$). According to the literature [216,222], the value of the lattice misfit parameter can be estimated by using different approaches, depending on the elastic properties of the materials. However, it should be noted that all the above-mentioned approaches for the lattice strain calculations are relatively simple and imprecise. For instance, delocalized coherency, i.e. a local rearrangement of the atoms at the interface, may result in a reconstructed interface structure [223] that reduces the interface energy. The possibility of interface reconstruction makes these purely geometrical models questionable. Nevertheless, the observed atomic structures of the Σ3 [111] GBs from both simulation and experiments are in excellent agreement with each other and paved a useful insight into understanding the influence of grain boundary structure multiplicity on the properties of the delimiting Σ3 [111] tilt boundaries in Al.

Disconnections in Σ3 [111] GBs

The occurrence of different types of Σ3 [111] disconnections with Burgers vector $b_1 = 1/6[\overline{11}2]$ and $b_2 = 1/2[\overline{1}01]$ with varying heights in both ORs is attributed to the substantial deviation in the misorientation and the GB plane inclination from the symmetric orientation. To the authors' knowledge, this is the first time that the atomic-scale experimental observations of GB disconnections in incoherent Σ3 [111] tilt GBs in pure Al are being reported. Numerous studies [76,78,82] show that the GB kinetics are highly controlled by the dynamics of disconnections, such as the nucleation and the propagation of disconnections along with the GB in a polycrystalline material. The experimentally observed large number of disconnections at the Σ3 [111] GBs could indicate the nucleation and propagation of these disconnections and steps at the GB from the triple junctions during annealing. The motion and annihilation of these disconnections may have contributed differently to the GB migration at high temperatures. However, it is difficult to elaborate globally whether all these facets or disconnections already existed due to a deviation from exact CSL misorientation/habit plane or nucleated from the triple junctions at elevated temperatures. Nevertheless, the existence of only one type of disconnection in ORI may suggests

the possibility of a lower migration rate for ORI in comparison to ORII, where more than one type of disconnections are observed. However, for quantitative study of the energies of these disconnections and their effect on the mechanism of GB migration, more studies such as in-situ annealing experiments in combination with in-depth simulations are needed which is beyond the scope of the current article.

5.2.4 Summary and Conclusion

In the present work, a detailed systematic study is conducted to investigate the structure multiplicity and structural defects in incoherent $\Sigma 3$ $[11\bar{1}]$ (211) tilt GBs using aberration corrected high-resolution transmission electron microscopy technique. Furthermore, MD and DFT simulations are utilized to understand the impact of the two different microstructural states of two ORs on GB properties. We found two different microstates, $|E|$ and $|E'|$, of the GB structure. Simulations predict that these states transform into each other with applied stress or strain by coupling to the different excess volume of the microstates. $|E|$ motifs were associated with GBs with ORI and $|E'|$ motifs with ORII. This suggests that these microstates are the result of different strain states due to different local stress states present at the interfaces. Also, the atomic structure of both the GBs along <110> zone axis is investigated in detail with HAADF-STEM. Different magnitudes of translation of {111} planes are observed across the whole GB from the bottom near the substrate up to the surface of the Al film, for both ORs. The asymmetric variants of the GBs at the two ORs incorporate different types and density of facets into the structure of $\Sigma 3$ GB. In case of $\Sigma 3$ from ORI, GB consists of long facets separated by small steps with a single step height of typically 0.3 nm. However, $\Sigma 3$ from ORII comprises of a large number of facets incorporating different kind of disconnections with varying step height. The ORII GB exhibits two different types of disconnections with Burgers vector $1/6[\bar{1}\bar{1}2]$ and step height $h = 2a_{dsc}$ and $5a_{dsc}$, while for ORI, only a single disconnection type with step height $h = 2a_{dsc}$ is observed. Furthermore, in ORII, another type of disconnection with Burgers vector $1/2[\bar{1}01]$ and varying step heights were found in contrast to absence of such disconnections in ORI. This suggests the possibility of a lower migration rate in ORI in comparison to ORII, where more than one type of disconnections are observed.

5.2.5 Supplementary information to Chapter 5.2

STEM Simulation

STEM image simulations were carried out using the multi-slice algorithm within abTEM [168,169] with simulation cells (at $\varepsilon \approx 0$ % and $\varepsilon \approx 0.5$%) from **Figure 5-15** used were of the different thickness (t) ranging from t = 14 nm to 56 nm to understand the influence of thickness on the projected atomic structure. The simulated images clearly show that there is no influence of the
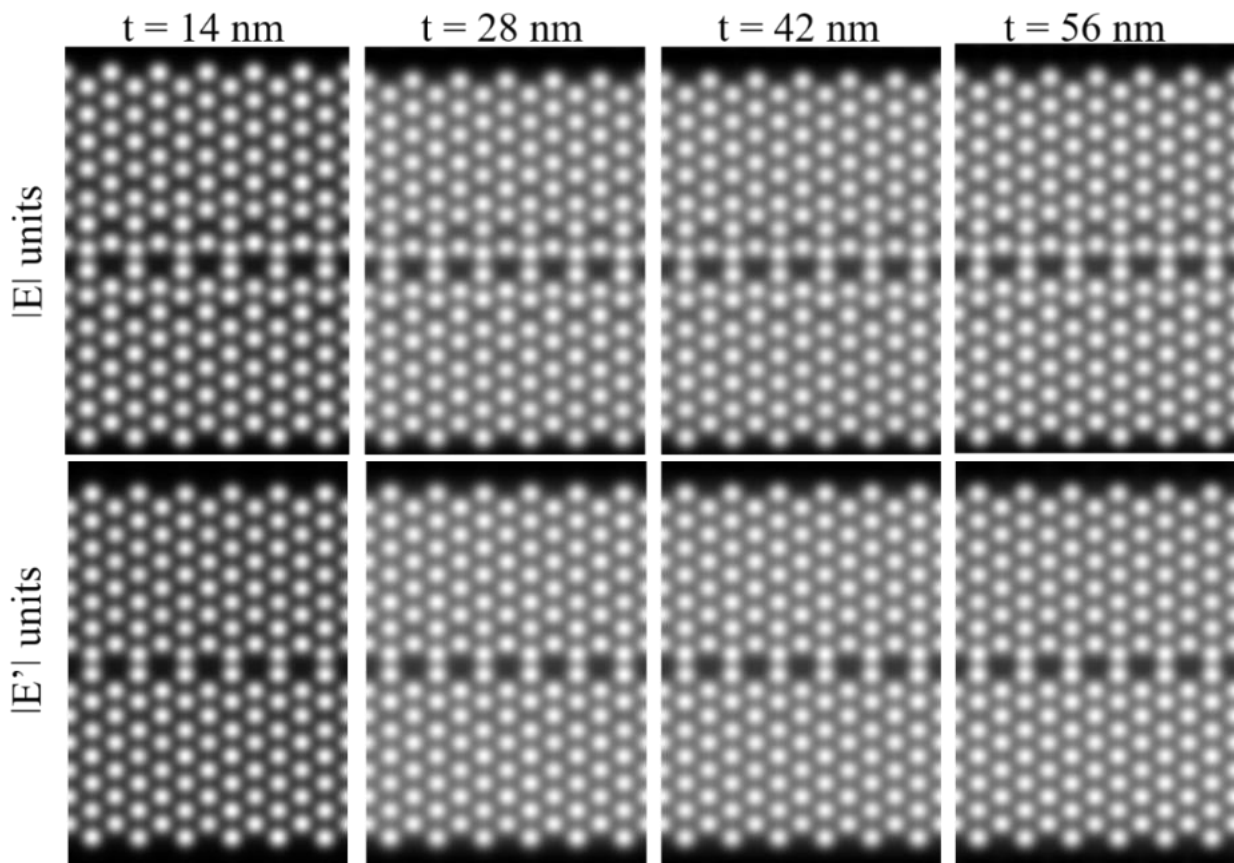
Figure 5-21: STEM simulated images of E and E' units along [111] direction at different thicknesses starting from t=14nm to 56nm under the same initialized convergent beam as in the experiments to match the settings used in the experiment.

thickness or beam convergence on the atomic positions at the GB other than the brighter atomic contrast on increasing the thickness of the simulation cell (See **Figure 5-21** and **Figure 5-22**).
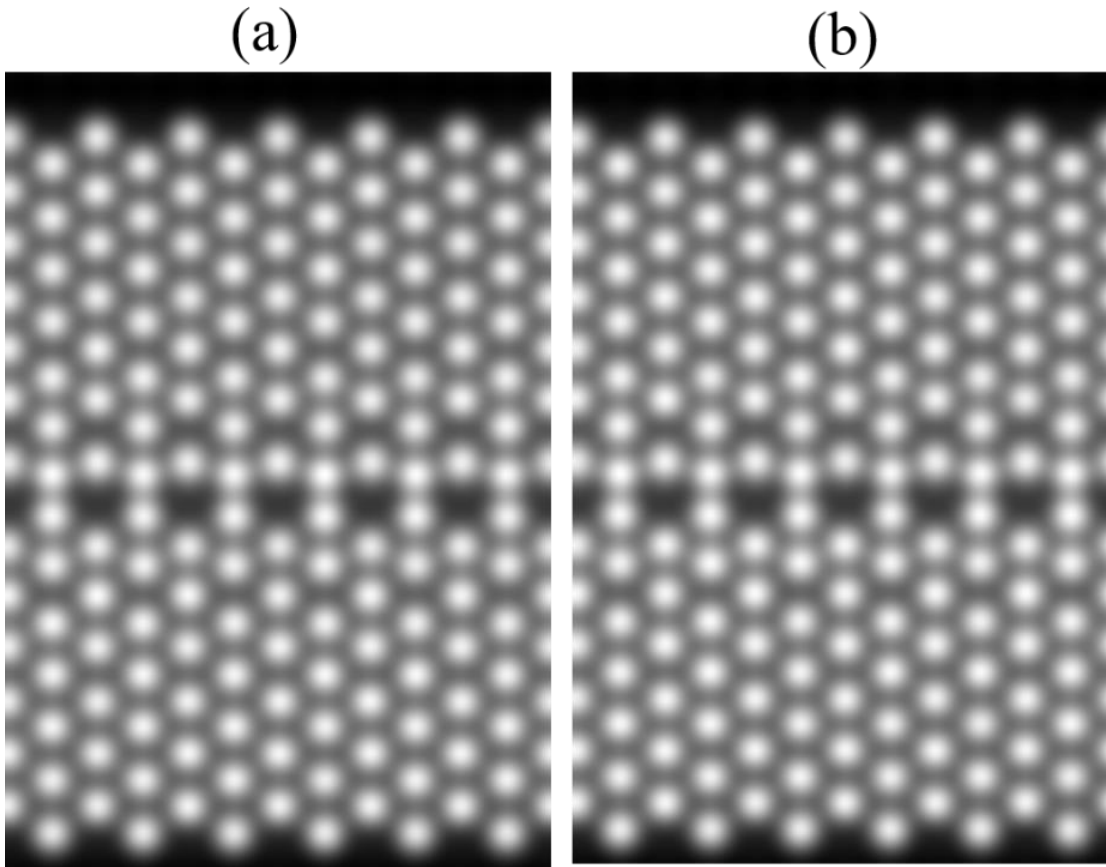
Figure 5-22: STEM simulated images of E units along [111] direction at an inner HAADF angle of (a 40.5 mrad and **b)** 77.8 mrad. It shows that there is no change in the atomic positions at the GB due to the beam convergence

Comparison of the experimental and the simulated structure

On closely inspecting the regions surrounding the units, it is found that the atoms near the structural units of ORII are also translated more in comparison to ORI (shown in **Figure 5-23**). It is well known that the instrument and the sample instabilities may create substantial image distortions. In order to rule out the effect of STEM distortions on the images, the atomic distances and angles within the grains from the two ORs are also evaluated. The measured distances and angles within the grains were same in both the images.
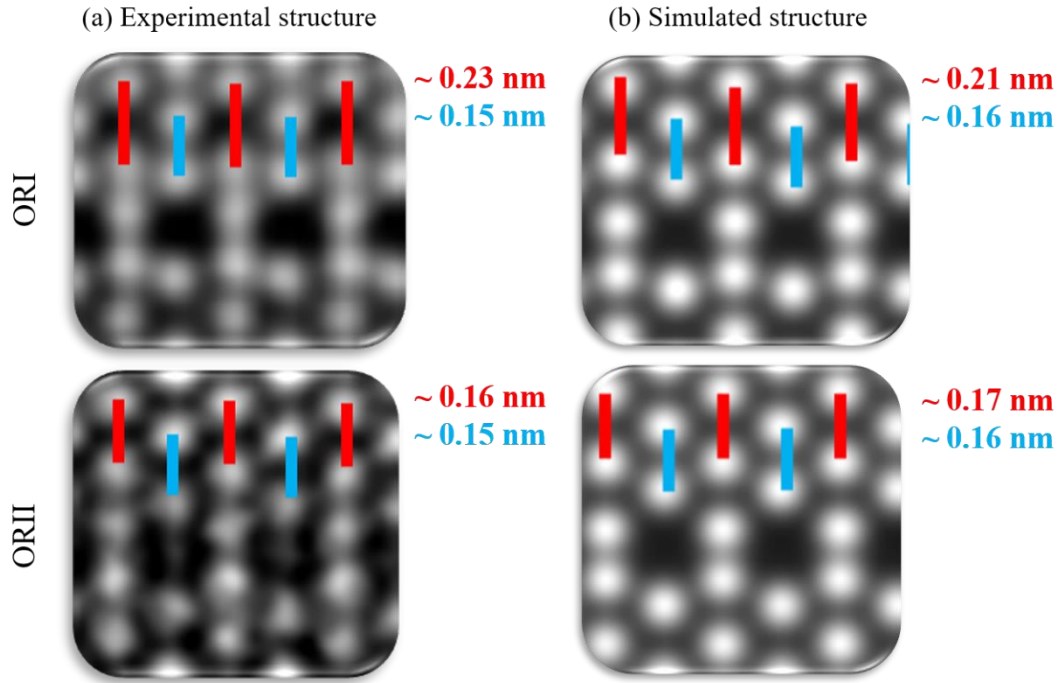
Figure 5-23: Comparison of translations in the regions surrounding the structural units in both ORs (a) Experimental structures and **(b)** STEM simulated structure**.**

GB plane trace analysis via SEM imaging and EBSD:
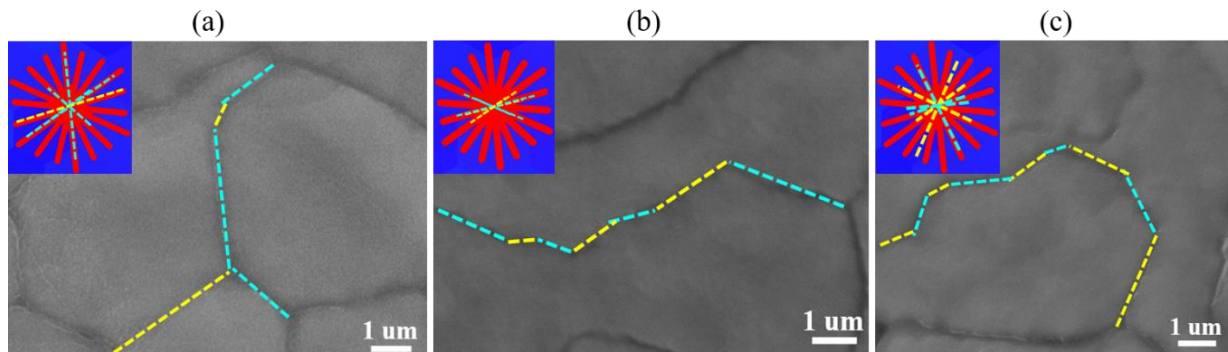
Figure 5-24: Plane trace analysis for GB curvature in ORI by using SEM imaging and EBSD for three different Σ3 boundaries as shown in **(a), (b)** and **(c)**. Blue color inset shows the (111) surface orientation of the Al film from the IPF map. Green and yellow dotted lines in SEM images represent the local GB plane traces. Red lines in the inset show the {211} plane traces from the adjoining grains in EBSD. On superimposing the plane traces from the image onto the inset it is found that the majority of the GB planes in ORI are lying exactly on {211} traces.
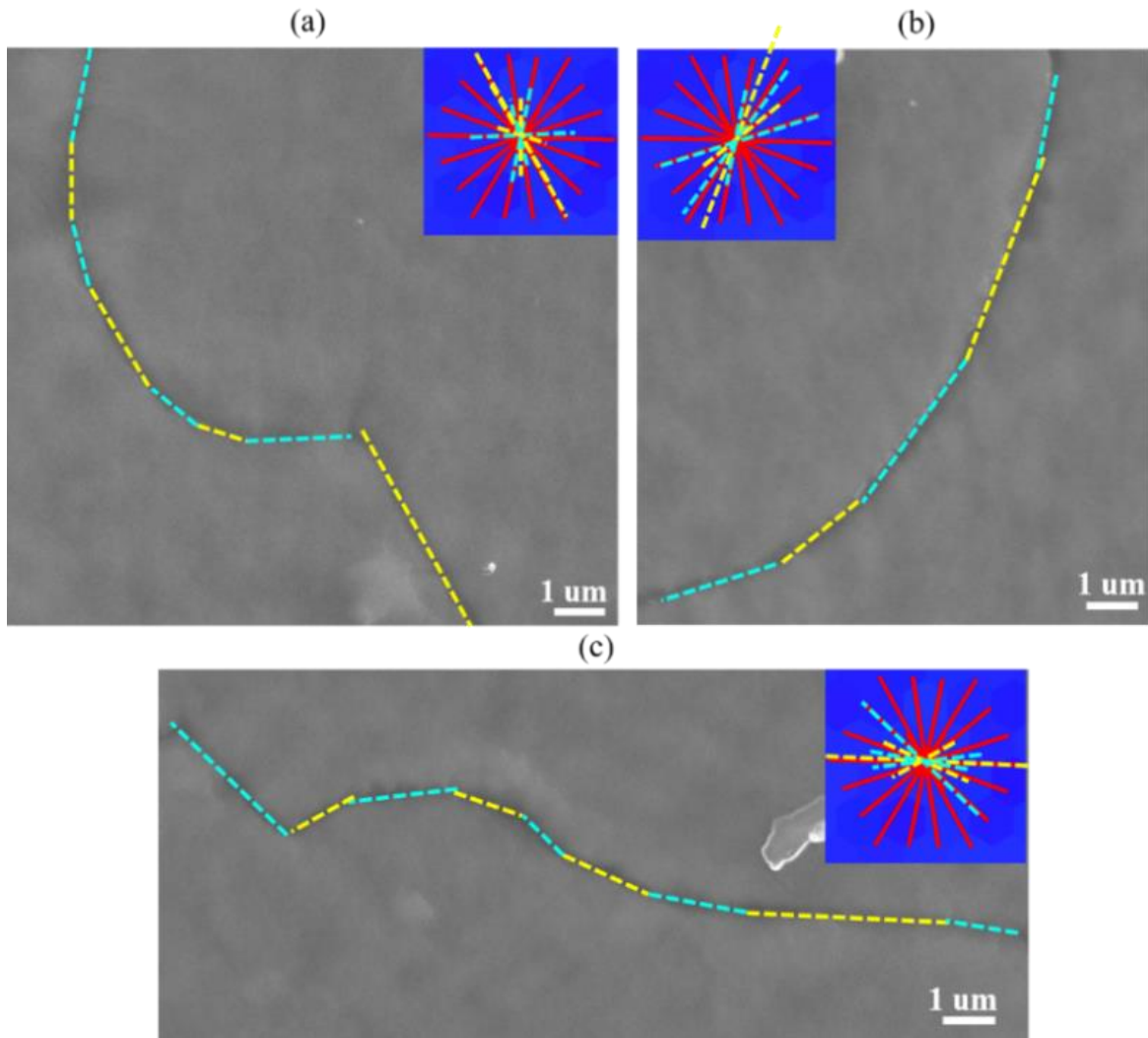
Figure 5-25: Plane trace analysis for GB curvature in ORII by using SEM Imaging and EBSD for three different Σ3 boundaries as shown in **(a), (b)** and **(c)**. Blue color inset shows the (111) surface orientation of the Al film from the IPF map. Green and yellow dotted lines in SEM images represent the local GB plane traces. Red lines in the inset show the {211} plane traces from the adjoining grains in EBSD. On superimposing the plane traces from the image onto the inset, it is found that only some of the GB planes are lying exactly on {211} traces which clearly indicate that the GB plane is deviated more in ORII from the exact {211} plane compared with ORI.

Distribution of misorientation deviation in ORI and ORII
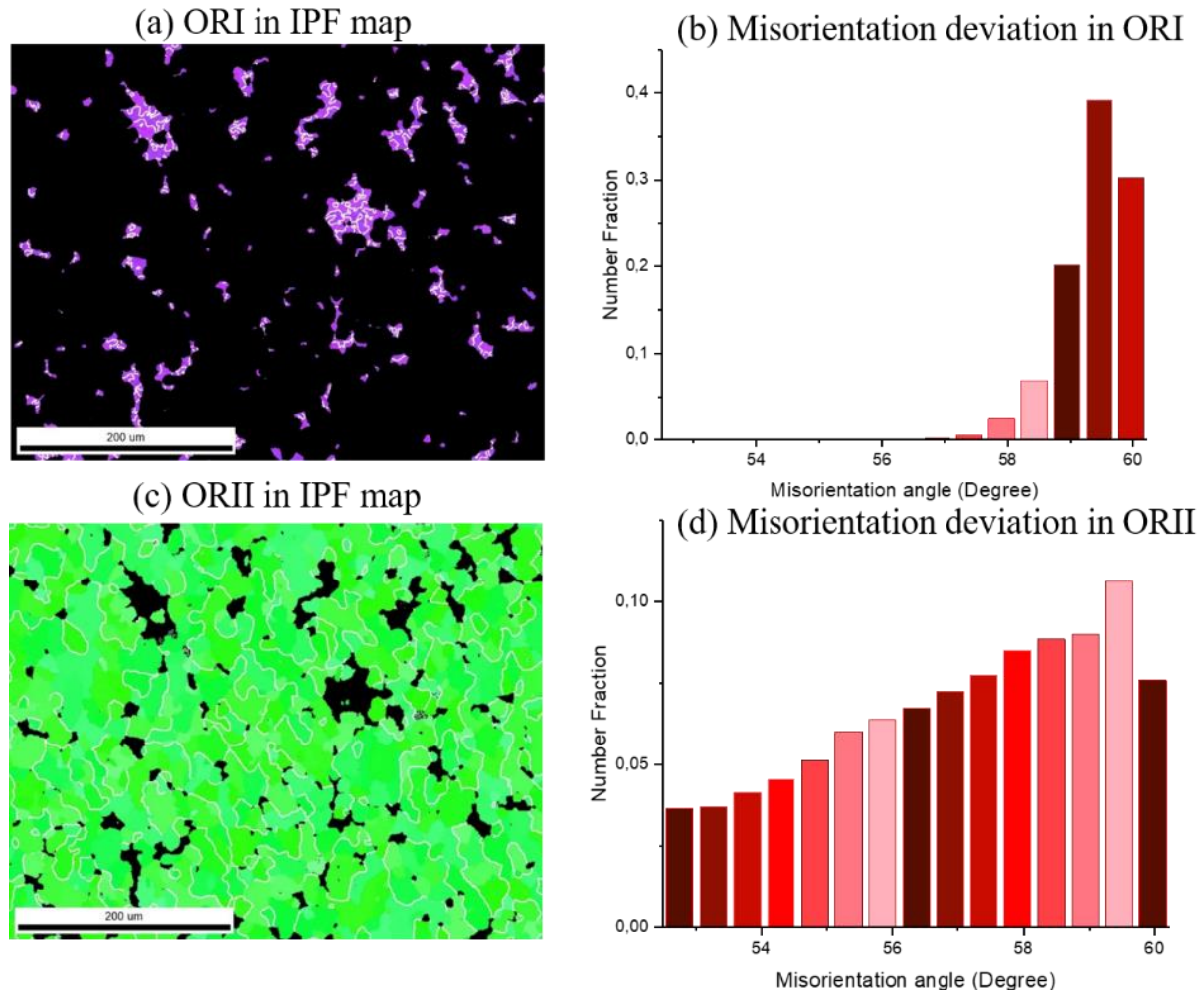
Figure 5-26: Misorientation deviation in ORI and ORII in Al thin film from EBSD (a) and (c) represent isolated IPF maps of ORI and ORII, **(b) and (d)** depict the number fraction of Σ3 at different misorientation. These plots indicate that the Σ3 misorientation in ORII is deviated more from the exact CSL misorientation in comparison to ORI.

Verification of plane strain conditions at different values of ε₁₁
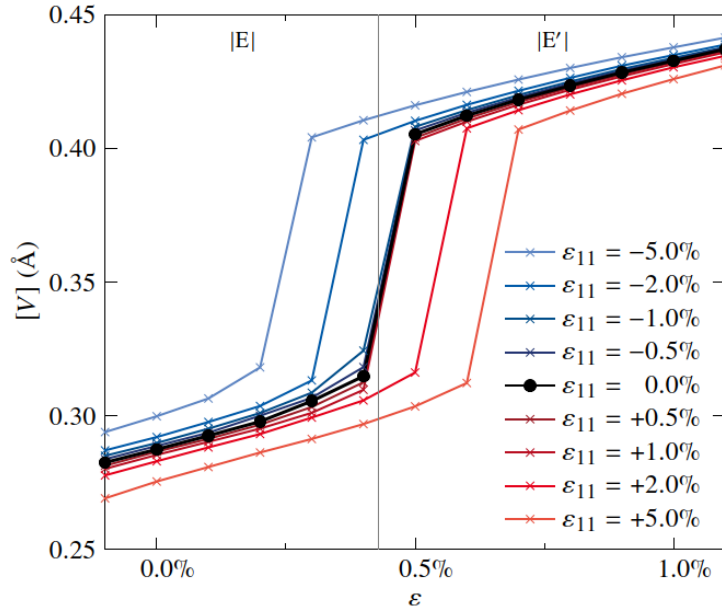
Figure 5-27: Influence of a strain in tilt axis direction (equivalent to the normal of the film surface in the experiment) on the simulation results. Due to the boundary conditions, it is not possible to model plane-stress conditions without introducing size effects (note that these size effects are the result of the ratio of GB volume over bulk volume and are also necessarily present in the experiment). To obtain reproducible data we thus chose plane-strain conditions, but verify here that the results are qualitatively the same if the film expands or contracts in the direction normal to the substrate. This plot is a repetition of **Figure 5-15 d)** with additional values of ε11 (which was zero in the Figure in the main text) and shows that the jump in excess volume is only shifted by a small amount due to the additional strain component. We verified that the same |E| and |E'| motifs occur in all cases. The conclusions are therefore unaffected by the choice of plane strain over plane stress.

5.3 Deciphering the atomic structures of [111] tilt GBs as a function of 5 macroscopic parameters in Al by correlating STEM with atomistic simulations

This chapter investigates the detailed atomic structures (in terms of SUs) of different [111] tilt GBs for different misorientation angles and the GB planes, by using STEM together with the atomistic simulations. The excess properties and the atomic structure along the z direction were calculated for different atomic structures. This study bridges the gap between the structure and the properties of the GBs. The work in this section is based on the manuscript III.[§§]

5.3.1 Introduction

It is well known that a deeper understanding of the correlation between the atomic structure and the properties of a GB needs atomic resolution imaging of the GB. In the last few decades, numerous studies [21,36–38,72] explored the atomic structures of several coincidence-site lattice (CSL) GBs and their properties in a variety of fcc materials, but usually by employing atomistic simulations. It has been found that the modeled structures from several simulations [36,37,39] for the same GB type are inconsistent with one another. This makes it difficult to identify which GB structure truly exists in reality. By combining the results of the calculated boundary structures with relevant experimental observation has resulted in new discoveries [24,96–98,172]. However, very few of these investigations have been conducted for [111] tilt GBs [40,42]. Meiners et al. [40] conducted one such study at Σ19b [111] {1 7 8} GB, where he employed atomic-resolution imaging and molecular dynamics modeling to investigate the coexistence of two unique GB structures/phases (i.e. pearl and domino) and their transformation kinetics. Similar coexistence of two different structures was found at Σ37c [111] {1 10 11} GB [42]. It's interesting to note that the majority of experimental research on [111] tilt GBs is done for Cu. Therefore, it is essential to look into the structures to see whether similar phase coexistence takes place at the GBs in other metals, like Al.

Furthermore, it's also important to recognize that just one or two distinct types of [111] tilt GBs have been the subject of experimental research. Even a small misorientation variation has an

---

[§§] Based on manuscript III by S. Ahmad, T. Brink, C. H. Liebscher and G. Dehm

impact on GB attributes due to the incorporation of steps, defects, or additional structural units into the GB. Hence, it is required to empirically investigate the structures of several different GBs with different misorientation in order to establish the structure-property correlation. To the author's knowledge, no experimental studies have been conducted to determine how the change in the misorientation angle alters the atomic structure of [111] tilt GBs in pure fcc metals. According to the literature [23,25,224], altering the GB plane may potentially result in altering an entirely new atomic structure with different properties. Thus, we also need to investigate the structure of GBs with fixed misorientation but a different GB plane.

The current study examines the relationship between the structures of various GBs throughout a misorientation (θ) range for a particular tilt axis i.e. [111] and inclination of the boundary plane by using aberration corrected scanning transmission electron microscopy (STEM). STEM investigations of the symmetric variant I of Σ21a, Σ13b, Σ7, Σ19b, Σ37c and Σ3 GBs revealed two different misorientation groups consisting of two distinct type of structural units (SUs), respectively. The Σ21a, Σ13b and Σ7 CSL GBs belong to group 1 with misorientation range ($21°$ $< \theta < 34°$) and have "bow and arrow" type structure. While Σ19b, Σ37c and Σ3 GBs are associated to group 2 with misorientation range ($46° < \theta < 60°$) and have "zipper" type structure. Additionally, how the structural units vary at the GBs with a slight deviation from the ideal misorientation and influence the excess properties of the GBs are explored. Further investigation of the symmetric variants II of the GBs of group 2 reveals significantly different atomic structures, even though only the GB plane inclination changes by $30°$. Furthermore, it is determined by simulation how the excess properties of the two different atomic structures of the two symmetric variants of a CSL GB are affected.

5.3.2 Results

Atomic structures of pure [111] tilt GBs as a function of misorientation

As illustrated in **Figure 5-28**, along the [111] tilt axis in fcc, two symmetric GBs exist, corresponding to each symmetric variant. **Figure 5-29** and **Figure 5-30** show the evolution of the atomic structures of variant I of six symmetric [111] tilt GBs (Σ21a, Σ13b, Σ7, Σ19b, Σ37c and Σ3) as a function of misorientation angle (**Θ' (Our experiments)**), as described in **Table 4**. The characteristic structural units (SUs) are used to describe the complete atomic structure of all the Σ GBs [28,72].

Table 4: Type of [111] CSL boundaries, examined experimentally in S/TEM. The Ө (Theoretical) and Ө'' (**Brandon Criterion**) represents the CSL misorientation angle between the two grains and deviation from the exact CSL misorientation according to Brandon criteria, respectively. The Brandon criteria represents the allowable angular deviation ($\Delta\theta \leq 15\ \Sigma^{-1/2}$ degrees) from the exact coincidence [225]. The **Ө' (Our experiments)** represents the measured experimental value of misorientation angle for various CSL boundaries investigated and shows that it slightly deviates from the exact **Ө (Theoretical)** but follows the Brandon criteria. It should be noted that the measurement error for computing **Ө'** is within ± 1º.

[111] CSLs(Σ)	Σ21a	Σ13b	Σ7	Σ19b	Σ37c	Σ3
Ө (Ideal)	21.8°	27.8°	38.2°	46.6°	50.5°	60°
Ө'' (Brandon Criterion)	±3.28°	±4.16°	±5.67°	±3.44	±2.47°	±8.67°
Ө' (Our experiments)	24.8°	26.8°	34.0°	46.0°	48.5°	60.0°

······· Symmetric variant I ({352} planes in Σ19b GB)

······· Symmetric variant II ({178} planes in Σ19b GB)
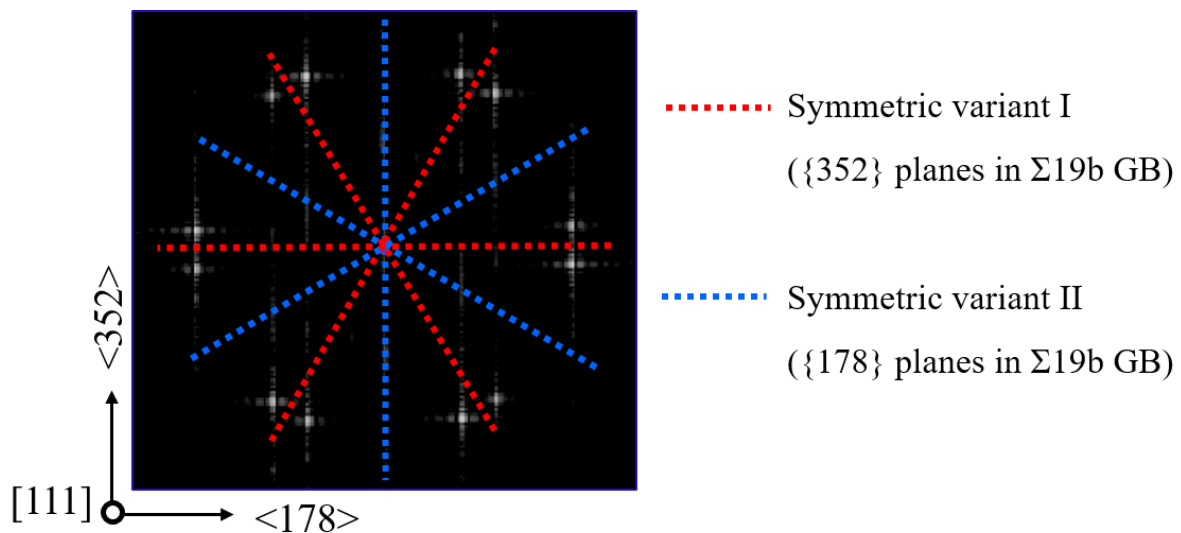
Figure 5-28: Fast Fourier Transform (FFT) of a Σ19 [111] GB. Two adjacent grains are oriented along [111] zone axis and rotated w.r.t each other. Each GB has two symmetric variants, as represented by dashed red and blue lines, respectively, for a Σ19 GB. With respect to the symmetric variation I, the GB plane for the symmetric variant II is rotated by 30°.
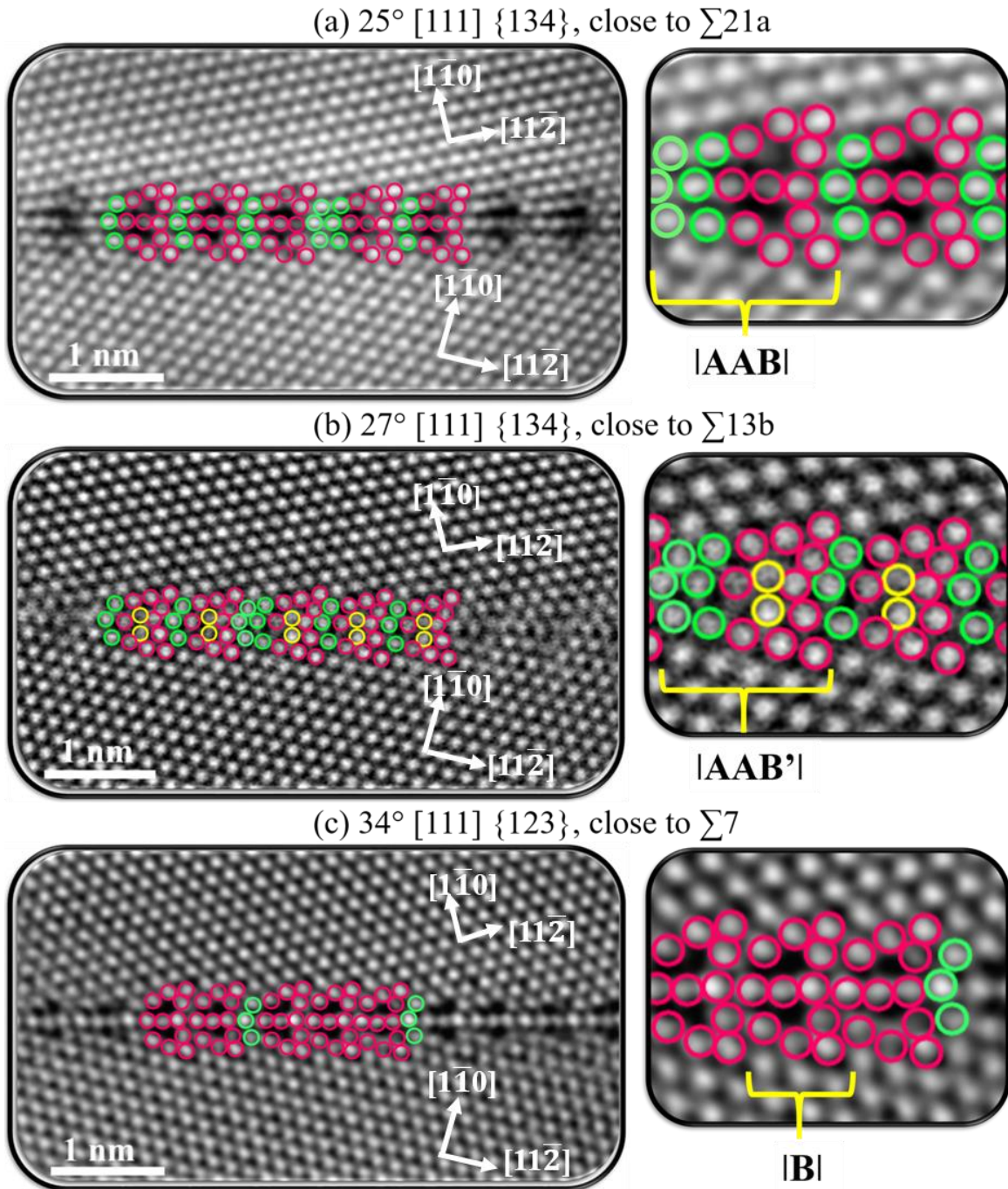
Figure 5-29: STEM-HAADF images showing the atomic-resolution details of symmetric Σ21a, Σ13b and Σ7 GBs viewed along the [111] zone axis. Atomic structure of symmetric **a)** Σ21a {134} **b)** Σ13b {134} and **c)** Σ7 {123}. }. The different color of the atomic columns assists to emphasize the structural units. The red and green color circles together form the fundamental SUs (i.e. A and B) for each GB. Note that the GB planes reported here are approximate.

According to the SU model specification [72], the GB structure for Σ21a, Σ13b and Σ7 can be written as |AAB . AAB|, |AAB'. AAB'| and |B . B|, where B and B' represent the similar types of

93

bow and arrow shaped red sub-units. With respect to the resemblance of structural units, the GB structure for all the three GBs is called bow and arrow structure. In the projection, the atomic structure of Σ21a {134} and Σ13b {134} is mainly comprised of two type of the preliminary sub-units (i.e. A and (B/B')), as highlighted by red circles and green circles, in **Figure 5-29 a)-c)**, respectively. The red sub-unit of the symmetric Σ21a {134} GB with a misorientation of 25°, exhibits a bow and arrow shape formed by 11 atomic columns while the green sub-unit are formed by 3 atomic columns.

In case of Σ13b {134} with a misorientation of 27°, the red sub-unit appears slightly different to the Σ21a structure and possesses a distorted bow and arrow shape with an extra atomic column in the center of the GB (highlighted in yellow with total 12 atomic columns). The presence of this extra atomic column in the SUs of Σ13b makes it denser as compared to the SUs of Σ21a. This depicts that a misorientation increase of 2° from Σ21a (25°) introduces only a minor change in the inner structure of the primary structural units in the Σ13b (27°) GB. The outer shape of the structural unit remains the same. Hence, the bow and arrow structural units are designated as B'.

Additionally, the atomic structure of the Σ7 (34°) GB reveals that it consists mainly of the same bow and arrow shaped unit B from Σ21a (25°) GB, incorporated by the additional green A units (consisting of three atomic columns). It is crucial to remember that there is not a fixed repeating distance for the emergence of green A units into the GB w.r.t the misorientation.

Furthermore, the atomic resolution images of Σ19b (46°), Σ37c (49°), Σ3 (60°) are presented in **Figure 5-30** and can be written as |EF . EF|, |EEF . EEF| and |E|. The full atomic structure of the Σ19b is divided into two sub-units E and F, as highlighted by red and green circles in **Figure 5-30 a)**. The red sub-unit E exhibits a distorted square shape formed by 8 atomic columns, followed by the green sub-unit F, a trapezoid consisting of 4 atomic columns. No other disruptions of this sequence at the symmetric segments are observed. The fundamental SU of Σ37c in **Figure 5-30 b)** consists of a contiguous double distorted square (13 atomic columns) E sub-unit, followed by a similar trapezoidal F sub-unit as in Σ19b.

In addition, it is important to note that the misorientation angle of the Σ37c GB in **Figure 5-30 b)** is approximately 49°, which lies in between the nominal Σ19b (48.6°) and Σ37c (50.5°) misorientation. This may lead to the presence of a mixture of both of the preliminary structural units from the ideal Σ19b and Σ37c, according to the SU model. The red sub-unit E present in Σ3

exhibits a perfect square shape consisting of eight atomic columns as also explained in [226]. Here, the GB structures are termed as zipper structures by virtue of the analogy to the Σ19b {2 5 3} GB structure in Cu [25].
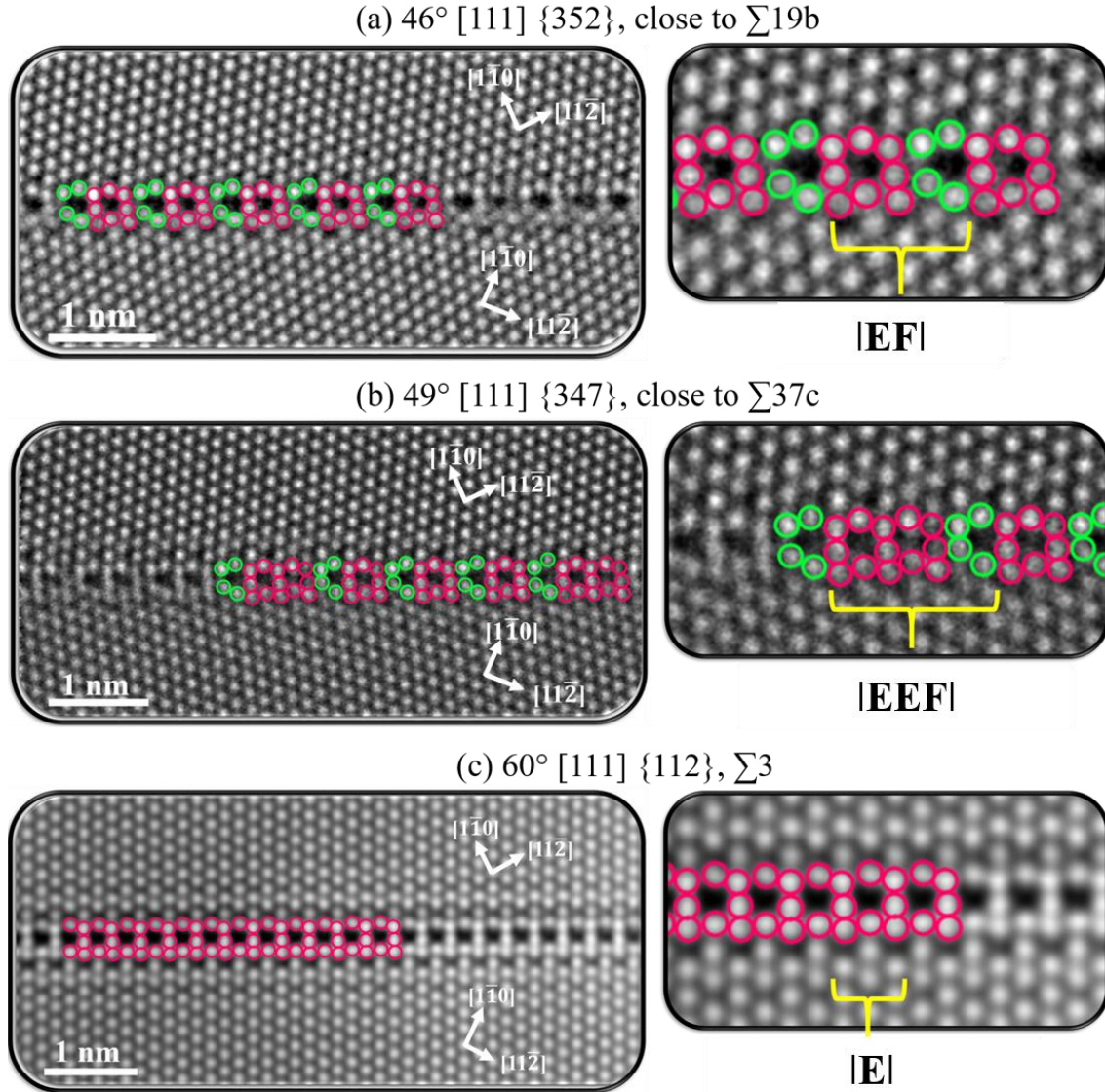
Figure 5-30: STEM-HAADF images showing the atomic-resolution details of symmetric Σ19b, Σ37c and Σ3 GBs viewed along the [111] zone axis. Atomic structure of symmetric a) Σ19b {352} **b)** Σ37c {347} and **c)** Σ3 {112}. The red color circles represent the square shaped SU (i.e. E). Note that the GB planes reported here are approximate.

Atomistic simulation of symmetric variant I of Σ21a, Σ13b and Σ7 GBs

So far, the experimentally observed structures are from the GBs, which deviate slightly (within the Brandon criterion) from the nominal CSL misorientation and the GB habit plane (see **Table 4**). The

atomic structures and the properties of the exact CSL GBs are experimentally not accessible here. Furthermore, how slight deviations in misorientation from the exact CSL affect the atomic structure and properties of GB is not well understood in pure Al along [111] axis.
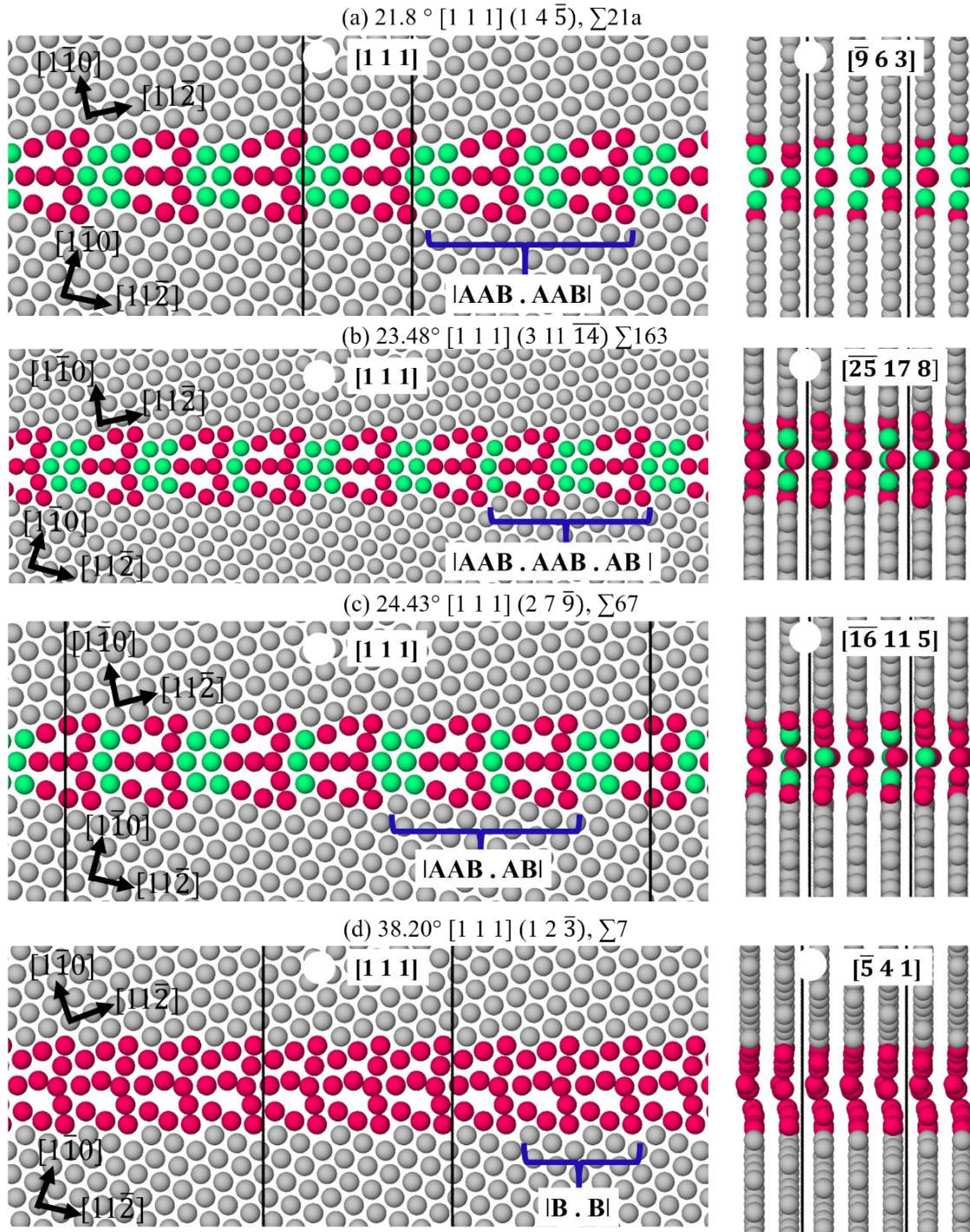
Figure 5-31: Simulation atomic structures of the GBs a) Σ21a (21.79°), **b)** Σ163 (23.48°) and **c)** Σ67 (24.43°) GBs. The figure shows the atomic structures of the three GBs along the [111] tilt axis and z-axis.
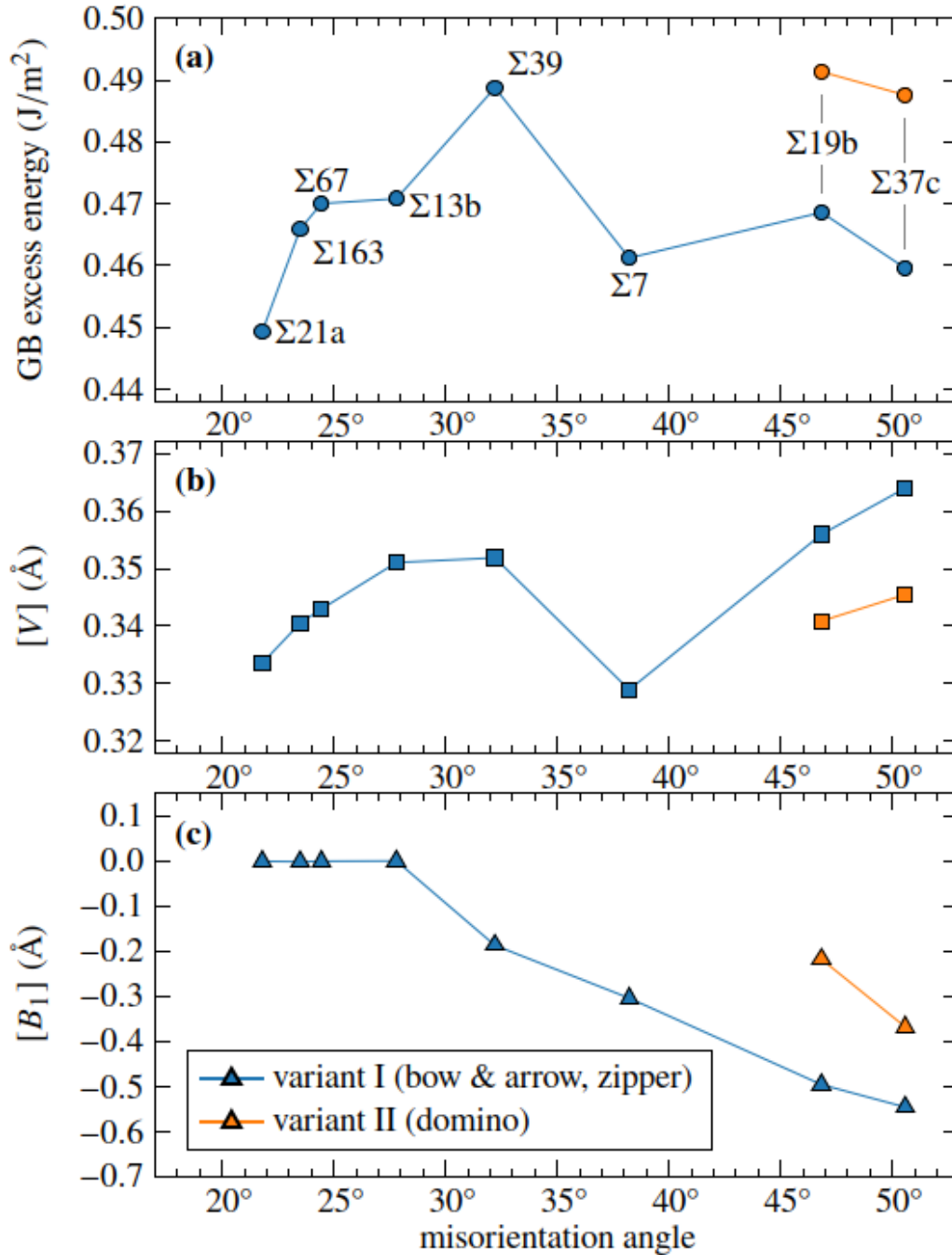
Figure 5-32: Excess properties of the GB structures as predicted by the computer simulation. **a), b)** and **c)** represent the change in GB excess energy, excess volume [V] and excess shear [B₁] along the [111] tilt axis as a function of increasing misorientation angle. The symmetric variants I and II of the GBs are shown by the blue and orange data points, respectively.

Moreover, it is not known whether the experimentally observed green A units (see **Figure 5-29**) in the lower misorientation range are some additional minority units or belong to the equilibrium structural unit from any of the Σ GBs. Therefore, to answer the aforementioned questions, the

progression of GB structural units as a function of GB macroscopic parameters (misorientation and GB plane) and their influence on thermodynamic excess properties are explored using atomistic simulations. **Figure 5-31 a)-d)** depicts the change in the atomic structures of the GBs (symmetric variant I) as a function of misorientation angle, starting from the exact Σ21a misorientation (i.e. from 21.8° up to 38.2°), at 0K without externally applied stress. Furthermore, **Figure 5-32 a)-c)** illustrates their interfacial excess properties.

In the case of Σ21a (21.8°) the atomic structure comprises of the bow and arrow red SUs, identical to the observed experimental structural units (i.e. B units). In addition, the GB structure also embodies two A units consisting of three atomic columns (see **Figure 5-29 a)**). Hence, the complete simulated atomic structure of the ideal ∑21a GB is described as |AAB . AAB|. Furthermore, in the case of Σ163 (23.5°) GB, which has a slight deviation of typically 1.69° from the ideal Σ21a misorientation, it is found that the number of A units are reduced at the GB. Moreover, on further increasing the deviation to 2.64°, i.e. Σ67 (24.4°), a similar trend like for the Σ163 (23.5°) GB is observed i.e. the number of A units is decreased.

For the Σ7 GB with a misorientation of 38.2°, it is found that the A units completely disappear and the atomic structure comprises of only B type units. This suggests that as the misorientation angle of the GB increases up to the 38.2°, the GB increases building blocks of B type units and wants to reduce the A type units due to geometric reasons.

This introduces a change in the GB excess properties, as depicted in **Figure 5-32**. Since the Σ21a GB consists of two type of contiguous units as repeating units for the GB, it cannot be considered as the delimiting or favored GB. Conversely, Σ7 GB consists of only one type of SU, it is seen as a delimiting boundary as a result. Furthermore, the atomic structure of the GBs along the cross-section revealed that no translation of {111} planes across the GB is observed up to the Σ67 GB. However, a visible translation of {111} planes of ~0.3 Å is observed for the Σ7 GB.

Atomic structures of symmetric variants II of Σ19b, Σ37c and Σ3 GBs

The atomic structure of symmetric variants II of Σ19b {178} and Σ37c {189} shows a very distinct atomic structure with a change in GB inclination by 30°. The total GB structure of both the GBs is composed of a combination of the two inclined characteristic sub-units, as indicated by red circles (see **Figure 5-33 a)** and **b)**).

(a) 47° [111] {178}, close to $\sum$19b

(b) 50.5° [111] {189}, close to $\sum$37c
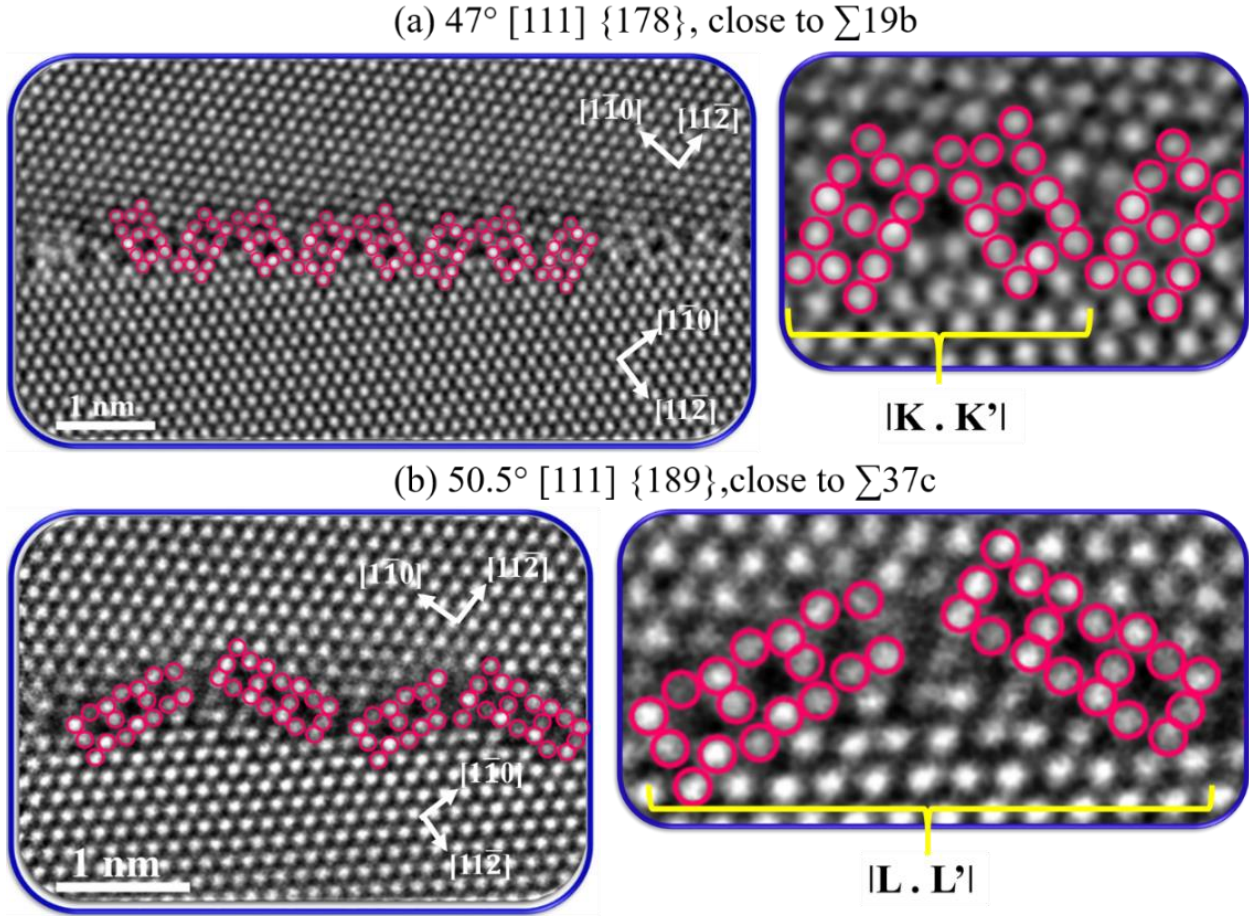
Figure 5-33: STEM-HAADF images showing the atomic-resolution details of the symmetric variant II of Σ19b, Σ37c and Σ3 GBs viewed along the [111] zone axis. Here, the GB plane inclination is 30° w.r.t the GBs observed in **Figure 5-30**. Atomic structure of symmetric **a)** Σ19b {178} and **b)** Σ37c {189}. The red color circles represent the inclined square shaped and trapezoidal shaped SUs while dark red color circles represent the mirrored structural units of the inclined units

In Σ19b, the SU notation is | K . K'|, where K represents the low inclined domino shaped unit (w.r.t the normal of the GB plane) while K' is the mirror image of the inclined sub-units (i.e. K) along the GB plane. Here, the structural units appear different to that of the zipper structure and referred to as domino structures due to their resemblance to the structures in Σ19b {178} GB in Cu [25,40]. A certain distinct arrangement of two of these sub-units builds up the repetitive unit of the GB. The full domino structure is composed of two sub-units alternating between one low inclined K and one-mirrored K' unit. Similarly, the domino structure in Σ37c is |L . L'|, where L represent the high inclined domino unit and L' are the mirrored L domino with respect to the GB plane. Furthermore, the atomic structure of a Σ3 {110} comprises indeed of {112} inclined facets of

approximately 3.4 nm in length (see **Figure 5-34**). Here, the atomic structure of these {112} facets consists of E square units as described above for the Σ3 {112} structure. In addition, on performing Burgers circuit analysis around the facet junctions using method from Medlin et al [217], it is found that these facets are separated by a dislocation defects at the junctions that are associated with the Burgers vector **b** = 1/2 [$\bar{1}$10] (see **Figure 5-34 b**)).
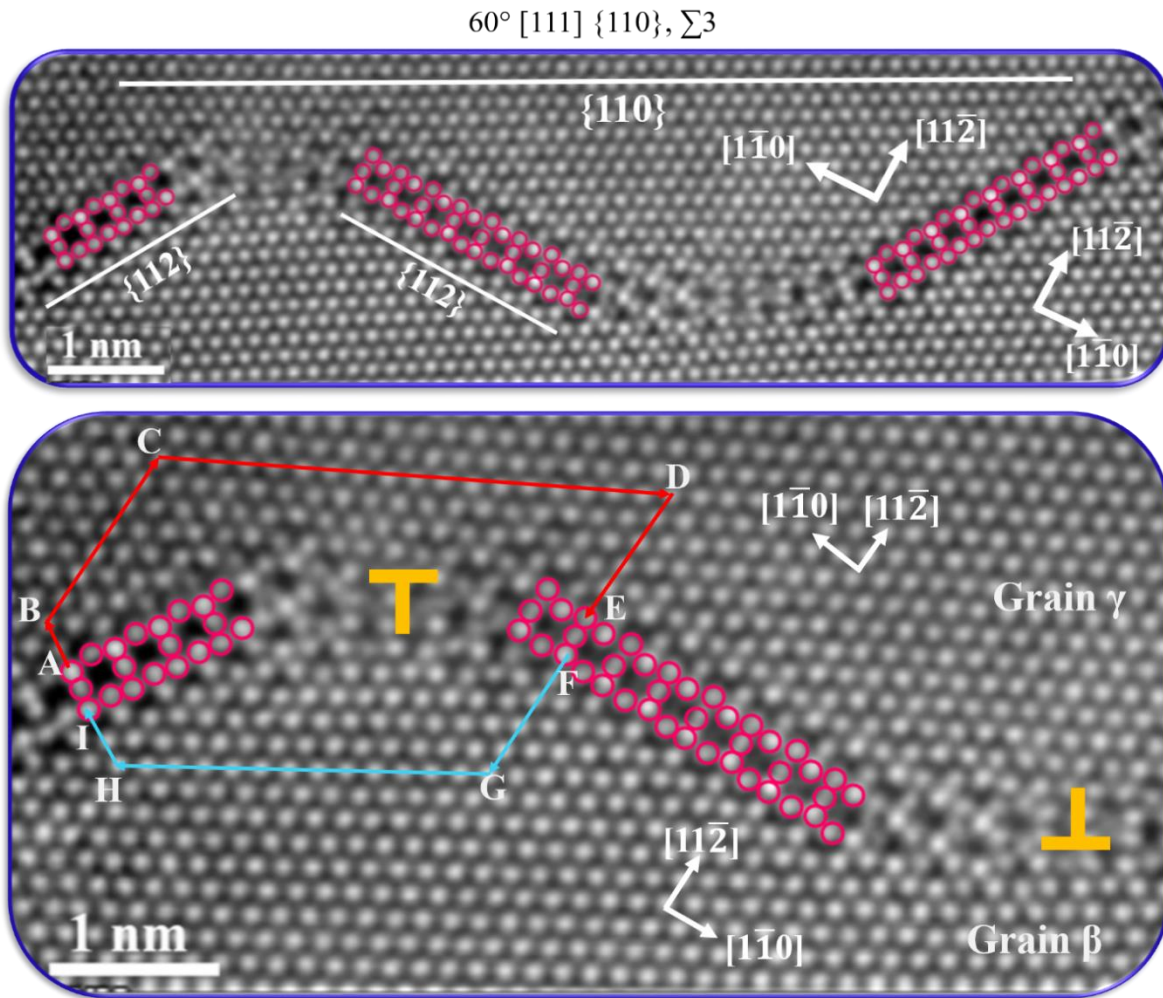
Figure 5-34: STEM-HAADF images showing the atomic-resolution details of a symmetric Σ3 {110} grain boundary viewed along the [111] zone axis. Note that globally the GB plane is {110} but locally it is facetted into {112} planes. The red color circles represent the inclined square shaped SUs while dark red color circles represent the mirrored structural units of the inclined squared units. A to E show the Burgers circuit in grain γ while F to I indicate the Burgers circuit in grain β. The calculation using Medlin et al. [217] method show that these facet junctions are associated to Burgers vector of b = $\frac{1}{2}[\bar{1}10]$.

Atomistic simulations of symmetric variants II of Σ37c GB

We have so far discovered from the experimental observation that the symmetric variant II of the same type of boundaries (Σ19b, Σ37c and Σ3) exhibits different atomic arrangement as a result of different atomic planes. To determine whether or not these different structures belonging the same boundary have different GB properties, we have simulated the atomic structures and the excess properties of two symmetric variants of Σ37c GB (with the habit plane of {3 4 7} and {1 10 11}, respectively) as illustrated in **Figure 5-35**.
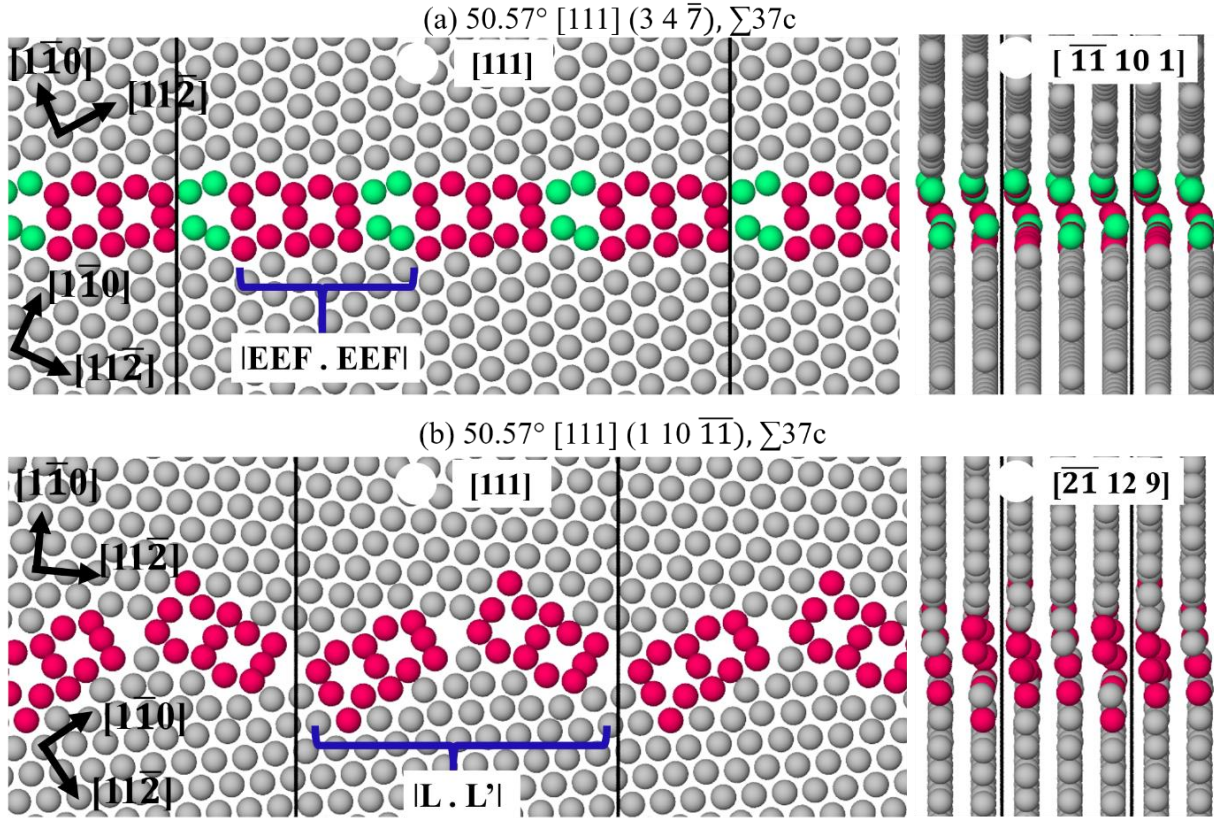
Figure 5-35: Simulation of two symmetric variants of Σ37c GB. **a)** Σ37c {347} and **b)** Σ37c {1 10 11} GBs along the <111> tilt axis and the cross section. The simulation depicted two different atomic structures corresponding to two different GB planes.

The simulated atomic structure of Σ37c {3 4 7} GB exhibit a zipper kind of structure having two distorted square units, followed by a trapezoidal unit, also observed experimentally above (see **Figure 5-30 b**)). In contrast, the Σ37c {1 10 11} structure possesses a domino kind of structure. As indicated in **Figure 5-32**, two distinct types of structures are found with differing thermodynamic excess features (indicated by orange color data points), in agreement with the experimental result. In addition, analyzing the cross-sectional view reveals different magnitudes of translation of {111} planes across the GB with 0.55 Å and 0.37 Å for the zipper and domino structures, respectively.

101

5.3.3 Discussion

Atomic structures of symmetric variant I of the GBs as a function of misorientation

The variation of the atomic structure of [111] tilt GBs with the misorientation angle and the GB plane is discussed here with respect to the structural unit model. To the author's knowledge, so far there are no experimental studies on the variation of the atomic structure of [111] tilt GBs as a function of the misorientation in pure fcc metals. However, there are three theoretical studies from Frost [39] , Sutton [37] and Wang [36], and three experimental studies [25,40,42] reporting the structure of several [111] tilt GBs in pure Al and Cu. None of the SUs proposed by Frost using the hard sphere model [39] matches with the observed experimental ones in our study. The true structure of the [111] tilt GBs cannot be predicted by this hard sphere model since it is too simple.

Interestingly, Sutton and co-workers [37] simulated the atomic structures of [111] tilt GBs and found a discontinuous change in the boundary structure between two favored (delimiting) GBs in Al. According to Sutton [37], near the discontinuity, each GB had two possible structures, differing in their translation states parallel and perpendicular to the tilt axis. He proposed that two groups of boundary structures existed, characterized by the translation of {111} planes (denoted by T_z) along <110> zone axis i.e. $T_z \sim 0$ and $0.235 < T_z < 0.283$, for each group respectively (see

Table 5). The fundamental SUs at the GBs of the two groups were A and B* units and C, D, E and F units, respectively. No SUs of one group ($0° < \theta < 17.90°$) were found to be mechanically stable in the misorientation range of another group ($38.21° < \theta < 60°$).

However, in the range ($17.90° < \theta < 38.21°$), mechanically stable structures from both groups were found near the discontinuity such as in the case of Σ21a and Σ13b GBs (see

Table 5). A closer look reveals that none of the SUs (For example: the atomic structures of Σ7 and Σ3 GBs) from Sutton's theoretical study (in **Figure 5-36 a**)) matches with our experimental SUs for any of the boundaries (see **Figure 5-29** and **Figure 5-30**).

Table 5: Simulation results from Sutton [37], which shows there are two groups of boundary structure depending on the type of structural units existing at the GB. The boundaries in the two respective groups are marked by grey and

black color, respectively. The fundamental structural units of the boundaries in first and second group are A and B* and C, D, E and F units, respectively. For the GB structures, please refer to Sutton [37].

GB type	θ	T_z	Structure
Σ 57	13.17°	-0.017	|AAAAAB*|
Σ 43	15.18°	-0.014	|AAAAB*. AAAAB*. AAAAB*|
Σ 31a	17.90°	-0.015	|AAAB*. AAAB*. AAAB*|
Σ 21a	21.79°	-0.021	|AAB*|
Σ 21a	21.79°	+0.264	|C|
Σ 13b	27.80°	-0.020	|AB*. AB*. AB*|
Σ 13b	27.80°	+0.274	|D. D. D|
Σ 7	38.21°	+0.283	|E. E. E|
Σ 19b	46.83°	+0.277	|EF. EF. EF|
Σ 37c	50.57°	+0.277	|EFF. EFF. EFF|
Σ 3	60°	+0.235	|F|

Later, Wang [36] used the extended structural unit model, taking into account how the delimiting (consisting of just one SU) GBs might have metastable structures that could affect the intervening GBs in Cu. The structures of all the intervening GBs were described in terms of units of boundaries delimiting the misorientation range (0° to 60°) i.e. Σ1 (110) and Σ3 (211). The units of these delimiting boundaries were called E for the Σ1 GB, F (stable) and F' (metastable) for the two structures of the Σ3 GB. The boundary structure changed continuously with the misorientation between two adjacent delimiting GBs.

On comparing their predicted structure in Cu (see **Figure 5-36 c**) and **d**)) to the experimentally observed ones in Al (see **Figure 5-29, Figure 5-30,** and **Figure 5-33**), some resemblance is found in the appearance of the SUs from the boundaries such as Σ3 and Σ7, but their atomic distances and angles are not identical to each other because of the different material. However, no other similarity is found in our experiment. This might have occurred because these simulations by Sutton and Wang used straightforward pair potentials with poor transferability that do not take into account the impact of nearby atoms on a pair's interaction [227]. Furthermore, the GBs in different

materials can have different microstates, as was also observed in the case of Σ3[111] in Al [226]. This may lead to the differing structure of the same boundary in different materials.

Since, there has been no experimental observation of the real structure of the boundaries in Al, we examined the atomic structures of several GBs directly by aberration corrected S/TEM. The evolution of atomic structures of symmetric variant I of six [111] tilt GBs (i.e. Σ21a, Σ13b, Σ7, Σ19b, Σ37c and Σ3) with increasing misorientation angle has been the subject of our initial investigation. At least from the projected experimental structures, it seems that there are two distinct groups of GBs (i.e. group 1 and 2) consisting of different SUs belonging to a specific misorientation range. For the GBs (i.e. Σ21a, Σ13b and Σ7 GBs) in group 1 with low misorientation range ($21° < \theta < 34°$), similar structures were found for all three GBs (see **Figure 5-37 a)**). The structure of three GBs in group 1 are termed as "bow and arrow" structure. For high misorientation
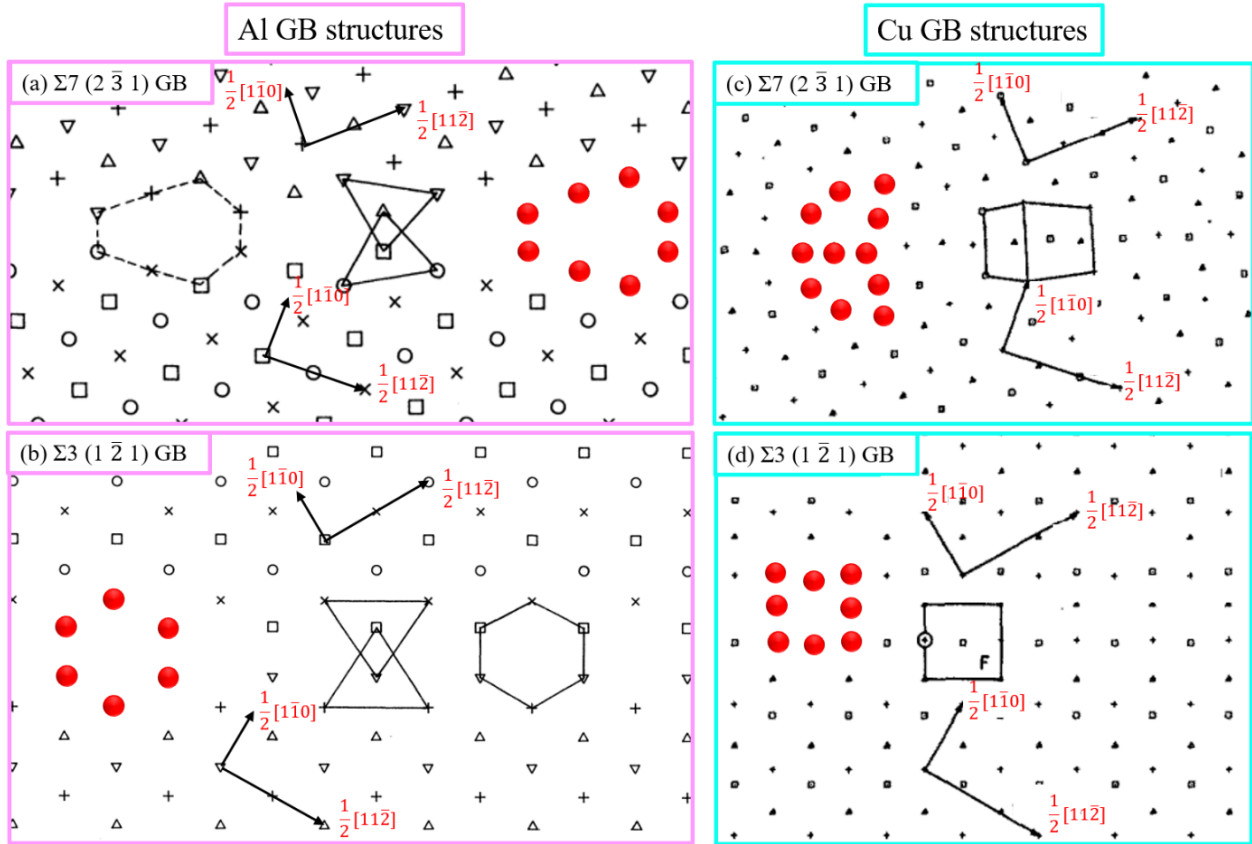
Figure 5-36: Theoretical structures of Σ7 and Σ3 GBs along [111] tilt axis from literature [36] [37]**.** At the GBs, the red circles form repeating SUs. **a)** and **b)** show the SUs of Σ7 and Σ3 in Al from Sutton et al. [37]. **c)** and **d)** show the SUs of the same GBs in Cu from Wang et al. [36]. The figure clearly depicts that the structures look different in both theoretical studies.

angles θ of ($46° < \theta < 60°$), another three structures (for Σ19b, Σ37c and Σ3 GBs) of the same type

are observed (see **Figure 5-37 b**)), which are different from the low misorientation range of $21° < \theta < 34°$. All the GB structures in this misorientation range are called "zipper" structure. However, it is yet difficult to explain whether the bow and arrow and square shaped units are fundamentally different to each other or not. Nevertheless, in the projection, they look moderately different. According to our experimental investigations, we found two delimiting boundaries in total i.e. Σ7 (38°), and Σ3 (60°), GBs. On following the experimental motifs as per the SU model in the full misorientation range, it suggests that there has to be two more delimiting GBs, each consisting of only A or F units at some misorientation angle in the range of $(\theta < 21°)$ and $(38° < \theta < 46°)$, respectively, despite not being observed in the experiment. Therefore, the intervening boundaries in the low misorientation range $(21° < \theta < 34°)$ consists of combinations of two delimiting SUs i.e. A and B/B' units. Similarly, the intervening boundaries in the high misorientation range $(46°$

(a) Bow and arrow type structures (Σ21a, Σ13b and Σ7 GBs)

|AAB| |AAB'| |B|

(c) Domino type structures (Σ19b and Σ37c GBs)

|K . K'|

(b) Zipper type structures (Σ19b, Σ37c and Σ3 GBs)

|EF| |E'F| |E"|

|L . L'|
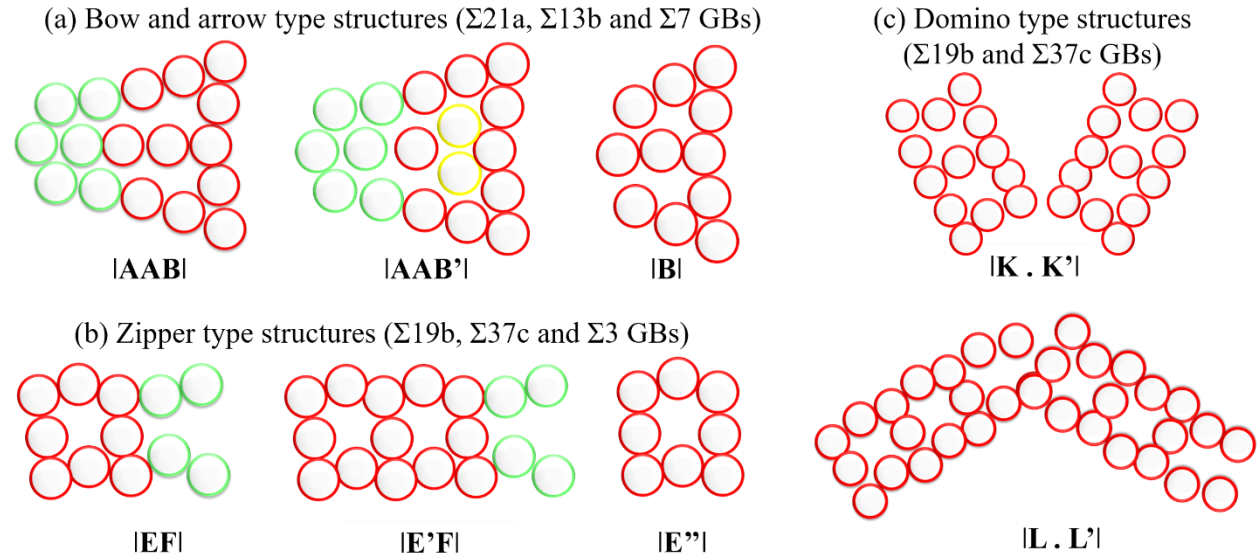
Figure 5-37: Schematics illustration of the atomic structures for different GBs as a function of misorientation angle and GB planes as found by STEM studies in this work. **a)** and **b)** represent the SUs of Σ21a, Σ13b and Σ7 GBs (from left to right) as a function of misorientation (symmetric variant I) **c)** shows structures for the Σ19b, Σ37c and Σ3 GBs (from left to right) with the same misorientation as in **b)** but with different GB plane (symmetric variant II).

$< \theta < 60°)$ consists of combinations of two delimiting SUs i.e. trapezoidal units F and square units E.

In order to gain further insights into the influence of these different structural motifs on the GB behavior, the atomic structures of the GBs along the <111> tilt direction and the z direction together with their interfacial properties have been calculated by atomistic simulations for the Σ21a

(21.79°), Σ163 (23.48°), Σ67 (24.43°) and Σ7 (38.20°) GBs. On comparing the simulated and the experimental SUs of the GBs, it is found that our simulations predict the same trend as in the experiment i.e. the reduction in the A motifs as the misorientation deviates from the exact CSL parameters, thus changing the excess properties. Furthermore, on performing the Burgers circuit analysis around the different parts of the GB, it is found that the absence or presence of the structural motifs is not related to the occurrence of DSC dislocations at the near Σ21a GB.

Although, the atomic structures along the cross section shows that the magnitude of the shifts in the {111} planes across the GB is increasing with misorientation, yet no obvious trend in the excess properties of the GBs w.r.t the misorientation is observed. Nevertheless, it is depicted that even a slight change in the misorientation can substantially influence the GB excess properties. For example: the experimentally observed structure of Σ21a (25°) (**Figure 5-29 a**)) resembles the simulated structure of Σ67 (24.43°), which has distinct excess properties than the ideal Σ21a (21.8°) GB (see **Figure 5-32**). Though this small deviation in misorientation may not sound big and can be easily overlooked in EBSD measurements, it can play a significant role in influencing GB related phenomena like microstructural evolution, GB migration and thermodynamic driving force for the segregation of solute elements at the GBs in a polycrystalline Al. For example: GBs with a higher grain boundary energy are more prone to segregation of solute elements than those with a lower energy [228]. In addition, GB energy also plays an important role in controlling other properties such as diffusion and mobility. Furthermore, it is often found that higher energy GBs are more prone to structural transitions, that eventually impact the mobility of the GBs and control the grain growth in the material [94,229]. Therefore, the GBs like Σ21a (21.8°) and Σ67 (24.4°) GBs (please see **Figure 5-29 a)** and **Figure 5-31 a)-c)**) in the current study may respond differently towards segregation and grain growth phenomena in reality.

Atomic structures of symmetric variant II of the GBs

It has been discovered that in addition to the misorientation, GBs with differing plane also possess different properties and behavior such as segregation tendency [25,38]. Hence, we have also investigated the atomic structure of the symmetric variant II of Σ19b, Σ37c and Σ3 GBs, exhibiting the same grain misorientation but different GB planes (30° rotated).

To the authors' knowledge, so far there are no theoretical or experimental studies done in order to understand the atomic structures of symmetric variants of the [111] tilt GBs except in Cu for the Σ19b GB by Meiners et al. [25]. He reported two different atomic structures of Σ19b GB with two different GB planes in Cu, called zipper and pearl structure for {253} and {187} planes, respectively. Furthermore, in the stable pearl phase for Σ19b {187}, Meiners et al. [40] also observed the presence of another metastable GB structure, termed the domino phase. Each of these phases has distinct excess qualities and can be transformed into the other.

Our investigation revealed that there are two different structures present for the two symmetric variants of Σ19b and Σ37c GBs. For Σ19b {352}, a similar zipper structure is observed as in Cu while for Σ19b {187} instead of pearl, domino structure is found as the most stable structure. Furthermore, no pearl phase is ever observed, despite investigating ample number of lamellas having Σ19b {187} GB. However, it still does not rule out the possibility of the presence of the pearl phase in Σ19b {187}. One of the reasons for the complete absence of pearl phases in Σ19b {187} experimentally in Al can be that the pearl phase is the high-energy phase (metastable) compared to the domino phase [230].This would be opposite to Cu.

Additionally, on investigating the two symmetric variants of Σ37c i.e. with {437} and {189} GB planes, we observed the zipper and domino structure at the Σ37c {437} and Σ37c {189} GBs, respectively. We observed that similar SUs exist in Al as for the stable domino phase of Cu at Σ37c {189} GB [231]. However, similar to Σ19b {187}, we always identify domino type structure as the stable one and never observed any pearl phase, also at Σ37c {189}, in contrast to results on Cu [42]. The study revealed that some SUs between Al and Cu coincide despite the different lattice parameter, atomic bonding and stacking fault energies of Al and Cu. Furthermore, the additional properties of the domino and zipper structures of Σ37c GB in Al have also been evaluated. It is discovered that not only the two structures of the same boundary look different in terms of their atomic arrangement, they also possess significantly different excess properties. The calculated grain boundary energy for the zipper structure is found to be 6% lower than the one for the domino structure, which will ultimately lead to a change in how the Σ37c GB behaves.

5.3.4 Summary and Conclusion

This paper focuses on a detailed systematic study of the atomic structure of [111] high angle tilt GBs in Al in relation to its crystallographic parameters and establishes a link between the structure and GB properties. In the first part, to comprehend the evolution of the atomic structures of the symmetric variant I of the GBs with an increase in misorientation angle (from 21° up to 60°), aberration corrected high-resolution electron microscopy is used. Secondly, whether a change in inclination results in different SU for GB of the same misorientation (symmetric variant II) is examined. Finally, MS simulations are used to assess how the various structures affect the GB properties.

➢ For the symmetric variant I, we identified two different groups of GBs in terms of their misorientation range consisting of two noticeably different structures. For group 1 with a low misorientation range of $21° < \theta < 34°$, we found three similar type of atomic structures consisting of bow and arrow shaped SUs named B/B' units with additional A units. The GB structures for all the three GBs in this range are called "bow and arrow" structures. As the misorientation increases, fewer A type units are observed at the GBs. While the GBs in the high misorientation range of $46° < \theta < 60°$ consists of three additional structures collectively referred to as the "zipper structure". They are either square shape units (E, E' and E'') or a combination of square units and trapezoidal (F) shape units.

➢ Additionally, atomistic simulation performed on Σ21a, Σ163, Σ67 and Σ7 GBs ($21° < \theta < 34°$) predicted the same atomic structures as those shown in the experiments, i.e. "bow and arrow" structure. It is found that as the misorientation increases steadily from the exact Σ21a, the number A units is found to decrease at the GB and eventually vanishes at a misorientation angle of 38° (i.e. Σ7). This leads to different GB excess properties.

➢ The experimentally resolved atomic structures of the symmetric variant II of all the three GBs (Σ19b, Σ37c and Σ3) in the high misorientation range of $46° < \theta < 60°$ revealed that they feature a unique arrangement of SUs called domino structure. Additionally, atomistic simulation demonstrated that symmetric Σ37c {1 10 11} has a higher GB energy than the Σ37c {3 4 7}. This demonstrates how differing habit planes can cause distinct symmetric segments of the same GB type to exhibit variation in their behaviors.

5.4: Interaction of Cu and Zr with the atomic structures of pure [111] tilt boundaries in Aluminum

In this section, the interaction of Cu and Zr with the pure Σ21a and Σ13b [111] tilt Al GBs is investigated in detail. Furthermore, the atomic structure of the pure and alloyed Al GBs are directly compared. The aim of this study is to understand the segregation induced transformation of the atomic structure for two different GBs. The work in this section is based on the manuscript IV.[***]

5.4.1 Introduction

As described in the **Chapter 2**, Cu is routinely utilized for strengthening the Al alloys via precipitation hardening. It has a strong segregation tendency towards Al GBs and can enhance the cohesive strength of the Al GBs that leads to an increase in the resistance to inter-granular fracture at Al GBs. Yet, in many cases, Al-Cu alloys are prone to failure due to several GB related phenomena such as intergranular corrosion, electro-migration and abnormal grain growth [15,232,233]. To overcome such problems, Zr is frequently added to the Al-Cu alloys to improve GB related properties. Generally, Al-Cu-Zr alloys are heat treated to form second phase precipitates like $CuAl_2$, Al_3Zr, etc. at the GBs, which enhances the strength of these alloys but at the same time also influences the GB behaviour like abnormal grain growth. For example: the Zener pining of the GBs by these secondary phase precipitates like $CuAl_2$ ceases the grain growth that plays an important role in controlling the behaviour and properties of GBs [14,15]. It is often found that the amount of secondary phase present at the normal GB are higher than the abnormal ones, which suggests that precipitation behaviour is different for different GB type. However, the effect of segregation of Cu and Zr solute prior to the precipitation on the local atomic structure and the properties of Al GBs is still not clearly understood. Therefore, in order to have a better understanding and control on such phenomena and for designing advanced Al alloys, it is of great interest to understand the influence of solute elements like Cu and Zr on the local atomic structure of the GBs. In the current study, we have examined the interaction of segregating elements like Cu and Zr with the atomic structures of pure Σ21a and Σ13b GBs with the help of conventional TEM,

---

[***] Based on manuscript IV by S. Ahmad, S. Evertz, J. Schneider, C. H. Liebscher and G. Dehm

aberration corrected STEM and EDS techniques. Furthermore, how these solute elements induce structural transformation at the GB is explored and their implications on the GB properties are discussed comprehensively.

5.4.2 Results and Interpretation

GB segregation behaviour: Al (Zr-Cu) film annealed at 450°C for 6 hrs

The overview plan view image along [111] direction reflecting a change in the Σ13b GB curvature is shown in **Figure 5-38**, which indicates that the GB consists of symmetric and asymmetric facets of varying length.
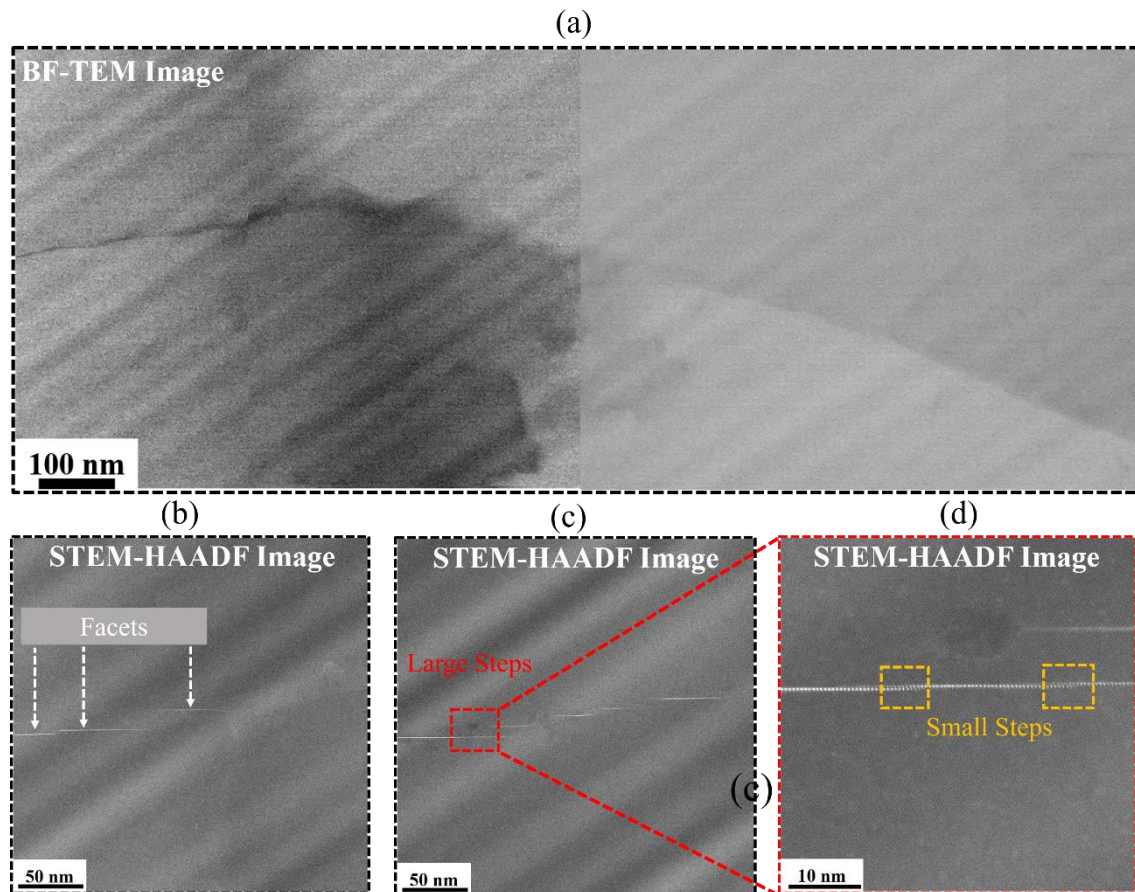
Figure 5-38: Overview STEM-HAADF images of Σ13b GB along [111] tilt direction from the Al film annealed at 450°C for 6 hr. **a)** Low magnification stacked BF-TEM images showing the overall curvature of the GB. **b) c)** and **d)** STEM-HAADF images represent that the Σ13b GB is facetted. The white dashed arrows represent the facets separated by large and small steps, marked by the orange and the red rectangles respectively. **d)** depicts the magnified view of symmetric facets, which are separated by a large step. Note that the symmetric facets are connected by asymmetric facets. These asymmetric facets are not clearly visible due to their high inclination w.r.t the electron beam.
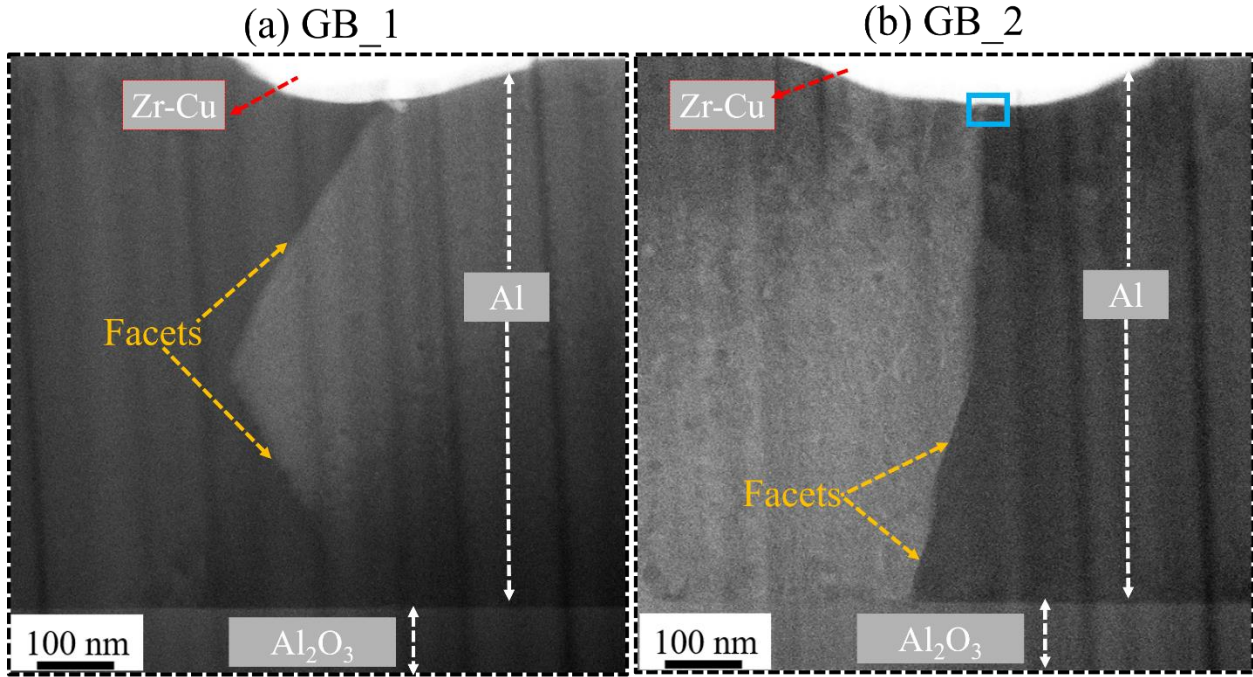
Figure 5-39: STEM-HAADF images of the cross-sectional view of the two Σ13b GBs along [110] direction. a) GB_1 **b)** GB_2. The orange rectangles indicate the presence of the facets at both the GBs. The blue inset marked in **b)** represents the HAADF image of the top region of the Al GB including the top layer of Zr-Cu.

Along the GB, a high number of steps of different size such as large and small steps, marked by red and orange rectangle in **Figure 5-38 b)** and **c)** separates these facets. Furthermore, it is found that in the straight symmetric segment, even though the Σ13b GB looks perfectly straight and edge-on at lower magnification, the GB plane is still slightly inclined. This prevents atomic resolved imaging of the GB structure. As discussed in the **Chapter 3** above, the intensity of a HAADF image is directly proportional to the atomic number (Z^2) of the elements in the specimen [152]. Therefore, the repeating bright intensity atomic columns at the GB in **Figure 5-38 c)** corresponds to a Cu segregation at the Al GB, which is further discussed in detail in the upcoming sections. Since the Al film was annealed at a high temperature of up to 450°C, it has been observed that the boundary inclination is changing and incorporating facets and steps along the GB. This is also reflected in the cross sectional STEM HAADF images of the GBs along <110> direction, as shown in **Figure 5-39 a)** and **b)**. The sapphire (Al_2O_3) substrate is present at the bottom, the Al film with a GB is positioned in the centre and the remaining Zr-Cu reservoir (~120 nm thin) after 450°C_6hrs annealing is located on the top of the surface of the Al film. The thickness of the film is now reduced to ~700 nm after Ar plasma cleaning as compared to the initial 805 nm thick film.
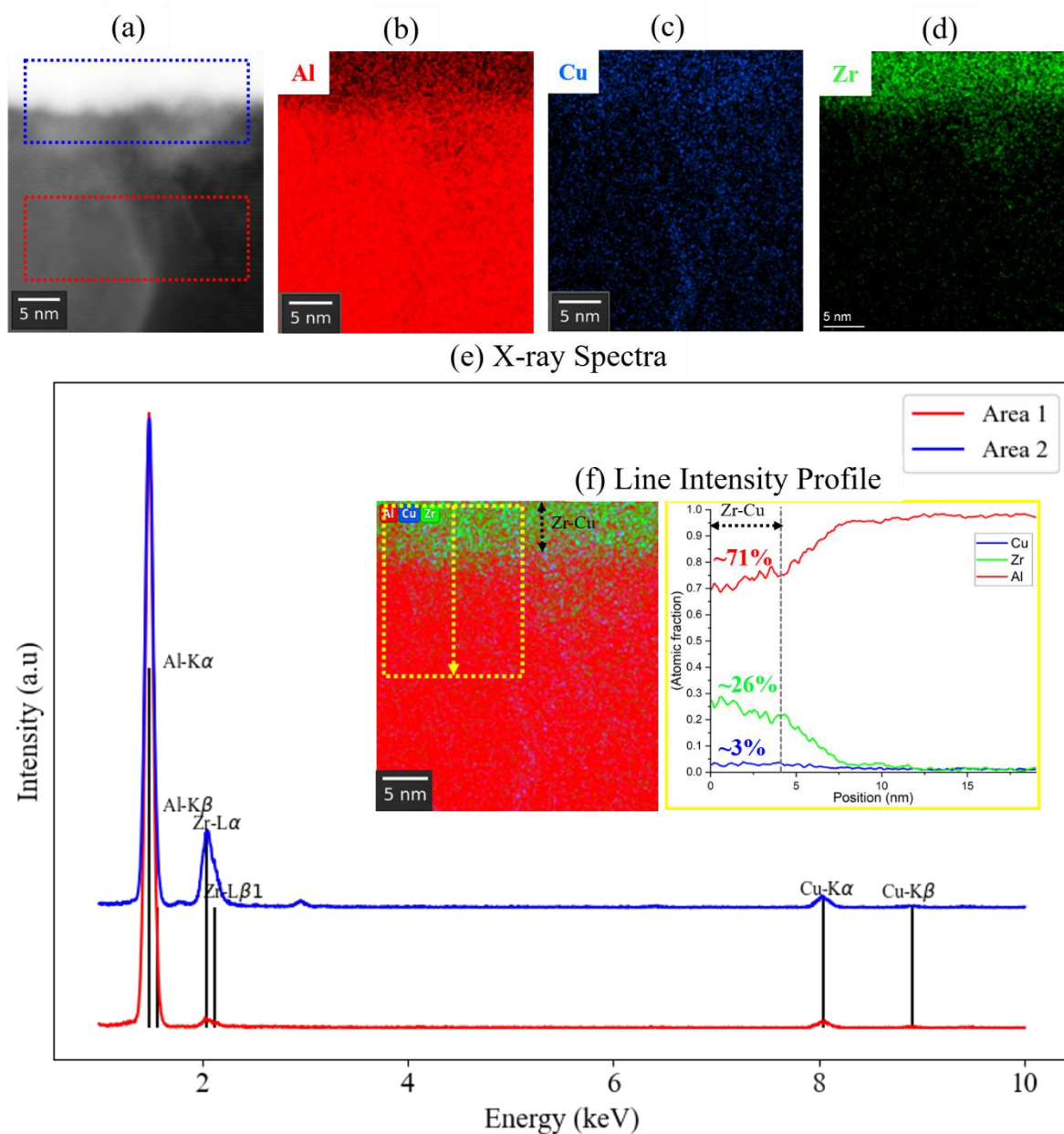
Figure 5-40: STEM-EDS measurements from the topmost region of the GB along the cross-section (<110> axis). **a)-d)** show the STEM HAADF image and the elemental maps of Al, Cu, and Zr, respectively, from the blue rectangular region marked in **Figure 5-39 b)**. **e)** STEM-EDS measurements showing two X-ray spectra that are plotted together belonging to the red and blue regions respectively, marked in **a)**. The blue region consists of both the film and a part of the Zr-Cu reservoir while the red region consist of only the Al film. Elemental maps of Al, Cu, and Zr and the intensity plot (from the blue and red rectangles) after 450°C_6hrs annealing clearly reveal that brighter contrast regions within the blue rectangle correspond to the Zr-Cu reservoir, which is formed after inter-diffusion. **f)** shows the line intensity profile across the Zr-Cu reservoir into the film revealing the composition of Cu, Zr and Al. The top layer contains ~3 at% Cu and ~26 at% Zr after annealing at 450°C for 6hrs.

The results clearly depict a very large change in GB inclination as the GB is not straight from the

bottom near the sapphire substrate to the top of the Al film. A similar kind of behaviour is also observed for the Σ21a GB, which is not shown here (see Appendix **A.3**). EDS map analysis of the top region (near the Zr-Cu/Al interface) of the cross section leads to intensity vs energy profile as shown in **Figure 5-40 e).** It is found that although, both Zr and Cu are existing as a reservoir at the top of the Al film, only Cu segregation occurred at the Al GB. This is further confirmed by the EDS from the Al film region within 100 nm next to the sapphire substrate with a straight GB segment, as depicted in **Figure 5-41**. While Cu was detected, no Zr was found at all along the GBs.
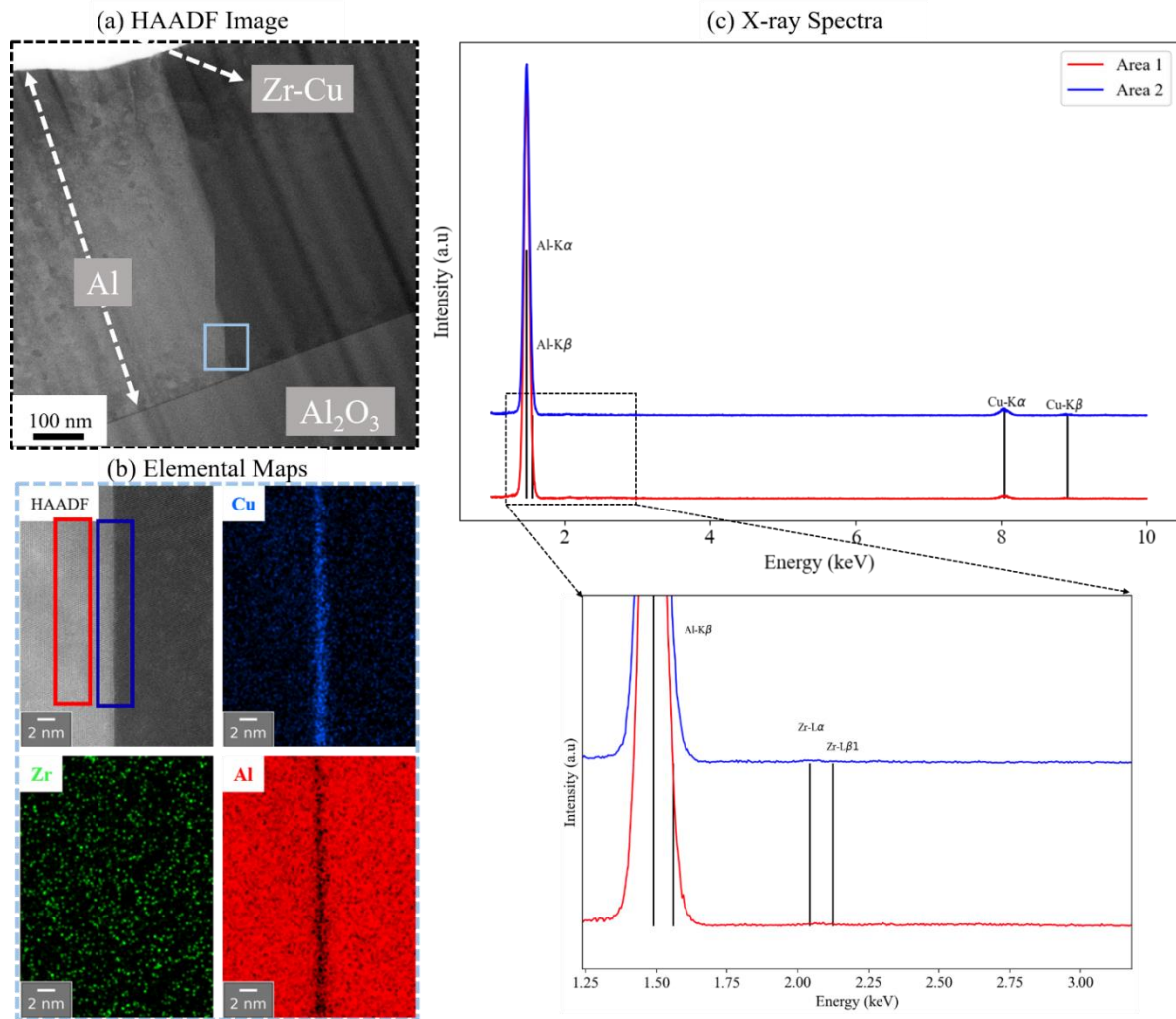
Figure 5-41: STEM-EDS measurements from the bottom of cross-section of the GB along <110> direction. a) STEM HAADF image of the Al film. **b)** STEM-EDS elemental maps, corresponding to the light blue rectangle marked at the bottom of the GB in **a),** reveal Cu segregation at the Al GB. **c)** shows the X-ray spectra belonging to the red and blue regions shown in **b)** in STEM-HAADF image of the GB**.** The magnified view of the spectra **c)** reveals that there is no Zr detected, neither in the bulk nor in the GB.

Atomic resolution imaging and chemical analysis of Cu segregated Al GBs:
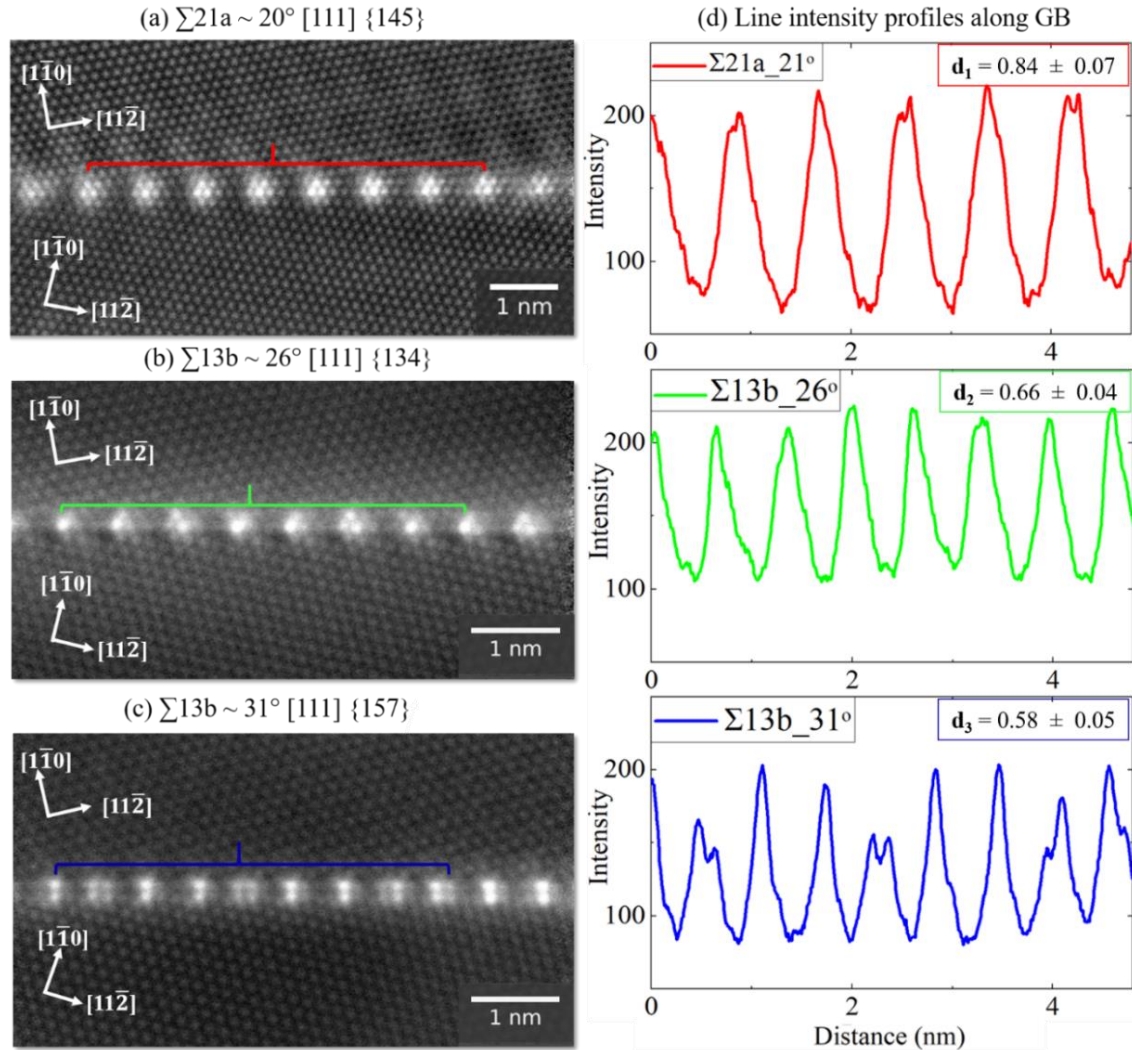
Figure 5-42: STEM-HAADF images revealing the atomic structures. a) Σ21a (20°) GB b) Σ13b (26°) and c) Σ13b (31°) GBs along [111] direction. d) Line intensity profile along all the three GBs. The red, green and blue region marked in a)-c) correspond to the length of the GB from which the line profile has been taken.

The transformation in the atomic structure of Σ21a and Σ13b GBs upon segregation is reflected in its corresponding STEM-HAADF images in **Figure 5-42 a)-c)**. The results indicated that all three GBs are atomically straight consisting of bright spots with varying image contrasts at the GB. The low contrast spots at the GB and within the grain interior indicate pure Al atomic columns while the brighter spots depict the Al atomic columns containing the segregating elements. According to the Brandon criteria, both the GBs in the **Figure 5-42 b)** and **c),** despite exhibiting the same GB type (Σ13b), have different segregation induced structural transformation termed as monolayer and

bilayer type segregation, respectively. However, it is important to take into account that both the GBs have still a quite significant difference in the misorientation angle (5°) and the GB plane (5°), which might influence the segregation behaviour.
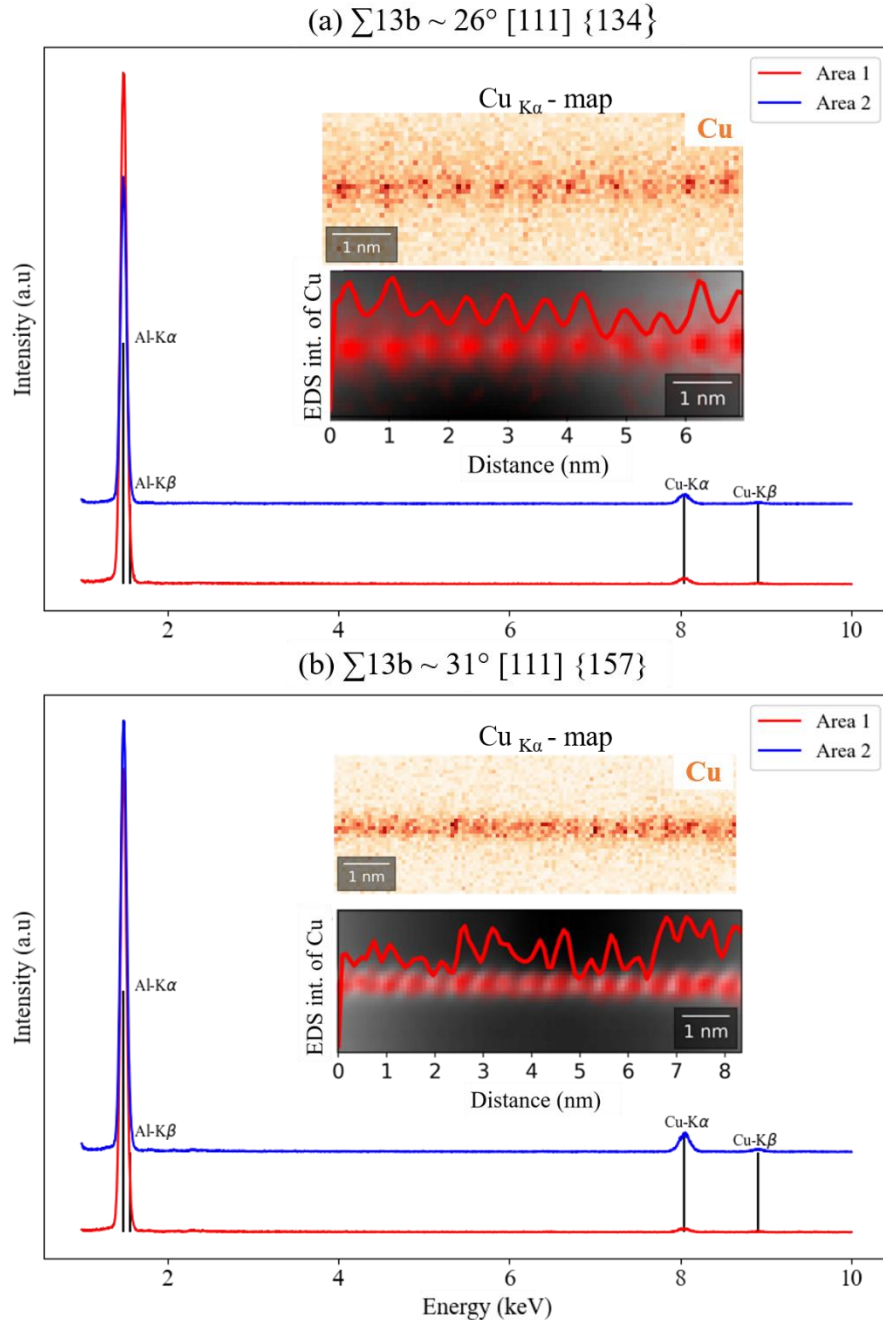
Figure 5-43: STEM-EDS measurements at 120 keV results from a) Σ13b (26°) and **b)** Σ13b (31°) GBs along [111] direction**.** Each diagram contains two X-ray spectra that are plotted together belonging to the red (matrix) and green (GB) regions respectively, marked in the inset. EDS spectra from the GB containing area clearly show that the bright spots in the HAADF image correspond to the Cu segregation at the GB. No Zr peak is present in any of the spectra. The EDS $Cu_{K\alpha}$ map shows highest Cu concentration at specific GB positions.

The line profiles extracted along the GBs are summarized in **Figure 5-42 d)**, which shows that the corresponding average distance between the bright segregated spots is decreasing with the increasing misorientation angle. This suggests a tendency of increased segregation with an increase in misorientation angle. Furthermore, we have also performed atomic resolution EDS of the Σ13b GBs in order to analyse the chemical identity of the brighter atoms at the GB. A comparison of the HAADF image with EDS map as shown in **Figure 5-43**, determine the bright spots as Cu rich atomic columns. The absence of Zr peaks in the X-ray spectra shows that none of the GBs exhibit Zr segregation, in agreement with the cross-sectional studies of the GB (**Figure 5-41**).

Comparison of pure and Cu segregated Σ21a and Σ13b Al GBs
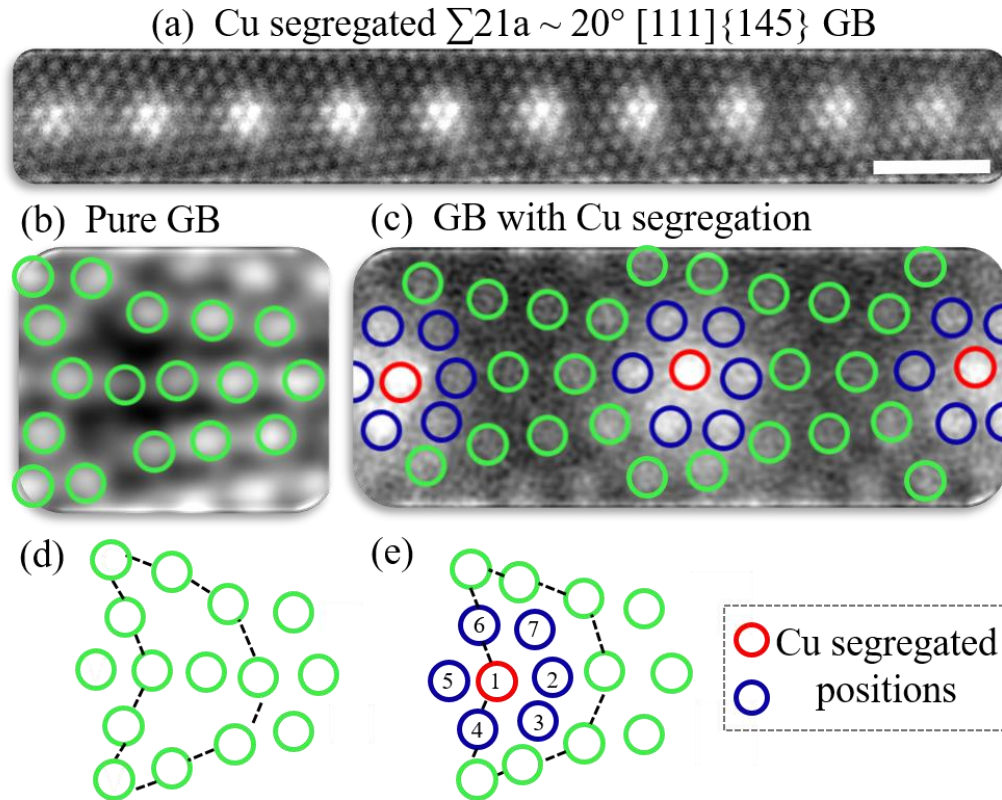
Figure 5-44: Comparison of pure and alloyed Σ21a [111] Al GBs. a) overview of the Cu segregated Σ21a (~20°) [111] Al GB. There is a **1 nm** scale bar in **a)**. **b)** and **d)** depict the structural unit of the pure Σ21a GB. The structural unit of the alloyed Σ21a GB is displayed in **c)** and **e)**. Blue and red circles with numbers 1 to 7 marked in **c)** indicate the positions of the Cu-segregated atomic columns, while empty green colored circles represent the pure Al atomic columns. No atomic column was present in positions 3 and 7 in the pure Σ21a SU, but in the alloyed SUs, they may be entirely pure Al or contain some Cu.

116

In order to have a deeper understanding of the pure and alloyed Σ21a Al GBs, their structural units are compared along [111] direction, as depicted in **Figure 5-44**. The pure Al GB structure in **Figure 5-44 b)** consists of bow and arrow shaped structural units reported earlier in **Chapter 5.2**.

On closely inspecting the structural units of the alloyed Al GB, it is found that the outer atomic arrangement of the alloyed and pure Al SU remain the same. However, some of the atomic columns in the alloyed one are segregated with Cu from position 1 to 7, as highlighted by red and blue circles in **Figure 5-44 c)**.

Furthermore, the alloyed SUs become denser as two more atomic columns are incorporated at the position 3 and 7 (see **Figure 5-44 c)**), in contrast to pure Al SU. The two different colored red and blue circle in **Figure 5-44 c)** signify a high and low content of Cu segregation of the atomic columns. It is important to note that although the position 3 and 7 possess the highest volume in the pure SUs, yet the most intense bright Cu spot in the alloyed SU is on the central position 1. This reveals that the extra volume does not solely decide the segregation tendency. Furthermore, it is important to consider that the low contrast corresponding to blue colored sites could also occur due to the effect of probe de-channeling, which depends on the orientation and thickness of the specimen [234]. The dynamic scattering in the thicker sample may lead to an extension of the probe intensity from one atomic column to the neighboring atomic columns and hence the contrast can go back and forth among the columns.

Similarly, the structural units of pure and alloyed Σ13b (~26°) Al GBs are compared along the [111] direction, as shown in **Figure 5-45**. Even though both the GBs belong to Σ13b (~26°) (according to the Brandon criteria), yet two completely different kind of segregated units are found in the Cu segregated GBs (see **Figure 5-45 a)** and **b)**). A detailed investigation of the SUs of the Σ13b (~26°) GB with Cu revealed that it has a similar bow and arrow shape as in the pure Al GB, however few of the atomic columns are segregated with Cu like for the Σ21a GB. Position 1 to 8 represents the Cu segregated units, as highlighted by red and blue circles in **Figure 5-45 d)**. However, the most intense bright Cu atomic column belongs to position 1, similar to alloyed Σ21a GB. Hence, the segregation behaviour in the case of Σ21a and Σ13b (~26°) is referred to as monolayer type segregation, supported by the fact that the average spacing between the Cu segregated units is the same as that of the CSL spacing, based on the assumption that only the CSL sites lie exactly at the GB. Conversely, the atomic structure of alloyed Σ13b (~31°) in **Figure 5-45 e)** shows that the

117

SUs is completely different from the bow and arrow structures and consists of a total of 8 atomic columns. Here, instead of one, there are two most intense (bright) Cu atomic columns present at the GB, indicated by positions 1 and 2 (in the red coloured circle), parallel to each other. Hence, the segregation behaviour here is termed as parallel line segregation.
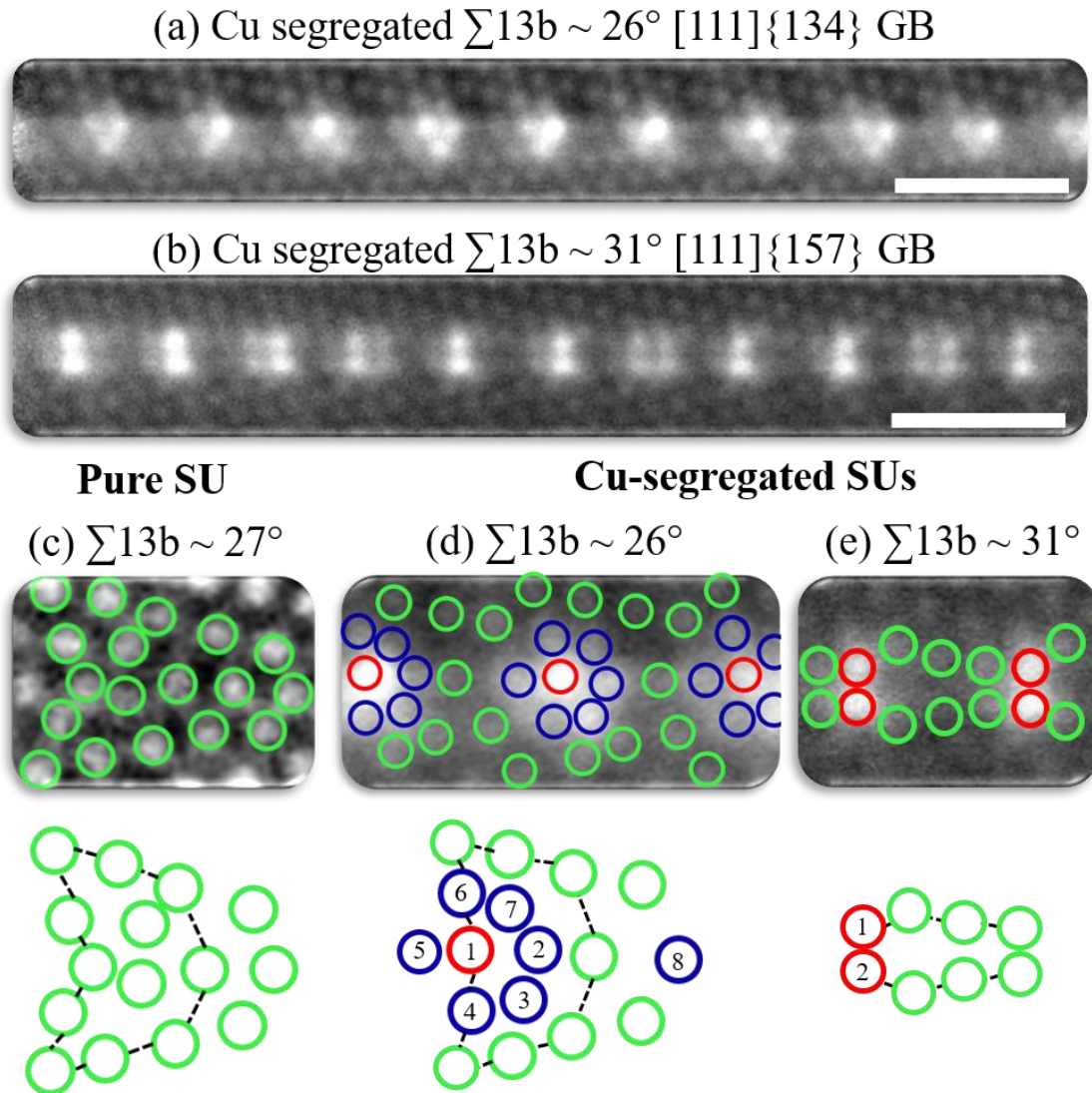
Figure 5-45: Comparison of pure and alloyed Σ13b [111] Al GBs. a) and **b)** represent the overview images of the Cu segregated Σ13b (~26°) and Σ13b (~31°) Al GBs, respectively. The scale bar corresponds to **1 nm** in **a)** and **b)**. **c)** Structural unit of pure Σ13b GB while **d)** and **e)** represents the structural unit of alloyed segregated Σ13b (~26°) and Σ13b (~31°) GBs, respectively. Blue and red circles with numbers 1 to 8 marked in **d)** and **e)** indicate the positions of the Cu-segregated atomic columns while empty green colored circles represent the pure Al atomic columns. **d)** and **e)** represent monolayer and bilayer segregation.

GB segregation behaviour: Al (Zr-Cu) film annealed at 520°C for 32 hrs

So far, we have seen that on annealing the film to 450°C for 6 hrs, we have only Cu segregation at the GBs, which is leading to a change in the atomic structure of a GB i.e. a chemically induced phase transitions of the GBs. Furthermore, in order to diffuse Zr into the Al GBs, the alloyed Al film is annealed to 520°C for 32 hrs.
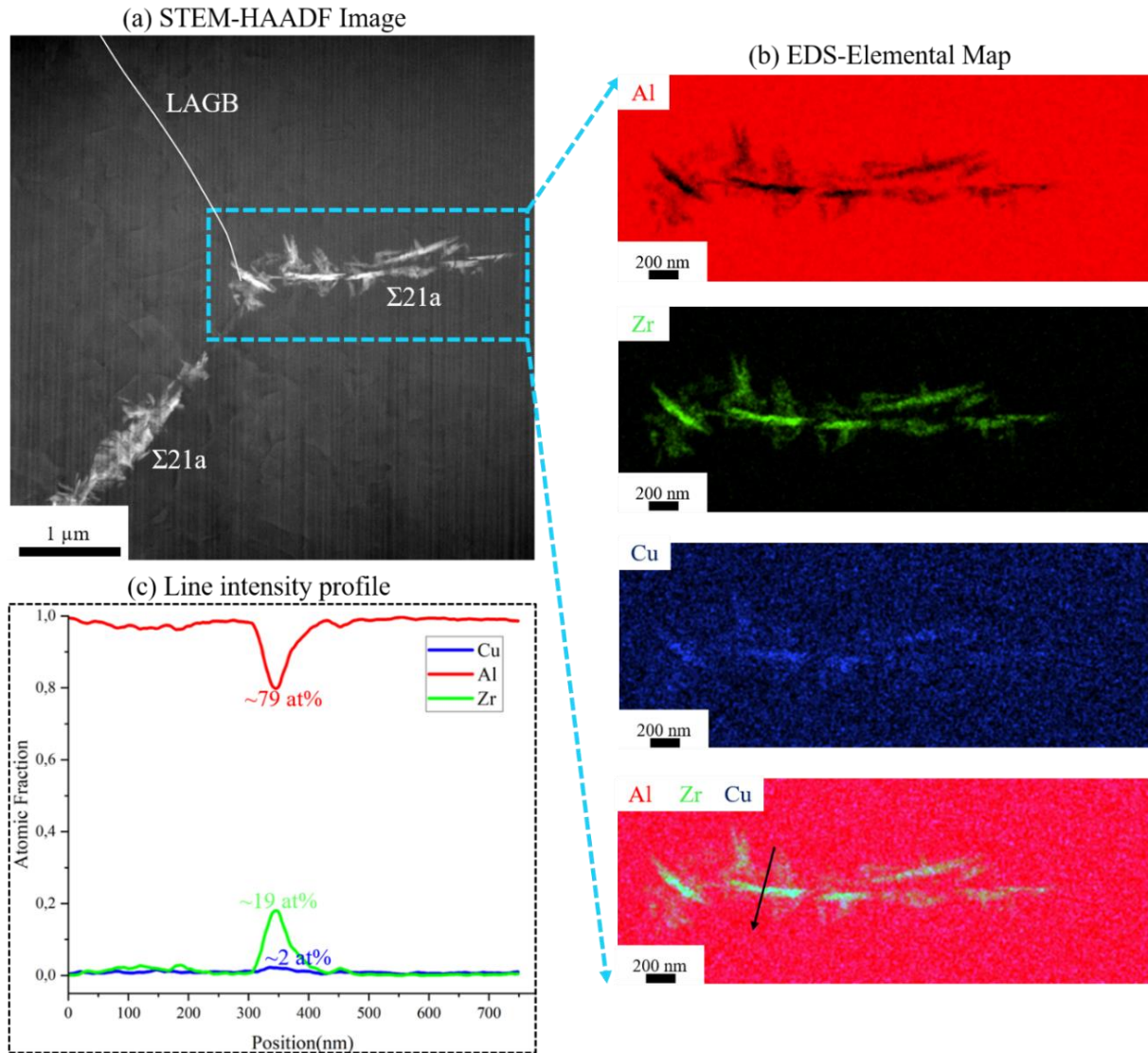
Figure 5-46: STEM HAADF and EDS measurements from the GBs annealed at 520°C for 32 hrs. a) STEM-HAADF image showing a triple junction comprising of one low angle GBs and two Σ21a GBs. **b)** STEM EDS elemental maps from the region consisting of needle shaped precipitates at the Σ21a GB, marked by a blue rectangle in **a)**. **c)** Line intensity profile across the precipitate, indicated by black arrow in **b)** shows that it consists of Al, Zr and Cu with atom percent of ~79, ~19, and ~2, respectively.

(a) BF-TEM Image

(b) Diffraction Pattern

(c) Dark-Field Images
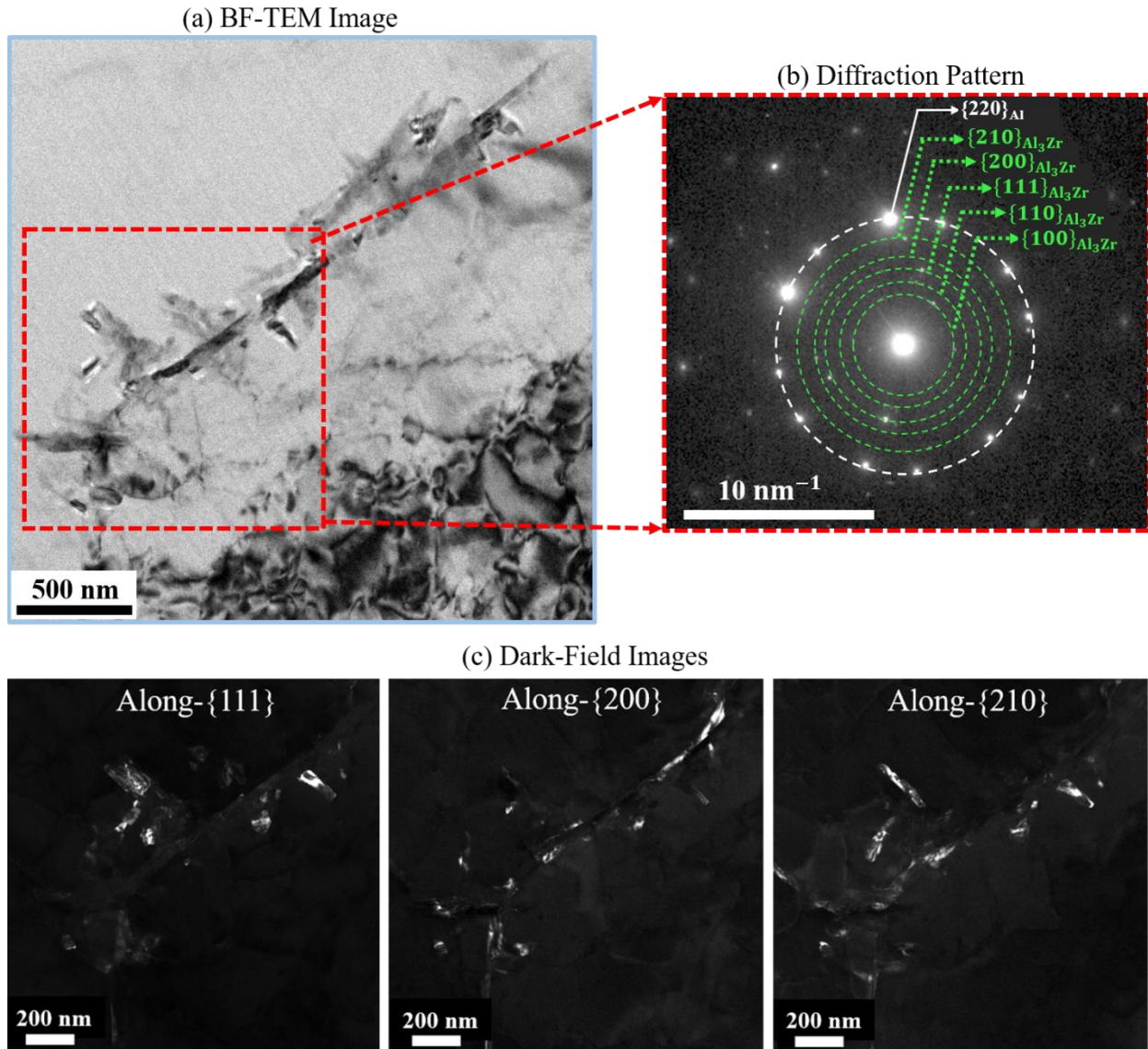
Figure 5-47: TEM investigation of Σ21a GB annealed at 520ºC for 32 hrs. a) represents a BF-TEM micrograph of the Σ21a GB decorated with needle shaped precipitates. Unlike in STEM, the precipitates here appear dark in the BF-TEM image due to the diffraction contrast. **b)** displays the diffraction pattern from the red region marked by a red rectangle in **a)** showing diffraction spots corresponding to [111] Al zone axis with some extra diffraction spots. These extra spots correspond to the Al_3Zr phase having $L1_2$ structure. **c)** shows the dark-field images along {111}, {200} and {210} planes. The bright region in these dark field images confirms that these precipitates belong to the Al_3Zr phase.

The results of the S/TEM investigation of a plane-view lamella consisting of a LAGBs and two Σ21a GBs are summarized in **Figure 5-46** and **Figure 5-47**. The STEM-HAADF image in **Figure 5-46 a)** reveals the presence of bright needle shaped precipitates, only at the Σ21a GBs. However, no such precipitates are found in LAGBs. In order to find out the composition of the secondary phase

120

precipitates, STEM EDS was performed on the Σ21a GB (see **Figure 5-46 b)** and **c))**. The STEM-EDS elemental maps of Al, Cu and Zr taken from the blue region of **Figure 5-46 a)** are illustrated in **Figure 5-46 b).** The EDS maps clearly depict that the GB is decorated with the secondary phase precipitates, consisting mostly of Al and Zr. The line intensity profile across the precipitate corresponding to a black arrow in **Figure 5-46 b)** is shown in **Figure 5-46 c),** which reveals that the precipitate comprises of ~79 at% Al, followed by ~19 at% Zr and ~2 at% Cu, which is close to the composition of Al_3Zr phase.

The quantified values of the concentration from EDS are highly sensitive to the thickness of the precipitates w.r.t the thickness of the TEM specimen. Thus, in order to identify the phase unambiguously, we have performed diffraction analysis via conventional TEM as depicted in **Figure 5-47**.

The BF-TEM image of the needle shaped precipitates at Σ21a GB is shown in **Figure 5-47 a)**, which looks darker than the Al matrix due to the diffraction contrast. The diffraction pattern corresponding to the red region in **Figure 5-47 a)** is illustrated in **Figure 5-47 b)**, which shows that apart from the diffraction spots associated with [111] Al zone axis, there are also some extra diffraction spots present. Indexing of these extra spots (marked by green circles) reveals that they correspond to the $L1_2$ Al_3Zr phase (metastable), having a cubic structure [235]. Additionally, the dark field images taken from these extra spots of Al_3Zr confirm that these needle shaped precipitates belong to the Al_3Zr cubic phase.

5.4.3 Discussion

Segregation behaviour: Al (Zr-Cu) film annealed at 450°C for 6 hrs

In the current study, the effect of segregating elements like Cu and Zr on the pure Al GBs is discussed. On annealing the Al (Zr-Cu) film to 450°C for 6 hrs, the STEM investigations revealed that there was no native oxide present on the top of the Ar-sputtered clean film, which was present in the Al film without plasma cleaning. Hence, the absence of the native oxide on Al surface allowed diffusion of Cu into the GB during annealing. This is because the native Al_2O_3 in the uncleaned surface (with oxide) was acting as a barrier to the surface diffusion of the solute elements [236,237]. The effect of segregation is seen as a change in GB curvature and inclination, observed along <111> and <110> directions. It is important to note that despite annealing to such

a high temperature of 450°C for Al, no precipitates of Al-Cu are formed, as the solubility of Cu is quite high. This happened due to a lower concentration (~3 at.%) of Cu in the Zr-Cu reservoir present on the top of the Al film. On closely investigating the GBs via STEM-EDS along both <111> and <110>, it is evident that only Cu is segregating to the GBs. This is because of the high solid solubility for Cu of 2.5 at.% at 550°C compared to only 0.083 at.% Zr at 660°C [238,239]. Furthermore, the diffusivity (D) of Cu ($D_{\text{Cu at 500°C}} = 4.0 \times 10^{-14} \, m^2 s^{-1}$) into the Al is also very high as compared to that of Zr ($D_{\text{Zr at 500°C}} = 3.2 \times 10^{-18} \, m^2 s^{-1}$) [240]. It is important to take into account that the diffusivity values reported here correspond to bulk diffusion. Hence, the diffusion at the GB will be higher but a similar ratio for $\frac{D_{Cu}}{D_{Zr}}$ should be present as well for GB diffusion.

The findings suggest that as the temperature reaches to 450°C, Cu solubility and the rate of diffusion increases, hence, Cu starts diffusing into both the GBs and the grain interior. However, as the film is cooled down slowly, Cu solubility decreases, which led to the segregation of Cu at the GBs. It is often found that the low solubility of an element leads to a pronounced segregation of the solute at the GB [241], which reduces the overall energy of the system. Furthermore, it is reported in the literature that Zr can easily diffuse into the Cu GBs on annealing at 400°C for 5 hr [25]. Since, Zr has very similar diffusivity into the Cu and Al, similar behavior can be expected in the case of Al. Hence, the findings clearly indicate that Cu prevents the diffusion and segregation of Zr into the GBs.

Atomic-scale investigation of Σ21a and Σ13b GBs annealed at 450°C for 6 hrs

Furthermore, a comprehensive investigation of the influence of the solutes (Cu and Zr) on the local atomic arrangement at the Σ21a and Σ13b GBs in STEM revealed that there exist two different kinds of segregation behaviour at the GBs called monolayer and bilayer type segregation, having single and two parallel intense bright Cu segregated atomic columns, respectively. A similar kind of Cu segregation behaviour depending on the misorientation was found in an interesting study done by Prakash and coworkers in 7075 Al Alloy (with Al 96.77%, Zn 0.15%, Mg 1.47%, Cu 1.13%, Si 0.5%) [125]. It is interesting to note that even though both Mg ($D_{\text{Mg at 500°C}} = 9.9 \times 10^{-14} \, m^2 s^{-1}$) and Zn ($D_{\text{Zn at 500°C}} = 1.8 \times 10^{-13} \, m^2 s^{-1}$) have even much higher diffusivity than Cu in Al, yet only Cu segregation was found at the GBs [125,240]. Therefore, in a multi-

component system like 7075 Alloy, the influence of other alloying elements having high diffusivities and the different GB misorientations and planes on the occurrence of such segregation behaviour cannot be disregarded.

We, therefore, compared the structural units of Cu alloyed Σ21a (~20°) {145}, Σ13b (~26°) {134} and Σ13b (~31°) {157} GBs with the pure atomic structure of Σ21a and Σ13b. We found that for Σ21a (~20°) {145}, Σ13b (~26°) {134}, the overall shape of the SUs remain the same as in the pure Al case, yet some specific atomic columns are now enriched with Cu. This depicts that most amount of the Cu is segregating at the substitutional positions followed by the lower amount of Cu at the interstitial positions. Some uncertainties in interpretation arises due to the de-channeling of the probe in STEM. To rule out de-channeling, image simulations would be required. Nevertheless, it seems that segregation energy for these substitutional sites is lower than the other sites. However, to confirm this, atomistic simulation studies are needed to evaluate the segregation energy for the specific sites of the GBs. Furthermore, in the case of Σ13b (~31°) {157}, a completely new structural unit with eight atomic columns emerged at the GB, with the two most intensely bright atomic columns enriched with Cu, indicating bilayer type segregation. Furthermore, on extracting an intensity line profile along the GB, it is found that the distance between the Cu-enriched regions follows the same trend as in Ref. [125] i.e. decreases with an increase in the misorientation, which suggests that the segregation tendency is also increasing. This is further supported by the EDS, which shows that the ratio of Cu concentration at the GB to the grain $\frac{Cu_{(GB)}}{Cu_{(Grain)}}$ is roughly twice as high for the Σ13b (~31°) GB as compared to the Σ13b (~26°) GB (see Appendix **A.2**).

Furthermore, it is also important to take into account that apart from the misorientation angle, the GB planes are also different for both Σ13b GBs. One of the reasons for differences in segregation patterns could be the different atomic densities in the two different symmetric planes. At 31° misorientation, since all the CSL sites are completely saturated with Cu, Cu started segregating to the sites at the nearest neighbouring atomic planes, inducing a structural transformation of the GB.

Segregation behaviour: Al (Zr-Cu) film annealed at 520°C for 32 hrs

As discussed above, no Zr is found anywhere at any of the GBs at 450°C, the same Al film is further annealed to 520°C for 32 hrs in order to increase the diffusion rate of Zr into the GBs.

During the TEM investigation, it is found that the 95% of the GBs (including LAGBs) were not edge on anymore. This is due to the strong faceting that happened during high-temperature annealing, which leads to the higher inclination of the GB plane. Furthermore, a detailed conventional TEM and STEM-EDS analysis revealed that certain needle shaped precipitates formed at some regions of the high angle Σ21a GB and have composition of ~79 at.% of Al, ~19 at.% of Zr and ~2 at.% of Cu. This is quite close to the intermetallic Al_3Zr phase composition i.e. 75 at.% of Al, 25 at.% of Zr. While at very few symmetric edge-on regions of the Σ21a GB, we found only monolayer kind of segregation of Cu similarly to the GBs annealed at 450°C. Furthermore, diffraction pattern analysis of the needle shaped precipitates confirmed that Al_3Zr phase have the cubic $L1_2$ (metastable) structure, which is often found in the form of fine and stable precipitates in Al (Zr-Cu) alloys and enhances their properties [242]. These cubic $L1_2$ phase precipitates have very high resistance to coarsening, even at very high temperatures. Generally, the Al_3Zr intermetallic phase has tetragonal DO_{23} equilibrium structure, however it is also found as a cubic $L1_2$ metastable structure, formed via rapid cooling [243,244]. Moreover, this metastable phase can also be stabilized at lower temperatures by minor additions of certain elements like Cu, Li, Ni and Fe, etc. in the Al alloys [245,246]. For example: small amount of Cu additions in the Al-Zr system can accelerates the precipitation of cubic $L1_2$ (metastable) Al_3Zr phase during annealing [49,247]. The major reason for the occurrence of this cubic Al_3Zr phase is associated with the similarity in its structure to the fcc Al and the lower lattice mismatch between the Al_3Zr intermetallic phase and Al [248]. The lattice parameter of the Al_3Zr phase is 4.08 Å [244], which is very similar to that of Al in 4.05 Å [249]. The results at 520°C annealing indicate that Cu diffusion is accelerating into both GBs and the bulk in comparison to 450°C. Therefore, some of the pre-segregated Cu present at the GB may have also started diffusing from the GB to the grain interior, thus, providing a pathway for Zr diffusion into the GBs. This together with the accelerated diffusion of Cu from the top reservoir to the GBs and inter-diffusion of Cu and Zr led to the nucleation of $Al_3(Cu_xZr_{(1-x)})$ precipitates.

5.4.4 Summary and Conclusion

In this research, interaction of the alloying elements i.e. Cu and Zr with the pure [111] tilt GBs in Al is investigated with the help of CTEM and aberration corrected STEM techniques in combination with STEM EDS. The main findings of the study are as follows:

On annealing an Al film at 450°C for 6 hrs with a Zr-Cu reservoir on the Al film surface, it is observed that the inclination of the GBs is changed as compared to the pure GBs. Additionally, we found Cu as the primary segregating element, which is being enriched on all type of GBs up to Σ13b (having a misorientation of 31°, experimentally) with two discrete segregation pattern called monolayer and bilayer segregation. Furthermore, the segregation tendency increases with misorientation, as observed for GB misorientation angles ranging from 20° to 31°. However, no Zr segregation was discerned at the GBs after annealing at 450°C. On further annealing the GBs to 520°C for 32 hrs, it is observed that Zr does not like to segregate onto the pre Cu-segregated GBs. Instead of that, needle shaped precipitates are formed at high angle GBs like Σ21a. The precipitates belong to the $Al_3(Cu_xZr_{(1-x)})$ (metastable) phase with $L1_2$ cubic structure. It's nucleation is highly influenced by the pre-segregation of Cu at the GBs. We believe that this study improves our understanding on the competition of segregation behavior of Cu and Zr at pure Al GBs on an atomic scale, which may be helpful in future to design novel Al alloys via GB segregation engineering. Additionally, it advances our knowledge of how to trigger specific precipitates at the GBs in order to prevent grain growth in the material.

Chapter 6 Summary and Conclusion

The focus of the present thesis is a comprehensive study of atomic structures of several types of [111] tilt GBs in pure Al and Zr/Cu alloyed Al by using mainly aberration-corrected S/TEM and its analytical technique EDS. Furthermore, the current studies attempts to bridge the gap in understanding the atomic structures and properties of the GBs, with the help of atomistic simulations.

Firstly, in order to get a wide distribution of [111] tilt columnar Al GBs, pure Al thin films were grown on sapphire oriented along (0001) direction that results in strongly [111] textured film having desired features that includes smooth and dense surface, large grain size (>10 μm) and film thickness of greater than 600 nm. A closer investigation of the structure evolution of the Al films via scanning and transmission electron microscopy techniques revealed that for a deposition rate of 3 Å/s, the optimum deposition temperature to obtain such [111] tilt GBs should be close or greater than 300°C. At this temperature of ~0.6 T_m, all diffusion mechanisms in the films are active, including bulk diffusion. Furthermore, the experimentally observed atomic structure of three different low angle tilt GBs in Al revealed that in contrast to the bulk, the dissociation of ½ [110] perfect edge dislocations into two partials of <211> type occurs at GBs, irrespective of the high SFE in Al. Additionally, it is found that the distances between the two partials along the GB and perpendicular to GB are different to each other. Both of them decreases in distance with an increase in the misorientation angle. Along the GB, the spacing follows Frank's rules relating misorientation angle and Burgers vector with dislocation spacing. The formation of these partial dislocations at the low angle GBs could play a vital role in the mechanical and physical properties of the material such as GB phase transformation and during plastic deformation via dislocation motion of dissociated dislocations. Additionally, grain growth in a material will also be impacted because GB migration frequently involves dislocations and occurs via steps or disconnections. Hence, the influence of these partial dislocations on all these phenomena needs to be further understood in detail in order to control and improve the mechanical properties of the material.

Furthermore, since the GBs with the fixed macroscopic parameters may also behave differently in reality due to the microscopic translations at the atomic level, hence, we have further examined how these infinitesimal translations of the atoms influence the atomic structure and properties of

the GB. For the investigation of the structure multiplicity and structural defects in incoherent $\Sigma 3$ [111] ($11\bar{2}$) tilt GBs, aberration corrected STEM techniques were utilized. Two distinct microstates, |E| and |E'|, of the GB structure were found for two different ORs, present in an Al film. Simulation studies predicted that these states transform into each other with applied stress or strain of 0.5% and possess different excess volume of the microstates. |E| motifs were associated with GBs with ORI and |E'| motifs with ORII. This suggests that these microstates are the result of different strain states due to different local stress states present at the interfaces. In addition, the atomic structures of both the GBs along <110> zone axis were investigated in detail, which reveals the different magnitudes of translation of {111} planes across the whole GB from the bottom near the substrate up to the surface of the Al film, for both ORs. Furthermore, the asymmetric variants of the GBs at the two ORs was found to introduce different types and density of facets. In case of $\Sigma 3$ from ORI, GB consists of long facets separated by small steps with a single step height of typically 0.3 nm (i.e. $h = 2a_{dsc}$). However, $\Sigma 3$ from ORII comprises of a large number of facets incorporating different kind of disconnections with varying step height. The ORII GB possesses two different types of disconnections with Burgers vector $1/6[\bar{1}\bar{1}2]$ and step height $h = 2a_{dsc}$ and $5a_{dsc}$. Furthermore, in ORII, another distinct type of disconnection with Burgers vector $1/2[\bar{1}01]$ and varying step heights were found in contrast to the absence of such disconnections in ORI. These findings suggests the possibility of a lower migration rate in ORI in comparison to ORII (where more than one type of disconnections are observed). This is often observed in general during the annealing experiments of Al thin films with two ORs. Hence, the local stresses in the film even after global relaxation of the Al film may give rise to a different atomic structure to the same GB, which in turn affect the behaviour of GBs during microstructural evolution.

Thereafter, a detailed systematic study of the atomic structure of [111] tilt high angle GBs in Al was done in order to establish the relationship between the structures of various high angle GBs throughout a misorientation (θ) range (21° to 60°) for a particular tilt axis i.e. [111] and the boundary plane were inspected. Detailed STEM investigations revealed two different misorientation groups (group 1 and 2), consisting of two distinct types of structural units (SUs), respectively. The $\Sigma 21a$, $\Sigma 13b$ and $\Sigma 7$ CSL GBs belong to group 1 with the misorientation range $21° < \theta < 34°$ and have either bow and arrow shaped SUs designated as B/B' or a mix of B/B' and A units. All the structures in group 1 are called ''bow and arrow'' type structure. While $\Sigma 19b$,

Σ37c and Σ3 GBs are associated with group 2 with a misorientation range of $46° < \theta < 60°$. They comprise either square shaped units (E, E'') or a combination of E units and trapezoidal F shape unit. The atomic structure of GBs in group 2 have ''zipper'' type structure. Furthermore, it was also found that as the misorientation is increased, the number of A type units consisting of three atomic columns (in the projection view) are reduced at the GBs. A similar trend was found in the atomistic simulations, where the frequency of A type units were decreasing with misorientation and eventually diminishing at ideal Σ7 misorientation. This led to a change in the excess properties of the GBs, which eventually controls the overall behaviour of the boundaries such as GB mobility, GB diffusion and GB sliding. For example: the GB sliding is highly dependent on the atomic shuffling at the GB, which in turn is controlled by the atomic structure of the GB.

In addition, the atomic structures of the symmetric variants of all the three GBs in higher misorientation range revealed that they have a different combination of SUs i.e. domino type of structures and hence exhibit different interfacial properties, as indicated by the atomistic simulation. From these results, it was possible to establish a correlation between the structure and the properties of several [111] tilt high angle GBs in Al, as the GB misorientation and the habit plane changes. Although, we are little far from tailoring these structures yet, but one could work out by closely analyzing the response of these experimentally observed GBs towards stress and different temperature i.e. normal GB motion and shear couples GB migration, which will further enhance our understanding of how they behave in reality.

As we know that, the introduction of alloying elements into the material influences the cohesive strength of the GBs in the material, which eventually affect its creep and fatigue resistance. Moreover, solute segregated GBs are more prone to have suppressed GB migration due to the pinning of the GBs via solute element. Thus, in the last part of the thesis, how the alloying elements like Cu and Zr interacted with the pure Al GBs and influence their atomic structures were explored. For that, firstly, the native oxide on the top of a pure Al film was removed via Ar-cleaning in the sputtering chamber. Furthermore, a (Zr-Cu) reservoir was deposited on the top of the Al film via sputtering and then annealed together in two different steps. After first annealing to 450°C for 6 hrs, it is discovered that GBs start to curve and facet across the film thickness and become decorated with Cu. Interestingly, Cu was determined to be the only element segregating to the Al GBs (up to Σ13b) with no Zr observed. Two distinct types of segregation patterns, called

monolayer and bilayer type segregation, were found, which are influenced by the misorientation angle. Cu segregation was observed with monolayer segregation at misorientation angle of $\leq 26°$ and bilayer segregation at a misorientation of $31°$. As the measured distance between the Cu segregated column positions was found to be decreasing with increase in the misorientation, it suggests that the segregation tendency increases with the increasing in misorientation from $20°$ up to $31°$. The absence of Zr suggests that its segregation is affected by the preferred segregation of Cu at the GB, which limits the diffusion of Zr. Furthermore, the results obtained after second time annealing the film to $520°C$ for 32 hrs revealed that that both Zr and Cu diffusion were taking place. However, instead of segregation, needle shaped precipitates formed at the high angle GBs. The precipitates correspond to the $Al_3 (Cu_xZr_{(1-x)})$ (metastable) phase possessing a cubic $L1_2$ structure. These findings indicate that the inter-diffusion of Zr and Cu together with the diffusion of pre segregated Cu at the GBs increases the probability of nucleation of Al_3Zr precipitates at $520°C$. Hence, in the future, it would be interesting to look into the segregation of pure Zr (without any Cu) into the GBs and understand its implications on the atomic structure and properties of the GBs, which would further advance our knowledge on the atomistic mechanism of segregation.

Chapter 7 Appendix

Appendix A.1 Validation and comparison of EAM potentials[†††]

The validity of the predictions of the atomistic computer simulations depends on the interatomic potential. We compared three different embedded atom method (EAM) potentials for Al [176,250,251]: Mishin et al. (1999), Liu et al. (2004), and Mendelev et al. (2008). For each potential, the lattice constant and cohesive energy at 0 K were calculated. Then, we performed the γ-surface search as described in the methods section.

Table 6: The theoretical values of different excess properties at $T = 0$, $\sigma = 0$, and $\varepsilon = 0$ for different potentials and DFT calculations are listed. Here, a and E_{coh} are the fcc lattice constant and cohesive energy; γ_0, [V], [τ_{ji}] represent the GB energy, excess volume and GB stress tensor values, where (i, j = 1,2). The angle α is defined in **Figure 5-12**. [B_1] and [B_2] are the components of the microscopic translation vector between the two crystallites in the GB plane.

	DFT	Mishin et al. (1999)	Liu et al. (2004)	Mendelev et al. (2008)	
a	4.040	4.050	4.032	4.045	Å
E_{coh}	-	−3.36	−3.36	−3.41	eV/atom
motif	|E|	|E|	|E'|	|E|	
γ_o	0.390	0.355	0.322	0.418	J/m²
[V]	0.258	0.288	0.480	0.414	Å
α	151°	151°	126°	143°	
[B_1]	±0.350	±0.351	±0.780	±0.266	Å
[B_1]·$\sqrt{3}$/a	±0.150	±0.150	±0.335	±0.114	
[B_2]	±1.428	±1.432	±1.426	±1.430	Å
[B_2]·$\sqrt{2}$/a	±0.5	±0.5	±0.5	±0.5	
[τ_{11}]	-	0.94	1.85	0.78	J/m²
[τ_{22}]	-	0.50	0.50	0.95	J/m²

[†††] Dr. Tobias Brink is highly thanked for performing DFT calculations

$[\tau_{12}]$	-	0.00	0.00	0.00	J/m²

We also tested this with two other potentials [252,253], but found that numerical problems lead to wildly fluctuating or even very large negative GB energies. We thus did not further investigate these potentials. In the remaining simulations, we always found structures that resembled either the |E| or |E'| motifs. The excess properties at $T = 0$, $\sigma = 0$, and $\varepsilon = 0$ are listed in **Table 6**. The excess properties at $T = 0$, $\sigma = 0$, and $\varepsilon = 0$ are listed in Table 2. Since we found that the potentials differ significantly in the expected ground-state motif, as well as in the excess properties, we additionally performed density functional theory (DFT) calculations using VASP 5.4.4 [254–257]. Since we found that the potentials differ significantly in the expected ground-state motif, as well as in the excess properties, we additionally performed density functional theory (DFT) calculations using VASP 5.4.4 [254–257]. For this, we prepared a smaller simulation cell with 72 atoms, dimensions of around 7×2×60 Å³, and full periodic boundary conditions, resulting in two identical grain boundaries in the cell. We also set up an equivalent reference structure containing no grain boundaries. The simulations were set up and analyzed using pyiron [258]. We employed the projector-augmented wave (PAW) method [259] within the generalized gradient approximation (GGA) with the Perdew–Burke–Ernzerhof (PBE) parametrization [260]. The PAW potentials [261] used three valence electrons ($3s^2 3p^1$) for Al.

Due to the sensitivity of GB excess properties to numerical errors, we used high-accuracy parameters for the DFT simulations. First, the Al lattice constant was determined using a cubical fcc unit cell to be 4.040(5) Å using a plane-wave energy cutoff of 450 eV and a 19×19×19 k-point mesh on a Γ-centered Monkhorst–Pack grid [262]. The GB simulations used the same parameters, except for a 27×27×2 k-point mesh. The equilibrium excess energy and volume at 0 K was found by scaling the box normal to the grain boundary planes, fitting a third order polynomial to the total energy as a function of the box length, and finding the minimum of that function. Stresses obtained by DFT and by the derivative of the energy agreed quite well due to the high accuracy of the simulations (very small Pulay stress). We therefore used the stresses calculated by VASP directly. Then, excess energy, volume, $[B_1]$, and α as a function of σ_{33} (the external stress normal to the GB plane) were computed as described in Ref. [86] using the defect-free reference system at corresponding σ_{33} values (Figure 13). The GB excess stresses $[\tau_{ij}]$ were strongly affected by even very small residual stresses of the reference system and we regard them therefore as unreliable. We find that all potentials deviate qualitatively from the DFT results, especially at finite stresses.

This is expected, since such empirical potentials are often only fitted to undeformed structures. Nevertheless, the potential by Mishin et al. (1999) [176] reproduces the ground state values quite well and is the only potential that captures the fact that the transformation from |E| to |E'| units occurs at tensile stresses on the order of 1 GPa. We therefore used this potential for the work described in the main text.
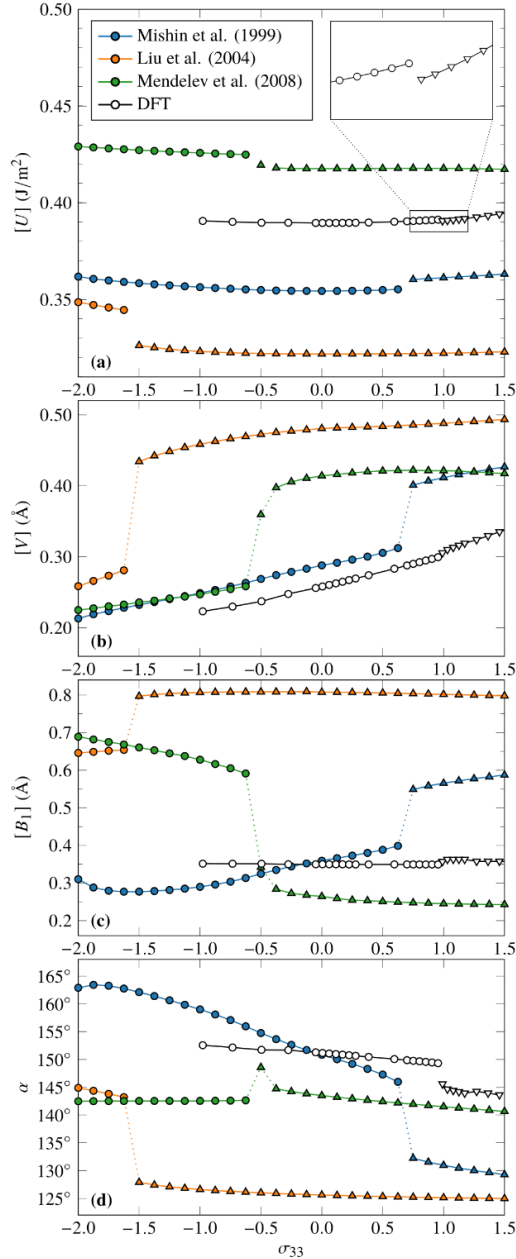
A 1: Comparison of different excess properties calculated with DFT simulations and EAM potentials. Data points represent either |E| units (OR I, circles) or |E'| units (OR II, triangles). The changes are less pronounced in the DFT simulations than in the EAM potentials, but the potential by Mishin et al. [176] matches quite well in the stress-free state and most closely reproduces the stress required for the transformation from |E| to |E'|.

Appendix A.2 STEM HAADF and STEM EDS results related to Chapter 5. 4
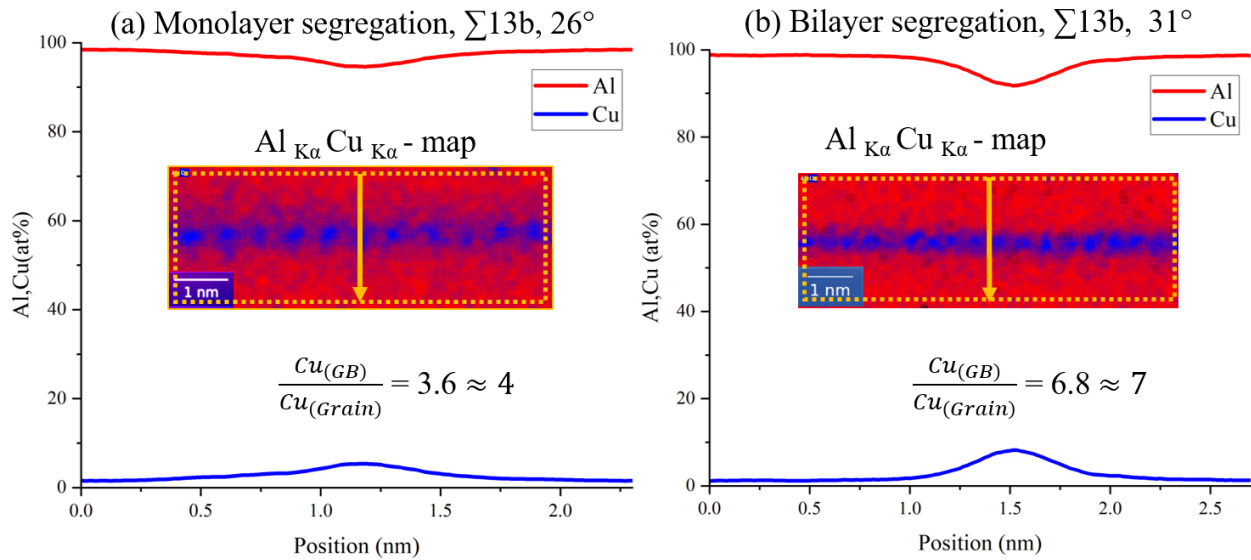
A 2: STEM-EDS quantification at 120 keV a) Monolayer segregation for the Σ13b (26°) and **b)** Bilayer segregation for the Σ13b (31°) GBs**. a)** and **b)** show the line profiles extracted across the GB, indicated by the yellow arrow (integrated over the whole area, marked by the yellow rectangle). The quantification from the plots reveals that the ratio of Cu concentration (in at %) at the GB to the grain $\frac{Cu_{(GB)}}{Cu_{(Grain)}}$ in the Σ13b (31°) GB is nearly twice that of the Σ13b (26°) GB. Note that the EDS measurements for both the GBs are taken from the same specimen under identical conditions such as the same orientation (along the [111] direction) and duration of the measurement.
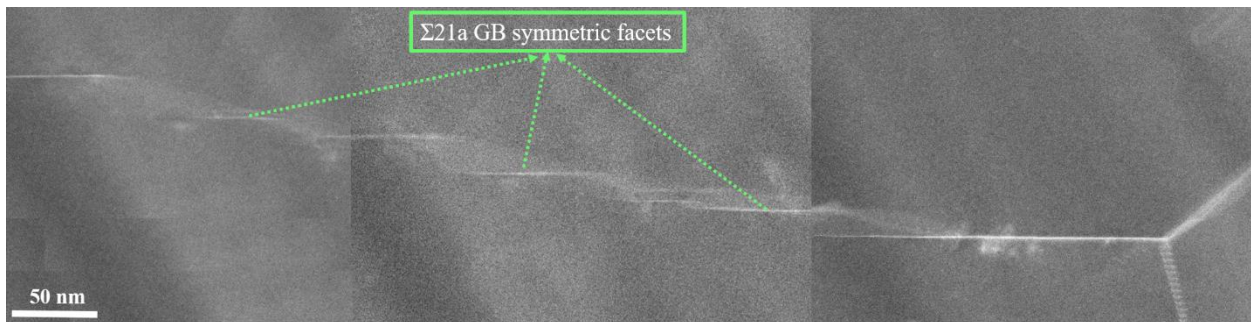
A 3: Overview STEM-HAADF images of Σ21a GB along [111] tilt direction from the Al film annealed at 450ᵒC for 6 hr. Low magnification stacked BF-TEM images showing the overall curvature of the GB. The green arrows depict the symmetric facets, which are separated by a large step. Note that the symmetric facets are connected by asymmetric facets. These asymmetric facets are not clearly visible due to their high inclination w.r.t the electron beam.

List of Figures

List of Tables

Reference

[1] M.A. Wahid, A.N. Siddiquee, Z.A. Khan, Aluminum alloys in marine construction: characteristics, application, and problems from a fabrication viewpoint, Mar. Syst. Ocean Technol. 15 (2020) 70–80. https://doi.org/10.1007/s40868-019-00069-w.

[2] A. Gloria, R. Montanari, M. Richetta, A. Varone, Alloys for aeronautic applications: State of the art and perspectives, Metals (Basel). 9 (2019) 1–26. https://doi.org/10.3390/met9060662.

[3] J. Hirsch, Aluminium alloys for automotive application, Mater. Sci. Forum. 242 (1997) 33–50. https://doi.org/10.4028/www.scientific.net/msf.242.33.

[4] E.A. Starke, J.T. Staley, Application of modern aluminum alloys to aircraft, Prog. Aerosp. Sci. 32 (1996) 131–172. https://doi.org/10.1016/0376-0421(95)00004-6.

[5] W.B. Frank, W.. Haupin, H. Vogt, Aluminum, Ullmann's Encycl. Ind. Chem. (2012). https://doi.org/10.1002/14356007.a01_459.

[6] Y. Song, C. Perez, G. Esteves, J.S. Lundh, C.B. Saltonstall, T.E. Beechem, J.I. Yang, K. Ferri, J.E. Brown, Z. Tang, J.P. Maria, D.W. Snyder, R.H. Olsson, B.A. Griffin, S.E. Trolier-Mckinstry, B.M. Foley, S. Choi, Thermal Conductivity of Aluminum Scandium Nitride for 5G Mobile Applications and beyond, ACS Appl. Mater. Interfaces. 13 (2021) 19031–19041. https://doi.org/10.1021/acsami.1c02912.

[7] Sara Montijo, A guide to the most popular, all-purpose aluminum alloys, (n.d.). https://www.kloecknermetals.com/blog/a-guide-to-the-most-popular-all-purpose-aluminum-alloys/.

[8] W.K. Krajewski, J. Buras, M. Zurakowski, A.L. Greer, M.N. Mancheva, K. Haberl, P. Schumacher, Development of environmentally friendly cast alloys. High-zinc Al alloys, Arch. Mater. Sci. Eng. 45 (2010) 120–124. https://doi.org/http://dx.doi.org/10.1007/s11837-007-0140-2.

[9] S.K. Das, J.A.S. Green, J.G. Kaufman, The development of recycle-friendly automotive aluminum alloys, Jom. 59 (2007) 47–51. https://doi.org/10.1007/s11837-007-0140-2.

[10]   J. Esquivel, R.K. Gupta, Review—Corrosion-Resistant Metastable Al Alloys: An Overview of Corrosion Mechanisms, J. Electrochem. Soc. 167 (2020) 081504. https://doi.org/10.1149/1945-7111/ab8a97.

[11]   T.C. Tsai, T.H. Chuang, Atmospheric stress corrosion cracking of a superplastic 7475 aluminum alloy, Metall. Mater. Trans. A Phys. Metall. Mater. Sci. 27 (1996) 2617–2627. https://doi.org/10.1007/BF02652355.

[12]   J.C. Williams, E.A. Starke, Progress in structural materials for aerospace systems, Acta Mater. 51 (2003) 5775–5799. https://doi.org/10.1016/j.actamat.2003.08.023.

[13]   M.O. Speidel, Stress corrosion cracking of aluminum alloys, Metall. Trans. A. 6 (1975) 631–651. https://doi.org/10.1007/BF02672284.

[14]   F. Najafkhani, S. Kheiri, B. Pourbahari, H. Mirzadeh, Recent advances in the kinetics of normal/abnormal grain growth: a review, Arch. Civ. Mech. Eng. 21 (2021) 1–20. https://doi.org/10.1007/s43452-021-00185-8.

[15]   J. Dennis, P.S. Bate, F.J. Humphreys, Abnormal grain growth in Al-3.5Cu, Acta Mater. 57 (2009) 4539–4547. https://doi.org/10.1016/j.actamat.2009.06.018.

[16]   M.M. Attallah, H.G. Salem, Friction stir welding parameters: A tool for controlling abnormal grain growth during subsequent heat treatment, Mater. Sci. Eng. A. 391 (2005) 51–59. https://doi.org/10.1016/j.msea.2004.08.059.

[17]   B. Wilshire, C.J. Palmer, Grain size effects during creep of copper, Scr. Mater. 46 (2002) 483–488. https://doi.org/10.1016/S1359-6462(01)01247-7.

[18]   X. Lu, C. Dong, X. Guo, J. Ren, H. Xue, F. Tang, Y. Ding, Effects of grain size and temperature on mechanical properties of nano-polycrystalline Nickel-cobalt alloy, J. Mater. Res. Technol. 9 (2020) 1316–13173. https://doi.org/10.1016/j.jmrt.2020.09.060.

[19]   A.P. Sutton, R.W. Baluffi, Interfaces in crystalline materials, Cladernon Press Oxford 1995, 1995. https://global.oup.com/academic/product/interfaces-in-crystalline-materials-9780199211067?cc=de&lang=en&.

[20]   K. Cheng, L. Zhang, C. Lu, K. Tieu, Coupled grain boundary motion in aluminium: The

effect of structural multiplicity, Sci. Rep. 6 (2016) 1–11. https://doi.org/10.1038/srep25427.

[21]   R.W. Balluffi, A.P. Sutton, Why should we be interested in the atomic structure of interfaces?, Mater. Sci. Forum. 207–209 (1996) 1–12. https://doi.org/10.4028/www.scientific.net/msf.207-209.1.

[22]   P. Lajek, Grain Boundary Segregation in Metals, Springer Science & Business Media, 2016. http://www.springer.com/series/856.

[23]   T. Frolov, D.L. Olmsted, M. Asta, Y. Mishin, Structural phase transformations in metallic grain boundaries, Nat. Commun. 4 (2013) 1–7. https://doi.org/10.1038/ncomms2919.

[24]   W. Krakow, Structural multiplicity observed at a Σ = 5/[001] 53·1° tilt boundary in gold, Philos. Mag. A Phys. Condens. Matter, Struct. Defects Mech. Prop. 63 (1991) 233–240. https://doi.org/10.1080/01418619108204847.

[25]   T. Meiners, J.M. Duarte, G. Richter, G. Dehm, C.H. Liebscher, Tantalum and zirconium induced structural transitions at complex [111] tilt grain boundaries in copper, Acta Mater. 190 (2020) 93–104. https://doi.org/10.1016/j.actamat.2020.02.064.

[26]   E.W. Hart, Two-dimensional phase transformation in grain boundaries, Scr. Metall. 2 (1968) 179–182. https://doi.org/10.1016/0036-9748(68)90222-6.

[27]   J.W. Cahn, Transitions and Phase Equilibria Among Grain Boundary Structures., J. Phys. (Paris), Colloq. 43 (1982) 199–213. https://doi.org/10.1051/jphyscol:1982619.

[28]   G.H. Bishop, B. Chalmers, A coincidence - Ledge - Dislocation description of grain boundaries, Scr. Metall. 2 (1968) 133–139. https://doi.org/10.1016/0036-9748(68)90085-9.

[29]   Q. Zhu, A. Samanta, B. Li, R.E. Rudd, T. Frolov, Predicting phase behavior of grain boundaries with evolutionary search and machine learning, Nat. Commun. 9 (2018). https://doi.org/10.1038/s41467-018-02937-2.

[30]   S.J. Dillon, M. Tang, W.C. Carter, M.P. Harmer, Complexion: A new concept for kinetic engineering in materials science, Acta Mater. 55 (2007) 6208–6218. https://doi.org/10.1016/j.actamat.2007.07.029.

[31]   G. Duscher, M.F. Chisholm, U. Alber, M. Rühle, Bismuth-induced embrittlement of copper

grain boundaries, Nat. Mater. 3 (2004) 621–626. https://doi.org/10.1038/nmat1191.

[32]   T. Frolov, Y. Mishin, Phases, phase equilibria, and phase rules in low-dimensional systems, J. Chem. Phys. 143 (2015). https://doi.org/10.1063/1.4927414.

[33]   M. Tang, W.C. Carter, R.M. Cannon, Diffuse interface model for structural transitions of grain boundaries, Phys. Rev. B - Condens. Matter Mater. Phys. 73 (2006) 1–14. https://doi.org/10.1103/PhysRevB.73.024102.

[34]   P.R. Cantwell, M. Tang, S.J. Dillon, J. Luo, G.S. Rohrer, M.P. Harmer, Grain boundary complexions, Acta Mater. 62 (2014) 1–48. https://doi.org/10.1016/j.actamat.2013.07.037.

[35]   P.R. Cantwell, T. Frolov, T.J. Rupert, A.R. Krause, C.J. Marvel, G.S. Rohrer, J.M. Rickman, M.P. Harmer, Grain Boundary Complexion Transitions, Annu. Rev. Mater. Res. 50 (2020) 465–492. https://doi.org/10.1146/annurev-matsci-081619-114055.

[36]   G.J. Wang, A.P. Sutton, V. Vitek, A computer simulation study of 〈001〉 and 〈111〉 tilt boundaries: the multiplicity of structures, Acta Metall. 32 (1984) 1093–1104. https://doi.org/10.1016/0001-6160(84)90013-0.

[37]   A.P. Sutton, V. Vitek, On the structure of the structures of tilt grain boundaries in cubic metals: Symmetric   tilt   boundaries,   309   (1983)   1–36. https://doi.org/https://doi.org/10.1098/rsta.1983.0020.

[38]   M.A. Tschopp, S.P. Coleman, D.L. McDowell, Symmetric and asymmetric tilt grain boundary structure and energy in Cu and Al (and transferability to other fcc metals), Integr. Mater. Manuf. Innov. 4 (2015) 176–189. https://doi.org/10.1186/s40192-015-0040-1.

[39]   H.J. Frost, M.F. Ashby, F. Spaepen, A catalogue of [100], [110] and [111] symmetric tilt boundaries in face-centered cubic hard sphere crystals, (1982).

[40]   T. Meiners, T. Frolov, R.E. Rudd, G. Dehm, C.H. Liebscher, Observations of grain-boundary phase transformations in an elemental metal, Nature. 579 (2020) 375–378. https://doi.org/10.1038/s41586-020-2082-6.

[41]   N.J. Peter, T. Frolov, M.J. Duarte, R. Hadian, C. Ophus, C. Kirchlechner, C.H. Liebscher, G. Dehm, Segregation-Induced Nanofaceting Transition at an Asymmetric Tilt Grain

Boundary in Copper, Phys. Rev. Lett. 121 (2018) 255502. https://doi.org/10.1103/PhysRevLett.121.255502.

[42] L. Frommeyer, T. Brink, R. Freitas, T. Frolov, G. Dehm, C.H. Liebscher, Dual phase patterning during a congruent grain boundary phase transition in elemental copper, Nat. Commun. 13 (2022) 1–11. https://doi.org/10.1038/s41467-022-30922-3.

[43] S. Rajeshwari K., S. Sankaran, K.C. Hari Kumar, H. Rösner, M. Peterlechner, V.A. Esin, S. Divinski, G. Wilde, Grain boundary diffusion and grain boundary structures of a Ni-Cr-Fe- alloy: Evidences for grain boundary phase transitions, Acta Mater. 195 (2020) 501–518. https://doi.org/10.1016/j.actamat.2020.05.051.

[44] C. Wang, H. Duan, C. Chen, P. Wu, D. Qi, H. Ye, H.J. Jin, H.L. Xin, K. Du, Three-Dimensional Atomic Structure of Grain Boundaries Resolved by Atomic-Resolution Electron Tomography, Matter. 3 (2020) 1999–2011. https://doi.org/10.1016/j.matt.2020.09.003.

[45] T. Richeton, J. Weiss, F. Louchet, Dislocation avalanches: Role of temperature, grain size and strain hardening, Acta Mater. 53 (2005) 4463–4471. https://doi.org/10.1016/j.actamat.2005.06.007.

[46] R. Krobath, C. Bernhard, S. Ilie, J. Six, S. Hahn, P. Pennerstorfer, The Role of Grain Boundary Oxidation on Surface Crack Formation under Continuous Casting Conditions, BHM Berg- Und Hüttenmännische Monatshefte. 164 (2019) 461–465. https://doi.org/10.1007/s00501-019-00902-0.

[47] J. Reiser, A. Hartmaier, Elucidating the dual role of grain boundaries as dislocation sources and obstacles and its impact on toughness and brittle-to-ductile transition, Sci. Rep. 10 (2020) 1–18. https://doi.org/10.1038/s41598-020-59405-5.

[48] Y. Li, P.A. Korzhavyi, R. Sandström, C. Lilja, Impurity effects on the grain boundary cohesion in copper, Phys. Rev. Mater. 1 (2017) 1–5. https://doi.org/10.1103/PhysRevMaterials.1.070602.

[49] J.D. Robson, Analytical electron microscopy of grain boundary segregation: Application to Al-Zn-Mg-Cu (7xxx) alloys, Mater. Charact. 154 (2019) 325–334.

https://doi.org/10.1016/j.matchar.2019.06.016.

[50]   H.P. Longworth, C. V. Thompson, Abnormal grain growth in aluminum alloy thin films, J. Appl. Phys. 69 (1991) 3929–3940. https://doi.org/10.1063/1.348452.

[51]   T. Minoda, H. Yoshida, Effect of microstructure on intergranular corrosion resistance of 6061 alloy extrusion, Mater. Sci. Forum. 331 (2000). https://doi.org/10.4028/www.scientific.net/msf.331-337.1689.

[52]   L. Priester, Atomic Order of Grain Boundaries, Springer Science & Business Media, 2013. https://doi.org/10.1007/978-94-007-4969-6_3.

[53]   R.C. Pond, V. Vitek, Periodic Grain Boundary Structures in Aluminium - 1. a Combined Experimental and Theoretical Investigation of Coincidence Grain Boundary Structure in Aluminium., Proc R Soc London Ser A. 357 (1977) 453–470. https://doi.org/10.1098/rspa.1977.0179.

[54]   W.T. Read, W. Schockley, Dislocation Models of Crystal Grain Boundaries, Phys. Rev. 78 (1950) 275.

[55]   Tec-science, Crystallographic defects, (n.d.). https://www.tec-science.com/material-science/structure-of-metals/crystallographic-defects/.

[56]   N. Fletcher, Crystal-interface models- a crirical survey, Adv. Mater. Res. (1971) 281–314.

[57]   L. Zhang, Y. Gu, Y. Xiang, Energy of low angle grain boundaries based on continuum dislocation structure, Acta Mater. 126 (2017) 11–24. https://doi.org/10.1016/j.actamat.2016.12.035.

[58]   V. V. Bulatov, B.W. Reed, M. Kumar, Grain boundary energy function for fcc metals, Acta Mater. 65 (2014) 161–175. https://doi.org/10.1016/j.actamat.2013.10.057.

[59]   Y. Ikuhara, H. Nishimura, A. Nakamura, K. Matsunaga, T. Yamamoto, K. Peter, D. Lagerlöf, Dislocation structures of low-angle and near-Σ3 Grain boundaries in alumina bicrystals, J. Am. Ceram. Soc. 86 (2003) 595–602. https://doi.org/10.1111/j.1151-2916.2003.tb03346.x.

[60]   H. Bishara, S. Lee, T. Brink, M. Ghidelli, G. Dehm, Understanding Grain Boundary

Electrical Resistivity in Cu: The Effect of Boundary Structure, ACS Nano. 15 (2021) 16607–16615. https://doi.org/10.1021/acsnano.1c06367.

[61] M.L. Kronberg, F.H. Wilson, Secondary Recrystallization in Copper, Jom. 1 (1949) 501–514. https://doi.org/10.1007/bf03398387.

[62] B. Straumal, B. Baretzky, Grain boundary phase transitions and their influence on properties of polycrystals, Interface Sci. 12 (2004) 147–155. https://doi.org/10.1023/B:INTS.0000028645.30358.f5.

[63] G. Gottstein, D.A. Molodov, L.S. Shvindlerman, D.J. Srolovitz, M. Winning, Grain boundary migration: Misorientation dependence, Curr. Opin. Solid State Mater. Sci. 5 (2001) 9–14. https://doi.org/10.1016/S1359-0286(00)00030-9.

[64] P. Lin, G. Palumbo, U. Erb, K.T. Aust, Influence of grain boundary character distribution on sensitization and intergranular corrosion of alloy 600, Scr. Metall. Mater. 33 (1995) 1387–1392. https://doi.org/10.1016/0956-716X(95)00420-Z.

[65] V.Y. Gertsman, S.M. Bruemmer, Study of grain boundary character along intergranular stress corrosion crack paths in austenitic alloys, Acta Mater. 49 (2001) 1589–1598. https://doi.org/10.1016/S1359-6454(01)00064-7.

[66] J. Han, S.L. Thomas, D.J. Srolovitz, Grain-boundary kinetics: A unified approach, Prog. Mater. Sci. 98 (2018) 386–476. https://doi.org/10.1016/j.pmatsci.2018.05.004.

[67] A.P. Sutton, R.W. Balluffi, Overview no. 61 On geometric criteria for low interfacial energy, Acta Metall. 35 (1987) 2177–2201. https://doi.org/10.1016/0001-6160(87)90067-8.

[68] G.C. Hasson, C. Goux, Interfacial energies of tilt boundaries in aluminium. Experimental and theoretical determination, Scr. Metall. 5 (1971) 889–894. https://doi.org/10.1016/0036-9748(71)90064-0.

[69] M.A. Tschopp, D.L. McDowell, Asymmetric tilt grain boundary structure and energy in copper and aluminium, Philos. Mag. 87 (2007) 3871–3892. https://doi.org/10.1080/14786430701455321.

[70]   D.L. Olmsted, S.M. Foiles, E.A. Holm, Survey of computed grain boundary properties in face-centered cubic metals: I. Grain boundary energy, Acta Mater. 57 (2009) 3694–3703. https://doi.org/10.1016/j.actamat.2009.04.007.

[71]   K. Wang, W.G. Zhang, J.Q. Xu, W.J. Dan, The impact of misorientation on the grain boundary energy in bi-crystal copper: an atomistic simulation study, J. Mol. Model. 28 (2022). https://doi.org/10.1007/s00894-022-05037-7.

[72]   J. Han, V. Vitek, D.J. Srolovitz, The grain-boundary structural unit model redux, Acta Mater. 133 (2017) 186–199. https://doi.org/10.1016/j.actamat.2017.05.002.

[73]   D.N. Pawaskar, R. Miller, R. Phillips, Structure and energetics of long-period tilt grain boundaries using an effective Hamiltonian, Phys. Rev. B - Condens. Matter Mater. Phys. 63 (2001) 1–14. https://doi.org/10.1103/PhysRevB.63.214105.

[74]   J. Rittner, D. Seidman, ⟨110⟩ Symmetric Tilt Grain-Boundary Structures in Fcc Metals With Low Stacking-Fault Energies, Phys. Rev. B - Condens. Matter Mater. Phys. 54 (1996) 6999–7015. https://doi.org/10.1103/PhysRevB.54.6999.

[75]   Y. Oh, V. Vitek, Structural multiplicity of $\sum = 5(001)$ twist boundaries and interpretation of X-ray diffraction from these boundaries, Acta Metall. 34 (1986) 1941–1953. https://doi.org/10.1016/0001-6160(86)90253-1.

[76]   K.L. Merkle, L.J. Thompson, F. Phillipp, Thermally activated step motion observed by high-resolution electron microscopy at a (113) symmetric tilt grain-boundary in aluminium, Philos. Mag. Lett. 82 (2002) 589–597. https://doi.org/10.1080/09500830021000038074.

[77]   E. Hosseinian, M. Legros, O.N. Pierron, Quantifying and observing viscoplasticity at the nanoscale: Highly localized deformation mechanisms in ultrathin nanocrystalline gold films, Nanoscale. 8 (2016) 9234–9244. https://doi.org/10.1039/c6nr00710d.

[78]   A. Rajabzadeh, F. Mompiou, S. Lartigue-Korinek, N. Combe, M. Legros, D.A. Molodov, The role of disconnections in deformation-coupled grain boundary migration, Acta Mater. 77 (2014) 223–235. https://doi.org/10.1016/j.actamat.2014.05.062.

[79]   W.Bollman, Crystal Defects and Crystalline Interfaces, Springer Science & Business Media, 1970. https://doi./https://doi.org/10.1007/978-3-642-49173-3_12.

[80] A.H. King, D.A. Smith, The effects on grain-boundary processes of the steps in the boundary plane associated with the cores of grain-boundary dislocations, Acta Crystallogr. Sect. A. 36 (1980) 335–343. https://doi.org/10.1107/S0567739480000782.

[81] J.P. Hirth, R.C. Pond, Steps, dislocations and disconnections as interface defects relating to structure and phase transformations, Acta Mater. 44 (1996) 4749–4763. https://doi.org/10.1016/S1359-6454(96)00132-2.

[82] Q. Zhu, G. Cao, J. Wang, C. Deng, J. Li, Z. Zhang, S.X. Mao, In situ atomistic observation of disconnection-mediated grain boundary migration, Nat. Commun. 10 (2019) 1–8. https://doi.org/10.1038/s41467-018-08031-x.

[83] J.W. Gibbs, Gibbs G.W. - Collected works. Thermodynamics. Volume 1-Longmans .pdf, (1928).

[84] J.W. Cahn, Adapting thermodynamics for materials science problems, J. Phase Equilibria. 15 (1994) 373–379. https://doi.org/10.1007/BF02647556.

[85] T. Frolov, Y. Mishin, Thermodynamics of coherent interfaces under mechanical stresses. I. Theory, Phys. Rev. B - Condens. Matter Mater. Phys. 85 (2012) 12–15. https://doi.org/10.1103/PhysRevB.85.224106.

[86] T. Frolov, Y. Mishin, Thermodynamics of coherent interfaces under mechanical stresses. II. Application to atomistic simulation of grain boundaries, Phys. Rev. B - Condens. Matter Mater. Phys. 85 (2012). https://doi.org/10.1103/PhysRevB.85.224107.

[87] C. Rottman, Theory of Phase Transitions At Internal Interfaces, Le J. Phys. Colloq. 49 (1988) C5-313-C5-326. https://doi.org/10.1051/jphyscol:1988538.

[88] J.W. Gibbs, The collected works of J. Willard Gibbs, New Haven Yale Univ. Press. (1948).

[89] T. Frolov, S. V. Divinski, M. Asta, Y. Mishin, Effect of interface phase transformations on diffusion and segregation in high-angle grain boundaries, Phys. Rev. Lett. 110 (2013) 1–5. https://doi.org/10.1103/PhysRevLett.110.255502.

[90] V. Turlo, T.J. Rupert, Grain boundary complexions and the strength of nanocrystalline metals: Dislocation emission and propagation, Acta Mater. 151 (2018) 100–111.

https://doi.org/10.1016/j.actamat.2018.03.055.

[91] F.Y. Cui, A. Kundu, A. Krause, M.P. Harmer, R.P. Vinci, Surface energies, segregation, and fracture behavior of magnesium aluminate spinel low-index grain boundary planes, Acta Mater. 148 (2018) 320–329. https://doi.org/10.1016/j.actamat.2018.01.039.

[92] J. Luo, H. Cheng, K.M. Asl, C.J. Kiely, M.P. Harmer, The role of a bilayer interfacial phase on liquid metal embrittlement, Science (80-.). 333 (2011) 1730–1733. https://doi.org/10.1126/science.1208774.

[93] S. V. Divinski, H. Edelhoff, S. Prokofjev, Diffusion and segregation of silver in copper Σ5(310) grain boundary, Phys. Rev. B - Condens. Matter Mater. Phys. 85 (2012) 1–10. https://doi.org/10.1103/PhysRevB.85.144104.

[94] S.A. Bojarski, M.P. Harmer, G.S. Rohrer, Influence of grain boundary energy on the nucleation of complexion transitions, Scr. Mater. 88 (2014) 1–4. https://doi.org/10.1016/j.scriptamat.2014.06.016.

[95] W. Sigle, G. Richter, M. Rühle, S. Schmidt, Insight into the atomic-scale mechanism of liquid metal embrittlement, Appl. Phys. Lett. 89 (2006) 87–90. https://doi.org/10.1063/1.2356322.

[96] J.M. Pénisson, U. Dahmen, M.J. Mills, Hrem study of a î = 3(112) twin boundary in aluminium, Philos. Mag. Lett. 64 (1991) 277–283. https://doi.org/10.1080/09500839108214622.

[97] M.J. Mills, M.S. Daw, G.J. Thomas, F. Cosandey, High-resolution transmission electron microscopy of grain boundaries in aluminum and correlation with atomistic calculations, Ultramicroscopy. 40 (1992) 247–257. https://doi.org/10.1016/0304-3991(92)90121-Y.

[98] N. Sakaguchi, H. Ichinose, S. Watanabe, Atomic structure of faceted ∑3 CSL grain boundary in silicon: HRTEM and Ab-initio calculation, Mater. Trans. 48 (2007) 2585–2589. https://doi.org/10.2320/matertrans.MD200706.

[99] C.J.D. Hetherington, U. Dahmen, R. Kilaas, A.I. Kirkland, A. R. R. Meyer, D.L. Medlin., HREM analysis of Σ3 {112} boundaries in gold bicrystal films, in: Electron Microsc. Anal. Dundee, 2001, CRC Press, Philadelphia, 2001: p. vol. 168, pp. 59-62.

[100] M.P. Seah, Grain boundary segregation, J. Phys. F Met. Phys. (1980). https://doi.org/10.1016/0001-6160(59)90080-X.

[101] L.S. Chang, E. Rabkin, B.B. Straumal, S. Hofmann, B. Baretzky, W. Gust, Grain boundary segregation in the Cu-Bi system, Defect Diffus. Forum. 156 (1998) 135–146. https://doi.org/10.4028/www.scientific.net/ddf.156.135.

[102] R.G. Faulkner, Segregation to boundaries and interfaces in solids, Mater. Sci. Forum. 189–190 (1995) 81–94. https://doi.org/10.4028/www.scientific.net/msf.189-190.81.

[103] P. Wynblatt, D. Chatain, Anisotropy of segregation at grain boundaries and surfaces, Metall. Mater. Trans. A Phys. Metall. Mater. Sci. 37 (2006) 2595–2620. https://doi.org/10.1007/BF02586096.

[104] J.W. Gibbs, The collected works of J. Willard Gibbs, Yale Univ. Press, 1948.

[105] D. McLean, McLean D. - Grain boundaries in metals, Clarendon Press, Oxford, 1957.

[106] M.P. Seah, E.D. Hondos, Grain boundary segregation, Proc. R. Soc. London. A. Math. Phys. Sci. 335 (1973) 191–212. https://doi.org/10.1098/rspa.1973.0121.

[107] E.D. Hondos, The influence of phosphorus in dilute solid solution on the absolute surface and grain boundary energies of iron, Proc. R. Soc. London. Ser. A. Math. Phys. Sci. 286 (1964) 479–498. https://doi.org/10.1098/rspa.1965.0158.

[108] E.D. Hondros, M.P. Seah, Theory of Grain Boundary Segregation in Terms of Surface Adsorption Analogues., Met. Trans A. 8 A (1977) 1363–1371. https://doi.org/10.1007/BF02642850.

[109] D. Raabe, M. Herbig, S. Sandlöbes, Y. Li, D. Tytko, M. Kuzmina, D. Ponge, P.P. Choi, Grain boundary segregation engineering in metallic alloys: A pathway to the design of interfaces, Curr. Opin. Solid State Mater. Sci. 18 (2014) 253–261. https://doi.org/10.1016/j.cossms.2014.06.002.

[110] T. Savaşkan, A.P. Hekimoglu, G. Pürçek, Effect of copper content on the mechanical and sliding wear properties of monotectoid-based zinc-aluminium-copper alloys, Tribol. Int. 37 (2004) 45–50. https://doi.org/10.1016/S0301-679X(03)00113-0.

[111] Al market size, share and COVID 19 Impact Analysis, Fortune Bus. Insights. (2020).

[112] Automotive Aluminum Market: Global Industry Trends, Share, Size, Growth, Opportunity and Forecast 2022-2027, IMARC Gr. (2022).

[113] R.M. Chlistovsky, P.J. Heffernan, D.L. DuQuesnay, Corrosion-fatigue behaviour of 7075-T651 aluminum alloy subjected to periodic overloads, Int. J. Fatigue. 29 (2007) 1941–1949. https://doi.org/10.1016/j.ijfatigue.2007.01.010.

[114] L. Huang, A. Gu, H. Liu, T. Jiang, Corrosion failure of aluminum alloy parts on airplane used in marine environment, Beijing Hangkong Hangtian Daxue Xuebao/Journal Beijing Univ. Aeronaut. Astronaut. 34 (2008) 1217–1221.

[115] Z. Gao, Y. He, S. Zhang, T. Zhang, F. Yang, Research on corrosion damage evolution of aluminum alloy for aviation, Appl. Sci. 10 (2020) 1–16. https://doi.org/10.3390/app10207184.

[116] R.J. Bucci, Selecting aluminum alloys to resist failure by fracture mechanisms, Eng. Fract. Mech. 12 (1979) 407–441. https://doi.org/10.1016/0013-7944(79)90053-5.

[117] J.R. Lloyd, J.J. Clement, Electromigration damage due to copper depletion in Al/Cu alloy conductors, Appl. Phys. Lett. 69 (1996) 2486–2488. https://doi.org/10.1063/1.117506.

[118] A.C.U. Rao, V. Vasu, M. Govindraj, K.V.S. Srinadh, Stress corrosion cracking behaviour of 7xxx aluminum alloys: A literature review, Trans. Nonferrous Met. Soc. China (English Ed. 26 (2016) 1447–1471. https://doi.org/10.1016/S1003-6326(16)64220-6.

[119] G. Sha, L. Yao, X. Liao, S.P. Ringer, Z.C. Duan, T.G. Langdon, Segregation of solute elements at grain boundaries in an ultrafine grained Al-Zn-Mg-Cu alloy, Ultramicroscopy. 111 (2011) 500–505. https://doi.org/10.1016/j.ultramic.2010.11.013.

[120] Z. Liu, X. Chen, X. Han, Y. Gu, The dissolution behavior of θ' phase in Al-Cu binary alloy during equal channel angular pressing and multi-axial compression, Mater. Sci. Eng. A. 527 (2010) 4300–4305. https://doi.org/10.1016/j.msea.2010.03.046.

[121] Y. Chen, N. Gao, G. Sha, S.P. Ringer, M.J. Starink, Microstructural evolution, strengthening and thermal stability of an ultrafine-grained Al-Cu-Mg alloy, Acta Mater. 109

(2016) 202–212. https://doi.org/10.1016/j.actamat.2016.02.050.

[122] H. Zhao, F. De Geuser, A. Kwiatkowski da Silva, A. Szczepaniak, B. Gault, D. Ponge, D. Raabe, Segregation assisted grain boundary precipitation in a model Al-Zn-Mg-Cu alloy, Acta Mater. 156 (2018) 318–329. https://doi.org/10.1016/j.actamat.2018.07.003.

[123] D. Zhao, O.M. Løvvik, K. Marthinsen, Y. Li, Segregation of Mg, Cu and their effects on the strength of Al Σ5 (210)[001] symmetrical tilt grain boundary, Acta Mater. 145 (2018) 235–246. https://doi.org/10.1016/j.actamat.2017.12.023.

[124] G.H. Campbell, J.M. Plitzko, W.E. King, S.M. Foiles, C. Kisielowski, G.J.M. Duscher, Copper segregation to the ∑5 (310)/[001] symmetric tilt grain boundary in aluminum, Interface Sci. 12 (2004) 165–174. https://doi.org/10.1023/B:INTS.0000028647.72322.90.

[125] P. Parajuli, D. Romeu, V. Hounkpati, R. Mendoza-Cruz, J. Chen, M.J. Yacamán, J. Flowers, A. Ponce, Misorientation dependence grain boundary complexions in <111> symmetric tilt Al grain boundaries, Acta Mater. 181 (2019) 216–227. https://doi.org/10.1016/j.actamat.2019.09.010.

[126] K. Deane, P. Sanders, Effect of Zr additions on thermal stability of Al-Cu precipitates in as-cast and cold worked samples, Metals (Basel). 8 (2018). https://doi.org/10.3390/met8050331.

[127] J. Liu, P. Yao, N. Zhao, C. Shi, H. Li, X. Li, D. Xi, S. Yang, Effect of minor Sc and Zr on recrystallization behavior and mechanical properties of novel Al-Zn-Mg-Cu alloys, J. Alloys Compd. 657 (2016) 717–725. https://doi.org/10.1016/j.jallcom.2015.10.122.

[128] Y. Wang, Q.L. Pan, Y.F. Song, C. Li, Z.F. Li, Q. Chen, Z.M. Yin, Recrystallization of Al-5.8Mg-Mn-Sc-Zr alloy, Trans. Nonferrous Met. Soc. China (English Ed. 23 (2013) 3235–3241. https://doi.org/10.1016/S1003-6326(13)62858-7.

[129] A. Baptista, F. Silva, J. Porteiro, J. Míguez, G. Pinto, Sputtering physical vapour deposition (PVD) coatings: A critical review on process improvement andmarket trend demands, Coatings. 8 (2018). https://doi.org/10.3390/COATINGS8110402.

[130] F.M. Mwema, O.P. Oladijo, S.A. Akinlabi, E.T. Akinlabi, Properties of physically deposited thin aluminium film coatings: A review, J. Alloys Compd. 747 (2018) 306–323.

https://doi.org/10.1016/j.jallcom.2018.03.006.

[131] The University of Akron, Thin Film Physical Vapor Deposition (PVD) System, (n.d.). https://www.uakron.edu/soa/instruments/pvd/.

[132] N.K. Jain, M. Sawant, S.H. Nikam, Metal Deposition: Plasma-Based Processes, Encycl. Plasma Technol. (2017) 722–740. https://doi.org/10.1081/e-eplt-120053919.

[133] N.S. Xu, S.E. Huq, Novel cold cathode materials and applications, Mater. Sci. Eng. R Reports. 48 (2005) 47–189. https://doi.org/10.1016/j.mser.2004.12.001.

[134] A.A. Tracton, Coatings Technology: Fundamentals, Testing, and Processing Techniques, CRC Press: Boca Raton, FL, USA, 2007.

[135] K.S. Sree Harsha, Principles of Vapor Deposition of Thin Films, 2006. https://doi.org/10.1016/B978-0-08-044699-8.X5000-1.

[136] R.D. Arnell, P.J. Kelly, Recent advances in magnetron sputtering, Surf. Coatings Technol. 112 (1999) 170–176. https://doi.org/10.1016/S0257-8972(98)00749-X.

[137] S. Swann, Magnetron Sputtering, Compr. Mater. Process. 4 (1988) 57–73. https://doi.org/10.1016/B978-0-08-096532-1.00403-9.

[138] M. Ezzahmouly, A. Elmoutaouakkil, M. Ed-Dhahraouy, H. Khallok, A. Elouahli, A. Mazurier, A. ElAlbani, Z. Hatim, Micro-computed tomographic and SEM study of porous bioceramics using an adaptive method based on the mathematical morphological operations, Heliyon. 5 (2019) e02557. https://doi.org/10.1016/j.heliyon.2019.e02557.

[139] C. Scheu, W.D. Kaplan, Introduction to Scanning Electron Microscopy, in: In-Situ Electron Microsc., Wiley Online Library, 2012: pp. 3–37.

[140] D.B. Williams, C.B. Carter, Transmission electron microscopy: A textbook for materials science, 2009. https://doi.org/10.1007/978-0-387-76501-3.

[141] Y. Liao, Practical electron microscopy and database. An Online Book., 2006. https://www.globalsino.com/EM/page4584.html.

[142] B.J. Griffin, A comparison of conventional Everhart-Thornley style and in-lens secondary electron detectors-a further variable in scanning electron microscopy, Scanning. 33 (2011)

162–173. https://doi.org/10.1002/sca.20255.

[143] L. Reimer, Scanning electron microscopy: Physics of image formation and microanalysis, 2000.

[144] A.J. Schwartz, M. Kumar, B.L. Adams, D.P. Field, EBSD in Materials Science, 2009. http://dx.doi.org/10.1016/j.actamat.2012.

[145] S. Zaefferer, G. Habler, Scanning electron microscopy and electron backscatter diffraction, in: Miner. React. Kinet. Microstruct. Textures, Chem. Isot. Signatures, W. Heinrich, R. Abart, 2017. https://doi.org/https://doi.org/10.1180/EMU-notes.16.3.

[146] X. Zhong, C.A. Wade, P.J. Withers, X. Zhou, C. Cai, S.J. Haigh, M.G. Burke, Comparing Xe+pFIB and Ga+FIB for TEM sample preparation of Al alloys_ Minimising FIB-induced artefacts _ Enhanced Reader.pdf, (2020).

[147] H.S. Nam, D.J. Srolovitz, Effect of material properties on liquid metal embrittlement in the Al-Ga system, Acta Mater. 57 (2009) 1546–1553. https://doi.org/10.1016/j.actamat.2008.11.041.

[148] K.A. Unocic, M.J. Mills, G.S. Daehn, Effect of gallium focused ion beam milling on preparation of aluminium thin foils, J. Microsc. 240 (2010) 227–238. https://doi.org/10.1111/j.1365-2818.2010.03401.x.

[149] L.V. Kouwen, Introduction to focused ion beams, ion sources, and the nano-aperture ion source, Adv. Imaging Electron Phys. 212 (2019) 181–216. https://doi.org/http://dx.doi.org/10.1016/bs.aiep.2019.09.001.

[150] R.F. Egerton, Physical Principles of Electron Microscopy, 2005. https://doi.org/10.1007/b136495.

[151] E.J. Kirkland, R.F. Loane, J. Silcox, Simulation of annular dark field stem images using a modified multislice method, Ultramicroscopy. 23 (1987) 77–96. https://doi.org/10.1016/0304-3991(87)90229-4.

[152] Stephen J. Pennycook, P.D. Nellist, Scanning Transmission Electron Microscopy: Imaging and Analysis, 2011.

[153] L. Reimer H. Kohl, Transmission Electron Microscopy_Physics of Image Formation_5th Edition, 2007.

[154] F. Krumeich, Introduction Into Transmission and Scanning Transmission, (2018).

[155] ThermoFisher, An Introduction to Electron Microscopy Brochure, ThermoFisher Sci. (n.d.). https://www.fei.com/introduction-to-electron-microscopy/stem.

[156] P.D. Nellist, The Principles of STEM Imaging, Scanning Transm. Electron Microsc. (2011) 91–115. https://doi.org/10.1007/978-1-4419-7200-2_2.

[157] Y. Kotaka, Direct visualization method of the atomic structure of light and heavy atoms with double-detector Cs-corrected scanning transmission electron microscopy, Appl. Phys. Lett. 101 (2012). https://doi.org/10.1063/1.4756783.

[158] M.M.J. Treacy, A. Howie, C.J. Wilson, Z contrast of platinum and palladium catalysts, Philos. Mag. A Phys. Condens. Matter, Struct. Defects Mech. Prop. 38 (1978) 569–585. https://doi.org/10.1080/01418617808239255.

[159] A. Howie, Image Contrast And Localized Signal Selection Techniques, J. Microsc. (1979) 11–23. https://doi.org/https://doi.org/10.1111/j.1365-2818.1979.tb00228.x.

[160] D.B. Williams, C.B. Carter, Transmission electron microscopy: Diffraction, Imaging and Spectroscopy, 2011. https://doi.org/10.31399/asm.tb.mfadr7.t91110461.

[161] M. Watanabe, D.W. Ackland, A. Burrows, C.J. Kiely, D.B. Williams, O.L. Krivanek, N. Dellby, M.F. Murfitt, Z. Szilagyi, Improvements in the X-ray analytical capabilities of a scanning transmission electron microscope by spherical-aberration correction, Microsc. Microanal. 12 (2006) 515–526. https://doi.org/10.1017/S1431927606060703.

[162] G. Kothleitner, M.J. Neish, N.R. Lugg, S.D. Findlay, W. Grogger, F. Hofer, L.J. Allen, Quantitative elemental mapping at atomic resolution using X-ray spectroscopy, Phys. Rev. Lett. 112 (2014) 1–5. https://doi.org/10.1103/PhysRevLett.112.085501.

[163] R. Castaing, Application of Electron Probes To Local Chemical and Crystallographic Analysis, (1951) 166.

[164] G. Cliff, G.W. Lorimer, The quantitative analysis of thin specimens, J. Microsc. (1975)

203–207. https://doi.org/https://doi.org/10.1111/j.1365-2818.1975.tb03895.x.

[165] C. Ophus, A fast image simulation algorithm for scanning transmission electron microscopy, Adv. Struct. Chem. Imaging. 3 (2017) 1–11. https://doi.org/10.1186/s40679-017-0046-1.

[166] A. Pryor, C. Ophus, J. Miao, A streaming multi-GPU implementation of image simulation algorithms for scanning transmission electron microscopy, Adv. Struct. Chem. Imaging. 3 (2017). https://doi.org/10.1186/s40679-017-0048-z.

[167] K. Ishizuka, A practical approach for STEM image simulation based on the FFT multislice method, Ultramicroscopy. 90 (2002) 71–83. https://doi.org/10.1016/S0304-3991(01)00145-0.

[168] J. Madsen, T. Susi, C. Francis, M. Helmi, J.. Schiotz, Y.. Janssen, jacobjma/abTEM: 1.0.0beta23, (2021). https://doi.org/https://doi.org/10.5281/zenodo.5075527.

[169] J. Madsen, T. Susi, abTEM: ab Initio Transmission Electron Microscopy Image Simulation , Microsc. Microanal. 26 (2020) 448–450. https://doi.org/10.1017/s1431927620014701.

[170] T. Brink, Heterogeneities in metallic glasses. Atomistic computer simulations on the structure and mechanical properties of copper-zirconium alloys and composites, Technische Univ. Darmstadt (Germany)., 2017.

[171] A. Smolyanitsky, V.K. Tewary, Numerical simulation of nanoscale systems and materials, Elsevier Ltd., 2015. https://doi.org/10.1016/B978-1-78242-228-0.00003-X.

[172] M. Schaffer, B. Schaffer, Q. Ramasse, Sample preparation for atomic-resolution STEM at low voltages by FIB, Ultramicroscopy. 114 (2012) 62–71. https://doi.org/10.1016/j.ultramic.2012.01.005.

[173] C.A. Schneider, W.S. Rasband, K.W. Eliceiri, NIH Image to ImageJ: 25 years of image analysis, Nat. Methods. 9 (2012) 671–675. https://doi.org/10.1038/nmeth.2089.

[174] J.J.. Peters, Strain++: Measure strain in TEM images, (2021). https://jjppeters.github.io/Strainpp/.

[175] M.J. Hÿtch, E. Snoeck, R. Kilaas, Quantitative measurement of displacement and strain

fields from HREM micrographs, Ultramicroscopy. 74 (1998) 131–146. https://doi.org/10.1016/S0304-3991(98)00035-7.

[176] Y. Mishin, D. Farkas, M.J. Mehl, D.A. Papaconstantopoulos, Interatomic potentials for monoatomic metals from experimental data and ab initio calculations, Phys. Rev. B - Condens. Matter Mater. Phys. 59 (1999) 3393–3407. https://doi.org/10.1103/PhysRevB.59.3393.

[177] S. Plimpton, Fast parallel algorithms for short-range molecular dynamics, J. Comput. Phys. 117 (1995) 1–19. https://doi.org/10.1006/jcph.1995.1039.

[178] E. Suhir, Y.C. Lee, Micro- and Opto-Electronic Materials and Structures: Physics, Mechanics, Design, Reliability, Packaging, Springer, 2007. https://doi.org/https://doi.org/10.1007/0-387-32989-7.

[179] G. Haas, J.E. Waylonis, Optical Constants and Reflectance and Transmittance of Evaporated Aluminum in the Visible and Ultraviolet, J. Opt. Soc. Am. 51 (1961). https://doi.org/https://doi.org/10.1364/JOSA.51.000719.

[180] A.T. Voutsas, Y. Hibino, R. Pethe, E. Demaray, Structure engineering for hillock-free pure aluminum sputter deposition for gate and source line fabrication in active-matrix liquid crystal displays, J. Vac. Sci. Technol. A Vacuum, Surfaces, Film. 16 (1998) 2668–2677. https://doi.org/10.1116/1.581398.

[181] K.H. Guenther, Corrosion-resistant front surface aluminum mirror coatings, Opt. Eng. 32 (1993) 547. https://doi.org/10.1117/12.60845.

[182] C.W. Hollars, R.C. Dunn, Evaluation of thermal evaporation conditions used in coating aluminum on near-field fiber-optic probes, Rev. Sci. Instrum. 69 (1998) 1747–1752. https://doi.org/10.1063/1.1148836.

[183] H. Takatsuji, T. Arai, Pinholes in Al thin films: Their effects on TFT characteristics and a taguchi method analysis of their origins, Vacuum. 59 (2000) 606–613. https://doi.org/10.1016/s0042-207x(00)00323-7.

[184] F. Malik, Thin film interconnect processes, Thin Solid Films. 206 (1991) 70–75. https://doi.org/10.1016/0040-6090(91)90395-E.

[185] J.C. Doan, J.C. Bravman, P.A. Flinn, T.N. Marieb, The evolution of the resistance of aluminum interconnects during electromigration, Microelectron. Reliab. 40 (2000) 981–990. https://doi.org/10.1016/s0026-2714(99)00340-6.

[186] E. Abedi Esfahani, H. Salimijazi, M.A. Golozar, J. Mostaghimi, L. Pershin, Study of corrosion behavior of Arc sprayed aluminum coating on mild steel, J. Therm. Spray Technol. 21 (2012) 1195–1202. https://doi.org/10.1007/s11666-012-9810-x.

[187] K. Bordo, H.G. Rubahn, Effect of deposition rate on structure and surface morphology of thin evaporated al films on Dielectrics and Semiconductors, Medziagotyra. 18 (2012) 313–317. https://doi.org/10.5755/j01.ms.18.4.3088.

[188] G. Dehm, H. Edongué, T. Wagner, S.H. Oh, E. Arzt, Obtaining different orientation relationships for Cu films grown on (0001) α-Al2O3 substrates by magnetron sputtering, Zeitschrift Fuer Met. Res. Adv. Tech. 96 (2005) 249–254. https://doi.org/10.3139/146.101027.

[189] G. Dehm, B.J. Inkson, T. Wagner, Growth and microstructural stability of epitaxial Al films on (0001) α-Al 2 O 3 substrates, Acta Mater. 50 (2002) 5021–5032.

[190] I. Petrov, P.B. Barna, L. Hultman, J.E. Greene, Microstructural evolution during film growth, J. Vac. Sci. Technol. A Vacuum, Surfaces, Film. 21 (2003) S117–S128. https://doi.org/10.1116/1.1601610.

[191] F.M. Mwema, E.T. Akinlabi, O.P. Oladijo, J.D. Majumdar, Effect of varying low substrate temperature on sputtered aluminium films, Mater. Res. Express. 6 (2019). https://doi.org/10.1088/2053-1591/ab014a.

[192] F.H. Wang, C.L. Chang, Effect of substrate temperature on transparent conducting Al and F co-doped ZnO thin films prepared by rf magnetron sputtering, Appl. Surf. Sci. 370 (2016) 83–91. https://doi.org/10.1016/j.apsusc.2016.02.161.

[193] G. Ojeda-Barrero, A.I. Oliva-Avilés, A.I. Oliva, R.D. Maldonado, M. Acosta, G.M. Alonzo-Medina, Effect of the substrate temperature on the physical properties of sprayed-CdS films by using an automatized perfume atomizer, Mater. Sci. Semicond. Process. 79 (2018) 7–13. https://doi.org/10.1016/j.mssp.2018.01.018.

[194] S.C. Her, Y.H. Wang, Temperature effect on microstructure and mechanical properties of aluminum film deposited on glass substrates, Indian J. Eng. Mater. Sci. 22 (2015) 268–272.

[195] V. Devulapalli, H. Bishara, M. Ghidelli, G. Dehm, C.H. Liebscher, Influence of substrates and e-beam evaporation parameters on the microstructure of nanocrystalline and epitaxially grown Ti thin films, Appl. Surf. Sci. 562 (2021). https://doi.org/10.1016/j.apsusc.2021.150194.

[196] H. Bishara, S. Berger, Piezoelectric ultra-sensitive aluminum nitride thin film on flexible aluminum substrate, J. Mater. Sci. 53 (2018) 1246–1255. https://doi.org/10.1007/s10853-017-1566-8.

[197] K. Barmak, J. Kim, C.S. Kim, W.E. Archibald, G.S. Rohrer, A.D. Rollett, D. Kinderlehrer, S. Ta'Asan, H. Zhang, D.J. Srolovitz, Grain boundary energy and grain growth in Al films: Comparison of experiments and simulations, Scr. Mater. 54 (2006) 1059–1063. https://doi.org/10.1016/j.scriptamat.2005.11.060.

[198] J.G. Brons, G.B. Thompson, A comparison of grain boundary evolution during grain growth in fcc metals, Acta Mater. 61 (2013) 3936–3944. https://doi.org/10.1016/j.actamat.2013.02.057.

[199] G.S. Rohrer, X. Liu, J. Liu, A. Darbal, M.N. Kelly, X. Chen, M.A. Berkson, N.T. Nuhfer, K.R. Coffey, K. Barmak, The grain boundary character distribution of highly twinned nanocrystalline thin film aluminum compared to bulk microcrystalline aluminum, J. Mater. Sci. 52 (2017) 9819–9833. https://doi.org/10.1007/s10853-017-1112-8.

[200] E. Iwamura, T. Ohnishi, K. Yoshikawa, A study of hillock formation on AlTa alloy films for interconnections of TFT-LCDs, Thin Solid Films. 270 (1995) 450–455. https://doi.org/10.1016/0040-6090(96)80076-9.

[201] S.J. Hwang, W.D. Nix, Y.C. Joo, A model for hillock growth in Al thin films controlled by plastic deformation, Acta Mater. 55 (2007) 5297–5301. https://doi.org/10.1016/j.actamat.2007.05.046.

[202] S.W. Hieke, B. Breitbach, G. Dehm, C. Scheu, Microstructural evolution and solid state dewetting of epitaxial Al thin films on sapphire (α-Al2O3), Acta Mater. 133 (2017) 356–

366. https://doi.org/10.1016/j.actamat.2017.05.026.

[203] X. Zhang, J. Han, J.J. Plombon, A.P. Sutton, D.J. Srolovitz, J.J. Boland, Never Flat, Science (80-.). 400 (2017) 397–400.

[204] A.J. Francis, P.A. Salvador, Epitaxial growth of Cu(100) and Pt(100) thin films on perovskite substrates, Thin Solid Films. (2005).

[205] P.B. Barna, M. Adamik, Fundamental structure forming phenomena of polycrystalline films and the structure zone models, Thin Solid Films. 317 (1998) 27–33. https://doi.org/10.1016/S0040-6090(97)00503-8.

[206] H.T.G. Hentzell, D.A. Smith, C. Grovernor, The development of grain structure during growth of metallic thin films, Acta Metall. 32 (1984) 773–781.

[207] G. Knuyt, C. Quaeyhaegens, J. D'Haen, L.M. Stals, A quantitative model for the evolution from random orientation to a unique texture in PVD thin film growth, Thin Solid Films. 258 (1995) 159–169. https://doi.org/10.1016/0040-6090(94)06353-2.

[208] G. Knuyt, C. Quaeyhaegens, J. D'Haen, L.M. Stals, A model for thin film texture evolution driven by surface energy effects, Phys. Status Solidi Basic Res. 195 (1996) 179–193. https://doi.org/10.1002/pssb.2221950121.

[209] J. Rittner, D. Seidman, K. Merkle, Grain-boundary dissociation by the emission of stacking faults, Phys. Rev. B - Condens. Matter Mater. Phys. 53 (1996) R4241–R4244. https://doi.org/10.1103/PhysRevB.53.R4241.

[210] D.L. Medlin, S.M. Foiles, D. Cohen, A dislocation-based description of grain boundary dissociation: Application to a 90° 〈110〉 tilt boundary in gold, Acta Mater. 49 (2001) 3689–3697. https://doi.org/10.1016/S1359-6454(01)00284-1.

[211] R.G. Hoagland, R.J. Kurtz, The relation between grain-boundary structure and sliding resistance, Philos. Mag. A Phys. Condens. Matter, Struct. Defects Mech. Prop. 82 (2002) 1073–1092. https://doi.org/10.1080/01418610208240018.

[212] R.G. Hoagland, S.M. Valone, Emission of dislocations from grain boundaries by grain boundary dissociation, Philos. Mag. 95 (2015) 112–131.

https://doi.org/10.1080/14786435.2014.987842.

[213] G. Lu, E. Kaxiras, Can Vacancies Lubricate Dislocation Motion in Aluminum?, Phys. Rev. Lett. 89 (2002) 1–4. https://doi.org/10.1103/PhysRevLett.89.105501.

[214] S.G. Srinivasan, X.Z. Liao, M.I. Baskes, R.J. McCabe, Y.H. Zhao, Y.T. Zhu, Compact and dissociated dislocations in aluminum: Implications for deformation, Phys. Rev. Lett. 94 (2005) 1–4. https://doi.org/10.1103/PhysRevLett.94.125502.

[215] D. Hull, D.J. Bacon, Dislocations in Face-centred Cubic Metals, Introd. to Dislocations. (2001) 82–101. https://doi.org/10.1016/b978-075064681-9/50005-5.

[216] D.L. Medlin, K.F. McCarty, R.Q. Hwang, S.E. Guthrie, M.I. Baskes, Orientation relationships in heteroepitaxial aluminium films on sapphire, Thin Solid Films. 299 (1997) 110–114.

[217] D.L. Medlin, K. Hattar, J.A. Zimmerman, F. Abdeljawad, S.M. Foiles, Defect character at grain boundary facet junctions: Analysis of an asymmetric $\Sigma = 5$ grain boundary in Fe, Acta Mater. 124 (2017) 383–396. https://doi.org/10.1016/j.actamat.2016.11.017.

[218] H. Ichinose, Y. Ishida, N. Baba, K. Kanaya, Lattice imaging analysis of $\Sigma 3$ coincidence-site-lattice boundaries in gold, Philos. Mag. A Phys. Condens. Matter, Struct. Defects Mech. Prop. 52 (1985) 51–59. https://doi.org/10.1080/01418618508237605.

[219] W.M. Haynes, D.R. Lide, T.J. Bruno, CRC handbook of chemistry and physics, CRC Press/Taylor & Francis, 2016.

[220] W.M. Yim, R.J. Paff, Thermal expansion of AlN, sapphire, and silicon, J. Appl. Phys. 45 (1974) 1456–1457. https://doi.org/10.1063/1.1663432.

[221] C.A.M. Mulder, J.T. Klomp, On the internal structure OF Cu- qnd Pt-sapphire interfaces, Le J. Phys. Colloq. 46, No. C4 C4-111. 46 (1985) C4-111. https://doi.org/https://doi.org/10.1051/jphyscol:1985412.

[222] A.E. Romanov, T. Wagner, On the universal misfit parameter at mismatched interfaces, Scr. Mater. 45 (2001) 325–331. https://doi.org/10.1016/S1359-6462(01)01035-1.

[223] H. Meltzman, D. Mordehai, W.D. Kaplan, Solid-solid interface reconstruction at

equilibrated Ni-Al 2O 3 interfaces, Acta Mater. 60 (2012) 4359–4369. https://doi.org/10.1016/j.actamat.2012.04.037.

[224] I. Adlakha, M.A. Bhatia, M.A. Tschopp, K.N. Solanki, Atomic scale investigation of grain boundary structure role on intergranular deformation in aluminium, Philos. Mag. 94 (2014) 3445–3466. https://doi.org/10.1080/14786435.2014.961585.

[225] D.G. Brandon, The Structure of High-Angle Grain Boundaries in Aluminium, Phys. Status Solidi. 31 (1969) 193–201. https://doi.org/10.1002/pssb.19690310123.

[226] S. Ahmad, T. Brink, C.H. Liebscher, G. Dehm, Microstates and defects of incoherent Σ3 [111] twin boundaries in aluminum, Acta Mater. (2022). https://doi.org/https://doi.org/10.1016/j.actamat.2022.118499.

[227] N. Chistyakova, T.M.H. Tran, A study of the applicability of different types of interatomic potentials to compute elastic properties of metals with molecular dynamics methods, AIP Conf. Proc. 1772 (2016). https://doi.org/10.1063/1.4964599.

[228] L. Li, R.D. Kamachali, Z. Li, Z. Zhang, Grain boundary energy effect on grain boundary segregation in an equiatomic high-entropy alloy, Phys. Rev. Mater. 4 (2020) 53603. https://doi.org/10.1103/PhysRevMaterials.4.053603.

[229] S.A. Bojarski, J. Knighting, S.L. Ma, W. Lenthe, M.P. Harmer, G.S. Rohrer, The relationship between grain boundary energy, grain boundary complexion transitions, and grain size in Ca-doped Yttria, Mater. Sci. Forum. 753 (2013) 87–92. https://doi.org/10.4028/www.scientific.net/MSF.753.87.

[230] T. Brink, L. Langenohl, H. Bishara, G. Dehm, Universality of grain boundary phases in fcc metals: Case study on high-angle [111] symmetric tilt grain boundaries, Phys. Rev. B. 107 (2023). https://doi.org/10.1103/PhysRevB.107.054103.

[231] L. Frommeyer, T. Brink, R. Freitas, T. Frolov, G. Dehm, C.H. Liebscher, Dual phase patterning during a congruent grain boundary phase transition in elemental copper, (2021). http://arxiv.org/abs/2109.15192.

[232] M.L. de Bonfils-Lahovary, L. Laffont, C. Blanc, Characterization of intergranular corrosion defects in a 2024 T351 aluminium alloy, Corros. Sci. 119 (2017) 60–67.

https://doi.org/10.1016/j.corsci.2017.02.020.

[233] M.K. Rahman, A.M.M. Musa, B. Neher, K.A. Patwary, M.A. Rahman, M.S. Islam, A Review of the Study on the Electromigration and Power Electronics, J. Electron. Cool. Therm. Control. 06 (2016) 19–31. https://doi.org/10.4236/jectc.2016.61002.

[234] J. Liu, L.F. Allard, Surface channeling in aberration-corrected scanning transmission electron microscopy of nanostructures, Microsc. Microanal. 16 (2010) 425–433. https://doi.org/10.1017/S1431927610000450.

[235] S. Tian, J. Li, J. Zhang, Z. Wulabieke, D. Lv, Effect of Zr and Sc on microstructure and properties of 7136 aluminum alloy, J. Mater. Res. Technol. 8 (2019) 4130–4140. https://doi.org/10.1016/j.jmrt.2019.07.022.

[236] L.P.H. Jeurgens, W.G. Sloof, F.D. Tichelaar, E.J. Mittemeijer, Structure and morphology of aluminium-oxide films formed by thermal oxidation of aluminium, Thin Solid Films. 418 (2002) 89–101. https://doi.org/10.1016/S0040-6090(02)00787-3.

[237] S.W. Hieke, G. Dehm, C. Scheu, Annealing induced void formation in epitaxial Al thin films on sapphire (α-Al2O3), Acta Mater. 140 (2017) 355–365. https://doi.org/10.1016/j.actamat.2017.08.050.

[238] J.L. Murray, The aluminium-copper system, Int. Met. Rev. (1985) 211–234. https://doi.org/https://doi.org/10.1179/imtr.1985.30.1.211.

[239] J. Murray, A. Peruzzi, J.P. Abriata, The Al-Zr (aluminum-zirconium) system, J. Phase Equilibria. 13 (1992) 277–291. https://doi.org/10.1007/BF02667556.

[240] F. Czerwinski, Thermal stability of aluminum alloys, Materials (Basel). 13 (2020) 1–49. https://doi.org/10.3390/ma13153441.

[241] C.L. Briant, Solid solubility and grain boundary segregation, Philos. Mag. Lett. 73 (1996) 345–350. https://doi.org/10.1080/095008396180614.

[242] G. Ghosh, S. Vaynman, M. Asta, M.E. Fine, Stability and elastic properties of L12-(Al,Cu)3(Ti,Zr) phases: Ab initio calculations and experiments, Intermetallics. 15 (2007) 44–54. https://doi.org/10.1016/j.intermet.2006.03.003.

[243] H. Hu, M. Zhao, X. Wu, Z. Jia, R. Wang, W. Li, Q. Liu, The structural stability, mechanical properties and stacking fault energy of Al3Zr precipitates in Al-Cu-Zr alloys: HRTEM observations and first-principles calculations, J. Alloys Compd. 681 (2016) 96–108. https://doi.org/10.1016/j.jallcom.2016.04.178.

[244] E. Nes, Precipitation of the metastable cubic Al3Zr-phase in subperitectic Al-Zr alloys, Acta Metall. 20 (1972) 499–506. https://doi.org/10.1016/0001-6160(72)90005-3.

[245] P.B. Desch, R.B. Schwarz, P. Nash, Formation of metastable L12 phases in Al3Zr and Al-12.5%X-25%Zr (X ≡ Li, Cr, Fe, Ni, Cu), J. Less-Common Met. 168 (1991) 69–80. https://doi.org/10.1016/0022-5088(91)90035-3.

[246] A. V. Mikhaylovskaya, A.G. Mochugovskiy, V.S. Levchenko, N.Y. Tabachkova, W. Mufalo, V.K. Portnoy, Precipitation behavior of L12 Al3Zr phase in Al-Mg-Zr alloy, Mater. Charact. 139 (2018) 30–37. https://doi.org/10.1016/j.matchar.2018.02.030.

[247] K.E. Knipling, D.C. Dunand, D.N. Seidman, Precipitation evolution in Al-Zr and Al-Zr-Ti alloys during aging at 450-600 °C, Acta Mater. 56 (2008) 1182–1195. https://doi.org/10.1016/j.actamat.2007.11.011.

[248] D. Srinivasan, K. Chattopadhyay, Non-equilibrium transformations involving L12-Al3Zr in ternary Al-X-Zr alloys, Metall. Mater. Trans. A Phys. Metall. Mater. Sci. 36 A (2005) 311–320. https://doi.org/10.1007/s11661-005-0304-z.

[249] P.N.H. Nakashima, The Crystallography of Aluminum and Its Alloys, 2019. https://doi.org/10.1201/9781351045636-140000245.

[250] X.Y. Liu, F. Ercolessi, J.B. Adams, Aluminium interatomic potential from density functional theory calculations with improved stacking fault energy, Model. Simul. Mater. Sci. Eng. 12 (2004) 665–670. https://doi.org/10.1088/0965-0393/12/4/007.

[251] M.I. Mendelev, M.J. Kramer, C.A. Becker, M. Asta, Analysis of semi-empirical interatomic potentials appropriate for simulation of crystalline and liquid Al and Cu, Philos. Mag. 88 (2008) 1723–1750. https://doi.org/10.1080/14786430802206482.

[252] J.B. Sturgeon, B.B. Laird, Adjusting the melting point of a model system via Gibbs-Duhem integration: Application to a model of aluminum, Phys. Rev. B - Condens. Matter Mater.

Phys. 62 (2000) 14720–14727. https://doi.org/10.1103/PhysRevB.62.14720.

[253] X.W. Zhou, R.A. Johnson, H.N.G. Wadley, Misfit-energy-increasing dislocations in vapor-deposited CoFe/NiFe multilayers, Phys. Rev. B - Condens. Matter Mater. Phys. 69 (2004) 1–10. https://doi.org/10.1103/PhysRevB.69.144113.

[254] G. Kresse, J. Hafner, Ab initio molecular dynamics for liquid metals, Phys. Rev. B. 47 (1993) 558–561. https://doi.org/10.1103/PhysRevB.47.558.

[255] G. Kresse, J. Hafner, Ab initio molecular-dynamics simulation of the liquid-metalamorphous- semiconductor transition in germanium, Phys. Rev. B. 49 (1994) 14251–14269. https://doi.org/10.1103/PhysRevB.49.14251.

[256] G. Kresse, J. Furthmüller, Efficiency of ab-initio total energy calculations for metals and semiconductors using a plane-wave basis set, Comput. Mater. Sci. 6 (1996) 15–50. https://doi.org/10.1016/0927-0256(96)00008-0.

[257] G. Kresse, J. Furthmüller, Efficient iterative schemes for ab initio total-energy calculations using a plane-wave basis set, J. Phys. Chem. A. 124 (1996) 4053–4061. https://doi.org/10.1021/acs.jpca.0c01375.

[258] J. Janssen, S. Surendralal, Y. Lysogorskiy, M. Todorova, T. Hickel, R. Drautz, J. Neugebauer, pyiron: An integrated development environment for computational materials science, Comput. Mater. Sci. 163 (2019) 24–36. https://doi.org/10.1016/j.commatsci.2018.07.043.

[259] P.E. Blöchl, Projector augmented-wave method, Phys. Rev. B. 50 (1994) 17953–17979. https://doi.org/10.1103/PhysRevB.50.17953.

[260] J.P. Perdew, K. Burke, M. Ernzerhof, Generalized gradient approximation made simple, Phys. Rev. Lett. 77 (1996) 3865–3868. https://doi.org/10.1103/PhysRevLett.77.3865.

[261] G. Kresse, D. Joubert, From ultrasoft pseudopotentials to the projector augmented-wave method, Phys. Rev. B - Condens. Matter Mater. Phys. 59 (1999) 1758–1775. https://doi.org/10.1103/PhysRevB.59.1758.

[262] H.J. Monkhrost, J.D. Pack, Special points for Brillonin-zone integrations, Phys. Rev. B.

(1976) 2156–2164. https://doi.org/https://doi.org/10.1103/PhysRevB.13.5188.

Scientific Curriculum Vitae

Personal Information

Name: Saba

Date of Birth: 18th October, 1993

Place of Birth: Bijnor (Nagina), India

Nationality: Indian

Education

2012   **Senior Secondary school**

St. Mary's convent senior secondary school, Dhampur (India)

2012-2016   **Bachelor study**

(*Materials science and metallurgical Engineering*)

Degree: Bachelors in Technology

Chhatrapati Shahu Ji Maharaj University, Kanpur (India)

2015-2016   **Bachelor Thesis**

(*Improving the stress corrosion cracking resistance of Inconel 600 alloy through modification in grain boundary character distribution*)

Indian Institute of Technology, Kanpur (India)

Advisor: Dr. Shashank shekhar

2016-2018   **Master study**

(*Materials Engineering*)

Degree: Masters in technology

Indian Institute of Technology, Roorkee (India)

2017-2018   **Master Thesis (through DAAD fellowship)**

(*The Chemical Transport Mechanism of emitter- micro particles in tungsten (W) electrode- A metallurgical study*)

Technical University of Dresden (Germany)

Advisor: Prof. Dr. Habil Uwe Fuessel and Prof. P.K. Ghosh

2018-2023   **PhD Dissertation**

(*Fundamental investigation of the atomic structures of [111] tilt grain boundaries, their defects and segregation behaviour in pure and alloyed Al*)

Ruhr Universität Bochum (Germany) / Fakultät für Maschinenbau

Advisor: Prof. Dr. Gerhard Dehm

Advanced Training

2021   Electron energy loss spectroscopy Workshop from Gatan (Online)

Publications

2021   Prabhakar, J.M., Varanasi, R.S., da Silva, C.C., **Ahmad S.**, de Vooys, A., Erbe, A. and Rohwerder, M., 2021. Chromium coatings

166

from trivalent chromium plating baths: Characterization and cathodic delamination behaviour. Corrosion Science, 187.

2022   **Ahmad S.**, Brink T., Liebscher C.H., and Dehm. G., 2022. Microstates and defects of incoherent Σ3 [111] tilt boundaries in Al. Acta Materialia. p.118499.

2022   Siyuan Z., Xie Z., Keuter P., **Ahmad S.**, Abdellaoui L., Zhou X., Cautaerts N., Breitbach B., Aliramaji S., Kerzel S.K., Hans M., Schneider J.M. and Scheu C., 2022. Atomistic structures of ⟨0001⟩tilt grain boundaries in a textured Mg thin film. Nanoscale, 187.

Conference contribution

Oral presentation

2020   Ahmad, S.; Liebscher, C.; Dehm, G.: *To decipher the novel atomic structure of [111] tilt grain boundaries in Al*. Material Science and Engineering Congress - MSE 2020, virtual, Darmstadt, Germany (2020)

Poster presentation

2019   Ahmad, S.; Meiners, T.; Frolov, T.; Liebscher, C.; Dehm, G.: *Grain boundary structure and phase transitions in Cu and Al [111] tilt grain boundaries*. International Workshop on Advanced and In-situ Microscopies of Functional Nanomaterials and

Devices, IAMNano, Düsseldorf, Germany (2019)

2021   Ahmad, S.; Liebscher, C.; Dehm, G.: *Strain-Induced phase transition in Σ3 [111] (211) tilt grain boundaries in Al*. Microscopy conference Joint Meeting of Dreiländertagungn & Multinational Congress on Microscopy MC 2021, virtual, Vienna, Austria (2021)

2021   Ahmad, S.; Liebscher, C.; Dehm, G.: *Exploration of atomic structures in Σ3 [111] Al tilt grain boundaries*. Sixth Conference on Frontiers of Aberration Corrected Electron Microscopy PICO (2021), virtual

Achievements

2016   Awarded academic excellence award in 2016 for highest CGPA in Bachelors

2016-2017   Awarded MHRD fellowship by ministry of high education in India

2017-2018   Awarded IIT-MSP DAAD fellowship for Master's Thesis in TU Dresden

2021   Best poster award – at MC 2021 conference (Virtual)

20th January 2023